

**SILESIAIAN UNIVERSITY OF TECHNOLOGY**

Faculty of Mechanical Engineering



**Silesian  
University  
of Technology**

**MSc. Eng. Adam SKOWRONEK**

**DOCTORAL DISSERTATION**

**Improvement of the ductility of high-strength medium-Mn steels  
through intercritical annealing**

**Supervisor  
Professor Adam Grajcar**

**GLIWICE, POLAND, 2023**

*I would like to express my heartfelt gratitude to Professor Adam Grajcar for his invaluable guidance and support throughout the implementation of my doctoral thesis.*

*Professor Grajcar has been an exceptional scientific mentor, providing me with valuable insights and constructive feedback that have greatly contributed to the development and success of my research.*

*I would also like to thank the research centers:  
Łukasiewicz – Upper Silesian Institute of Technology, Gliwice, Poland,  
The National Center for Metallurgical Research, Madrid, Spain,  
and Ghent University, Ghent, Belgium,  
for support in my research.*

*The work was partially financially supported by the European Social Fund,  
grant InterPOWER (POWR.03.05.00-00-Z305).*

## List of symbols and abbreviations

<i>A</i>	<i>Austenite</i>	<i>PLC</i>	<i>Portevin-Le Chatelier effect</i>
<i>AHSS</i>	<i>Advanced High Strength Steels</i>	<i>Q&amp;P</i>	<i>Quenching and partitioning steels</i>
<i>B</i>	<i>Bainite</i>	<i>RA</i>	<i>Retained austenite</i>
<i>BH</i>	<i>Bake hardenable</i>	<i>RCL</i>	<i>Relative change in length</i>
<i>CI</i>	<i>Confidence index</i>	<i>SEDDQ</i>	<i>Super extra deep drawing quality</i>
<i>DP</i>	<i>Dual phase steels</i>	<i>SEM</i>	<i>Scanning electron microscopy</i>
<i>DSA</i>	<i>Dynamic strain aging</i>	<i>SFE</i>	<i>Stacking fault energy</i>
<i>EBSD</i>	<i>Electron backscatter diffraction</i>	<i>SIMT</i>	<i>Strain-induced martensitic transformation</i>
<i>EDS</i>	<i>Energy-dispersive spectroscopy</i>	<i>SIP</i>	<i>Shear band induced plasticity</i>
<i>F</i>	<i>Ferrite</i>	<i>TEL</i>	<i>Total elongation</i>
<i>F<sub>B</sub></i>	<i>Bainitic ferrite</i>	<i>TEM</i>	<i>Transmission electron microscopy</i>
<i>HER</i>	<i>Hole expansion ratio</i>	<i>TRIP</i>	<i>Transformation-induced plasticity</i>
<i>HS-IF</i>	<i>High strength interstitial free steels</i>	<i>TWIP</i>	<i>Twinning-induced plasticity</i>
<i>HSLA</i>	<i>High strength low alloy steels</i>	<i>UEL</i>	<i>Uniform elongation</i>
<i>IF</i>	<i>Interstitial free steels</i>	<i>UTS</i>	<i>Ultimate tensile strength</i>
<i>IQ</i>	<i>Image quality</i>	<i>XRD</i>	<i>X-ray diffraction</i>
<i>KAM</i>	<i>Kernel average misorientation</i>	<i>YS</i>	<i>Yield strength</i>
<i>M<sub>F</sub></i>	<i>Fresh martensite</i>	<i>θ</i>	<i>Carbides</i>
<i>M<sub>f</sub></i>	<i>Martensite finish temperature</i>	<i>α<sub>L</sub></i>	<i>Linear thermal expansion coefficient</i>
<i>M<sub>s</sub></i>	<i>Martensite start temperature</i>	<i>σ/σ<sub>T</sub></i>	<i>Stress / True stress</i>
<i>M<sub>T</sub></i>	<i>Tempered martensite</i>	<i>ε/ε<sub>T</sub></i>	<i>Strain / True strain</i>

# List of contents

<b>1. Introduction.....</b>	<b>7</b>
<b>2. State of the art.....</b>	<b>9</b>
2.1. Development of car body steel sheets .....	9
2.1.1. Conventional car body sheet steels.....	12
2.1.2. 1 <sup>st</sup> generation AHSS .....	13
2.1.3. 2 <sup>nd</sup> generation AHSS.....	16
2.1.4. 3 <sup>rd</sup> generation AHSS .....	19
2.2. Physical metallurgy and manufacturing technology of medium-Mn steels .....	21
2.2.1. Design of chemical composition .....	21
2.2.2. Technological challenges.....	24
2.2.3. Thermomechanical processing of medium-Mn steels .....	26
2.2.4. Intercritical annealing of medium-Mn steels .....	29
2.2.5. Intercritical annealing of hot-rolled steel sheets .....	30
2.2.6. Intercritical annealing of cold-rolled steel sheets .....	31
2.3. Effect of heat treatment on the microstructure and mechanical properties of intercritically annealed medium-Mn steels.....	34
2.3.1. Effect of heating rate in intercritical annealing .....	39
2.3.2. Effect of soaking temperature in intercritical annealing.....	40
2.3.3. Effect of soaking time in intercritical annealing.....	44
2.3.4. Effect of cooling rate in intercritical annealing .....	46
2.4. Summary of the state of art.....	46
<b>3. Experimental procedure .....</b>	<b>48</b>
3.1. Investigated material.....	48
3.2. Purpose and thesis of the work .....	49
3.3. Methodology.....	52
3.3.1. Simulations .....	54

3.3.2.	Dilatometry .....	54
3.3.3.	Investigations of mechanical properties .....	55
3.3.4.	Microstructural characterization .....	56
<b>4.</b>	<b>Modeling and experimental determination of critical temperatures of analyzed steel during heating and cooling.....</b>	<b>60</b>
4.1.	Experiment design .....	60
4.2.	Results .....	60
4.2.1.	Simulation results .....	60
4.2.2.	Dilatometric characterization.....	62
4.3.	Discussion.....	63
<b>5.</b>	<b>Influence of intercritical annealing temperature on microstructure and mechanical properties of steel .....</b>	<b>65</b>
5.1.	Experiment design .....	65
5.2.	Results .....	66
5.2.1.	Simulation results .....	66
5.2.2.	Dilatometric characterization.....	68
5.2.3.	Fraction and chemical composition of retained austenite.....	70
5.2.4.	Microstructural characterization .....	72
5.2.5.	Mechanical properties.....	78
5.3.	Discussion.....	80
5.3.1.	Comparison of simulations and the experimental approach.....	80
5.3.2.	Impact of the microstructural changes on the mechanical performance .....	81
<b>6.</b>	<b>Influence of intercritical soaking time on microstructure and mechanical properties of steel.....</b>	<b>84</b>
6.1.	Experiment design .....	84
6.2.	Results .....	85
6.2.1.	Dilatometric characterization.....	85
6.2.2.	Microstructural characterization .....	86

6.2.3. Fraction and stability of retained austenite .....	95
6.2.4. Mechanical properties.....	99
6.2.5. Properties and microstructure of post-tensile samples .....	101
6.3. Discussion.....	107
6.3.1. Impact of the phase composition on mechanical performance.....	107
6.3.2. Local stability of retained austenite controlled by its grain size.....	109
<b>7. Summary and general conclusions.....</b>	<b>113</b>
<b>References.....</b>	<b>118</b>
<b>Abstract .....</b>	<b>137</b>
<b>Streszczenie .....</b>	<b>138</b>
<b>Streszczenie poszerzone.....</b>	<b>139</b>

## **1. Introduction**

The automotive industry is a rapidly developing sector of the global economy. Intense competition in the market and the use of new low-density materials such as aluminium and magnesium alloys, polymers, and composite materials have challenged the steel manufacturers in the past two decades. A renewed focus on the role of individual chemical elements commonly used in steels and the potential of use of modern metallurgical technologies, metallurgical processing, and advanced heat treatment methods has led to the development of various types of steels with a wide range of mechanical properties and formability. The strength-to-density ratio is crucial as it determines the weight of the vehicle and subsequently the fuel consumption and ecological impact of exhaust emissions. While light-metal alloys have gained a larger share in the automotive industry, approximately 60 % of a car's weight is still composed of structural elements made from steel sheets with high strength, good plasticity and formability [1].

The significant reduction in the weight of cars over the last 40 years has been obtained due to the development of new steel grades. First, High Strength Low Alloy steels (HSLA) with a ferritic-pearlitic, ferritic-bainitic, bainitic or tempered martensite structure were designed. The next big step forward was the development of multi-phase steels, the most popular group of which are currently dual phase (DP) steels, whose microstructure consists of ferrite and martensite [2].

The limitation of the conventional steels is the decreasing plasticity with increasing strength. Since the early 1990s, the automotive industry has been in great demand for steels that combine high strength and good plasticity. A breakthrough step was the incorporation of metastable retained austenite (RA) into the steel microstructure. Thanks to its strain-induced martensitic transformation (SIMT), it was possible to obtain unprecedented strain hardening in steel products. This allowed to effectively delay the formation of the neck and thus increase the plasticity, while maintaining high strength or even its simultaneous increase. It opened the way to production of materials with new levels of properties. A new approach to the design of the chemical composition and heat treatment resulted in the development of Advanced High Strength Steels (AHSS) [3]. They allowed to overcome the dependence typical for conventional steels, where plasticity decreases with increasing strength.

However, the research and development of steels containing retained austenite has also led to number of dead ends. Examples can include:

- Austenitic high-Mn steels (2<sup>nd</sup> generation AHSS) despite excellent mechanical properties, turned out to be uneconomical and burdened with technological problems [4],
- Thermomechanically treated medium-Mn steels despite advanced chemical and processing design did not live up to their expectations, which is manifested by their limited plasticity [5].

The issue of austenite stabilization consists of numerous threads and factors that, despite many years of development of steel with this structural constituent, still have not been properly explained. It is necessary to take full advantage of the SIMT and thus the enhanced strain hardening by better understanding and controlling a fraction and stability of RA.

New types of steels such as medium-Mn steels belonging to 3<sup>rd</sup> generation of AHSS and heat treatment, such as intercritical annealing, are currently under intensive development [6]. The formation of multiphase steels with the appropriate proportion, arrangement, morphology, and stability of individual structural constituents requires both the precise chemical composition design and appropriate control of parameters during metal processing, especially heat-treatment operations. This effort has the potential to enable the production of new types of steel, whose combination of mechanical properties will be unmatched among all currently used construction materials. All these features of medium-Mn steels may be obtained at production costs similar to that of typical materials in the automotive industry.

## **2. State of the art**

### **2.1. Development of car body steel sheets**

At the beginning of the automotive industry steels with low strength and high plasticity were used for both structural parts and functional elements. They were characterized by good formability, weldability and paintability. This determined the design of simple production processes as well as enabled quick and cheap repair of finished elements. The strength of these steels usually did not exceed 350 MPa [7].

The year 1975 turned out to be critical in terms of materials used in the automotive industry. This year, a global oil crisis started. It caused strong, worldwide pressure to reduce the consumption of non-renewable energy sources. This pushed manufacturers towards more durable materials (creation of high-strength micro-alloyed HSLA steels [8], and dual-phase DP steels [9]). This has enabled the production of thinner and thus lighter components while maintaining or increasing the overall strength. Although the oil crisis ended relatively quickly, it had a very large impact on the automotive industry, which continues to this day [2,7].

Since 1975, the aspect aimed at reducing fuel consumption has evolved into ecological pursuits. The society forced the introduction of standards regulating the amount of exhaust gases emitted. As a consequence, the automotive industry is under increasing pressure forcing manufacturers to reduce their environmental impact (Figure 1). Drawing conclusions from the beginnings of the automotive industry, the aspect of safety was also introduced. Consumers are demanding safe cars, and officials are responding with new tests and standards that affect car designs and used materials [2,7,10].

Ever-increasing demands have forced the industry to develop intensively, which has been accomplished with the help of a number of international projects bringing together leaders in the auto body sheet industry: Ultralight Steel Auto Body (ULSAB), Ultralight Steel Auto Closure (ULSAC), Ultralight Steel Auto Suspension (ULSAS) and Advanced Vehicle Concepts (ULSAB-AVC). These projects aimed at creating designs of modern constructions: body-in-white, closure and suspension that would meet stringent weight and safety requirements. The culmination of this cycle was the FutureSteelVehicle project launched in 2008. Its goal was to further develop body materials towards Advanced High Strength Steels (AHSS) - a group of modern, multiphase steels invented at the beginning of ULSAB project. The project brought an increase in the strength of steel used in the automotive industry to a level exceeding 1 GPa. This allowed to reduce the weight of the car body by approx. 39 %, while limiting pollution during the product life cycle at the level of 60 % [2,7].

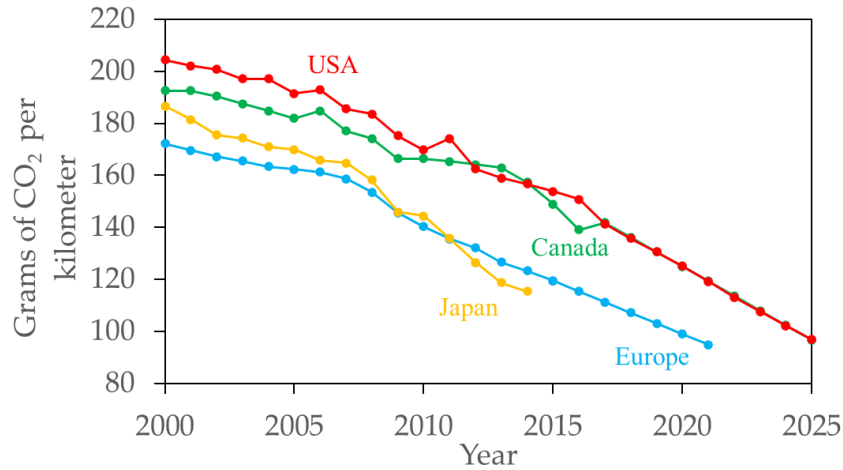


Figure 1 Global emissions regulations [11].

Nowadays, the trend of material development in the aspect of autobody is still strong, as evidenced by the latest project - The Light Vehicle 2025 (2018) [12]. It focuses on the further development of all the previously mentioned aspects. However, it introduces an additional issue regarding electromobility and autonomy of land traffic vehicles - trends towards which the automotive industry is currently heading. In addition, it also emphasizes the use of modeling in conjunction with numerical simulations during the design process.

The development of materials goes hand in hand with progress of automotive industry, responding to ever new requirements. To sum up, three main aspects affecting the issue of car body sheets can be distinguished:

- Reduction of the amount of exhaust gases emitted to the environment by the weight reduction of the car body,
- Improvement of passenger safety through appropriate design of the car structure and the use of energy-absorbing materials,
- The use of materials characterized by high stiffness, and at the same time good formability and weldability.

The result is the creation and continuous development of a whole range of modern steels for the automotive industry (Figure 2), which are characterized by a wide range of strength and plastic properties. They are designed to fulfil the requirements for specific elements of the vehicle structure (Figure 3). The front and rear zones (crumple zones) have to be made of high strength but ductile materials, which are able to absorb the impact energy. The passenger area

(safety cage) cannot be deformed, thus guaranteeing safety. Therefore, it has to be constructed of ultra high strength and stiff materials.

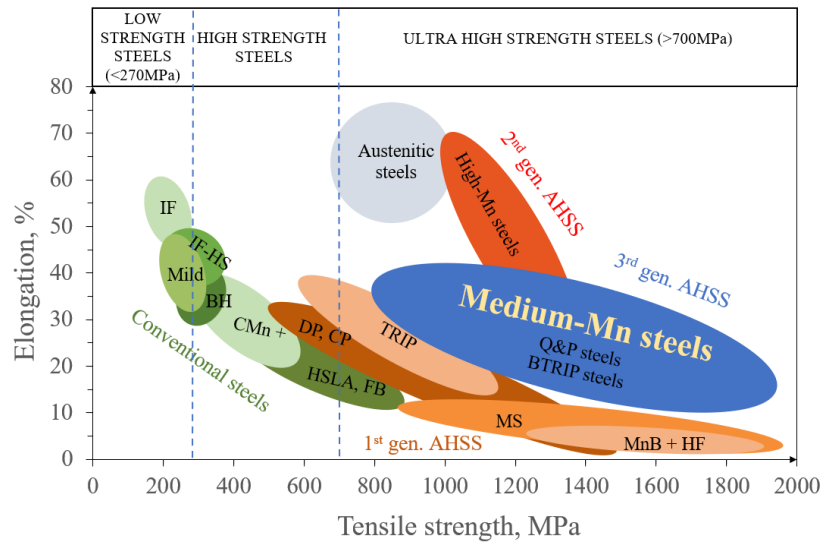


Figure 2 The strength – ductility diagram illustrating the range of mechanical properties available for today’s car body steels [2,13].

Current automotive steels are divided into several groups created with the development of the industry: Conventional car body sheet steels, Multiphase car body sheet steels [7], High-manganese car body sheet steels [14] and Medium-Mn car body sheet steels [15]. The main strategy when designing new materials of these groups is to improve the strength of the materials without compromising their ductility [2].



Figure 3 Steel types used in car body [16].

### **2.1.1. Conventional car body sheet steels**

The first steels referred to as car body materials were alloys showing very good plastic properties but at the expense of limited strength. At present, attention is focused on the introduction of increasingly durable materials in this area. Despite this, low-strength body steels are still widely used for lightly loaded or unloaded vehicle components. The main feature determining this use is their good deep drawing ability. There are several basic groups among conventional body steels [17–19]:

In the past, **Mild steels** were the most commonly used materials for car body construction. They contain carbon in the range of 0.015 % to 0.1 wt. %, which dominates their drawability class. Apart from this element, they contain only impurities (P and S), aluminium and 0.25 % to 0.6 % of manganese - which strengthens ferrite. Aluminium is added to deoxidize these steels, which has the additional effect of binding nitrogen in the AlN compound. This greatly reduces the susceptibility of these steels to aging. Steel strips are most often produced as cold-rolled and annealed both in batch and continuous lines. The ultimate tensile strength (UTS) of these steels usually does not exceed 400 MPa, and the total elongation (TEL) ranges from 28 % to 40 % [18,20].

**Interstitial free steels (IF)** also called extra deep drawing quality (EDDQ) are characterized by the lowest level of interstitial elements (below 0.004 wt.%) among all auto body steels. Such low carbon and nitrogen contents are obtained by vacuum degassing. The use of titanium and niobium (up to 0.025 %) affects the complete binding of C and N into stable carbonitrides. Due to the very small additions of elements other than iron in the steel, the resulting precipitates are so fine that they do not spoil the quality of the sheet surface. The removal of interstitial atoms from the solution results in the excellent deep drawing of IF steels. These steels are characterized by yield strength YS of 140 MPa to 220 MPa, UTS from 230 MPa to 300 MPa, TEL from 37 % to 50 % and Lankford coefficient  $r \leq 2$ . A characteristic feature of these steels is the lack of strain aging through the precipitation of cementite. This avoids overaging, which is needed in case of mild steels [10].

**High Strength Interstitial Free (HS-IF)** steels are a development of IF steels. Increased strength of these steels is obtained by intense solution hardening and precipitation hardening. This is possible due to the use of increased concentrations of Mn, Si and P. The tensile strength of these steels can reach 390 MPa. The tendency to segregate phosphorus at grain boundaries is leveled by the addition of boron. On the other hand, the intensification of the precipitation strengthening effect is obtained by increasing the content of Ti and Nb [21].

**Bake Hardenable (BH)** steels containing carbon in the range from 0.01 % to 0.08 % are solution strengthened with Mn, Si and P. There is also some precipitation strengthening through NbC particles. A characteristic feature of these steels is their strengthening (YS increase by 30 MPa to 60 MPa) during the paint-baking operation at a temperature of approx. 170 °C. The reason for this is the segregation of C atoms into dislocations amplified during the pressing process. This type of steel hardening has little effect on UTS. In the as-delivered condition, the steel therefore has good formability through cold plastic deformation and is relatively soft. However, the finished product has a much higher yield point. This results in a relatively good combination of very good deep drawing with increased strength. These steels are characterized by yield strength of 180 MPa to 240 MPa, tensile strength from 310 MPa to 360 MPa, total elongation from 36 % to 42 % and Lankford coefficient  $r$  of about 1.6 [7].

**C-Mn steels** are conventional unalloyed steels. They are characterized by a ferritic structure with a small proportion of pearlite. The plastic properties of these steels depend mainly on the content of carbon and manganese, used in the range of 0.5 % to 1 % [18,20].

**HSLA steels (High Strength Low Alloy)** have found an important place in the automotive industry. They are a next stage of C-Mn steel development. HSLA steels contain manganese up to 1.8 % and elements with high affinity to C and N, such as Nb, Ti and V. The total content of these microalloying elements usually does not exceed 0.2 %. Metallic elements form dispersed particles of carbonitrides with carbon and nitrogen during hot working. This results in precipitation strengthening and limitation of austenite grain growth during multi-pass rolling. It leads to obtaining fine-grained microstructures of the finished material [18,21].

### **2.1.2. 1<sup>st</sup> generation AHSS**

Despite the continuous development of conventional body steels, their use over the years has been limited to low-load or unloaded components. Conventional methods of increasing strength, such as solution, dislocation or precipitation strengthening reduce the ductility and increase the ductile to brittle transition temperature. Studies on a new group of steels consisting of at least two phases have led to the development of steels combining properties of each phase and resulted in materials with increased strength and ductility, at the same time. These steels are called Advanced High Strength Steels (AHSS). Their properties depend on a type, morphology, and what is most important on a volume fraction, grain size and distribution of individual phases. Additionally, retained austenite (RA) present in the microstructure of some grades of those steels exhibits metastability, which results in its martensitic transformation under loading. This leads to significantly increased strain hardening resulting in necking delay.

The most common structural constituents of multiphase steels are ferrite (F), bainite (B), tempered martensite ( $M_T$ ), fresh martensite ( $M_F$ ) and retained austenite (RA). Multiphase steels can be both cold- and hot-rolled as well as coated. They are usually characterized by the continuous yielding, relatively high uniform elongation, a small ratio of YS to UTS and high energy absorption capacity during dynamic deformation [2,19,21].

The main groups of multi-phase automotive sheet steels are:

**Dual Phase (DP)** steels were the first group of the AHSS family [22]. Their name is associated with the structure consisting of fine-grained ferrite and islands of hard martensite [23]. DP steels are produced by controlled cooling from the austenite region (in the case of hot-rolled) or by the intercritical annealing (a temperature range in which the F + A phase equilibrium exists). The purpose of this is first to obtain a ferritic – austenitic microstructure (by controlled cooling from finishing rolling temperature or intercritical annealing). Next, during final cooling austenite undergoes martensitic transformation resulting in final ferritic-martensitic microstructures. The basic chemical addition of these steels is carbon. It affects the critical temperatures and transformation kinetics, determining the final microstructure and mechanical properties. Due to the deterioration of steel weldability with increasing carbon content, its content in DP steels does not exceed 0.2 % (usually it is below 0.15 %). Important elements in these steels are also Mn and Si. Silicon promotes the formation of ferrite, while Mn delays the start of pearlitic and bainitic transformations. This facilitates the formation of martensite in the steel [24].

These steels, in addition to high tensile strength, are characterized by the lack of discontinuous yielding and a small  $r$  coefficient. They also show susceptibility to strengthening during paint-baking of up to 100 MPa, like BH steels. Due to the mentioned properties, DP steels are characterized by very good formability. In addition, due to the high strain hardening rate, the yield strength of cold-formed products is usually over 500 MPa [2,25]. Therefore, they are widely used in the automotive industry.

**Transformation-Induced Plasticity (TRIP)** steels are the first group that exhibits improved properties mainly due to the presence of retained austenite [26]. The introduction of intercritical annealing to heat treatment of modern steels has started new philosophy of phase stability and transformation [27]. As each phase exhibits different solubility of chemical elements, their redistribution at the intercritical temperature range is possible. The intercritical annealing in DP steels was used to control A to F ratio. In TRIP steels it is used also to stabilize high temperature austenite by its enrichment first in C and next in Mn, which allows to maintain

this phase partially to room temperature [23]. The conventional TRIP steels are composed of 50 % to 60 % of ferrite, 25 % to 40 % of bainite and 5 % to 15 % of retained austenite [28]. Retained austenite was introduced to steels to allow for Strain-Induced Martensitic Transformation (SIMT) (Figure 4) [29], which increases significantly the strain hardening rate [30]. This leads to a delay of neck formation in the deformed material and increases the uniform elongation. Typical TRIP steels have a tensile strength of 600 MPa to 1000 MPa, with a UTS x TEL product of approximately 20 GPa%. They also exhibit high fracture toughness and fatigue strength. This is due to the martensitic transformation taking place at the crack tip. It causes the blunting of the crack tip and the generation of compressive stresses in front of it due to the increase in volume accompanying this transformation [2,10,21].

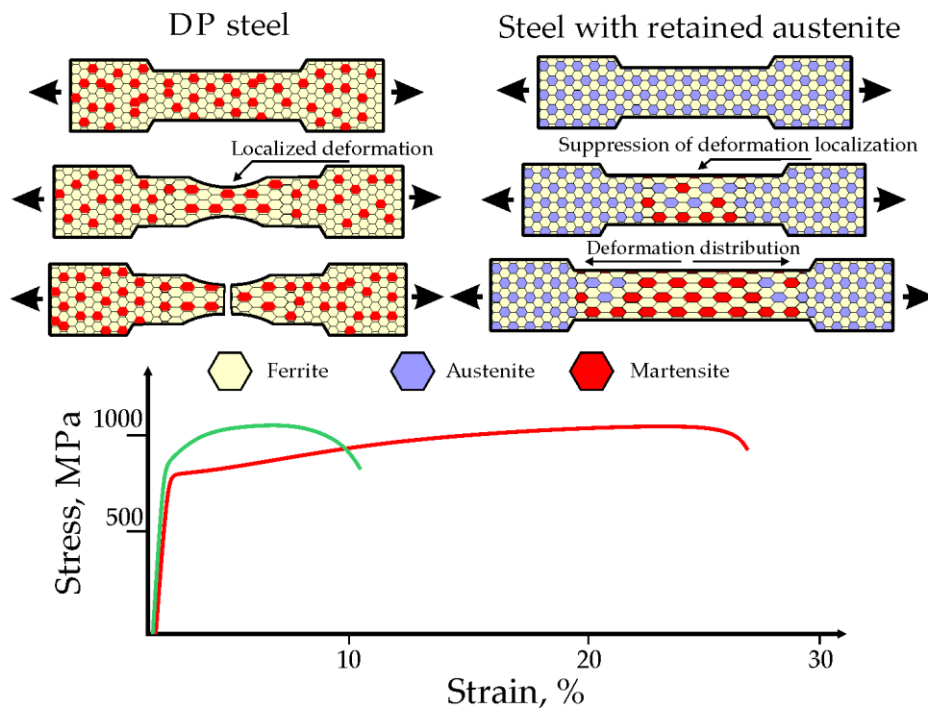


Figure 4 Scheme of the SIMT effect and resulting plastic properties [6].

To obtain austenite stable at room temperature in conventional TRIP steels, it is necessary to enrich it with carbon. This element lowers the  $M_s$  temperature, preventing the martensitic transformation during cooling. Therefore, the heat treatment is a critical step in the manufacturing of TRIP steels. In the first stage, it consists of annealing at the temperature between  $A_{c1}$  and  $A_{c3}$  (intercritical range) to obtain austenitic-ferritic microstructure as it is the case for DP steels. Carbon from a formed ferrite enriches austenite; however, its amount is not enough to stabilize remaining austenite. Therefore, the next stage consists of cooling the steel

to a temperature of approx. 400°C in order to partially transform austenite into bainitic ferrite ( $F_B$ ), which does not contain carbides. This allows the remaining part of the austenite to be enriched and stabilized by the additional carbon from bainitic ferrite. At the time of final cooling of the material, the austenite does not transform to martensite, thus determining the desired microstructure [7,18]. The carbide-free bainite is obtained by enriching the alloy composition with Si and/or Al. Carbon in such type of bainite is not localized in carbides but enriches the austenite (at least partially).

### 2.1.3. 2<sup>nd</sup> generation AHSS

Clear benefits from the presence of retained austenite in the microstructure started research into its wider application. Increasing the content of carbon in steel, as an element strongly stabilizing austenite, was not possible due to the deteriorating effect on steel weldability. For this reason, an increased content of Mn was added into the chemical composition, which has stabilizing properties similar to carbon.

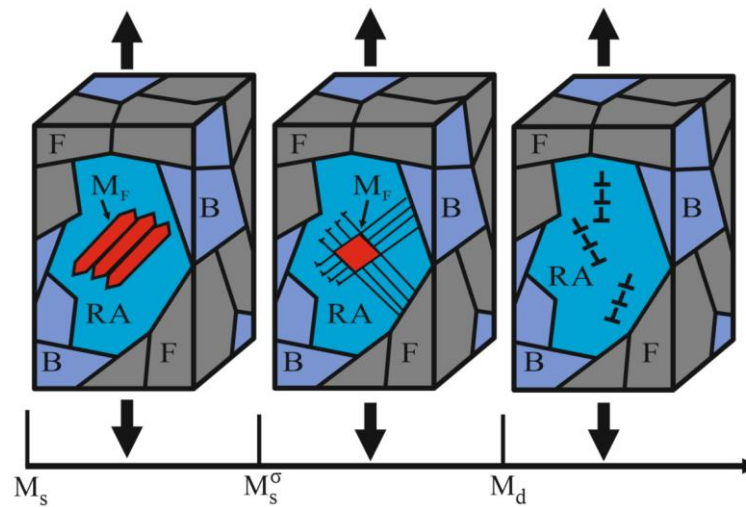


Figure 5 A scheme of mechanisms occurring in various temperature ranges, from the left: stress-induced plasticity; strain-induced plasticity; dislocation glide plasticity [31].

The result of these activities was the development of high-manganese steels. These steels contain from 15 wt.% to 30 wt.% of Mn, which allows the full stabilization of austenite to room temperature [32]. The main advantage of high-Mn steels over multi-phase steels results from the particularly high susceptibility of austenite to SIMT and intense mechanical twinning [33]. As a result, both high tensile strength of 600 MPa to 1000 MPa and very high elongation of 60 % to 100 % are obtained, with the value of  $YS \times TEI$  in the range of 40 GPa% to 80 GPa%

[34,35]. They are therefore characterized by a special ability to absorb energy (e.g., in crush events). Depending on the chemical composition affecting the  $M_s$  temperature of the steel, the dominant strengthening mechanism of these steels changes (Figure 5) [36]. For this reason, we distinguish 3 groups of high-manganese multiphase steels [4,14,37]:

**High-manganese TRIP steels** contain less than 25 % manganese. In this case, the main strengthening mechanism is the TRIP effect, which is a strengthening of steel as a result of martensitic transformation occurring during technological cold forming of sheets. The martensitic transformation usually takes place in two stages, i.e., first the deformed austenite is transformed into  $\epsilon$ -type martensite of hexagonal lattice, and then martensite of regular lattice nucleates at the intersection of  $\epsilon$ -martensite plates. The tensile strength ranges from 900 MPa to even 1200 MPa with an elongation of 30 % to 50 %. The martensitic transformation of austenite causes an intense increase in tensile strength [37].

The high plasticity of the steel (TRIP effect) is closely related to the high strain hardening rate of the steel and the delay in the formation of the neck in tensile tests. The SIMT effect occurs at the location of intense deformation. This leads to local strain hardening of the steel. The further plastic deformation occurs therefore in the adjacent areas characterized by lower yield stress, which subsequently are also strengthened by SIMT effect. This effect occurs both in multiphase steels containing dispersed retained austenite, as well as in high-manganese steels with a homogeneous austenitic matrix [2,4].

The  $\epsilon$  martensite is formed during plastic deformation, when the stacking-fault energy (SFE) of austenite at room temperature is in the range from 12 mJ/m<sup>2</sup> to 20 mJ/m<sup>2</sup>. The addition of aluminium increases the SFE and stability of the austenite, which leads to a damping effect on the martensitic transformation. On the other hand, the addition of silicon reduces the SFE and enables the epsilon martensite formation [38].

**Twinning-Induced Plasticity (TWIP) Steels** contain usually from 25 % to 30 % of manganese. Their main strengthening mechanism is the TWIP effect related to intense mechanical twinning during cold plastic deformation. These steels, along with the increase in plastic deformation, retain the austenitic structure, while the amount of mutually intersecting deformation twins gradually increases. The essence of the TWIP effect and the high ductility of the steel is related again to the high strain hardening rate provided in this case by the mutual interactions between forming twins and moving dislocations. Mechanical twins generated in austenite significantly increase the strain hardening rate being obstacles to dislocation motion, similarly as grain boundaries. With the increase in the deformation degree, the average free

dislocation path decreases, which results in the high strain hardening rate of the steel preventing the formation of a neck in the sample [37,39].

For this reason, TWIP steels exhibit high uniform and total elongation, and in particular, energy absorption capacity that may more than twice than that of conventional deep-drawing steels. In addition, these steels show high impact strength regardless of the test temperature in a wide range from -196 °C to 400 °C, which is a characteristic feature of Al lattice metals and alloys. The intense mechanical twinning occurs for steels with SFE values in the range between 20 mJ/m<sup>2</sup> and 60 mJ/m<sup>2</sup>. The TWIP effect also depends on a strain rate, temperature and a grain size of austenite [2,7].

**TRIPLEX steels** contain 0.5 % to 1.2 % of C, 18 % to 28 % of Mn and 8 % to 12 % of Al. Increasing the aluminium content in high-manganese steels allows to reduce the density of steel below 7 g/cm<sup>3</sup>. The weight of selected elements of the car body may be therefore limited by about 6 % to 10 %. In addition, these steels show increased resistance to corrosion and oxidation.

The name TRIPLEX comes from the three-phase structure of the steel, which consists of high-alloyed austenite - Fe (Mn, Al, C), high-alloyed ferrite - Fe (Mn, Al), as well as precipitates of carbide  $\kappa$  - (Fe, Mn)<sub>3</sub>AlC [40]. The fraction of ferrite usually ranges from 5 % to 15 %, while carbides - from 6 % to 9 %. The strengthening mechanism strongly depends on the chemical composition of the alloy (SFE) and conditions of plastic deformation. If the stacking fault energy range is from 60 mJ/m<sup>2</sup> to 100 mJ/m<sup>2</sup>, the main strengthening mechanism is dislocation slip, which provides moderate elongation values of the steel. This results in high strain hardening rate and prevents premature necking of the specimen during stretching or thinning of the sheet under drawing conditions. These steels have the highest yield point among all high-manganese steels, while the tensile strength and elongation values are intermediate between steels showing the TRIP and TWIP effects [7,14,37,39].

High-manganese car body sheet steels, despite their excellent properties, are not commonly used in the automotive industry. This is due to their several fundamental disadvantages of economic and technological nature [39]. The high content of Mn determines high production costs. It also affects the increased susceptibility of steel to corrosion as well as chemical segregation. These steels also show a tendency to unstable flow of the Portevin-Le Chatelier (PLC) type, and casting and hot working difficulties [41,42]. All these aspects are dominated by the very limited use of high-manganese steels. Further development, focusing on eliminating these disadvantages, has led to the creation of a new group - medium-Mn steels [19,39].

#### **2.1.4. 3<sup>rd</sup> generation AHSS**

**Bainitic TRIP steels** are TRIP steels in which the ferritic matrix has been replaced fully by bainitic ferrite [43]. The tensile strength, which conventional TRIP-aided steels (mentioned in the previous chapter) can achieve is usually up to approx. 1000 MPa. They also have disadvantages of relatively poor flanging and bending, and edge forming properties. Nowadays, there is an increasing demand for materials with a strength above 1 GPa and at the same time characterized by good edge formability [44]. The assumed requirements can be met thanks to modern bainitic steels with retained austenite [45,46]. Heat treatment of bainitic steels with the TRIP effect consists of classic isothermal holding in the bainitic region after earlier austenitizing of steel above the  $A_{c3}$  temperature. After the austenitization is complete, the material is cooled to the bainite transformation temperature, where bainitic ferrite is formed and remaining fraction of austenite is stabilized. The final structure of the steel consists of a lath matrix of bainitic ferrite and interlath retained austenite. These steels have a good balance between low susceptibility to edge cracking during stamping and relatively good elongation [47–49].

**Quenching and Partitioning (Q&P) steels** have a chemical composition similar to conventional TRIP steels. Sometimes they contain elevated concentrations of C, Mn and Ni as elements stabilizing austenite. Their heat treatment after cold rolling consists of steel austenitization above the  $A_{c3}$  temperature and subsequent rapid cooling to a temperature slightly lower than the  $M_s$  temperature, but higher than the temperature of the end of martensitic transformation  $M_f$  (Quenching). Under these conditions, some fraction of martensite in an austenitic matrix is formed. The next stage of heat treatment consists in increasing the temperature of steel sheets to a temperature higher than  $M_s$  temperature of steel and holding them for a period from several dozen seconds to several minutes (Partitioning) [50]. The purpose of this treatment is to enrich the remaining austenite with carbon from the formed martensite. During the final cooling of the steel to room temperature, the martensitic transformation of the austenite areas with low carbon enrichment occurs, while the austenite regions with higher carbon enrichment remain stable. Steels of this type are characterized by tensile strength in the range of 1300 MPa to 1500 MPa, yield strength 1100 MPa to 1300 MPa, and elongation at the level of 12 % to 15 % [2,47].

**Medium-Mn steels**, due to their chemical composition and specialized heat treatment, allowed to eliminate most of the defects of their predecessors – high-Mn steels [2,7,15,51]. The limitation of the manganese content to the range of 3 % to 12 % made it possible to reduce the

production costs. It also increases the corrosion resistance and reduces the tendency to chemical segregation. In addition, reducing the content of this element results in limitation of the impact of plastic instability (PLC effect) during deformation [52]. Medium-Mn steels appear to be almost free of casting and hot working problems, which occurred in steels with higher manganese contents. On the other hand, medium-Mn steels show strength and plasticity that may go beyond those of other multiphase steels from the 1<sup>st</sup> AHSS generation (Figure 6) [6,19,53].

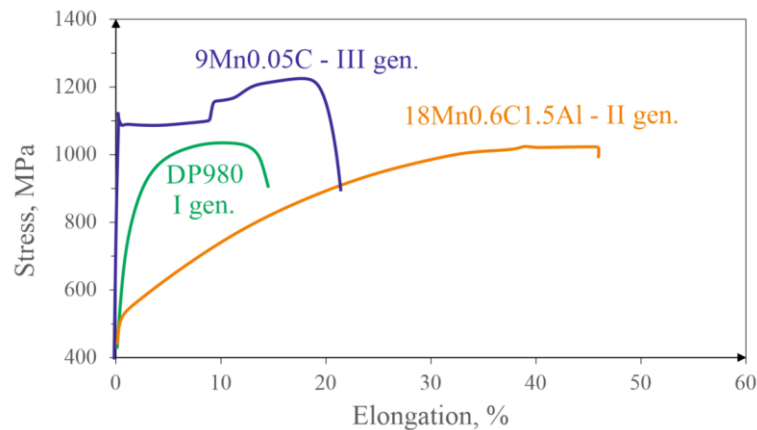


Figure 6 Comparison of the mechanical properties of conventional multiphase steel (DP980, I gen. AHSS), high-manganese steel (18%Mn-0.6%C-1.5%Al, in wt.%, II gen. AHSS), and cold-rolled medium-Mn steel (9%Mn-0.05%C, in wt.%, III gen. AHSS) [15].

The indicated combination of the advantages of both earlier generations of AHSS steels, while eliminating some of the disadvantages, caused great interest and rapid development of this group of automotive steels. This results in the recent introduction of pilot batches to steelworks [15], despite the relatively short time since their invention. Medium-Mn steels are characterized by fine grain size and the fraction of metastable retained austenite reaching over 20%. The high fraction of this phase contributes significantly to their plastic properties, which may reach over 25% at a high strength level of over 800 MPa. The matrix of medium-Mn steels, depending on the heat treatment and chemical composition, is: ferrite (for intercritical annealing) [54–57]; bainitic ferrite (for thermomechanical treatment) [5,54,58,59]; or martensite (in the case of double intercritical annealing or Q&P process) [60–63]. During the plastic deformation process, the metastable austenite undergoes martensitic transformation (TRIP effect) or/and intense mechanical twinning (TWIP effect). Both processes provide increased plasticity without loss of steel strength [6,15,53].

## **2.2. Physical metallurgy and manufacturing technology of medium-Mn steels**

### **2.2.1. Design of chemical composition**

The most important structural constituent of medium-Mn steels is retained austenite (RA). The usual main goal when designing the chemical composition is to obtain the highest possible fraction of this phase, which dominates the ductility and formability. At the same time, the content of alloying elements should be as low as possible to reduce the price of the material, as well as to prevent the occurrence of undesirable properties, like poor weldability and galvanability [64]. Medium-Mn steels contain usually four main chemical elements, which are C, Mn, Si, and Al in a wide range (Table 1). Each of the chemical elements plays an important role affecting specific physical and/or mechanical aspects:

**Carbon** is the strongest chemical element stabilizing retained austenite (decreasing  $M_s$  temperature). It thermally and mechanically inhibits martensite formation by increasing the Gibbs energy between the austenite and martensite phases,  $\Delta G_{A \rightarrow MF}$ . The strongly limited solubility of carbon in phases like ferrite, bainite and martensite causes that it almost completely diffuses to austenite during heat treatment. Moreover, this process occurs rapidly due to the high diffusivity of carbon [65]. This property is also partly responsible for the phenomena of plastic instability associated with Lüders bands and the PLC effect [66], resulting from the interaction of carbon atoms and dislocations. Carbon also affects the strong solution strengthening of the alloy as well as increases the SFE. Each 0.1 % of C increases the SFE by 2.5-4 mJ/m<sup>2</sup> [6,67]. One of the main disadvantages of carbon is its negative impact on weldability of steel [68,69]. This is a very important technological parameter, which usually forces the limitation of the content of this element in steel designed for automotive industry to about 0.2 wt.%. However, as visible in Table 1, higher C contents in medium-Mn steels were also investigated [70,71]. The harmful effect of carbon on the weldability of steel was one of the factors that resulted in the introduction of an increased addition of another austenite-stabilizing element: manganese.

**Manganese** is the most important chemical element in medium-Mn steels. Its primary role is to stabilize austenite. Addition of 1 wt.% Mn reduces the  $M_s$  temperature by ~30-40 °C [72] and the  $M_{d30}$  temperature (the temperature at which half of the austenite undergoes martensitic transformation under the influence of 30 % uniaxial strain by about 10 °C) [73]. Due to this relationship, the RA fraction usually increases with an increase in manganese content in the steel.

Table 1 Example chemical compositions of medium-Mn steels containing C, Mn, Si and Al.

No.	Chemical composition, wt.%					Ref.
	C	Mn	Si	Al	Total	
1	0.17	3.1	1.6	0.2	5.0	[5]
2	0.17	3.3	1.7	0.2	5.3	[5]
3	0.40	3.5	-	5.9	9.8	[74]
4	0.11	4.5	0.4	2.2	7.2	[75]
5	0.09	4.6	3.0	-	7.6	[76]
6	0.16	4.7	1.6	0.2	6.6	[5]
7	0.20	4.7	-	-	4.9	[77]
8	0.17	4.7	-	-	4.8	[78]
9	0.09	4.7	1.2	0.6	6.7	[79]
10	0.11	4.8	-	-	4.9	[78]
11	0.20	5.0	-	-	5.2	[70]
12	0.26	5.0	-	-	5.2	[70]
13	0.40	5.0	-	-	5.4	[70]
14	0.12	5.0	0.5	1.1	6.7	[80]
15	0.12	5.0	0.4	3.1	8.6	[80]
16	0.17	5.0	1.5	0.2	6.8	[5]
17	0.20	5.0	-	1.5	6.7	[81]
18	0.07	5.1	0.4	2.1	7.7	[75]
19	0.05	5.6	0.4	2.2	8.3	[75]
20	0.05	5.9	1.5	1.0	8.5	[82]
21	0.20	7.0	-	-	7.2	[70]
22	0.10	7.1	0.1	-	7.3	[66]
23	0.52	7.7	-	2.7	11.0	[71]
24	0.23	8.1	-	5.3	13.6	[83]
25	0.01	9.0	-	1.4	10.4	[84]
26	0.05	9.0	-	-	9.0	[57]
27	0.30	10.0	2.0	3.0	15.3	[85]
28	0.20	10.0	3.1	3.1	16.5	[86]
29	0.26	10.1	-	6.3	16.6	[87]
30	0.08	10.6	0.3	-	11.0	[88]
31	0.06	11.7	0.2	2.9	14.8	[89]
32	0.20	12.4	0.9	5.2	18.7	[83]

At the same time, manganese extends the  $A_{c1}$  and  $A_{c3}$  temperature range. This fact generates two different effects: (a) the required heat treatment temperature is lowered, which favors grain

refinement [90]; (b) lower temperature increases the diffusion time of manganese and carbon needed to stabilize austenite [91]. It was proved that in the Fe-Mn system, the stacking fault energy of austenite at room temperature initially decreases, and next increases with an increase of manganese content. This results in a typical parabolic SFE changes with the content of Mn in steel. On the other hand, calculations [92] show that manganese is able to combine into C-Mn clusters, which can reduce carbon diffusivity and increase its solubility in austenite. This can have a significant impact on mechanical properties of medium-Mn steels. The relatively large size of manganese atoms causes a significant lower A→F diffusion rate of this element in relation to carbon [53]. Medium-Mn steels contain usually between 3 wt.% to 12 wt.% of manganese (Table 1). However, the higher content of this element the highest price of the steel. With the increase of manganese addition also the hardenability of steel increases and hot working resistance [93].

**Silicon** in medium-Mn steels is also used to widen the intercritical region but its major role is to inhibit the formation of carbides. Thanks to this, carbon is not bound in the carbides, and may diffuse to austenite. The inhibition of carbide formation by silicon is related to the fact that its solubility in carbides is very low, which means that this element significantly reduces the driving force of their precipitation. The accumulation of Si around the cementite nucleus leads to an increase in carbon activity, which prevents its diffusion into the nucleus [94]. The minimum content of Si in the alloy for effective inhibition of cementite precipitation is about 0.8 wt. %. Silicon also increases carbon diffusivity, which favors the enrichment of austenite by it. It also causes significant solution strengthening of both ferrite and austenite [6].

Unfortunately, silicon also has some negative effects on steel. The use of silicon content greater than ca. 0.5 wt.% results in significant difficulty in sheet galvanizing [6,94,95]. This is due to the formation of an oxide film on the surface of the material, which prevents the liquid zinc from properly wetting the sheet surface. Moreover, the Si content higher than ~ 0.5 wt.% adversely affects the ductility and fracture toughness in low carbon ferritic steels [96]. For this reason, efforts are being made to at least partially replace silicon in medium-manganese steels with aluminium [97].

Like silicon, **aluminium** exhibits properties that inhibit martensitic transformation while favoring twinning due to the effect of increasing the SFE of austenite. An increase in the aluminium content by 1 wt.% causes an increase in the stacking fault energy of austenite by ~8.5 mJ/m<sup>2</sup>, which was confirmed by thermodynamic calculations [98]. It explains the appearance of the TWIP effect in medium-Mn steels containing high additions of Al. This

element also stabilizes ferrite and increases the area of F + A occurrence. A high Al content favors the formation of  $\delta$  ferrite [80]. An increase in the aluminium content in the alloy causes an increase in  $A_{c1}$  and  $A_{c3}$  temperatures [15], thus a higher annealing temperature is necessary to obtain the same fraction of austenite. On the other hand, higher temperature makes it possible to shorten the time necessary to enrich the austenite with manganese. Aluminium, unlike manganese and carbon, tends to enrich the ferrite fraction. An increase in the heat treatment temperature causes a decrease in a ferrite fraction, which leads to the enrichment of the formed austenite in aluminium [99].

### **2.2.2. Technological challenges**

Another important aspect in designing the chemical composition of sheet steels is their susceptibility to specific metal forming operations. The flange in the stamped element can be made by deforming the edge of the sheet using a bending operation. The edge of the flange may be stretched, compressed or remain undeformed, depending on the shape of the molded piece. Classic examples of flanges used in the automotive industry include car interior panel cutouts, window panel corners, wheel hub hole, etc. When the circumferential load exceeds a critical level during flange stretching operations, a neck failure and cracking occurs. The limiting criterion below which the sheet material should not fail during the stretching operation can be expressed by hole expansion ratio (HER), which is defined as [100]:

$$\text{HER} = 100 \frac{(d_f - d_0)}{d_0} \quad (1)$$

where  $d_f$  and  $d_0$  are the finish and start diameters of the hole.

One of the main factors limiting the wide application of AHSS steels in the automotive industry is cracking of the steel sheet during forming of the flange [101,102]. In multiphase steels, material damage begins with the formation of cracks in the harder phase and proceeds through propagation along the phase interface [103]. The local stress in the vicinity of the punched hole is generally much greater than the elongation measured in the tensile test. HER can be influenced by refinement of the grain and homogenization of the microstructure, both in terms of phase composition and morphology [100].

In the case of medium-Mn steels, there is no clear correlation between HER and plastic properties. However, this indicator usually decreases with the increase in the amount of retained austenite in steel. This is due to the fact that with an increase in the amount of RA, its saturation with carbon and manganese decreases [104], as they are distributed over a larger volume of

material. This results in a decrease in RA stability, which leads to very intensive martensitic transformation during edge forming. The closer to the edge of the shaped flange, the greater the deformation, often resulting in the transformation of the entire RA into martensite. A significant difference in hardness between the freshly formed, carbon-rich martensite and the surrounding ferritic, bainitic, or tempered martensite matrix causes the formation of cracks at the interface of both phases [100,105]. HER in medium-Mn steels can therefore be controlled by regulating carbon and manganese contents in the austenite and thus its stabilization [48].

Problems during sheet metal forming can also occur due to hydrogen embrittlement. As it is known, hydrogen damages, such as hydrogen bubbling and hydrogen cracking, occur in steel when the concentration of hydrogen exceeds a critical value [106]. The presence of internal and external stresses favors the diffusion and enrichment of steel with this element, leading to a decrease in its ductility. This phenomenon is called hydrogen-induced ductility or hydrogen embrittlement. Combined with the constant loading of the material, the presence of hydrogen promotes the nucleation and propagation of hydrogen cracks. This is called hydrogen-induced delayed cracking [106,107]. This is currently one of the decisive factors determining the use of medium-Mn steels. Due to their high strength, they may be susceptible to hydrogen embrittlement [108]. However, little is known about hydrogen embrittlement in these materials [106,107,109–111]. Their multiphase microstructure with highly variable phase conditions (e.g., fraction, distribution, and dislocation density) and strain-induced martensitic transformation make it difficult to study this phenomenon. The hydrogen embrittlement in medium-Mn steels is complicated to understand because of three factors: large differences in hydrogen diffusivity and solubility between austenite and ferrite; ferrite and austenite interfaces tend to store hydrogen; the martensitic transformation of RA causes a change in the state of the microstructure in terms of distribution and location of strains and stresses. This also changes the driving force of hydrogen migration. It is suggested that changing the phase ratio in medium-Mn steels can significantly affect the localization and migration of hydrogen [108], and even the dominant hydrogen embrittlement micromechanics, such as hydrogen-enhanced decohesion [112], enhanced local plasticity [113] or adsorption-induced dislocation emission [114]. Ryu et al. [109] reported that RA concentrates hydrogen more strongly compared to F in cold-rolled and annealed Fe-4.6Mn-0.12C-0.55Si-1.1Al and Fe-5.8Mn-0.12C-0.47Si-3.1Al steels. They claim that hydrogen is inherited from RA to  $M_F$  as a result of strain-induced transformation. This leads to deterioration of plasticity because the diffusivity of hydrogen in  $M_F$  is higher than in RA.

In order to enhance the achievable benefits of medium-Mn steels while reducing or eliminating possible problems and disadvantages, it is necessary to combine judicious chemical composition design considering the limitation of both C and Mn additions with the specialized heat treatment used in the production of these steels.

### 2.2.3. Thermomechanical processing of medium-Mn steels

One of the methods of heat-treatment proposed for medium-Mn steels was the thermomechanical processing adapted from TRIP-aided bainitic steels [90,91]. The typical heat-treatment of conventional TRIP steels consisting of first ferritic and next bainitic transformation may not be applied due to high steel hardenability caused by increased Mn addition [115]. The bainitic transformation during cooling of medium-Mn steels occurs relatively quickly, in contrast to the ferritic transformation, which is significantly delayed and requires long isothermal holding time [115,116]. This behavior is opposite to conventional low-carbon steels with a manganese content below 2 wt. %, where the ferritic transformation at the corresponding temperatures occurs very effectively (Figure 7).

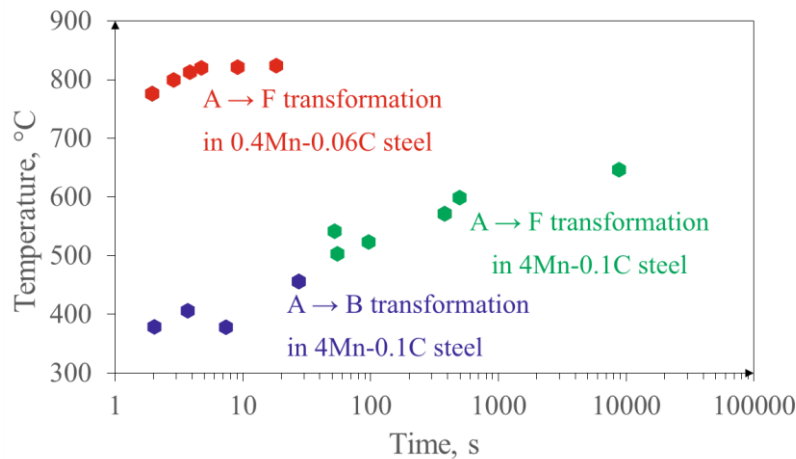


Figure 7 Time-temperature-transformation (TTT) diagram comparing the kinetics of isothermal transformations in the 0.4Mn-0.06C and the 4Mn-0.1C steels [117].

The thermomechanical processing of medium-Mn steels is a combination of hot working integrated with isothermal treatment at a bainitic transformation temperature (Figure 8). For this reason, this process is the most economically attractive because, unlike other methods, it does not require reheating of the material after hot rolling completion. However, it may be applied only to hot-rolled sheets of higher thickness.

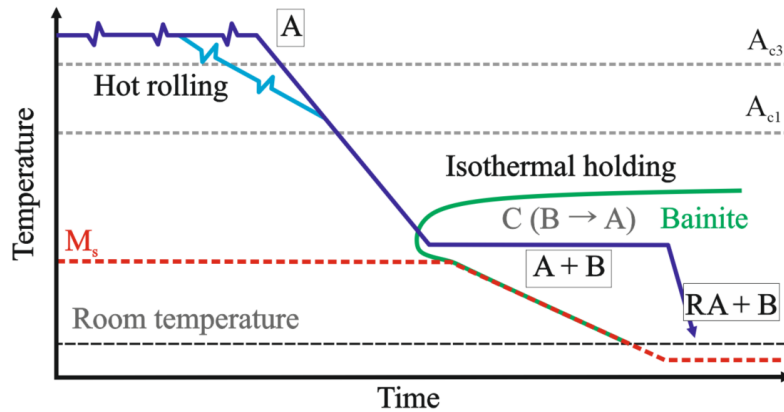


Figure 8 Schedule of the thermomechanical process of medium-manganese steels in the bainitic region.

In thermomechanical processing the steel may be hot-deformed above  $A_{c3}$  temperature, where the recrystallization of austenite occurs or below the recrystallization temperature. The latter leads to deformation of austenite, which is maintained to next heat treatment stages and promotes microstructure refinement [59]. After the hot-working completion, the material is cooled to the temperature of bainitic transformation. At this temperature, isothermal holding occurs. During this step, the bainitic matrix is formed [46,92]. In medium-Mn steels, identification of bainite is difficult. This is due to the presence of two types of bainite: carbide-containing bainite and carbide-free bainite [118]. The latter type is formed due to the addition of Al and Si in steel. These elements inhibit the precipitation of carbides, as described in the previous section, and thus lead to the formation of carbide-free bainite. Simultaneously with the bainitic transformation, the diffusion process begins. Carbon contained in excess in bainite is redistributed to austenite. This causes its stabilization and is crucial in this type of heat-treatment of medium-Mn steels [59,118,119]. Due to its limited diffusivity and relatively low process temperature, manganese redistribution is inhibited. The final effect of the described heat treatment is a fine-grained structure consisting of fine bainitic ferrite and retained austenite. RA, due to the nature of the bainitic transformation, shows lath-like or film-like morphology and is located between the bainitic ferrite plates. This affects its additional mechanical stabilization [34]. Austenite can also occur between bainite sheaves in the form of larger – blocky type grains. They can form austenitic-martensitic constituents partially during cooling. In this case, the martensite is usually located in the central part of the austenite grains [119] because their stability is lower due to lower chemical enrichment.

Previous research on the subject of bainitic transformation indicates the possibility of increasing the ratio of strength to plasticity of bainitic steels by lowering the bainitic

transformation temperature [120,121]. It has been proven that with the decrease of this temperature, the formed bainitic structure is more fine-grained, thus causing the reduction of the thickness of RA grains, which are located between the bainitic plates [122]. Reducing a grain size of RA shortens the diffusion path and thus stronger enrichment of this phase in carbon [123,124]. Moreover, the obtained microstructure generates compressive stresses, which additionally stabilize the austenite mechanically [125].

However, in order to lower the temperature of the isothermal holding compared to conventional processes, it is necessary to obtain a higher concentration of carbon in the austenite [126]. It affects not only the lowering of  $M_s$ , but also the simultaneous lowering of the bainitic transformation range. Long et al. [127] proposed to develop the conventional thermomechanical treatment with an additional step during bainitic holding (Figure 8). This is argued by the fact that during the first step, the retained austenite located between the bainite plates is enriched in carbon. This results in a decrease in the  $M_s$  temperature of remaining austenite, thus enabling the reduction of the bainitic transformation temperature - which is done in the second stage of this treatment [128].

The result of this type of thermomechanical treatment is obtaining a bainitic matrix, composed of two sizes of bainitic structures (standard, obtained during the first stage, and additionally refined, formed during the second stage) and retained austenite [129–131]. This treatment not only affects the grain refinement but also the morphology of the material. It causes the reduction or elimination of blocky RA for the benefit of film morphology [79]. This is achieved by isothermal holding below 400 °C [131].

Despite high economic indicators and relatively simple production process, medium-Mn steels produced by thermomechanical processing show limited industrial applicability. Carbide precipitates and bimodal morphology of film- and blocky-type austenite in medium-Mn steels produced in this way affect the susceptibility to cracking and lower plasticity of the steel (Figure 9). Bainite-based medium-Mn steels show very high strength but usually it is at the expense of limited formability of steel sheets (hard bainite). The inhibited Mn redistribution during low-temperature isothermal holding reduces the potential of designed chemical composition of these steels. These factors influence the interest in producing medium-Mn steels by other heat-treatment methods as intercritical annealing [93].

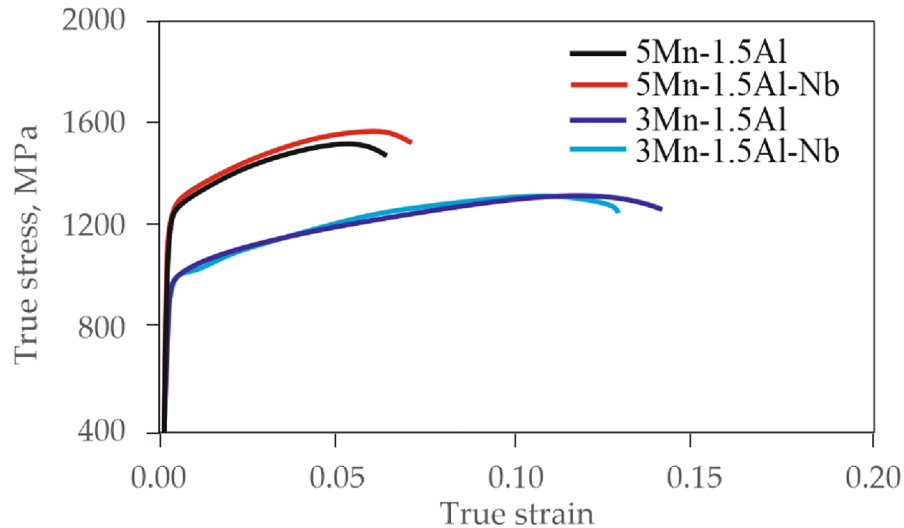


Figure 9 Mechanical properties of thermomechanically treated 5Mn and 3Mn steels [5].

#### 2.2.4. Intercritical annealing of medium-Mn steels

Currently, one of the most promising strategies of heat treatment of medium-Mn steels is so-called intercritical annealing [15,110]. It is applied as a separate isothermal holding in the range between  $A_{c1}$  and  $A_{c3}$  temperatures (Figure 10). Its combination with the hot working is rather not possible due to high hardenability of steel caused by Mn (Figure 7). During the heating and isothermal holding of the initial martensitic steel the following mechanisms occur [15]:

1. Martensite tempering,
2. Carbide dissolution,
3. Recrystallization - depending on the initial state of material,
4. Austenite nucleation,
5. Austenite growth,
6. Chemical redistribution.

The heating of the martensitic medium-Mn steel is accompanied by the tempering process. The formed carbides start to dissolve with an increase of the temperature. It promotes nucleation of austenite in C- and Mn - rich areas. A further increase of temperature and subsequent isothermal holding is accompanied by the progress of austenite nucleation and its growth. The excess carbon and manganese from ferrite diffuse to newly formed austenite (Figure 10) stabilizing it [15]. Si and Al show a greater affinity to ferrite; hence their diffusion takes place in the opposite direction than C and Mn [99].

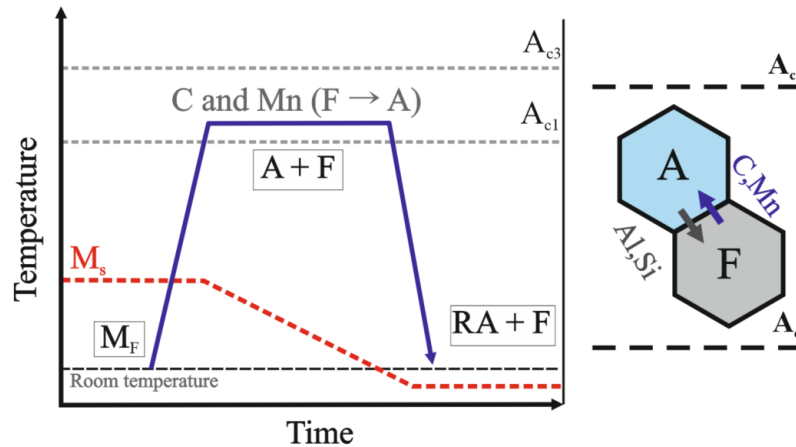


Figure 10 Scheme of intercritical annealing with phase evolution and chemical redistribution occurring between A and F.

Properly designed and performed intercritical annealing should result in full stabilization of austenite at room temperature. Therefore, after final cooling the microstructure consists of ferrite (or highly tempered martensite) and RA [132].

Intercritical annealing may be applied for both hot- and cold-rolled medium-Mn steels, which however significantly affects the resulting microstructure and mechanical properties.

### 2.2.5. Intercritical annealing of hot-rolled steel sheets

In hot-rolled medium-Mn steels the dominating mechanism is so called ART (austenite reverted transformation) process (Figure 11). The initial martensitic microstructure controls the nucleation and growth of austenite. After crossing the  $A_{c1}$  temperature, austenite starts to form on martensite lath boundaries, and triple joints, which act like nucleation sites. The C and Mn atoms tend to segregate to these areas [36]. Newly formed austenite grains start to grow along laths of tempered martensite. The austenite inherits therefore the morphology of parent martensite, so the final morphology for both phases after the process completion is lamellar. During annealing, after the phase equilibrium is obtained the microstructure undergoes only further tempering and sluggish recovery. It results in relatively high dislocation density retained in both phases after annealing completion. Hot-rolled and intercritically annealed medium-Mn steels exhibit beneficial continuous yielding (Figure 12) and the dynamic strain aging (DSA) effect is minor or not present [15].

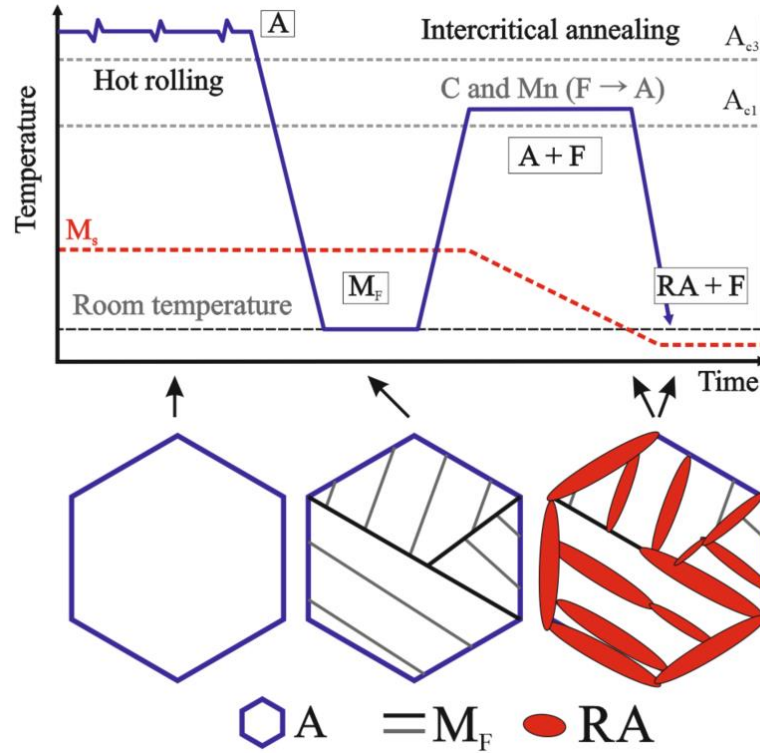


Figure 11 Scheme of the intercritical annealing process of hot-rolled medium-manganese steels with the microstructure evolution.

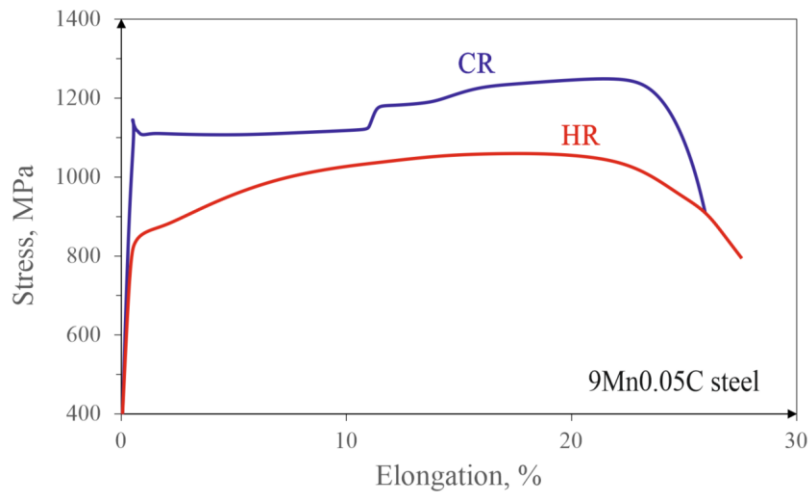


Figure 12 Differences in tensile curves of hot-rolled and cold-rolled medium-Mn steels; HR – hot-rolled, CR – cold-rolled [57].

### 2.2.6. Intercritical annealing of cold-rolled steel sheets

The cold-rolled steels have deformed martensitic microstructure prior to intercritical annealing. It affects the occurrence of additional mechanism during heating (beside ART process and recovery) – recrystallization. During heating of cold-rolled medium-Mn steels, the

deformed martensite undergoes recrystallization (Figure 13), which influences the austenite nucleation and growth in the microstructure of globular ferrite. It results in the final structure composed of globular retained austenite and ferrite. The globular ferrite exhibits lower dislocation density compared to the lamellar one. As showed by Han et al. [57] the thickness of retained austenite in intercritically annealed hot-rolled medium-Mn steels is lower by about 50 % than in cold-rolled samples treated under the same heat-treatment conditions. They also indicated that Mn partitioning occurred more actively in the hot-rolled specimen. It was most likely caused by accelerated diffusion of Mn atoms influenced by dislocations, elongated grain boundaries and vacancies. However, the most important difference between both initial types of rolling is the resulting mechanical behavior. Cold-rolled steels exhibit usually problematic discontinuous yielding with a large yield point elongation (Figure 12).

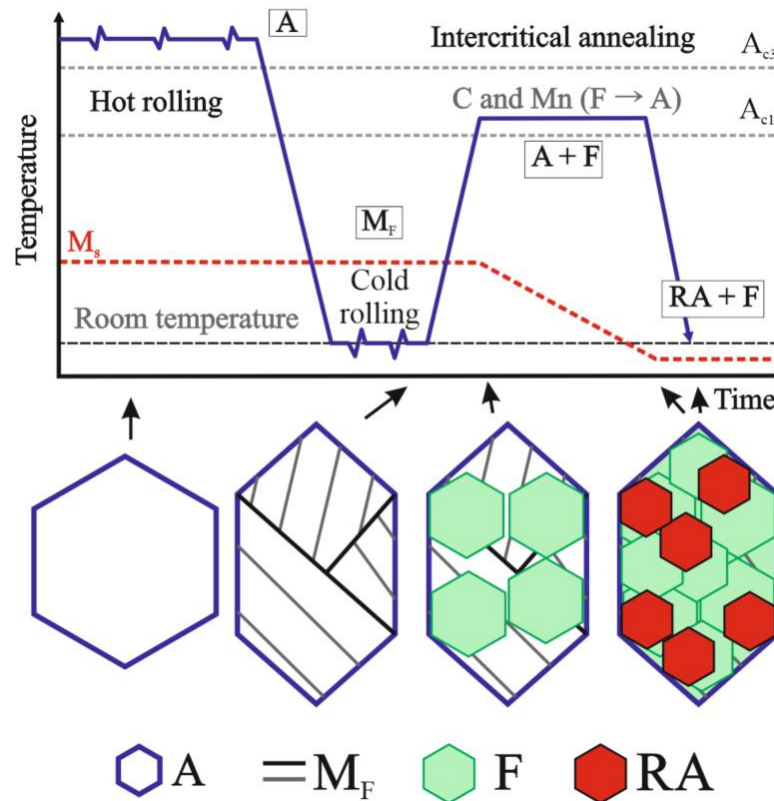


Figure 13 Scheme of the intercritical annealing process of cold-rolled medium-Mn steels with the microstructure evolution.

The difference in yielding behavior between hot- and cold-rolled steels is caused by different strain partitioning between ferrite and austenite. In cold-rolled steels the ferrite shows low density of dislocations due to recrystallization and is easily deformable. On the other hand, the

solution-hardened austenite (by Mn and C) is more resistant. It results in inhomogeneous local deformation. In hot-rolled steels both phases exhibit a similar strength level due to an increased dislocation density, which promotes continuous yielding [15,133].

Discontinuous yielding and Lüders strain are significant disadvantages of cold-rolled medium-Mn steels because non-uniform deformation may cause significant technological problems. The automotive industry is extremely sensitive to it due to the high demands placed on car structure quality. Therefore, the cold-rolled steels are often subjected to an additional austenitization step prior to intercritical annealing (Figure 14) [70,76,89]. It allows to relax the stresses in the steel and obtain a structure of undeformed martensite similar as in hot-rolled steels, which subsequently generates lath-like morphology. This technology requires however an additional heat-cycle step, which deteriorates economic indicators in comparison to hot-rolled sheets.

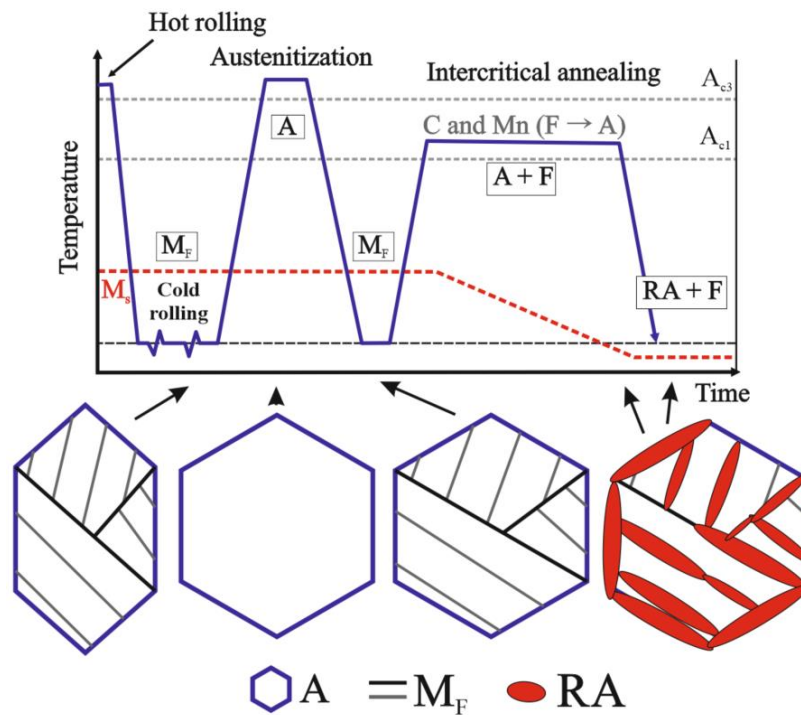


Figure 14 Scheme of the intercritical annealing process of cold-rolled and austenitized medium-manganese steels with the microstructure evolution.

Despite worse properties, longer and more energy consuming production process, currently most of the research focus is on intercritically annealed cold-rolled medium-Mn steels [57,66,70,71,74–78,78,80,83,85–89]. It is caused by their application range. Cold-rolled steels may be used to production of many parts in typical passenger vehicles because cold rolling

ensures production of thin sheets of high-quality surface. The less frequently investigated hot-rolled medium-Mn steels [15,57,79,84], which are cheaper in production and more environmentally friendly, may be applied for more responsible parts made of thicker steel sheets used in truck chassis, heavy duty vehicles, suspension elements, car wishbones, etc., after optimization of production process. Therefore, this field of science is still awaiting for exploration and development.

### **2.3. Effect of heat treatment on the microstructure and mechanical properties of intercritically annealed medium-Mn steels**

Mechanical properties of medium-Mn steels depend in majority on a fraction and stability of retained austenite. The latter is moderated by several factors:

#### **a. Chemical enrichment of retained austenite in C and Mn**

During the cooling of austenite, this phase undergoes a  $A \rightarrow F / B / M_F$  transformation depending on a cooling rate. However, when austenite is enriched with stabilizing elements such as carbon and manganese, its  $M_s$  temperature may be decreased below the room temperature. This results in retention of metastable retained austenite after cooling completion [134]. The  $M_s$  temperature is therefore considered as the most important parameter of the thermodynamic stability of austenite [6,64,135,136].

Barbier [135] and Van Bohemen [137] proposed formulas for determining the  $M_s$  temperature on the basis of the chemical composition of austenite:

$$M_s = 565 - 600 \cdot (1 - \exp(-0.96 \cdot C)) - 31 \cdot \text{Mn} - 13 \cdot \text{Si} - 10 \cdot \text{Cr} - 8 \cdot \text{Ni} - 12 \cdot \text{Mo} \quad [135] \quad (2)$$

$$M_s = 545 - 601.2 \cdot (1 - \exp(-0.868 \cdot C)) - 34.4 \cdot C - 13.7 \cdot \text{Si} - 9.2 \cdot \text{Cr} - 17.3 \cdot \text{Ni} - 15.4 \cdot \text{Mo} - 10.8 \cdot \text{Al} - 16.3 \cdot \text{Cu} - 361 \cdot \text{Nb} - 2.44 \cdot \text{Ti} - 3488 \cdot \text{B} \quad [137] \quad (3)$$

where chemical element contents are in wt.%

As visible, C and Mn are the most efficient stabilizing elements of austenite.

The empirical expressions presented are easy to apply and are continuously improved. Their main disadvantages are that they are usually correct only for a certain range of the chemical composition. Example formulas valid for typical compositions of medium-Mn steels are:

$$M_s = 565 - 27 \times Mn - 7 \times Si + 10 \times Al - 600 \times [1 - e^{-0.96 \times C}] \quad [138] \quad (4)$$

$$M_s = 545 - 432 \times C - 30.4 \times Mn \quad [139] \quad (5)$$

where  $M_s$  – martensite start temperature; chemical elements are in wt.%,

Figure 15 shows the graph illustrating changes in  $M_s$  temperature depending on C and Mn enrichment of austenite according to equation (4).

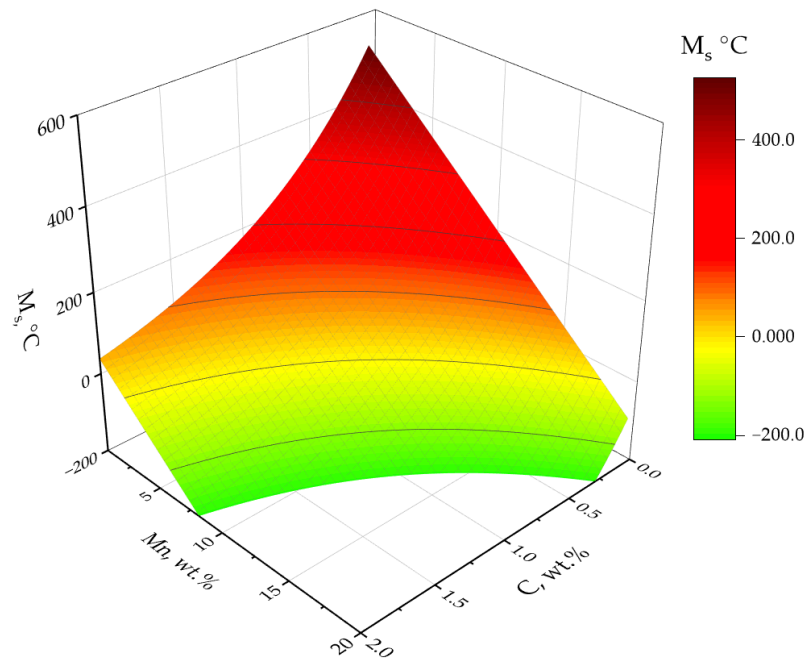


Figure 15 Changes in  $M_s$  temperature depending on C and Mn contents in austenite according to equation (4); own calculations.

Figure 16 is a slice of the graph presented in Figure 15. It shows changes in C and Mn needed for the  $M_s$  temperature to remain at 0 °C. As visible, to maintain the chemical stability of retained austenite, an enrichment of over 17 wt.% of Mn is needed in austenite containing 0.05 % of C. If the C content increases to 2 wt.%, only ~1.7 wt.% of manganese is required.

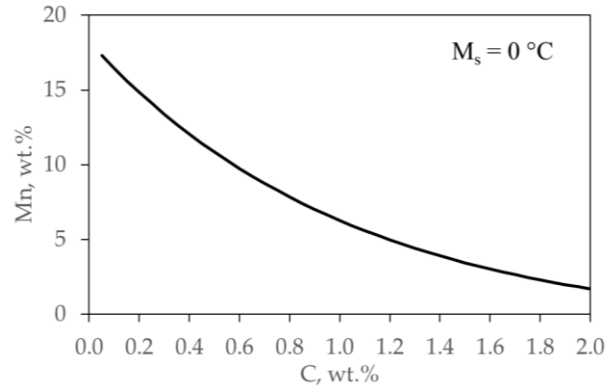


Figure 16 Chemical composition of austenite required to maintain  $M_s$  temperature at 0 °C; own calculations.

Another method to indicate the retained austenite stability is the use of thermodynamic driving force instead of temperature [31,140,141]. The chemical driving force of the reaction ( $\Delta G^{\text{chem}}$ ) is defined as the difference in Gibbs energy between austenite and martensite (Figure 17).

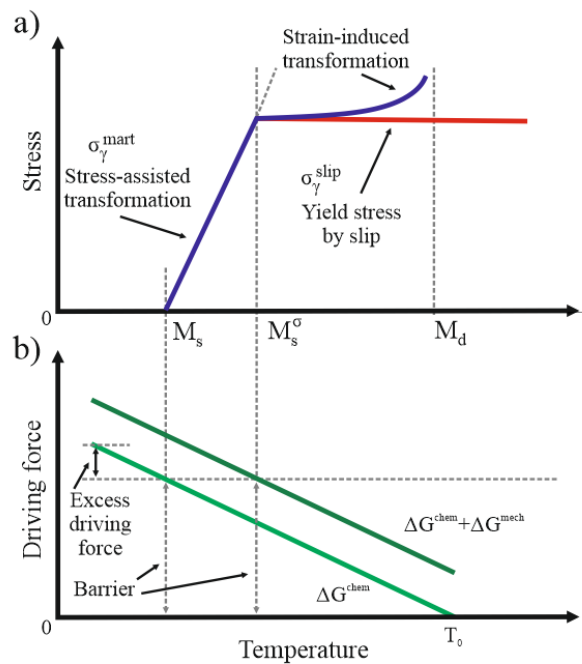


Figure 17 Schematic illustrations of: (a) the influence of temperature and stress on the martensitic transformation; (b) driving force of the martensitic transformation as a function of temperature [31,140].

This method consists in calculating  $\Delta G^{\text{chem}}$  based on the CALPHAD methods, and then determining the dependence of the composition on  $\Delta G$ , which is equal to  $\Delta G^{\text{chem}}$ . An example of the application of this method is [141]. In this work,  $M_s$  temperature was experimentally determined for martensite in several Fe-X alloys. Then,  $\Delta G^{\text{chem}}$  for  $M_s$  was calculated.

As a result, the expressions  $\Delta G$  for lath and plate martensite were obtained as [141]:

$$\Delta G_{\text{lath}} = 3640 - 2.92M_s + 346400 \frac{X_c^2}{1 - X_c} - 16430X_c + 7119X_{Mn} \quad (6)$$

$$\Delta G_{\text{plate}} = 2100 - 75000 \frac{X_c^2}{1 - X_c} - 11500X_c + 3574X_{Mn} \quad (7)$$

where  $X_c$  and  $X_{Mn}$  are the molar fractions of carbon and manganese, respectively.

### b. Retained austenite size and morphology

As visible in Figures 15 and 16, only chemical stabilization of RA is difficult to obtain as it requires significant additions of both C and Mn. However, in fact the RA stability is supported by fine or ultrafine grain size, which is present in intercritically annealed medium-Mn steels [142]. The RA grains in intercritically annealed steels are smaller than 2  $\mu\text{m}$  (more often  $<0.5 \mu\text{m}$ ) due to ART process [143]. The distribution of stabilizing elements is not equal even in particular grains and depends on a grain size and surrounding matrix. The RA stability depends directly on the C and Mn diffusion paths. In case of small, especially lath-like grains a surface to volume ratio is large, which amplifies enriching austenite in C and Mn from the surrounding matrix. Usually, the central areas of RA grains are less stable due to longer diffusion path and thus lower chemical enrichment. Wrong performed heat treatment determines that central areas of bigger grains transform to martensite during cooling. The size of RA affects its stability also in other way. Wang and Van der Zwaag [144] showed that decreasing the RA size increases the number of martensite nuclei needed to obtain a given martensite fraction. It is caused by RA boundaries acting as obstacles to martensite growth.

The empirical formulas for  $M_s$  temperature calculation may be enriched in a grain size factor to better reflect the real conditions:

$$M_s = 539 - 423 \times C - 30.4 \times Mn - \frac{56.5}{(D_{RA})^{0.5}} \quad [145] \quad (8)$$

$$M_s = 565 - 27 \times Mn - 7 \times Si + 10 \times Al - 600 \times [1 - e^{-0.96 \times C}] - 90 \times D_{RA}^{-\frac{1}{3}} \quad [138] \quad (9)$$

$$M_s = 545 - 432 \times C - 30.4 \times Mn - 60.5 \times V_{RA}^{-\frac{1}{3}} \quad [139] \quad (10)$$

where  $M_s$  – martensite start temperature is influenced both by chemical and grain size stabilization,  $D_{RA}$  – RA average diameter in  $\mu\text{m}$ ,  $V_{RA}$  – RA average volume in  $\mu\text{m}^3$ .

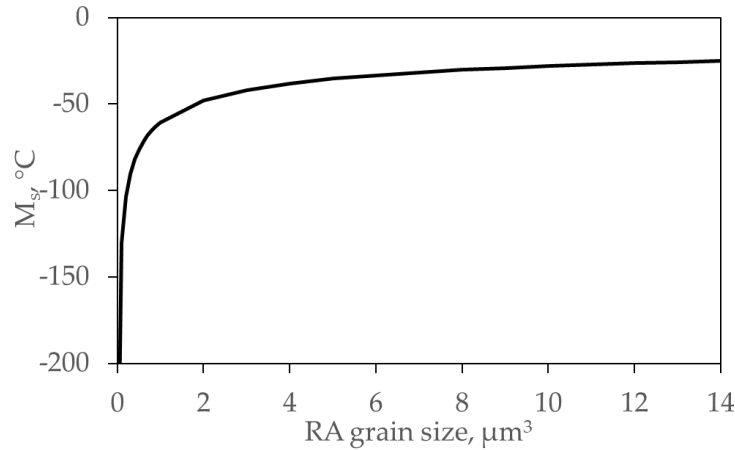


Figure 18 Separated influence of the grain size on the  $M_s$  temperature according to formula (10) (the chemical composition is not taken under consideration); own calculations.

As visible in Figure 18, the large RA grains do not affect significantly the  $M_s$  temperature. A strong stabilization occurs only for grains smaller than  $\sim 1 \mu\text{m}^3$ .

#### c. Strength and morphology of matrix

The nature of matrix also affects the stability of retained austenite [146]. Xiong et al. [147] determined that RA is mechanically less susceptible to martensitic transformation if it is surrounded by hard phases as martensite or bainite. They do not only increase strength of material but also introduce hydrostatic pressure [34] counteracting the increase in the volume of martensite during the transformation, supporting the stability of RA. Jacques et al. [148] reported similar ‘shielding’ effect of the more resistant martensite during strain partitioning. Fultz et al. [149] indicated that the dislocation distribution in harder phases surrounding retained austenite determines their capacity to plastically deform and to accommodate the volume expansion related to the SIMT effect. It influences the increase of RA stability.

#### d. Crystallographic orientation

Retained austenite grains oriented perpendicular and under  $45^{\circ}$  with respect to the strain direction are more prone to martensitic transformation due to the high force exerted on these grains by tensile and shear stresses, respectively [150]. The dependence of the austenite crystallographic orientation on its stability is defined by the theory of martensite crystallography. It predicts the global stability; however, compared to global factors local factors are more important in controlling the stability of retained austenite. Subsequent to transformation, the austenite grains rotate in order to accommodate the deformation.

Orientations with high transformation potentials transform to martensite instead of rotating significantly. In contrast, orientations with low transformation potentials rotate mainly 2–6° prior to the transformation [151].

All these parameters are influenced by intercritical annealing process parameters. Although intercritical annealing seems to be a simple heat treatment, it is performed under non-equilibrium conditions. This causes that each of the parameters plays a significant role affecting final performance of the material. Only their synergy under optimized conditions allows to obtain higher properties in relation to the previous generations of AHSS. Moreover, the final process must be feasible and relatively cheap to be introduced to industrial production. For example, the 2<sup>nd</sup> generation AHSS steels, despite their excellent properties, were not used practically in industry due to complicated and expensive production process. The most important parameters of intercritical annealing include: heating rate, soaking temperature, soaking time, cooling rate.

### **2.3.1. Effect of heating rate in intercritical annealing**

During heating of the hot-rolled (martensitic) medium-Mn steel the tempering occurs as first. Mn-rich cementite precipitates are present inside martensitic laths and on their boundaries. These areas are subsequently nucleation sites for austenite. In general, when the temperature crosses the  $A_{c1}$  point, the formation and evolution of dual phase microstructure starts. Austenite is formed and starts to grow and simultaneously the chemical element redistribution occurs. Therefore, slow heating rate increases the annealing time as a period between  $A_{c1}$  and a desired annealing temperature is longer. It is especially important in short – continuous annealing type lines - where several more seconds in the intercritical region may affect the results.

First Apple and Krauss [152] and next Han and Lee [153] have shown that a heating rate influences also the cementite precipitation. The increase in heating rate causes two effects: (1)  $A_{c1}$ ,  $A_{c3}$  and the cementite precipitation start temperatures increase. The difference for Fe–9Mn–0.05C (wt.%) steel reached 90 °C, 20 °C and 60 °C, respectively, with the heating rate increase from 0.1 °C/s to 65 °C/s [153]. (2) When the heating rate increases, the time for nucleation and growth of cementite is reduced, which results in more homogenized redistribution of C and Mn in the microstructure [15]. It results in less enriched RA in an initial stage of intercritical annealing because part of the C and Mn atoms are still dissolved in martensite. When the heating rate exceeds ~15 °C/s the cementite precipitation start temperature may not be recorded by dilatometry anymore. It indicates the transition of reversed

transformation mechanism from diffusive to diffusionless. Such effect was first observed in stainless steels [154]. In typical diffusive reversed transformation, the formed austenite is already enriched in C and Mn as it nucleates in areas rich in the mentioned elements. In diffusionless reversed transformation the formed austenite has the same chemical composition as the initial martensite. It prolongs significantly the time needed for austenite stabilization and decreases its overall stability compared to slower-heated steels [153].

### **2.3.2. Effect of soaking temperature in intercritical annealing**

The main role of the intercritical temperature is obtaining a desired ferrite-austenite composition, which is stabilized during soaking time [155]. Figure 19 shows the influence of intercritical annealing temperature on resulting phase composition. Medium-Mn steel annealed at a temperature slightly higher than  $A_{c1}$  will contain a low fraction but highly stabilized retained austenite, while annealing at a temperature close to  $A_{c3}$  will result in a high fraction of low stable austenite transforming to martensite during cooling. Such tendency is caused by the total content of C and Mn in steel. During soaking, they diffuse to newly formed austenite. However, their content is constant. Therefore, a low fraction of austenite may be highly enriched, and when its fraction increases the enrichment and thus austenite stability decreases [75]. Also the average grain size of austenite increases with temperature, which has a deteriorating effect on mechanical stability [156]. The role of properly selected intercritical temperature is to moderate the equilibrium phase ratio and transformation kinetics to ensure generation of high fraction of RA but characterized by a proper stability level.

Lee et al. [54] reported that the temperature of intercritical soaking has a significant influence on mechanical properties of medium-Mn steels. Since the retained austenite fraction increases plasticity increases too. The yield strength (YS) decreases because annealing promotes martensite tempering and structure softening [75]. However, the decrease in UTS is limited or even a growth is observed due to enhanced strain hardening caused by massive SIMT during cooling. When the austenite formed during intercritical annealing reaches the critical stability ( $M_s$  temperature close to room temperature) the tendency changes. For further increasing soaking temperatures the resulting microstructure contains less RA and an increasing fraction of martensite, which is formed during cooling. Therefore, the plastic properties decrease rapidly, whereas YS increases.

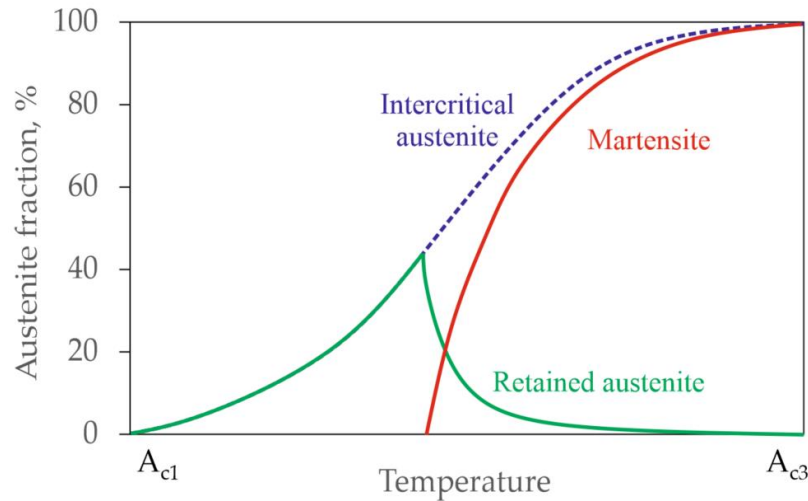


Figure 19 Schematic diagram of phase composition as a function of intercritical annealing temperature of 6Mn steel [155].

Lee and De Cooman [157] suggested that the optimal intercritical annealing temperature for 6Mn steel should be slightly lower than that at which a maximum fraction of austenite can be retained during cooling to room temperature. These rules are also confirmed in other works [15,140]. Figure 20a presents the influence of intercritical annealing temperature on a generated retained austenite fraction and resulting mechanical properties (Figure 20b), depending on a chemical composition of the alloy. It is visible that both the fraction of RA and mechanical properties of steel increase with the increase of Mn concentration. However, this generates the higher cost of steel.

The intercritical annealing temperature beside establishing the equilibrium phase ratio, influences also the kinetics of carbide dissolution, austenite formation and growth, and diffusion rate of chemical elements [158,159]. It means that these processes occur faster if the temperature is higher. It is especially important if the equilibrium state of material is not obtained during annealing due to short annealing time. As reported by Wan et al. [160] for steel containing 5.4 wt.% Mn the intercritical heating to 760 °C and immediate cooling allowed to obtain ~30 % of austenite due to mentioned earlier process acceleration, while the same steel annealed at 660 °C for one hour contained only 2 % of austenite in the microstructure.

Under industrial conditions, during typical continuous annealing process, a temperature is higher compared to the corresponding batch annealing. This is necessary to complete the recrystallization of the cold-rolled structure during shorter time. Controlling the fraction and stability of the austenite formed at higher annealing temperatures will therefore be essential for the application of the continuous annealing process in medium manganese steels.

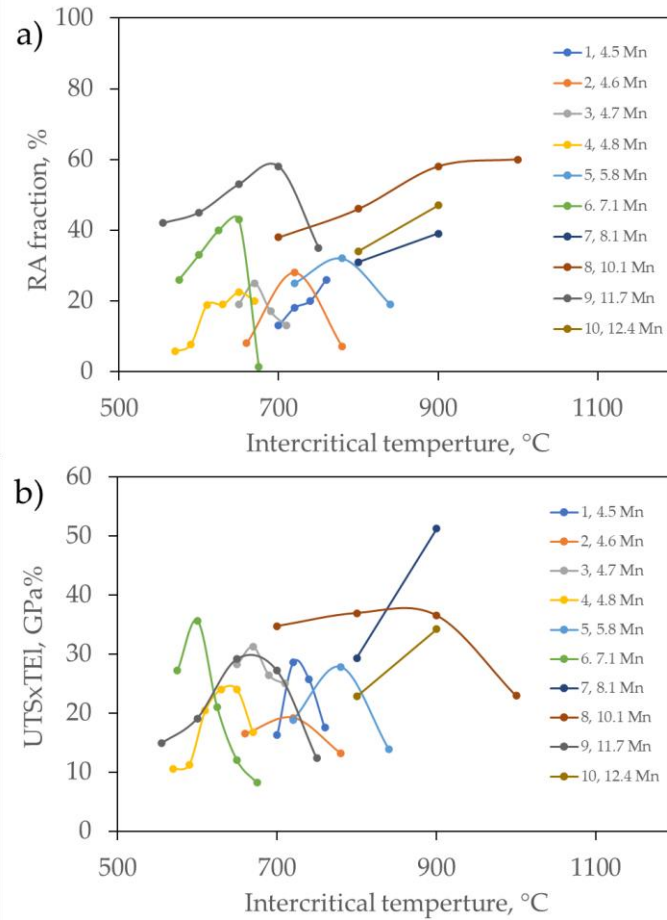


Figure 20 Retained austenite fractions (a) and resulting products of strength and plasticity (b) depending on intercritical annealing temperature for different alloy compositions. The chemical compositions are given in Table 2.

Table 2 Chemical composition of steels analyzed in terms of intercritical annealing temperature.

No.	Chemical composition, wt.%				Ref.
	C	Mn	Si	Al	
1	0.11	4.5	0.4	2.2	[75]
2	0.12	4.6	0.5	1.1	[80]
3	0.17	4.7	-	-	[78]
4	0.09	4.7	1.2	0.6	[79]
5	0.12	5.8	0.4	3.1	[80]
6	0.10	7.1	0.1	-	[66]
7	0.23	8.1	-	5.3	[83]
8	0.26	10.1	-	6.3	[87]
9	0.06	11.7	0.2	2.9	[89]
10	0.20	12.4	0.9	5.2	[83]

Figure 21 shows the phase equilibrium system of the Fe-0.12C-5Mn-0.5Si alloy as a function of the Al content. Calculations were performed using the CALPHAD method [161]. In the temperature range of 700 °C – 800 °C (recrystallization temperature of the cold-rolled structure), the austenite equilibrium fraction was calculated. It ranged from 67 % to 100 % for Al-free steel. In the case of an increase in the content of this element in steel, the amount of austenite gradually decreases. Upon reaching 3 wt.% Al the austenitic region disappears reducing the fraction of this phase to 20 % – 30 %. This means that Al can limit excessive austenite formation even at a high temperature used in the continuous annealing. This also has a positive effect on its stability. The influence of Al on the equilibrium phase fraction suggests that the design of the Al-containing microstructure may be one of the ways to manipulate mechanical properties of the intercritical austenite of medium-Mn steels [80].

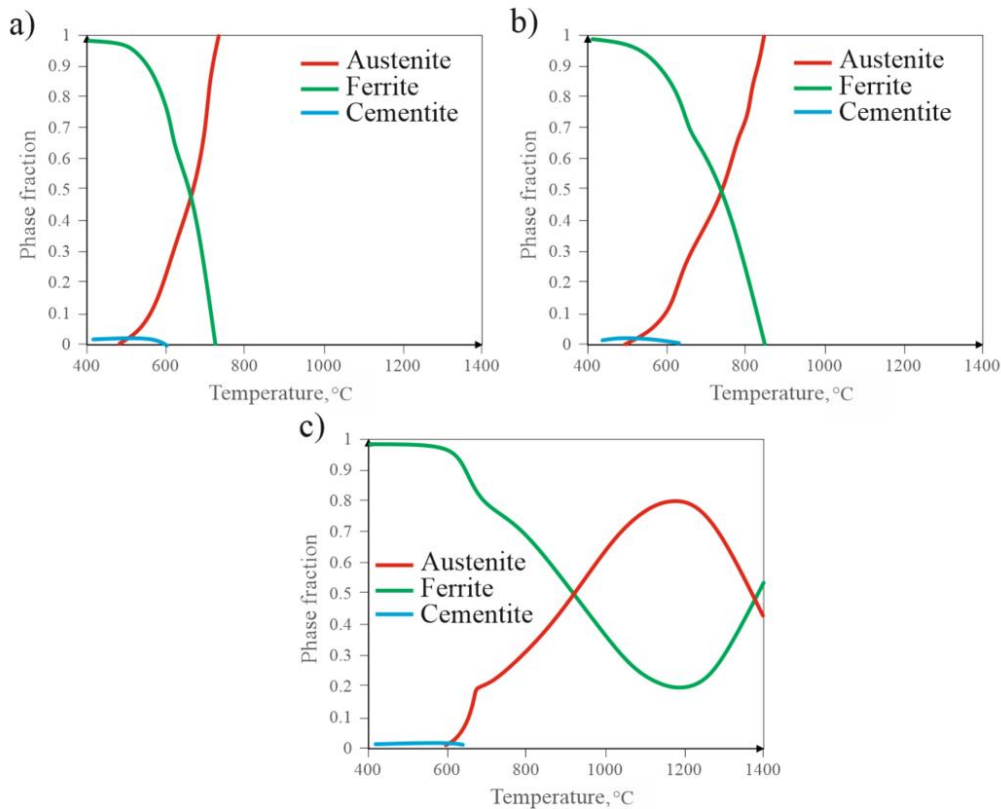


Figure 21 Equilibrium fractions of constituting phases in Fe-0.12C-5Mn-0.5Si alloy system containing: (a) 0 wt.% Al; (b) 1 wt.% Al; (c) 3 wt.% Al [80].

These examples indicate a next important parameter of intercritical annealing – soaking time [162], which has to be tuned together with the process temperature to obtain the desired fraction and stability of RA and thus optimal mechanical properties.

### **2.3.3. Effect of soaking time in intercritical annealing**

During the soaking at an intercritical temperature the microstructure strives to establish equilibrium conditions with respect to the phase ratio and chemical composition of each phase [15] controlled by temperature. Within the soaking time:

- Martensite undergoes further tempering, started during heating [146],
- Formed cementite dissolves enriching the formed austenite in C. This process transforms initial martensite and next tempered martensite to ferrite [163],
- The austenite nucleated during heating grows and new grains are formed. It increases the overall fraction of austenite [156],
- The chemical elements diffuse to austenite (C and Mn) and ferrite (Al and Si), respectively. Initially, the concentrations of C and Mn in austenite increase. However, when austenite fraction starts to grow fast, these elements are redistributed to an increased volume of this phase, which results in overall decrease in C and Mn concentrations in austenite [164],
- The grain size of formed austenite grows continuously. Smaller grains merge to bigger ones, which decrease the austenite stability.

All these processes contribute to the final phase composition and stability of retained austenite in medium-Mn steels. As discussed in the previous chapter their rate and kinetics depend on the intercritical soaking temperature. In 5Mn steel soaked at 760 °C [156] the maximum fraction of retained austenite is obtained after 120 s, while soaking at 650 °C required a time over 1 h to reach the maximum fraction of RA [54]. The progress of intercritical soaking is accompanied with an increase of austenite fraction. However, its overall stability decreases progressively due to lower enrichment in C and Mn and an increasing grain size. In work [165] it was reported that during annealing at 650 °C a RA grain size in cold-rolled 5Mn steel increased from 0.4 µm after 1 min up to 1 µm after 6 h of soaking. For hot-rolled steels a grain size is generally finer. Wang et al. [166] reported that in 5Mn steel annealed at 650 °C, a lath thickness of austenite increased from 0.2 µm after 1h to 0.33 µm after 48 h. It shows similar tendency as the one caused by the increase of process temperature. Despite continuously growing fraction of austenite with prolonging soaking (Figure 22a) the plasticity first rises and next starts to decrease (Figure 22b). It is related to the lower stability of this phase.

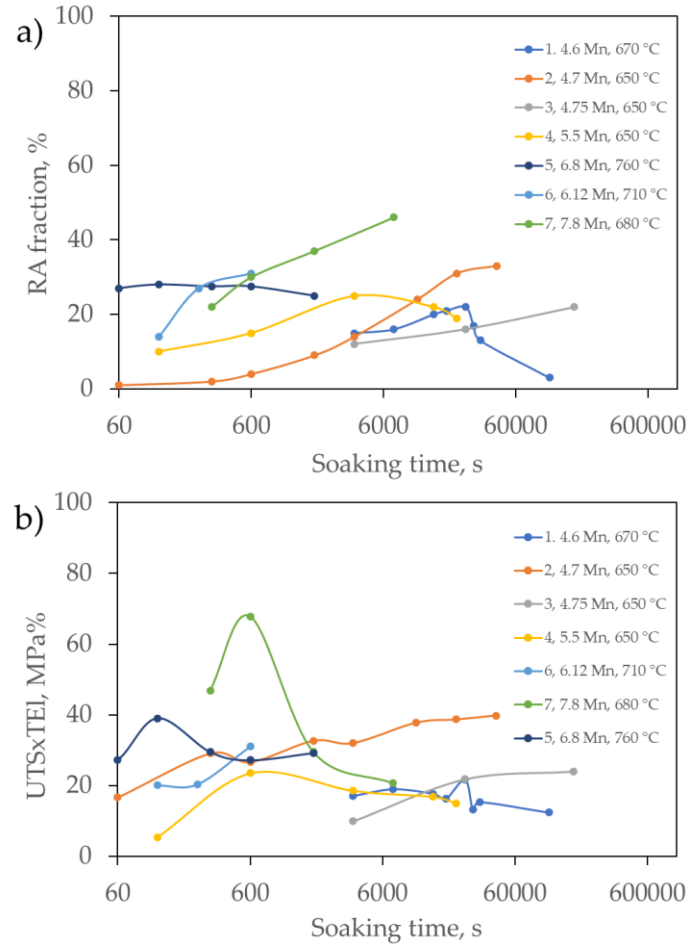


Figure 22 Retained austenite fractions (a) and resulting product of strength and plasticity (b) depending on soaking time at different temperatures and alloy compositions. The full chemical compositions are given in Table 3.

Table 3 Chemical composition of steels analyzed in terms of soaking time.

No	Chemical composition, wt.%				Ref.
	C	Mn	Si	Al	
1	0.09	4.6	3.0	-	[76]
2	0.20	4.7	-	-	[77]
3	0.09	4.7	1.2	0.6	[79]
4	0.06	5.5	0.2	-	[80]
5	0.12	5.8	0.4	3.1	[156]
6	0.21	6.1	1.6	0.4	[167]
7	0.14	7.8	-	1.6	[168]

### **2.3.4. Effect of cooling rate in intercritical annealing**

As during heating, slow cooling prolongs the period when medium-Mn steel is at the intercritical temperature range. Therefore, it contributes to the soaking time, which may influence significantly the short continuous-type intercritical annealing [169]. Increased additions of manganese ensure very high hardenability [115]. According to work [169] in steel containing 3 wt.% Mn even as slow cooling rate as 0.3 °C/s does not cause ferritic or pearlitic transformation during cooling. The bainitic transformation may be started with cooling rate of 1.5 °C/s. When the Mn concentration in steel reaches 5 wt.% even bainitic transformation does not occur at a cooling rate of 0.3 °C/s. The martensitic transformation is only present. Therefore, the phase composition of intercritically annealed steels is not sensitive to cooling rate in terms of phase transformations. If austenite was stabilized during soaking, the ferritic-austenitic microstructure will be maintained to room temperature despite the cooling rate. The only factor which may deteriorate the stability of austenite is the possible precipitation of carbides during very slow cooling. Furukawa et al. [170] reported that precipitation does not occur in medium-Mn steels containing less than 0.1 wt.% of C. However, for higher contents of this element a cooling rate changes may significantly influence the microstructure and mechanical properties. With increasing carbon concentration in steel, the amount of carbide precipitation along the austenite grains increases significantly. It influences the destabilization of austenite, which may even induce partial martensitic transformation of C and Mn depleted areas [15]. Moreover, mechanical properties of slowly cooled (furnace cooling) material deteriorate due to cracking and fracturing along the cementite-rich retained austenite boundaries. Therefore, the cooling rate from intercritical annealing should be relatively fast.

## **2.4. Summary of the state of art**

In addition to the search for new types of drive, the development of modern steel grades is the driving force of the automotive industry. Research on chemical composition, microstructure, heat treatment, resulting mechanical and technological properties of conventional and advanced high strength steels has been continued for many years [2,7,10,21,100,134,171–174]. Factors influencing the structure and properties of steels designed for the automotive industry have been the subject of research often conducted also in Polish universities and research centers, which resulted in numerous scientific works, for example: scientific publications [5,24,29,118,175–179], doctoral dissertations [22,26–

28,32,33,36,40,44–46,180,181], habilitation dissertations and books [18–20,23,25,39,43,182] related to this subject. The research efforts contained in these works cover a large part of the issues concerning many AHSS steels, mainly of 1<sup>st</sup> and 2<sup>nd</sup> generations. With the development of the market, however, new types of steel appear, requiring optimization of mechanical properties and factors affecting them. They create new research gaps.

As the above literature review shows one of the latest developments of modern high-strength steels are medium-Mn steels [15,183]. They are very promising materials in terms of obtaining beneficial strength-plasticity ratio with high economic indicators. Also, the uncomplicated heat treatment, i.e. intercritical annealing, is a cost-effective process. However, the issues of medium-Mn steels are far from being adequately characterized and explained. It is caused by the increased content of manganese, which affects significantly such aspects as the kinetics of phase transformations, critical temperatures of steel, austenite stability, high hardenability or slow austenite decomposition. The related microstructure, mechanical and technological properties adjustment and optimization require a dedicated approach to chemical composition and heat treatment parameters design. The thermodynamical and mechanical behavior of Mn-rich retained austenite in multiphase microstructures has to be described in detail. The issue of medium-Mn steel opens up new research areas and allows for novel findings. Involvement in the subject of chemical composition and heat treatment design of medium-Mn steels will allow for the simultaneous development of the discipline of materials engineering and automotive industry. These aspects are the motivation for undertaking this research topic.

### **3. Experimental procedure**

#### **3.1. Investigated material**

This work addressed investigations on medium-Mn steel with a chemical composition presented in Table 4. The content of individual alloying elements was selected to ensure high technological properties and economic indications considering its application. Medium-Mn steels contain usually from 3 to 12 % of Mn [15]. The investigated steel contains 4.7 % of this element to support RA formation and maintain low cost of the material. The relatively low carbon content was selected to limit its harmful influence on steel weldability [68]. Silicon and aluminium were added to prevent carbide precipitation. Si was replaced in majority by Al to improve hot-dip galvanability [94]. To ensure high metallurgical purity, the steel was produced using Balzers vacuum furnace.

*Table 4 Chemical composition of the investigated steel.*

Chemical element, wt. %							
C	Mn	Al	Si	Mo	S	P	Fe-balance
0.16	4.7	1.6	0.20	0.20	0.005	0.008	93.12

The mold has dimensions of: bottom— $\varnothing$  122 mm, top— $\varnothing$  145 mm, height—200 mm. Next, a 25 kg ingot was forged in a temperature range from 1200 to 900 °C to the final dimensions of 155 mm (width) x 22 mm (thickness). As the last hot working step, the material was hot rolled in a temperature range from 1100 °C to 750 °C to a final thickness of 4.5 mm. After hot working the material was air cooled to room temperature. Due to high hardenability the resulting microstructure consisted of martensite [184] with trace amounts of retained austenite (Figure 23). Chemical composition was measured by optical emission spectroscopy (OES) after casting and hot rolling in the 2/3 of the plate thickness.

The first approach to heat treatment of this steel was the thermomechanical treatment described in [5]. It produced the microstructure composed of bainitic ferrite, martensite and interlath austenite (~9 %) (Figure 24). Such microstructure resulted in very high strength of the material (YS of ~950 MPa and UTS of ~1400 MPa). However, its plasticity was limited to 6.2 % of UEl and 8.5 % of TEL. Therefore, another heat treatment approach had to be applied to improve microstructure-property relationships of this medium-Mn steel.

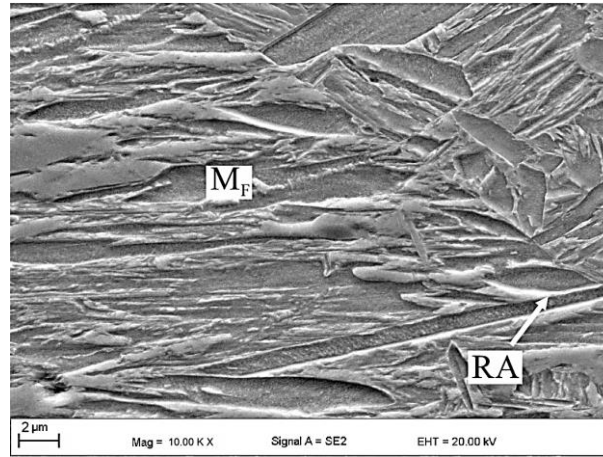


Figure 23 The microstructure of hot-rolled steel;  $M_F$  – fresh martensite, RA – retained austenite.

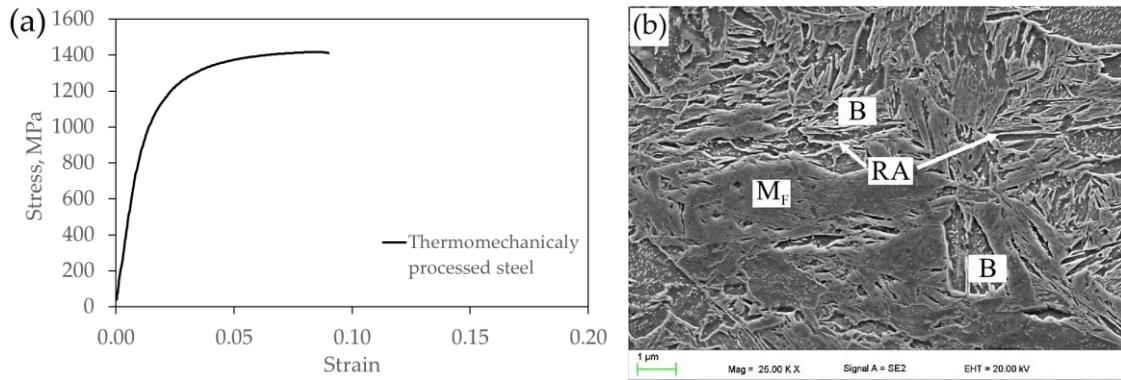


Figure 24 Mechanical properties (a) and microstructure (b) of investigated steel after thermomechanical processing,  $M_F$  – fresh martensite, RA – retained austenite, B – bainite [5].

### 3.2. Purpose and thesis of the work

The literature analysis on advanced high-strength multiphase steels allowed to conclude that the plasticity is strictly related to the fraction and stability of retained austenite in the microstructure. Currently, the heat treatment allowing for the formation of the highest phase ratio of retained austenite to matrix in medium-Mn steels is the intercritical annealing. The global studies performed so far prove the effectiveness of this approach in the context of obtaining high plasticity and formability of these steels. This heat treatment was adopted from DP steels since it allows for a precise control of phase composition of the alloy. Additionally, the temperature range of intercritical holding is favorable for a chemical redistribution of both C and Mn, which was limited for the former and not possible for the later in case of thermomechanical processing of these alloys.

Despite the ongoing research on intercritical annealing of medium-Mn steels, the complex nature of metastable retained austenite is still an obstacle in the way of optimizing their mechanical behavior during deformation. The fraction and stability of RA, which mainly influence the plasticity of the steel, are controlled by many factors, ranging from its chemical composition to crystallographic orientation of retained austenite. These factors in turn are controlled by intercritical annealing parameters. Based on the literature, the explanation of the impact and synergy of individual intercritical annealing parameters on resulting microstructure-property relationships has not been developed so far (Figure 25).

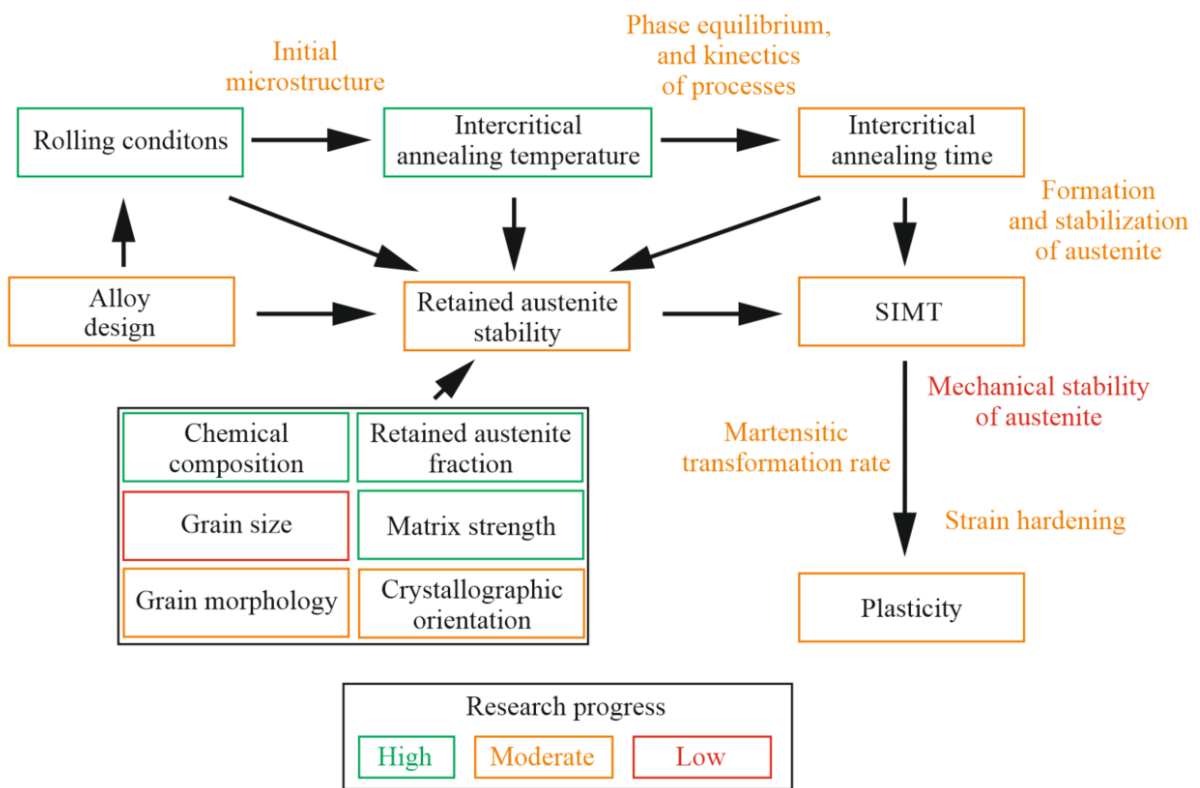


Figure 25 Factors influencing the intercritical annealing process, retained austenite characteristics, and resulting mechanical behavior, on the basis of previous investigations [15,60,145,155,185].

The research gaps regarding intercritical annealing of medium-Mn steels concern:

- Investigations on medium-Mn steels are mainly focused on cold-rolled steels, whereas hot-rolled ones provide different morphology and dislocation distribution in the material. Hot-rolled medium-Mn steels have to be thoroughly investigated as they may cover the wide area of heavy transport and other industries using thicker sheets.
- Initially medium-Mn steels were alloyed with Si, which deteriorates galvanizing ability. Silicon is needed to be replaced with Al to overcome this shortcoming.

Effects of Al on critical temperatures and transformation kinetics have to be described.

- The stabilization effects of C and Mn on retained austenite were already deeply investigated. However, the influence of grain size, its distribution in microstructure and impact on the mechanical stability and resulting mechanical performance have to be explained.
- Current medium-Mn steels are often produced in multi-hour process at relatively low temperatures. The possibility of intercritical annealing shortening by temperature increase has to be validated.

The development of these areas is necessary for optimization of the intercritical annealing process and thus properties of medium-Mn steels. It should allow to improve the ductility of intercritically annealed medium-Mn steels. It will contribute to the development in the field of materials engineering through new knowledge on the phase transformation behavior and microstructure-property relationships of medium-Mn automotive steels.

Taking into account the above factors and based on literature studies, it can be concluded that the production of a large fraction of retained austenite with the appropriate chemical composition, morphology and size requires a precise control of process parameters such as annealing temperature and annealing time. Considering the above aspects, **the aim of the work is to explain structural phenomena occurring during the intercritical annealing of hot-rolled Al-alloyed medium-Mn steel depending on the applied temperature-time parameters and optimization of these parameters resulting in improved steel plasticity.** The microstructural aspects have to be correlated with the obtained mechanical properties of the steel and their evolution with the deformation progress have to be investigated.

The conducted literature study and the interdependence of the phenomena occurring during the cold deformation of steel with the microstructure formed in the previous intercritical annealing justify the adoption of the following research thesis:

**Proper adjustment of the fraction and stability of the retained austenite through optimized soaking temperature and time of intercritical annealing allows to achieve gradual strain-induced martensitic transformation controlled by grain size and thus improved plasticity and strength-ductility product, particularly in comparison to thermomechanically processed steel.**

The target of the investigations is to obtain a multiphase steel with final microstructure containing more than 30 % of RA and fine-grained ferritic matrix. The minimum level of desired mechanical properties is: UEL of 15 %, TEL of 25 % and UTS of 900 MPa (Figure 26). This level of properties expressed by  $UTS \times TEL > 23 \text{ GPa}\%$  is so far exhibited by Mn-steels with higher additions of Mn [57,75]; therefore such improvement of mechanical properties of investigated 5Mn-1.6Al steel is a research challenge.

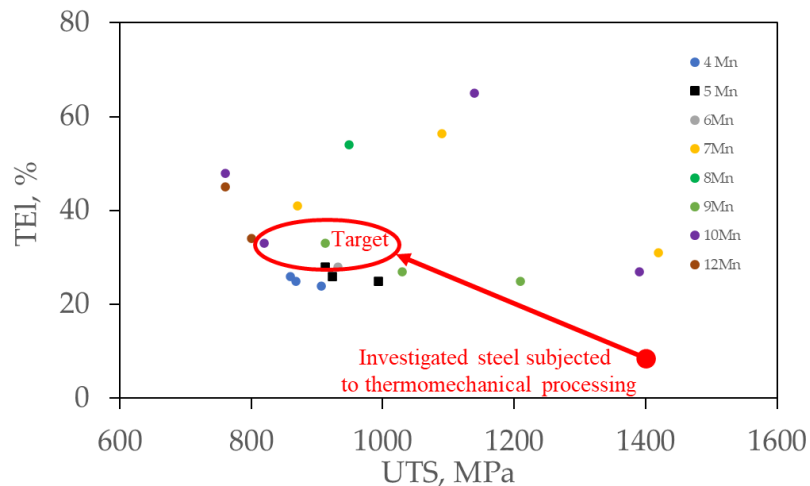


Figure 26 The aim of the investigations in relation to the currently investigated intercritically annealed medium-Mn steels (variants with the best ductility of each investigations were indicated) [57,66,70,74–79,83–85,88,186].

### 3.3. Methodology

In order to achieve the aim and to prove the thesis of the dissertation, research was carried out in accordance with the scheme presented in Figure 27. The first step consisted of thermodynamic simulations, the aim of which was to determine the steel phase evolution with increasing temperature and influence of this temperature on the chemical composition of individual phases. Critical temperatures of bulk steel such as  $A_{c1}$ ,  $A_{c3}$ ,  $M_s$  were also determined. Next, the cooling rate range influence on phase transformation was characterized and selected to avoid ferritic, pearlitic and bainitic transformations. Subsequently the dilatometry was used to verify results of simulations. This step allowed for section of the initial IA process parameters like heating and cooling rates, and the temperature range of the intercritical region.

Second step of the work consisted of investigations on the temperature of IA. Therefore, a wide temperature range covering the entire intercritical region was concerned in the variant selection (640 °C - 1000 °C for 1 h). Heat treatment was performed using dilatometry adapting

initial parameters determined in the first step of the investigations. The heat-treated samples were subjected to a series of qualitative and quantitative tests to determine changes in phase composition, size, and morphology (SEM, EBSD) with the increase of temperature. Also, the fraction and chemical composition of RA (which controls its stability) were determined (using EDS, TEM, XRD). Subsequently, hardness and tensile test were used to examine mechanical properties of steel after different heat treatment variants and to correlate them with microstructural features. This step allowed to select the optimal intercritical temperature for analyzed steel, characterized by the highest TEL and favorable fraction and stability of RA.

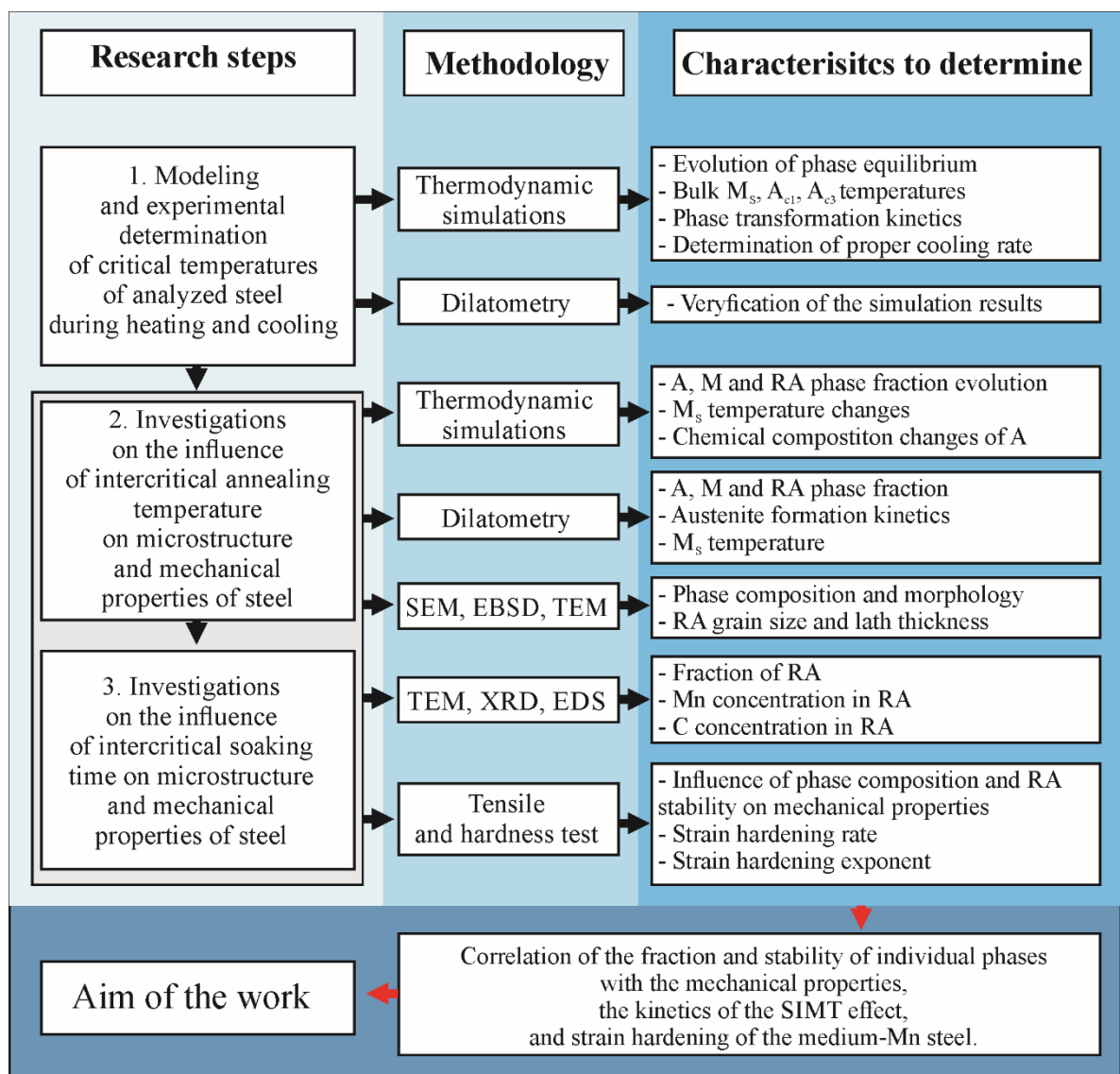


Figure 27 Stages in realizing the aim of the work on the basis of selected methods of investigations and result indices.

The last step of the investigation concerned the influence of soaking time on microstructure and mechanical performance of analyzed steel. A wide soaking time range between 1 min and 300 min at a temperature selected during second step of the investigations (680 °C) was applied to characterize IA process. This step covered to methodology described in the previous chapter. However, greater emphasis was placed on the characterization of the overall mechanical stability of RA and its distribution. For this purpose, the thermodynamic calculations and interrupted tensile test were applied. The deformed microstructures were also investigated in terms of phase composition, RA fraction and hardness changes. This made it possible to precisely determine the influence of individual phases on mechanical properties and to explain processes occurring during deformation.

### **3.3.1. Simulations**

The thermodynamic simulations were performed using JMatPro software with the implemented General Steels Module v11.2 database [187]. The calculations were performed in terms of ortho-equilibrium mode concerning all chemical elements present in steel. The simulations covered:

- Evolution of phase equilibrium with increasing temperature of the alloy,
- Changes in equilibrium chemical composition of ferrite and austenite with increasing temperature,
- Influence of the cooling rate on phase transformations,
- Influence of annealing temperature on austenite fraction and  $M_s$  temperature,
- Changes in martensite and austenite fraction during cooling from different intercritical annealing temperatures.

### **3.3.2. Dilatometry**

Dilatometry was used to determine critical temperatures during heating and cooling as well as the kinetics of phase transformations. It was also used to perform all designed variants of heat treatment. During the investigations, a BÄHR high resolution DIL805A/D dilatometer was used. The dilatometry specimens with the dimensions of  $\varnothing 4 \times 10$  mm were cut from the hot-rolled steel sheet along the rolling direction. During the experiments, induction heating was used. The sample length changes were measured via a Linear Variable Differential Transducer (LVDT) by fused silica pushrods. The temperature has been controlled by the S-type

thermocouple welded to the central part of each sample. Heating and soaking processes were performed in vacuum to prevent steel surface oxidation. Cooling was performed using helium. The dilatometry data was analyzed according to ASTM A1033-04 [188]. The beginning of the phase transformation was determined as the point where the dilatation curve deviates from the straight line [189,190].

During the investigations, a novel method of analyzing the dilatometric data was proposed. It was noticed that samples exhibiting a different ratio of ferrite and austenite exhibit different linear expansion coefficient  $\alpha_L$ , which may be calculated using the following equation [191]:

$$\alpha_L = \frac{dL}{L_0 \times dT}, 10^{-5} \times K^{-1} \quad (11)$$

where  $\alpha_L$  is the coefficient of linear thermal expansion,  $L_0$  is the initial length of the sample,  $dL$  is a change in length of sample and  $dT$  is a change in temperature.

The determination of linear expansion coefficients for ferritic and austenitic microstructure for analyzed steel allowed to design an equation determining the high-temperature phase equilibrium based on the slope of cooling curves of the samples [158]. It is based on the range of thermal linear expansion coefficient ( $\alpha_{L100\%} - \alpha_{L0\%}$ ):

$$A = \frac{100 * (\alpha_{Lx} - \alpha_{L0\%})}{(\alpha_{L100\%} - \alpha_{L0\%})}, \% \quad (12)$$

where A – austenite in vol. %

### **3.3.3. Investigations of mechanical properties**

- Tensile tests

Sub-sized flat tensile samples (according to ASTM E8 standard) with 40 mm gauge length, 6 mm width and 2.5 mm thickness were machined from the hot-rolled steel sheet along the rolling direction. Tensile samples were heat-treated using Nabertherm LT15/12/P330 muffle furnace under argon atmosphere according to parameters designed during dilatometric investigations. After soaking samples were quenched in water.

The tensile test has been performed according to ASTM E8 standard on a universal testing machine ZWICK Z020 at a strain rate of  $10^{-3} \text{ s}^{-1}$ . The elongation has been measured using an extensometer.

From the tensile data true stress - true strain diagrams have been calculated using common equations [192]:

$$\sigma_T = \frac{F}{S_T} = \sigma(1 + \varepsilon), \text{ MPa} \quad (13)$$

$$\varepsilon_T = \ln(1 + \varepsilon) \quad (14)$$

where  $\sigma_T$  – true stress,  $\varepsilon_T$  – true strain,  $F$  – load,  $S_T$  – true cross section of the sample,  $\sigma$  – engineering stress and  $\varepsilon$  – engineering strain.

Results were averaged over 3 trials for each heat-treatment variant.

Next, the strain hardening rate and instantaneous strain hardening exponent for uniform deformation range were calculated using following equations [193]:

$$SH = \frac{d\sigma_T}{d\varepsilon_T}, \text{ MPa} \quad (15)$$

$$n = \frac{\varepsilon_T d\sigma_T}{\sigma_T d\varepsilon_T} = \frac{d(\log \sigma_T)}{d(\log \varepsilon_T)} \quad (16)$$

where SH – strain hardening rate,  $n$  – strain hardening exponent,  $\sigma_T$  – true stress and  $\varepsilon_T$  – true strain.

- Hardness test

The hardness of samples before and after tensile tests was measured using a microhardness tester FB-700 at a load of 1 kgf. Ten measurements for each sample were taken. The extreme values were discarded and the average value was calculated using the remaining measurements.

### 3.3.4. Microstructural characterization

- Sample preparation

Both heat-treated and deformed samples were prepared for microstructural investigations according to standard procedures. The sample preparation consisted of the following steps:

1. Cutting. Dilatometric samples were cut in half, perpendicular to the rolling direction. From the samples after the static tensile test, fragments from the area of uniform elongation and the neck (total elongation) were cut out perpendicularly to the direction of rolling/tensile test.
2. Grinding. The hot-embedded in conductive resin samples were sanded using SiC paper with grid up to 2000.
3. Polishing. Samples were polished using diamond pasts with 3  $\mu\text{m}$  and 1  $\mu\text{m}$  grain sizes. The final polishing was performed using 35 nm colloidal silica to ensure a flat surface with minimal deformation.

4. Etching. For microstructural observations by scanning electron microscopy the samples were etched using 3 % nital for ~ 4 s at room temperature.

For transmission electron microscopy 8 x 8  $\mu\text{m}^2$  lamellas were cut along the rolling direction of samples by focused ion beam. The samples were prepared using the FEI Quanta 3D 200i.

- Scanning electron microscopy (SEM)

The microstructure of steel was investigated using JEOL JSM-7200F SEM microscope operating in Secondary Electrons mode. The accelerating voltage of 20 kV and the working distance of 10 mm were used for the investigations. The samples were characterized by ultrafine microstructure. Therefore, a magnification of 25 000x was used. Since the microstructure exhibited elongated lath-like morphology the commonly used grain size indicator, which is the grain diameter, is not appropriate. Therefore, the lath thickness of retained austenite was measured. At least 200 interceptions of retained austenite laths were measured for each sample using high-resolution SEM micrographs with magnification of 10 000x.

- Electron Backscatter Diffraction (EBSD)

EBSD was used to obtain more detailed information about the microstructure. The EBSD system was mounted on FEI Quanta FEG 450 SEM with field emission gun (FEG) filament. EBSD was performed at 20 kV on the sample tilted 70° and a probe current of ~2.5 nA using a hexagonal scan grid with 60 nm spacing. At least three 40x40  $\mu\text{m}^2$  scans were taken and analyzed for each sample. The EBSD data was processed using the OIM TSL data analysis software v. 7.3.1. A double cleaning procedure was applied. First, a grain confidence index (CI) standardization was used employing a grain tolerance angle of 5° and a minimum grain size greater than 3 pixels [175]. Next, the neighbor orientation correlation with CI=0.1 and clean up level 3 was used. The points with  $\text{CI} \leq 0.1$  were removed from the analysis as doubtful. The image quality (IQ) and phase (P) maps were used to characterize the microstructure. The dark regions in IQ maps of alpha phase, which contain higher density of lattice imperfections [194], were assigned to martensite [195,196]. The method based on differentiating the range of IQ values for ferrite and martensite [197,198] was used to distinguish these phases and calculate their surface fractions. The macrostrain distribution in analyzed samples was investigated using the kernel average misorientation (KAM) method [199,200], which provides quantitative information on the misorientation between neighbor pixels (concerning 3<sup>rd</sup> nearest neighbor) acquired via EBSD.

The following methodology was applied to determine the retained austenite grain volume. The retained austenite grains correspond mostly to the shape of ellipse. Therefore, the EBSD data was used to determine both semi-axes for each grain. As microstructure for each sample did not exhibit any significant difference in the RA grain thickness, it was assumed their thickness and width are similar. Therefore, a formula for ellipsoid volume has been applied:

$$V_E = \frac{4}{3} \times \pi \times A \times B^2, \mu\text{m}^3 \quad (17)$$

where  $V_E$  – ellipsoid volume, A, B – lengths of semi-axes of the ellipsoid

- Transmission electron microscopy (TEM)

TEM observations were performed in a S/TEM TITAN 80-300 microscope operating at 200 kV. It was equipped with an electron gun X-FEG (Extreme Field Emission Gun), STEM (Scanning Transmission Electron Microscopy) scanning system, BF (Bright Field), Dark Field, wide-angle annular condenser field detector, electron energy filter, EELS (Electron Loss Spectrometer), EDS (Energy Dispersive X-Ray Spectrometer). The test samples were cut from material soaked for 1 min, 15 min and 300 min at 680 °C, and from the deformed sample (UEI region) soaked at 680 °C for 15 min. The test results were recorded using the bright field (BF) and dark field (DF) techniques. Identification of the phases in the tested steels was carried out using SAED (selected area electron diffraction).

All images of the microstructure (including SEM, EBSD and TEM) were obtained with the same sample orientation. Therefore, for each micrograph/map, the vertical direction is the axis of hot-rolling and tensile strain.

- Energy-dispersive X-ray spectroscopy (TEM-EDS).

TEM-EDS was used to measure the changes in chemical composition of austenite after different variants of heat-treatment. At least 20 measurements of different areas for each sample were taken.

- X-ray diffraction (XRD)

The volume fraction of retained austenite was determined using XRD data. The measurements were conducted using Co-K $\alpha$  radiation in a Bruker D8 diffractometer working at 40 KV and 30 mA and equipped with a LynxEye Linear Position Sensitive Detector and a Goebel mirror. The scans in the  $\theta$ – $2\theta$  range were performed with a step size of 0.01°. The diffraction patterns were refined using the 4.2 version of the TOPAS Rietveld analysis program

(Bruker AXS). The Bragg-Brentano geometry was used for the diffraction studies. The identification of the phases was based on the data contained in the International Center for Diffraction Data ICDD database. The lattice parameter of austenite  $\alpha_\gamma$  was determined, which was used to calculate the carbon concentration in austenite using the following formula [201]:

$$\alpha_\gamma = 3.556 + 0.0453x_C + 0.00095x_{Mn} + 0.0056x_{Al} \quad (18)$$

where  $\alpha_\gamma$  is in Å,  $x_C$ ,  $x_{Mn}$  and  $x_{Al}$  are C, Mn, and Al concentrations in austenite (wt.%)

The measured concentrations of carbon and manganese, as well as the RA grain volume were used to calculate the thermal and mechanical stability of retained austenite. Thermal stability ( $M_s$ ) was calculated according to formula (10).

## 4. Modeling and experimental determination of critical temperatures of analyzed steel during heating and cooling

### 4.1. Experiment design

The first step of the investigations was aimed to characterize the analyzed steel by determining its critical temperatures (especially the intercritical range) and phase transformation kinetics. For this purpose, at first the phase equilibrium for different temperatures together with the chemical composition changes of main phases have been simulated using JMatPro software. Since the cooling rate has significant influence on the austenite decomposition, CCT diagrams have been also simulated. The critical temperatures  $A_{c1}$ ,  $A_{c3}$ ,  $M_s$  and cooling rate have been validated in terms of dilatometry. First a sample was heated up to 1200 °C to investigate a wide temperature range. The heating rate of 3 °C/s was selected on the basis of work [153] to allow for relatively short heating stage and simultaneously prevent diffusionless austenitic transformation. Next, basing on the heating results, a sample was austenitized at 1000 °C and continuously cooled. Cooling rate of 60 °C/s was selected on the basis of simulation results.

### 4.2. Results

#### 4.2.1. Simulation results

Figure 28 shows the changes in phase equilibrium state with increasing temperature. According to the simulations, microstructure of steel below 667 °C contains up to about 3 % of carbides. First, up to 430 °C they are  $M_{26}C_6$  type and next  $M_7C_3$  type.

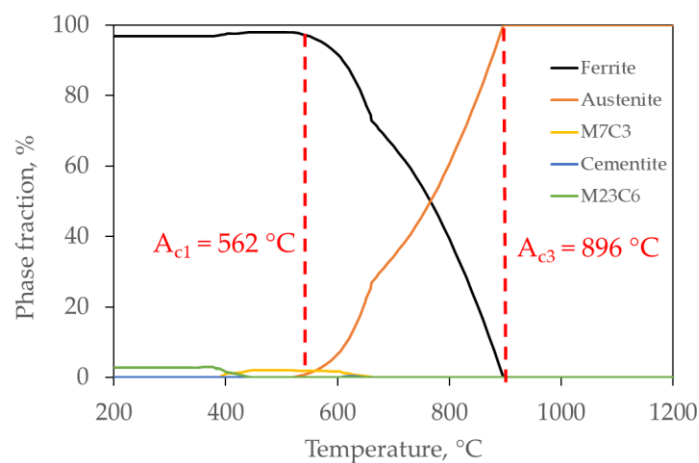


Figure 28 Evolution of phase equilibrium with increasing temperature of the alloy.

The steel's theoretical  $A_{c1}$  temperature is 562 °C and  $A_{c3}$  temperature is 896 °C according to simulations in JMatPro. The fraction of austenite grows rapidly along with carbides' dissolution process. Next, a slight deceleration of austenite formation kinetics is visible. The microstructure is composed of 50 % austenite and 50 % ferrite at about 765 °C.

The chemical composition of ferrite is influenced by the presence of carbides (Figure 29a). A peak for Mn concentration in ferrite is at about 560 °C (3.5 wt. %). Next it starts to drop and stabilizes eventually at a level of about 2.7 wt.%. With the increase of temperature, the concentration of Al in ferrite increases up to 2.2 wt.% at 896 °C. These changes are related to the austenitization process. Al diffuses from newly formed austenite (Figure 29b) enriching ferrite, while Mn and C enrich austenite.

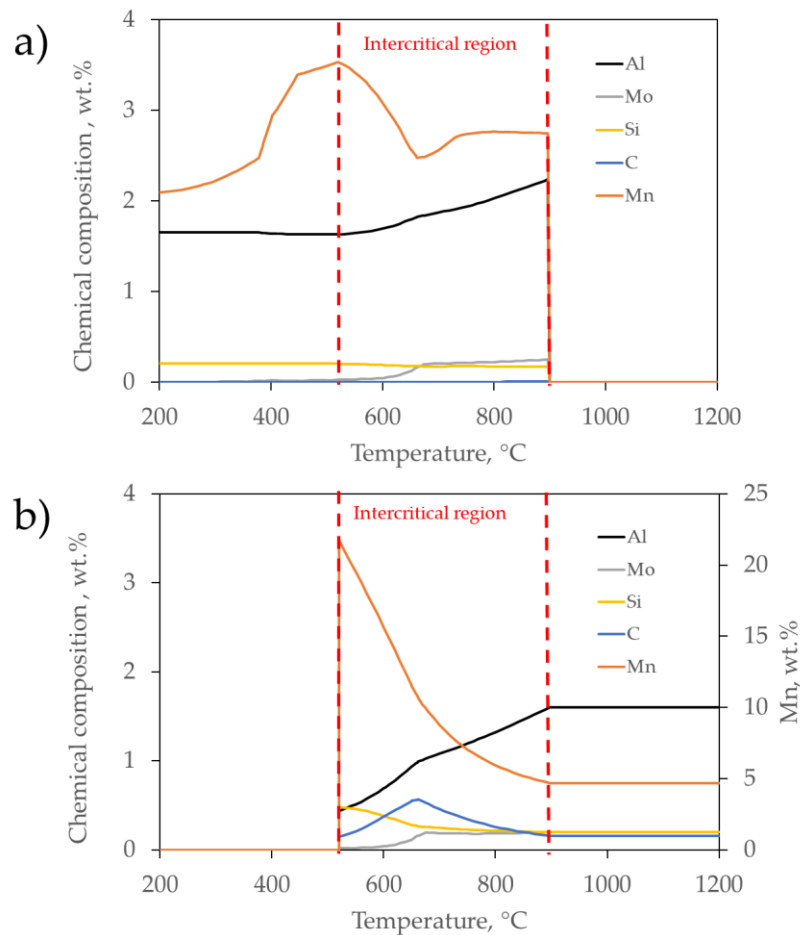


Figure 29 Changes in equilibrium chemical composition of (a) ferrite and (b) austenite with increasing temperature.

The concentration of Mn in austenite continuously decreases with an increase of the temperature due to increasing fraction of this phase. The C concentration in austenite initially

increases up to 0.57 wt.% at 660 °C, which is the highest temperature at which carbides are present in the microstructure. The dissolution of carbides provides some additional carbon to the solid solution. After their complete dissolution, the concentration of this element in the austenite begins to decrease faster with an increase of its fraction as in case of Mn.

The simulated CCT diagram presented in Figure 30 indicates that the minimal cooling rate allowing to prevent phase transformations other than martensitic is about 7 °C/s. The theoretical  $M_s$  and  $M_f$  temperatures of the investigated alloy are 312 °C and 193 °C, respectively. To allow for ferritic and pearlitic transformations, the alloy would have to be cooled slower than about 0.3 °C/s. Basing on these results the cooling rate for the heat treatment was selected to be 60 °C/s, which is faster than a critical cooling rate for martensitic transformation. It is the appropriate rate for dilatometry investigations, and it corresponds well to conventional quenching methods.

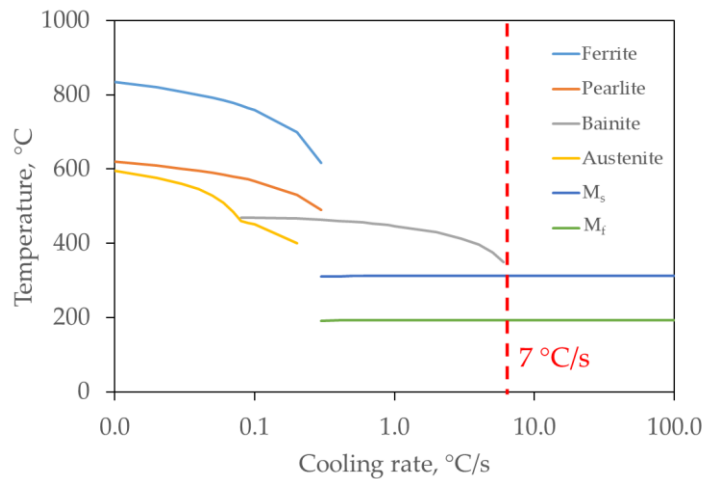


Figure 30 Influence of the cooling rate on phase transformation in investigated alloy;  $M_s$ ,  $M_f$  – martensitic transformation start and finish temperatures, respectively.

#### 4.2.2. Dilatometric characterization

The experimental heating curve presented in Figure 31a shows two processes occurring during heating. At first, the carbides precipitation [202] starts at about 495 °C and takes place up to 570 °C. Carbides precipitation process is caused by the initial martensitic microstructure of the sample (Figure 23). Next, at 648 °C the austenitization begins and lasts up to 924 °C. Later, up to 1200 °C the dilatometric results are linear, which indicates no further phase transformations. The cooling curve from the austenitization temperature of 1000 °C (Figure

31b) indicates only one process occurring at the applied cooling rate (60 °C/s) – martensitic transformation. The experimental  $M_s$  and  $M_f$  temperatures are 314 °C and 191 °C, respectively.

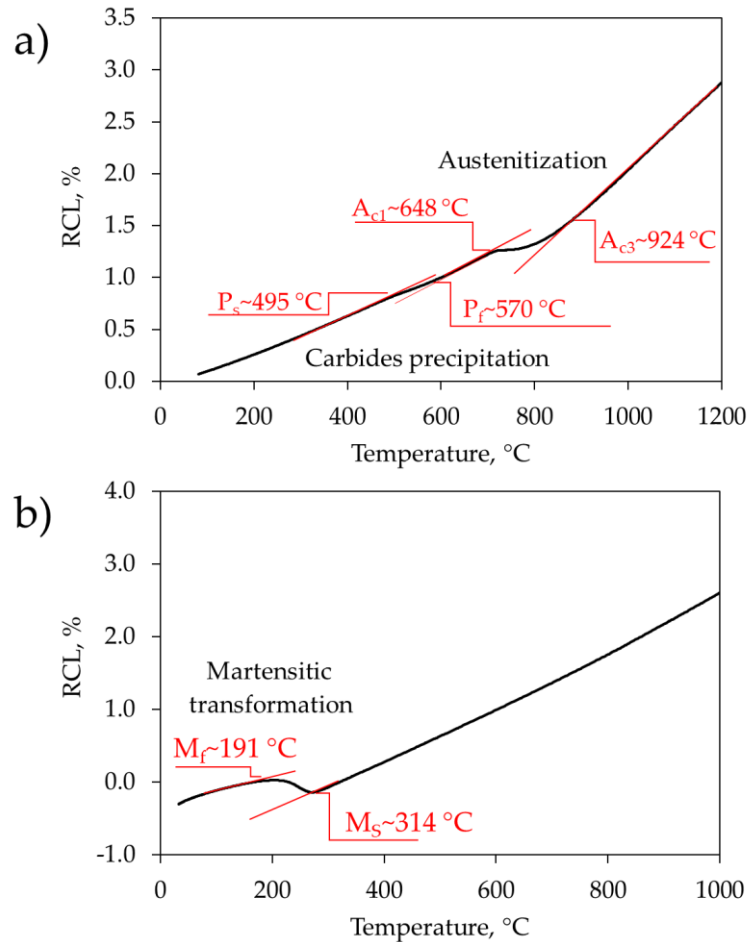


Figure 31 Dilatometric curves of investigated alloy during (a) heating at 3 °C/s and (b) cooling at 60 °C/s;  $P_s$ ,  $P_f$  – carbides precipitation start and finish, respectively.

### 4.3. Discussion

Both simulations and experimental results are in general in line, especially for the cooling stage.  $M_s$  and  $M_f$  temperatures for both methods are almost the same. The significant differences are visible in case of heating stage, where the experimental temperatures are significantly higher than the results of the simulations (88 °C for  $A_{c1}$  and 30 °C for  $A_{c3}$ ). Works [15,203] indicate that these differences may be explained by the inaccuracy of currently available models in the software used [204]. Diffusion kinetics is not included at this stage of the model development and needs to be addressed in future works because manganese gradients in austenite may be present due to slow diffusion coefficient of Mn, especially in austenite [205]. The differences

may be also influenced by the applied heating rate. While simulations assume the infinite time at each temperature allowing to obtain the phase equilibrium, the experimental investigations were performed at a heating rate of 3 °C/s. It is known that increasing heating rate results in increased  $A_{c1}$  and  $A_{c3}$  temperatures [153]. Moreover, the initial microstructure of steel was martensitic. During heating, the tempering process may interfere with austenitization. The tempered martensite/ferrite depleted in C and Mn concentrated in the newly formed carbides may be characterized by different kinetics of the transformation than the equilibrium state assumed in the simulations [206].

The measured intercritical range of investigated medium-Mn steel is much wider than for conventional carbon steels [207]. It is influenced by increased addition of Mn [92] and Al [15]. Such interaction may be favorable in terms of intercritical annealing process, as (1) wide intercritical region should ensure a wide technological temperature window, (2) process performed at an increased temperature should accelerate austenite formation and chemical redistribution allowing for reduction of required time [158,159].

The aim of this part of investigations was to indicate an intercritical range at the applied heating rate of 3 °C, select a proper cooling rate ensuring avoidance of ferritic, pearlitic and bainitic transformations and indicate the  $M_s$  temperature. They were needed for the proper design of the next investigation stages. The main results are as follows:

- The experimental  $A_{c1}$  and  $A_{c3}$  temperatures of the investigated alloy at a heating rate of 3 °C/s are 648 °C and 924 °C, respectively. They indicate the intercritical area, which is the subject of interest in the next stages of research. According to simulations the microstructure should be composed of 50 % austenite and 50 % ferrite at about 765 °C. The wide intercritical region range is caused by increased additions of Mn and Al in the alloy.
- The carbides may be present in the microstructure up to the temperature of 667 °C. Their presence is negative in relation to the enrichment of austenite in carbon and manganese. Therefore, the IA annealing temperature should be higher.
- The theoretical critical cooling rate is 7 °C/s. The cooling rate of 60 °C/s was applied in the experiment and allowed to obtain martensitic temperature.
- The experimental bulk  $M_s$  temperature of the investigated alloy is ~314 °C, which is in line with the simulations.

## 5. Influence of intercritical annealing temperature on microstructure and mechanical properties of steel

### 5.1. Experiment design

The first part of intercritical annealing optimization concerned the influence of the soaking temperature on the microstructure and mechanical behavior of the analyzed steel. Figure 32 shows a schedule of performed heat treatment. Heating and cooling rates were set to 3 °C/s and 60 °C/s, respectively, according to previous results. The former was selected to avoid diffusionless austenite transformation, which may significantly deteriorate the initial stability of austenite. The later was selected to avoid possible ferritic/pearlitic/bainitic transformations during cooling. The intercritical region of the material ranges from 648 °C to 924 °C at the applied heating rate. For thorough characterization, a wide range of temperature variants was selected: 640 °C (below  $A_{c1}$ ), 660 °C, 680 °C, 700 °C, 720 °C, 760 °C, 800 °C (intercritical range) and 1000 °C (above  $A_{c3}$ ). The samples were named as IAX, where X is the annealing temperature (for example IA800). The variants are densified at temperatures below 720 °C (interval of 20 °C), which is due to the theoretical fraction of austenite in this temperature range (Figure 28). Above 720 °C, basing on the simulations (Figure 28, 29) and literature (Figure 20a) the formed austenite will be hard to stabilize; therefore, the variants intervals are wider. The soaking time was selected to be 60 min as intermediate time used in other literature research (Figure 22a). The other purpose was to obtain phase equilibrium or get close to it to allow comparing simulations and experimental data. The different variants of heat treatment were first simulated in JMatPro and next performed using dilatometry. The samples were subjected to a series of tests: dilatometric analysis, SEM, EBSD, XRD, EDS, hardness, and tensile tests.

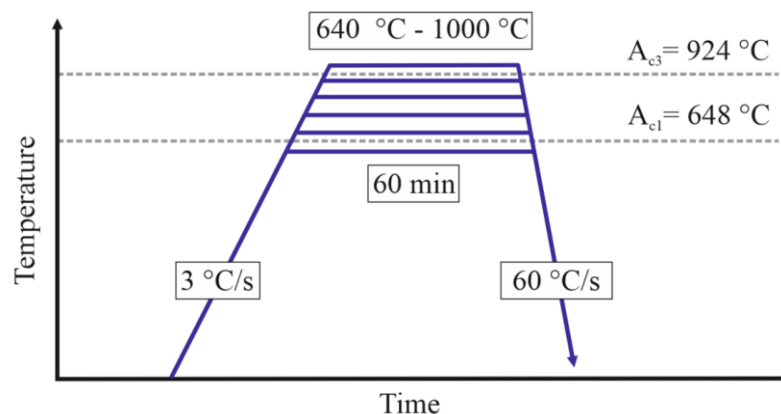


Figure 32 Scheme of IA at different temperatures for 1h.

## 5.2. Results

### 5.2.1. Simulation results

Figure 33 shows the diagram of simulated changes of austenite fraction and accompanying  $M_s$  temperature. It is visible that the stability of austenite decreases rapidly ( $M_s$  increases) with increasing fraction of this phase. The highest annealing temperature at which  $M_s$  temperature is about 0 °C is 695 °C. The results indicate that the highest fraction of stable austenite for investigated alloy should be about 33 %.

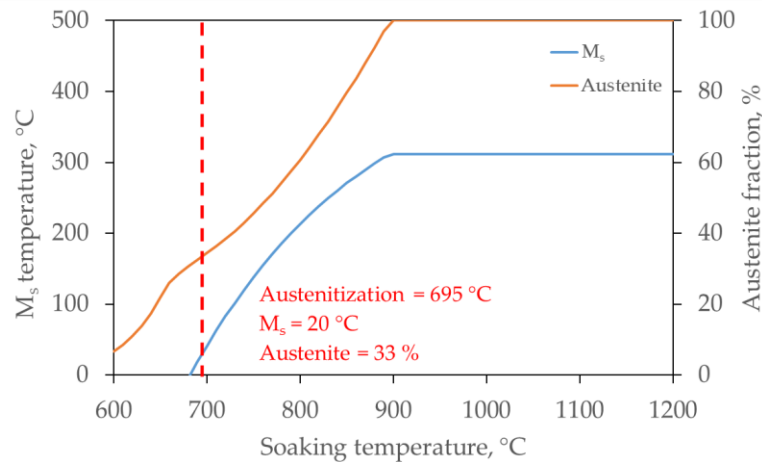


Figure 33 Influence of annealing temperature on austenite fraction and  $M_s$  temperature.

Figure 34 shows the evolution of martensite (Figure 34a) and austenite (Figure 34b) fractions for the selected annealing temperature variants. Again, the rapid increase of  $M_s$  temperature and kinetics of the martensitic transformation acceleration with increasing annealing temperature are visible. These results indicate also the austenite fraction retained after final cooling to room temperature. Figure 35 summarizes the results of austenite fraction during annealing and resulting RA and martensite ratio after cooling. Basing on the results the temperature variant ensuring the highest fraction of RA is 680 °C. After exceeding the temperature of  $\geq 700$  °C the retained austenite fraction starts to drop. At 720 °C and 760 °C its fractions amount to about 6 % and 2 %, respectively.

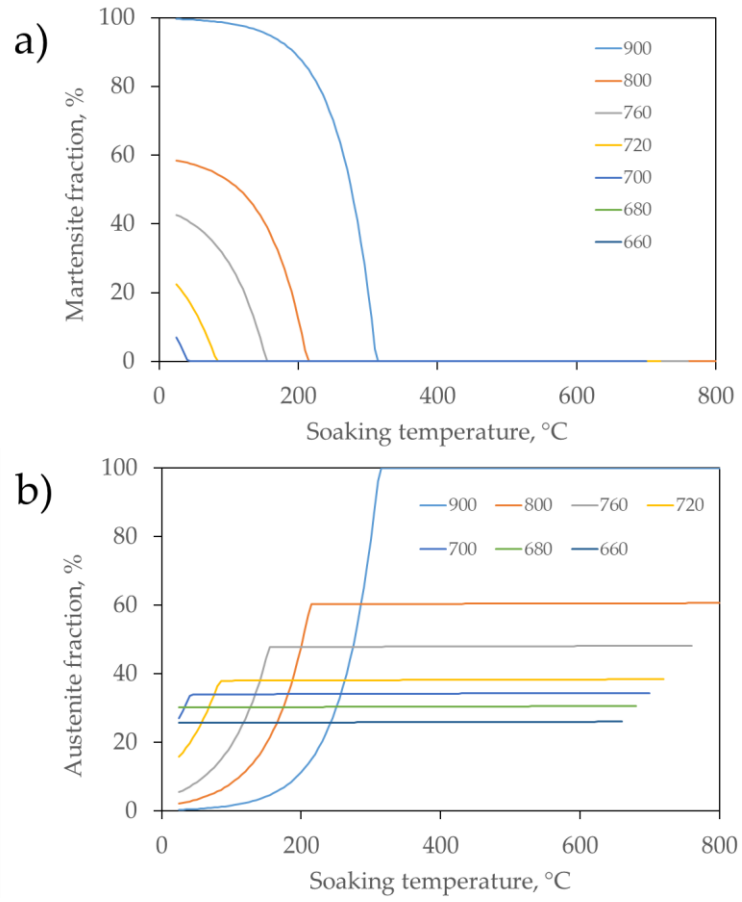


Figure 34 Changes in (a) martensite and (b) austenite fractions during cooling from different intercritical annealing temperatures.

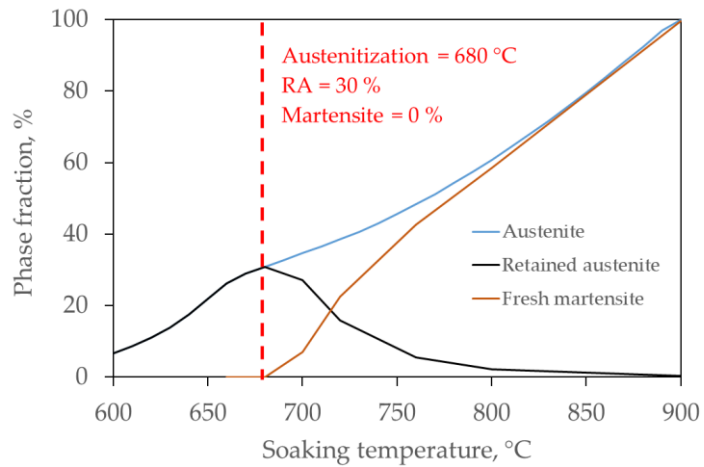


Figure 35 Relation of austenite fraction and resulting retained austenite and martensite fractions depending on the intercritical annealing temperature.

### 5.2.2. Dilatometric characterization

Figure 36 shows the kinetics of processes occurring during soaking. As the initial microstructure consists of martensite, two possible processes can take place during soaking – carbide dissolution (according to the equilibrium diagram (Figure 28)) and austenite formation (ART). Sample IA640 should not undergo austenitization because the experimental  $A_{c1}$  temperature is higher. Therefore, the visible contraction is probably related to the partial carbide dissolution [208,209]. The theoretical equilibrium fraction of carbides decreases from ~ 2 % at a temperature of precipitation finish to 1.2 % at 640 °C. At higher annealing temperatures the sample contraction is much more intense, which is related to austenite formation. However, the phase equilibrium (curve stabilization) is visible only for samples IA760 – IA800 °C. At lower temperatures, the applied soaking time of 60 min is not sufficient to obtain phase equilibrium. Sample IA1000 °C was fully austenitized during heating according to the heating curve (Figure 31a). Therefore, the soaking records are linear and horizontal. The half-transformation time (for recorded period) decreases from 12 min to 63 s for samples IA660 and IA800, respectively.

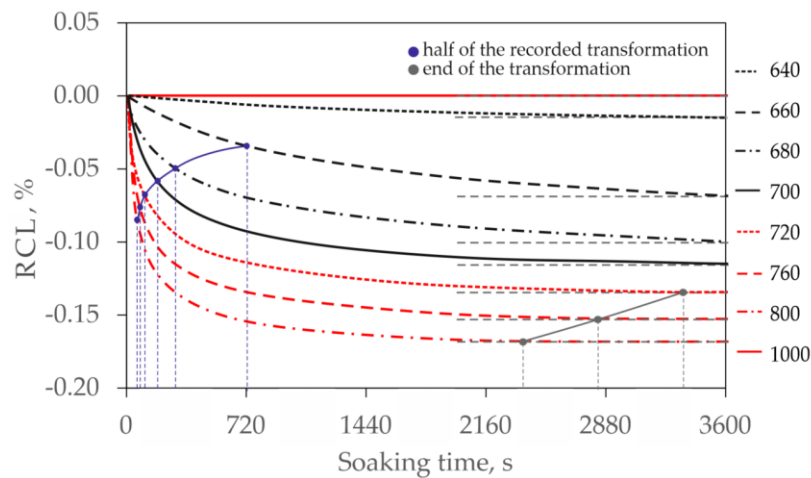


Figure 36 Kinetics of austenite formation at different austenitization temperatures.

The dilatometric cooling curves (Figure 37) do not show any disturbances associated with martensitic transformation for variants IA660 – IA700. It is assumed that all austenite formed in these samples was stabilized. Only samples annealed at temperatures higher than 700 °C exhibit length expansion related to austenite decomposition. The  $M_s$  temperature increases progressively with an increase of the annealing temperature up to 314 °C for the fully austenitized sample, which is the bulk  $M_s$  temperature.

During the investigations, a new method of analyzing dilatometric data was proposed. It is based on differences in linear thermal expansion coefficient, which is influenced by phase composition. The samples IA640 and IA1000 containing respectively 0 % and 100 % of austenite were used to determine the linear thermal expansion coefficient range (Figure 38). The coefficient of linear thermal expansion for ferrite was  $1.13 \times 10^{-5} \text{K}^{-1}$ , and for austenite was  $2.14 \times 10^{-5} \text{K}^{-1}$ . These results are in agreement with the literature data,  $\alpha_L$  for austenite:  $2.25 \times 10^{-5} \text{K}^{-1}$  [191],  $2.09 \times 10^{-5} \text{K}^{-1}$  [210],  $2.065 \times 10^{-5} \text{K}^{-1}$  [211] and for ferrite:  $1.24 \times 10^{-5} \text{K}^{-1}$  [211],  $\sim 1.10 \times 10^{-5} \text{K}^{-1}$  [212]. Next, the respective ferrite - austenite phase ratio was calculated for each sample.

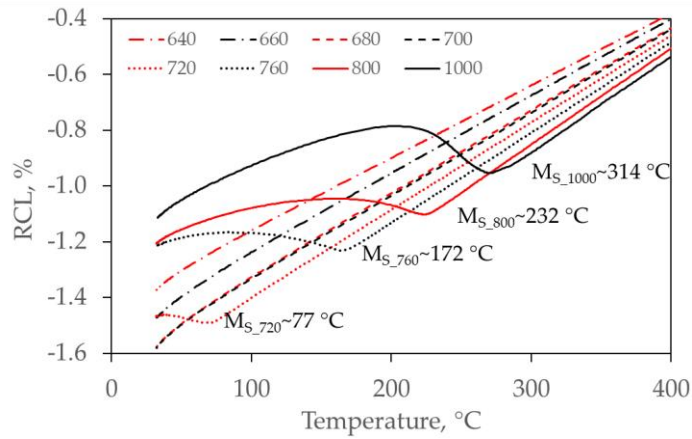


Figure 37 Dilatometric cooling curves of samples annealed at different temperatures.

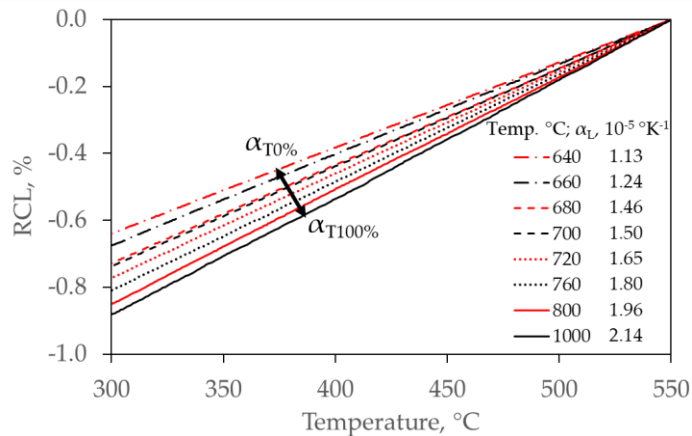


Figure 38 Changes in linear thermal expansion coefficient depending on the annealing temperature.

Summarized results of these calculations are presented in Figure 39 and compared with simulation results. It is visible that both experimental and simulation  $M_s$  temperatures show good consistency. However, the austenite fraction changes indicated by both methods show

different characteristics. In general, the experimental (dilatometric) fractions of austenite are significantly higher at annealing temperatures higher than 680 °C. The experimental increase of austenite fraction is parabolic, whereas the simulation results are close to the linear form.

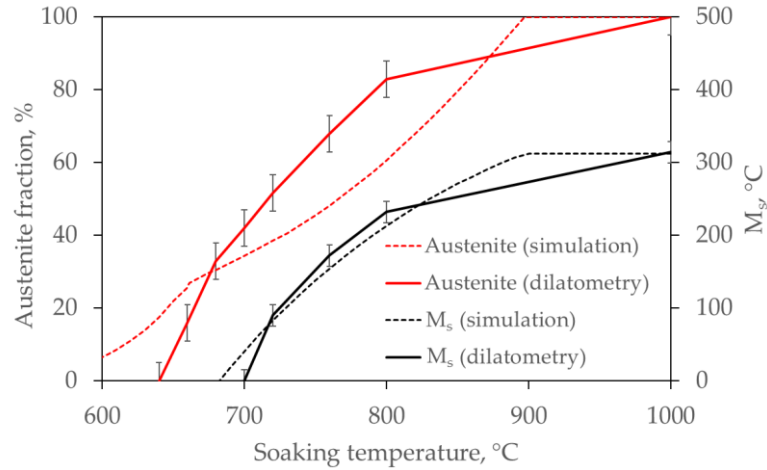


Figure 39 Experimental results of austenite fraction and resulting  $M_s$  during cooling from different annealing temperatures and compared to the simulations.

### 5.2.3. Fraction and chemical composition of retained austenite

The retained austenite fraction for each sample was determined by XRD method. The X-ray diffraction patterns are presented in Figure 40.

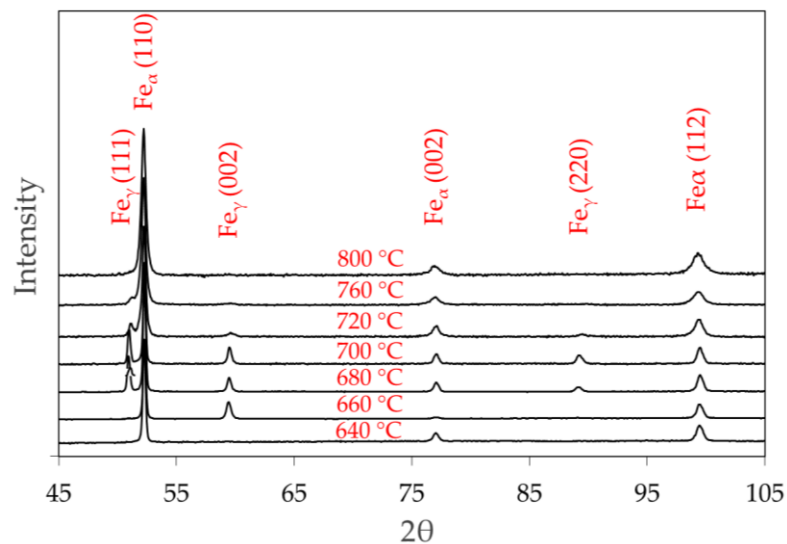


Figure 40 XRD diffraction patterns for samples annealed at different temperatures.

The quantitative results of RA fractions are shown in Figure 41a. It is visible that the XRD results indicating RA fractions and dilatometric results indicating fractions of high temperature austenite are in good agreement in a range where the martensitic transformation during cooling did not occur. This confirms the correctness of the proposed method, which is based on the dilatometry. As indicated by cooling curves the samples annealed at temperatures up to 700 °C maintain full stability of retained austenite. Its fraction is the highest for samples IA 680 and IA700 and amounts to about 36 % and 41 %, respectively. Annealing at higher temperatures results in a rapid decrease in RA fraction.

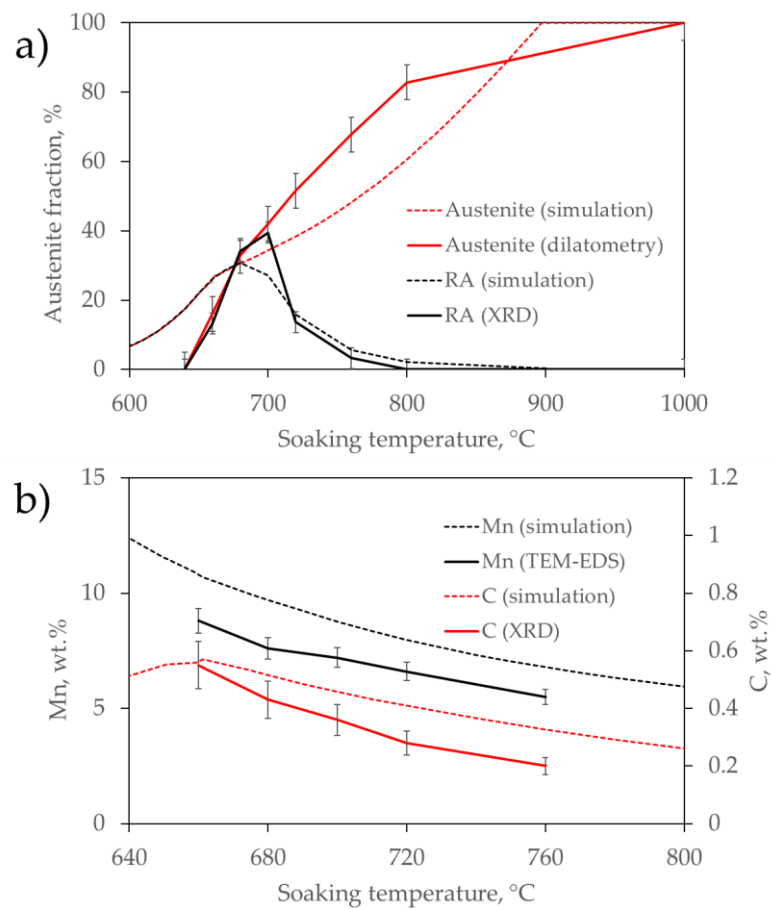


Figure 41 Changes in (a) austenite and resulting RA fractions depending on the annealing temperature and (b) chemical composition of retained austenite. Both are compared to simulation results.

It is visible that the experimental results for both high-temperature austenite and retained austenite fractions are shifted to higher fractions and temperatures than the simulations results. The temperature generating the highest RA fraction is about 20 °C higher and the fraction is higher by about 9 % than resulted from simulations.

To better describe the changes in austenite stability, the chemical composition of retained austenite was measured by means of EDS (Mn) and XRD (C). The results are shown in Figure 41b. As indicated by simulations the concentrations of both C and Mn should decrease with an increase in annealing temperature, which was confirmed by measurements. The 13 % of retained austenite measured in sample annealed at 660 °C contains 8.8 wt.% of Mn and 0.55 wt.% of C. For sample IA760 the concentrations decrease to 5.5 wt.% Mn and 0.23 wt.% C due to the high fraction of high temperature austenite: 68 %. It resulted in only 3 % of retained austenite retained in this sample after cooling (Figure 41a). Again, the simulations and experimental results are not in line. The experimental results of C and Mn concentrations in the austenite are lower than the theoretical ones.

#### **5.2.4. Microstructural characterization**

Figure 42 shows the SEM micrographs of microstructures obtained in sample annealed at different temperatures. All samples show fine, lath-like microstructures. Sample IA640 according to dilatometry and XRD does not contain grains which could be recognized as retained austenite or fresh martensite because annealing was performed below  $A_{c1}$  temperature. The initial martensitic structure underwent tempering as carbide precipitates are clearly visible for this sample (Figure 42a). According to XRD results, sample IA660 contains over 10 % of RA. It may be distinguished by bright, “smooth” appearance (Figure 42b). Such appearance is caused by nital etching, to which austenite is less prone [213]. It causes relief formation in the microstructure, where RA grains are higher than F,  $M_F$ , and  $M_T$ . The RA laths are localized at boundaries of tempered martensite. In sample IA660 the martensite tempering is more advanced. The number of carbides is significantly reduced and limited to coarser laths. Samples IA680 (Figure 42c) and IA700 (Figure 42d) show dual-phase ferritic-austenitic microstructures. The carbides are not visible, which indicates their complete dissolution. The fraction of RA is higher than in sample IA660. With the further increase of the annealing temperature (Figure 42e-g) a fraction of high-temperature austenite increases; however, also the fraction of fresh martensite increases significantly. Martensite may be distinguished by “rough” appearance; it is localized inside the parent high-temperature austenite grains. For sample IA800 the untransformed RA grains are not visible.

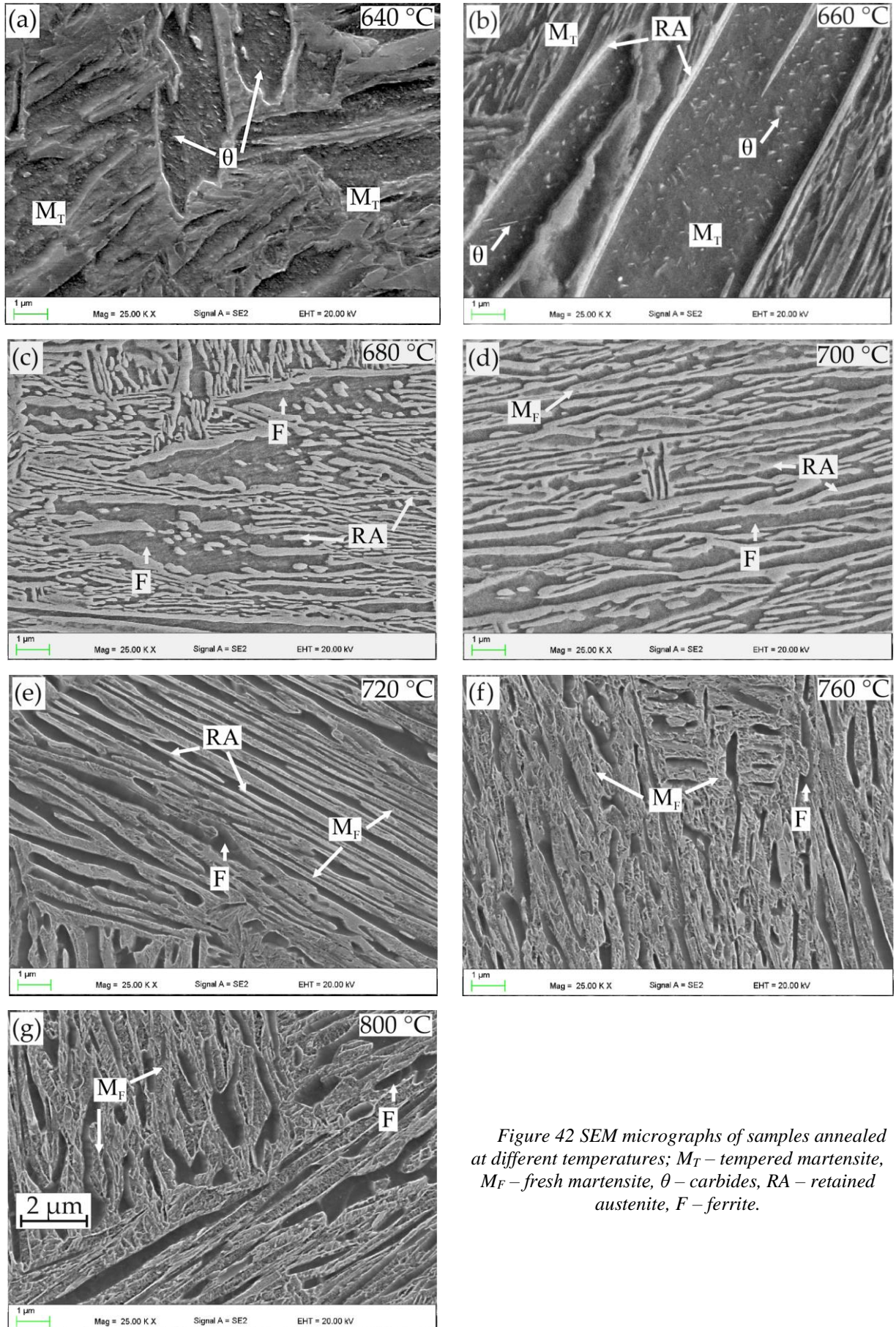


Figure 42 SEM micrographs of samples annealed at different temperatures;  $M_T$  – tempered martensite,  $M_F$  – fresh martensite,  $\theta$  – carbides, RA – retained austenite, F – ferrite.

The annealing temperature increase is accompanied by two additional effects: (1) the thickness of RA lath increases significantly from ~100 nm for sample IA660 to over 850 nm for sample IA800 (Figure 43), and (2) microstructure becomes more homogeneous in terms of morphology. The coarse tempered martensitic laths, which were present in samples IA640 – IA680, are not visible after annealing at higher temperatures due to fragmentation caused by nucleating and growing austenite.

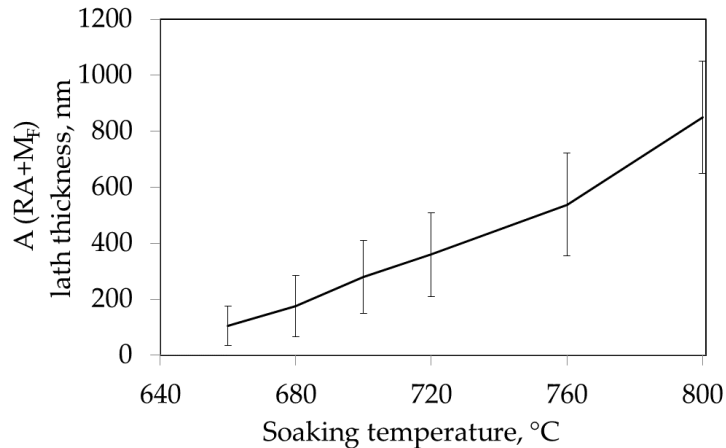


Figure 43 Thickness of austenite (A) laths formed during IA for samples annealed at different temperatures. For samples where martensitic transformation occurred during cooling the thickness of resulting RA+M<sub>F</sub> or M<sub>F</sub> was measured.

The EBSD results confirm the SEM observations (Figure 44). The nucleation of austenite occurs at martensite grain boundaries, especially at triple joints of martensitic grains. The main difference between SEM and EBSD results are observed in sample IA700. The RA fraction is lower than in sample IA680 despite opposite XRD results. A frequent fresh martensite grains are indicated by darker  $\alpha$  regions. As the martensite contains higher density of lattice imperfections than ferrite, they present lower image quality Kikuchi patterns [195,196], which may be used to distinguish both  $\alpha$  phases (Figure 45). The RA fraction measured by EBSD is usually underestimated, which may be caused by (a) incapability of resolving austenite films with dimensions smaller than 50-70 nm [214,215] or due to (b) the superficial nature of the test. The former may not be valid in analyzed case because visible high-temperature austenite grains are relatively thick. Therefore, the observed difference in austenite fraction is probably caused by sample preparation process [57].

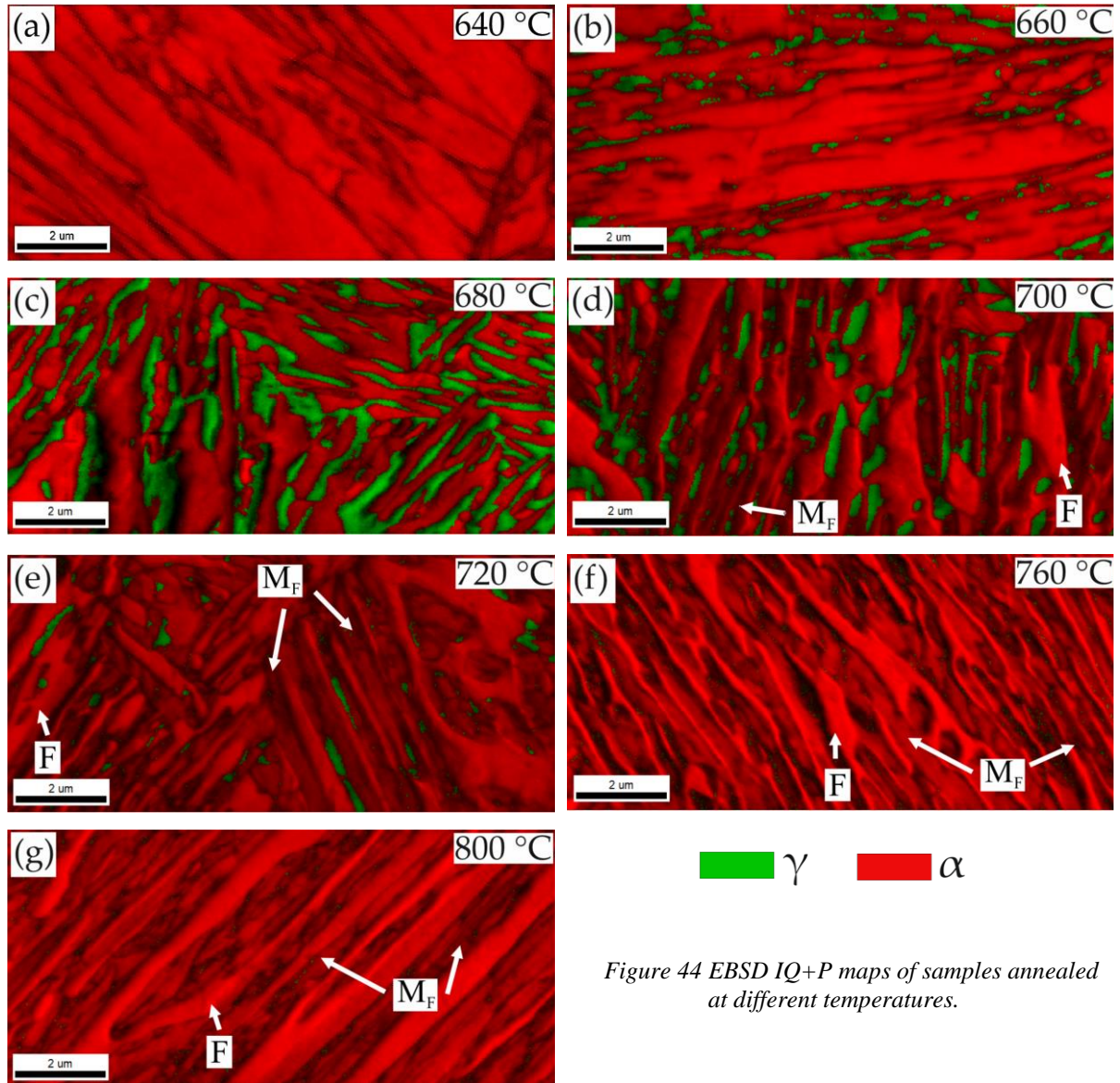


Figure 44 EBSD IQ+P maps of samples annealed at different temperatures.

SIMT effect occurring during grinding / polishing may have significant impact on the results. It is especially valid for sample IA700 because, according to the simulations (Figure 34) and experimental results (Figure 41a), its mechanical stability at room temperature is at the limit. Thus, the SIMT may be easily triggered. The comparison of high temperature austenite, retained austenite and fresh martensite fractions is shown in Table 5. A relatively good consistency for EBSD, XRD and dilatometric methods is achieved.

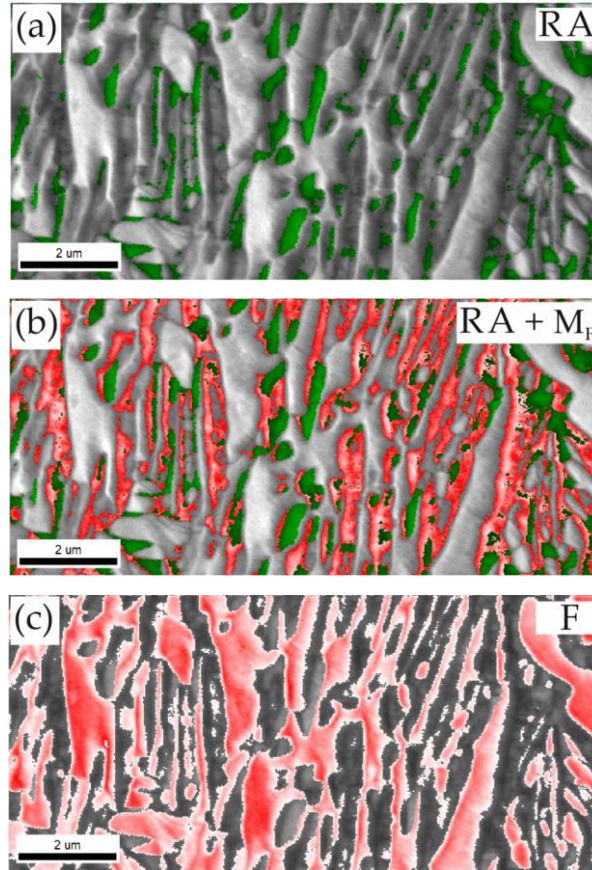


Figure 45 EBSD maps of sample IA700 with color indication of (a) RA (green), (b) RA (green) and  $M_F$  (red), and (c) F (red) on the basis of IQ value.

Table 5 Comparison of austenite (A), fresh martensite ( $M_F$ ) and retained austenite (RA) fractions measured by different methods.

Sample	RA (EBSD), % $\pm$ 3	RA (XRD), % $\pm$ 3	RA + $M_F$ (A) (EBSD), % $\pm$ 3	A (dil.), % $\pm$ 3
640	0	0	0	0
660	9	12	9	13
680	31	34	31	34
700	17	41	42	41
720	3	13	50	51
760	0	3	62	67
800	0	0	80	82

The KAM maps show that samples contain three main types of grain misorientation distributions. Sample IA640 (Figure 46a) contains mainly low angle ( $< 15^\circ$ ) and high angle ( $> 55^\circ$ ) boundaries related to increased dislocation density [216] and mutual orientation of

martensitic laths, respectively [217]. It is typical for martensite, tempered martensite and bainite structures. In sample IA680 (Figure 46b) the grain boundaries with misorientations of  $\sim 45^\circ$  dominate.

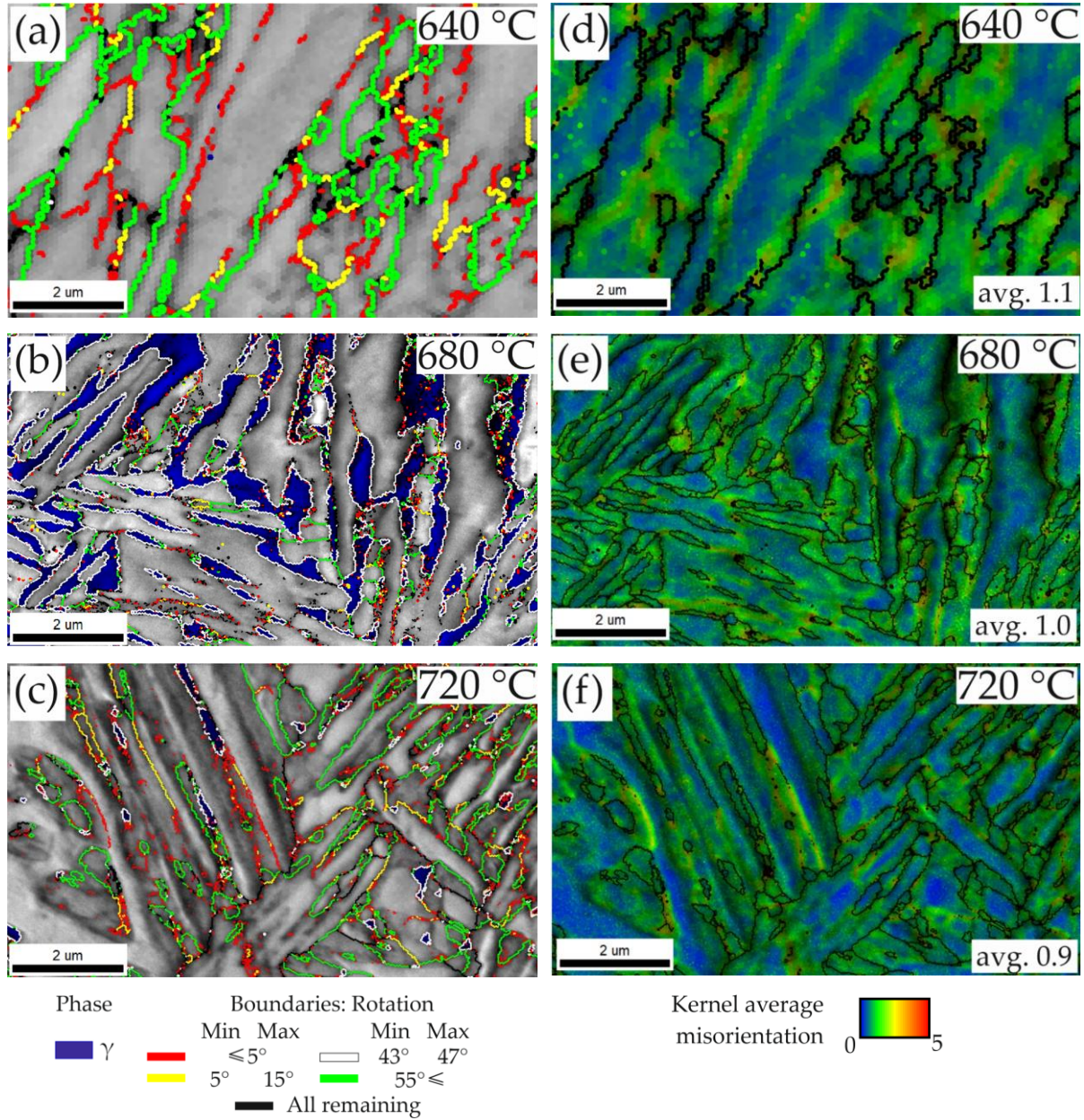


Figure 46 EBSD maps: IQ + misorientation angle (a), (b), (c), and IQ + KAM (d), (e), (f) for samples soaked at different temperatures.

They represent the ferrite – austenite grain boundary relationship [218], which highlights the homogeneous microstructure and phase distribution in this sample. For samples in which martensitic transformation occurred during cooling the martensite-related grain boundaries reappear (Figure 46c). The average KAM values for all samples (Figure 46-f) are about 1.0 (for

the 3<sup>rd</sup> neighbor). Recrystallized ferrite grains exhibiting very low KAM are not visible, which confirms that hot-rolled medium-Mn steel undergoes only slow recovery during IA. In sample IA680 (Figure 46e) the increased density of lattice defects in RA is revealed. It is even higher for regions of M<sub>F</sub> in sample IA720 (Figure 46f) due to highly distorted lattice of the high-carbon martensite.

### 5.2.5. Mechanical properties

The increasing annealing temperature is accompanied first with martensite tempering and an increase of RA fraction, and next by fresh martensite production during cooling (Table 5). This tendency is reflected in hardness results (Figure 47), where for samples IA640-IA700 the hardness values decrease slightly from 300 HV1 to 290 HV1, and next they increase rapidly up to 450 HV1 for sample IA800, where the hardness is only slightly lower than the initial hardness of the hot rolled material (468 HV1).

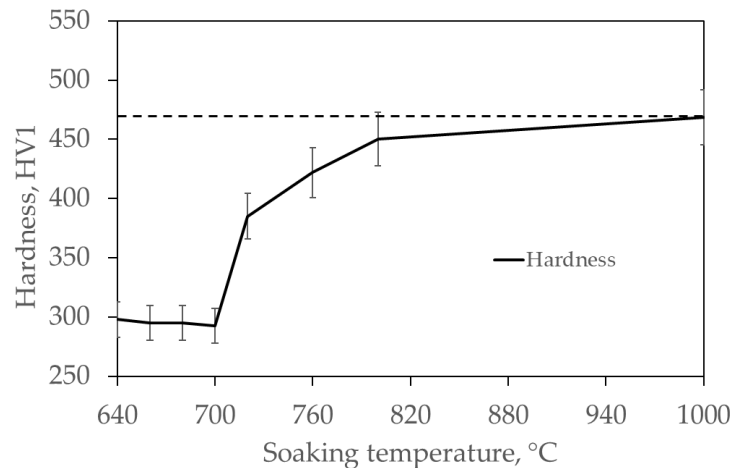


Figure 47 Changes in hardness depending on the annealing temperature.

Figure 48a shows tensile curves for different annealing temperature variants. None of the samples exhibits discontinuous yielding. The YS values have similar tendency as hardness results. They decrease from 803 MPa to 531 MPa with the annealing temperature increase from 640 °C to 700 °C. It is caused by martensite tempering and an increasing fraction of austenite. Along the further increase of annealing temperature, the YS increases up to 1020 MPa for sample IA800 due to a high fraction of fresh martensite. Regarding UTS, its values continuously increase with an increase in annealing temperature from 880 MPa for sample IA640 up to 1360 MPa for sample IA800. Both the UEl and TEI increase from 9 % and 18 % for sample IA640

to 17.5 % and 31 % for sample IA680. Both UEL and TEL decrease to 7 % and 8 %, respectively, for sample IA800.

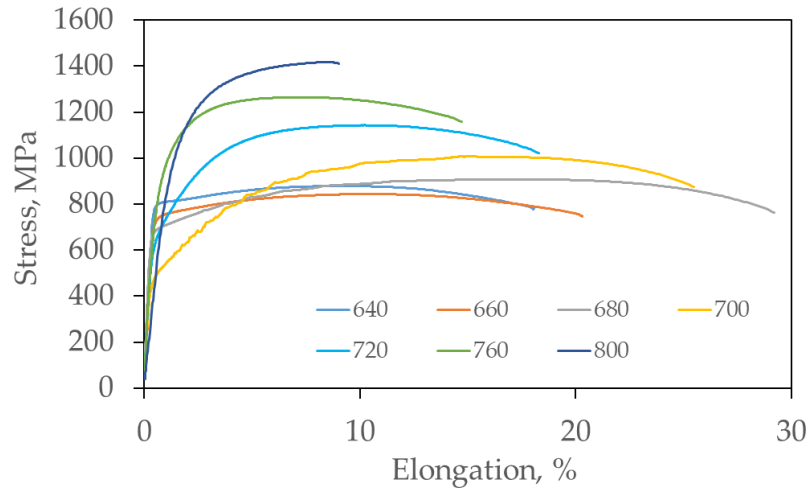


Figure 48 Stress-elongation curves of samples after the heat treatment at different IA temperatures.

In the tensile curves of the IA680 and IA700 samples, features of inhomogeneous deformation (serrations) are visible. They are classified as a DSA effect [219]. A special attention is required for strain hardening exhibited by samples after different soaking temperature. The strain hardening rate and its exponent are shown in Figure 49. For samples IA640 and IA660 both characteristics are similar: the strain hardening rate decreases rapidly at the beginning of plastic deformation and is maintained at a low level for the rest of tensile test. In case of strain hardening exponent, its initial value is about 0.05 and increases up to about 0.11 in later stages of deformation. Sample IA680, which is characterized by the best plasticity, exhibits most gradual changes of both strain hardening rate and work hardening exponent. Sample IA700 shows high strain hardening rate during the entire deformation. However, its exponent achieves maximum at a true strain of about 0.08 and next starts to decrease. It indicates the point, where SIMT effect is exhausted, or its intensity significantly decreases. Samples IA720 – IA800 show strain hardening rate and  $n$  exponent values typical for high-strength DP steels [220] or ferritic/pearlitic steels [221], where both strain hardening characteristics decrease rapidly with the strain progress. It is caused by a very limited fraction of RA or its absence, which does not have the significant contribution to plastic deformation.

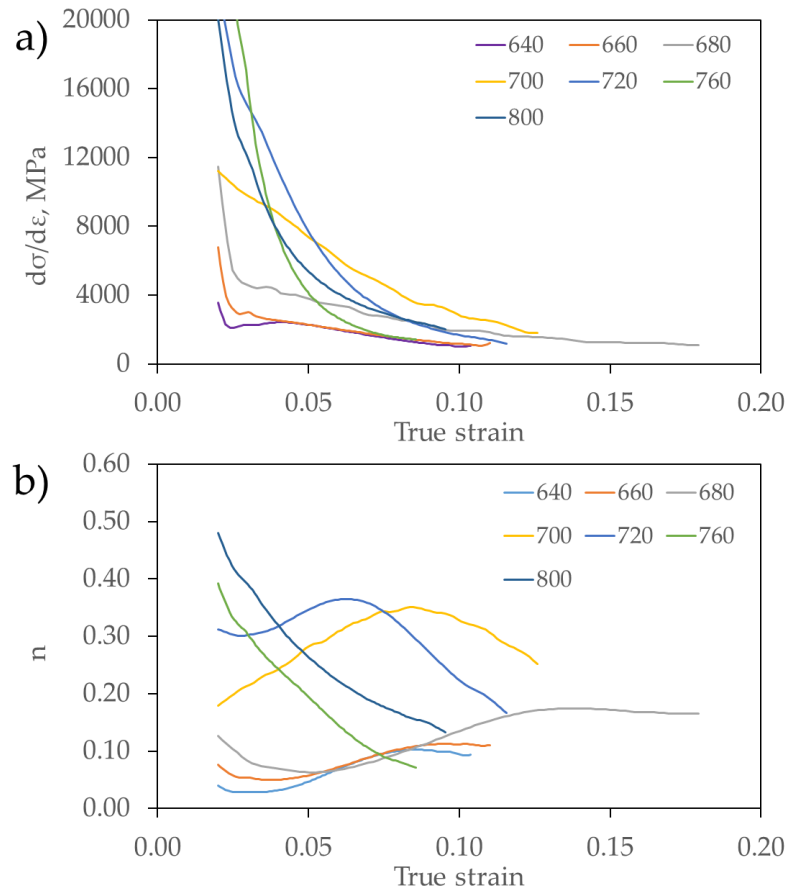


Figure 49 Work hardening rate (a), and work hardening exponent (b) of steel after annealing at different temperatures.

### 5.3. Discussion

#### 5.3.1. Comparison of simulations and the experimental approach

In general, the simulations and experimental results show relatively good agreement. The main differences are related to the amount and chemical composition of the retained austenite. This discrepancy in both cases may be due to the equilibrium nature of the simulations, which assumes infinity time of soaking, while experimental process lasts for 60 min. However, the equilibrium diagram does not indicate any carbides at these temperatures, which could limit retention of RA or influence its chemical enrichment. Moreover, the dilatometric curves concerning soaking time indicate that austenitization of sample annealed at a temperature lower than 720 °C is not completed within 60 min. Therefore, the chemical equilibrium can not be also established. Similar differences regarding model and experimental results were obtained in other works [15,203] concerning soaking time of even 1 week [66]. They report that the differences may be again explained by the inaccuracy of currently available models [204].

### **5.3.2. Impact of the microstructural changes on the mechanical performance**

The increase in the annealing temperature of analyzed steel is accompanied with:

- Initial martensite tempering and softening,
- First the formation and then the dissolution of carbides,
- Austenite formation at martensite grain boundaries and its further growth along these boundaries, and austenite thickening,
- Continuous decrease in stability of austenite due to the lower chemical enrichment and grain thickening,
- First an increase in RA fraction up to a point where the limit stability at room temperature is obtained, and next a fast decrease in its fraction accompanied with formation of fresh martensite.

All of these results are summarized in Figure 50 and their tendencies are in line with the literature for medium-Mn steels of different chemical compositions [15,75,167,206,209]. The resulting evolution of microstructure has a significant influence on mechanical properties. The continuous yielding is ensured due to austenitization without recrystallization, which is a feature of hot-rolled steels. It affects not only the lath-like morphology but also high dislocation density of both phases, and therefore uniform strain partitioning [15,133]. The discontinuous yielding, which may be avoided in hot rolled medium-Mn steels, is a significant disadvantage of the mostly investigated cold-rolled steels [76,89].

The analysis and comparison of phase evolution (Figure 50) and resulting mechanical properties (Figure 51) allow to assign a role of each phase. The YS (Figure 51a) and hardness values (Figure 51b) are directly related to the initial microstructure. They both decrease with the progress of martensite tempering and austenite formation due to overall microstructure softening [222]. Next, since the fraction of hard and high-strength fresh martensite rises due to instability of austenite, both YS and hardness increase. Regarding the UTS values, the initial microstructure generated during heat treatment seems to have limited influence. The value of UTS increases continuously with the increase of annealing temperature, regardless of RA :  $M_F$  ratio. Therefore, both the presence and stability of RA do not have a significant influence on UTS of intercritically annealed medium-Mn steel. It is rather dependent on a final fresh martensite fraction in the structure. This relation has not been yet pointed in the literature for medium-Mn steel due to the frequent analysis and comparison of results only for samples

characterized by thermal stability of austenite at room temperature [66,89]. The changes in ferrite fraction do not contribute clearly to the UTS value.

A different tendency is observed in case of the plastic properties of the tested steel (Figure 51c). Both UEL and TEL increase as RA fraction increases but their values drop significantly when fresh martensite is present in the initial microstructure, which is in agreement with literature [66]. What is important here, the plasticity is already limited in sample IA700 containing initially the highest fraction of RA among all temperature variants. The reason of that is the low stability of RA. Sample IA680, containing over 5 % less of RA, achieves over 30 % TEL due to relatively gradual SIMT reflected by stable work hardening rate and work hardening exponent values (Figure 49). On the other hand, for sample IA700 the thermal and also mechanical stability of retained austenite are at the limit, which is indicated by simulations, dilatometry and even EBSD results. Therefore, in sample IS700 the massive SIMT effect is present at a low strain level (Figure 49), which results in the intense strain hardening. However, it occurs at the cost of limited plasticity [89] due to fast increasing strength of the alloy (Figure 48). These results are in contrary to the opinion established in work [223] that ductility of medium-Mn steels depends mainly on the retained austenite fraction and is less sensitive to its mechanical stability. This issue has to be elaborated.

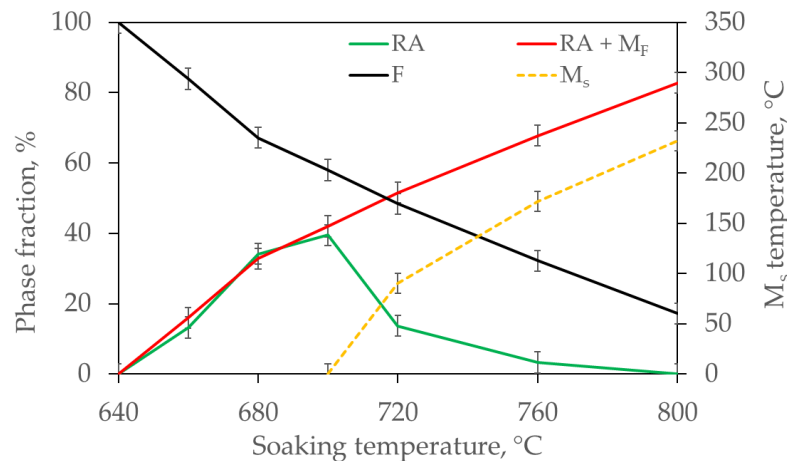


Figure 50 Changes in phase composition and  $M_s$  temperature depending on the IA temperature.

The increase of RA fraction and a decrease in its stability seem to trigger another mechanism. The dynamic strain aging (DSA) effect [219] is identified in samples containing the highest fraction of RA. It is especially intense in sample IA700 exhibiting low stability of RA [52]. DSA leads to local instabilities throughout the material, i.e., to the nucleation and propagation

of deformation bands during plastic deformation. However, the physical mechanisms explaining the room temperature dynamic strain aging are still under debate among the scientific community [224].

Samples annealed in the temperature range from 660 °C to 720 °C exhibit improved plasticity in comparison to the thermomechanically processed samples (Figure 24) [5].

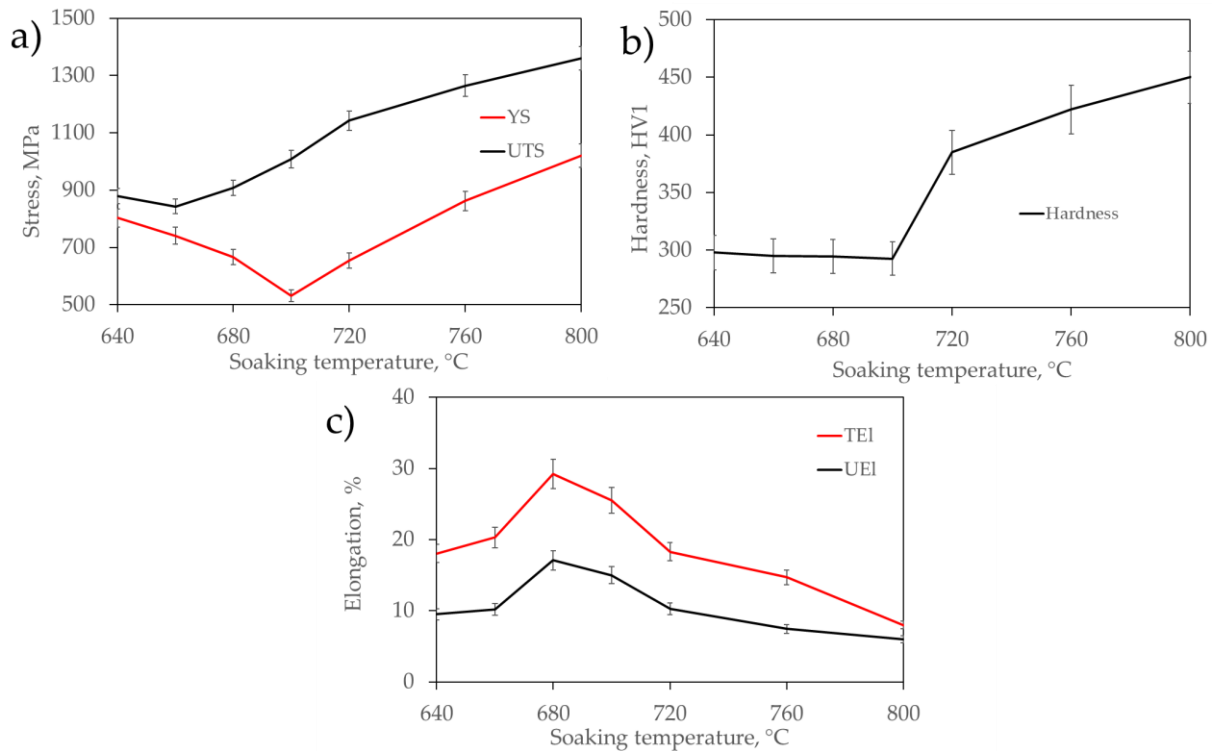


Figure 51 Summarized mechanical properties of analyzed steel with increasing annealing temperature: (a) strength properties, (b) hardness (c) plasticity.

The aim of this part of investigations was to characterize the phase transformation and chemical redistribution kinetics for different regions of the intercritical range. It allowed to establish a temperature technological window, which is between 680 °C and 700 °C for the given soaking time of 60 min, at which both the phase composition of the alloy and chemical stability of retained austenite are optimal in terms of mechanical properties. However, the factors influencing the RA stability and its plasticity-driven role have to be thoroughly characterized. For this reason, the next part of the research will be devoted to these factors.

## 6. Influence of intercritical soaking time on microstructure and mechanical properties of steel

### 6.1. Experiment design

The investigations on the influence of intercritical annealing temperature on microstructure and mechanical properties of investigated medium-Mn steel allowed to distinguish two annealing temperatures (680 °C and 700 °C), which ensure the highest RA fraction after 60 min of process and corresponding favorable plasticity. The investigations also indicated that the temperature of 700 °C provides relatively low stability of RA at room temperature, and thus the plasticity is lower than for sample IA680. Therefore, the intercritical annealing temperature of 680 °C has been selected as optimal in terms of RA fraction and stability relationship, and resulting plastic properties, which are the major topic of this work. This temperature variant was used in the next stage of investigations, where the influence of intercritical annealing time is under consideration. For a thorough analysis a wide soaking time range including 1 min, 5 min, 15 min, 60 min, 120 min, and 300 min was selected (Figure 52), which covers the soaking time ranges investigated in other works (Figure 22). The samples soaked intercritically for various times are named as ISX, where X is the soaking time in min (for example IS300).

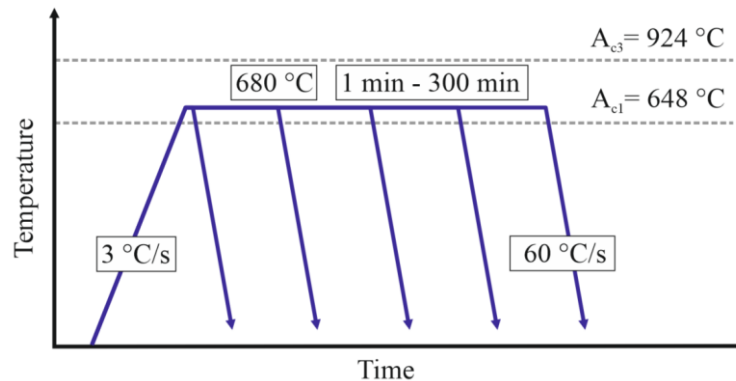


Figure 52 Scheme of IA at 680 °C for different times.

The intervals for variants shorter than 60 min are smaller due to expected dynamic changes in phase fraction, chemical redistribution, stability of RA and resulting mechanical properties in the initial stage of annealing. For variants longer than 60 min the intervals are bigger due to the expected less significant changes. The experiment results are compared to the equilibrium simulations conducted in the chapter concerning the influence of intercritical temperature. The heat treatment was again performed initially using dilatometry. The samples were next subjected to a series of tests: dilatometric analysis, SEM, EBSD, EDS, hardness, and full and

interrupted tensile tests. The RA stability was determined based on thermodynamic calculations.

## 6.2. Results

### 6.2.1. Dilatometric characterization

Figure 53 shows the dilatometric curves for samples soaked for different times. The medium-Mn steels are often susceptible to segregation of manganese during solidification [225]. Consequently, the RCL values for different samples for the same heat treatment may differ. The recorded dilatometric curves of austenitization are highly consistent. It means that the analyzed steel does not present strong microsegregation of alloying elements. The dilatometric curves indicate that the austenite formation is completed after about 160 min. Therefore, it is the soaking time needed to obtain phase equilibrium at 680 °C, which is in agreement with the tendency registered for samples annealed at higher temperatures, as it is about 3 times longer than in case of sample IA720. It takes about 4 min and 50 min to achieve 50 % and 90 % of the austenitic transformation, respectively. As expected, the soaking process is the most intense at the beginning of soaking and decelerates when the equilibrium is closer to be obtained.

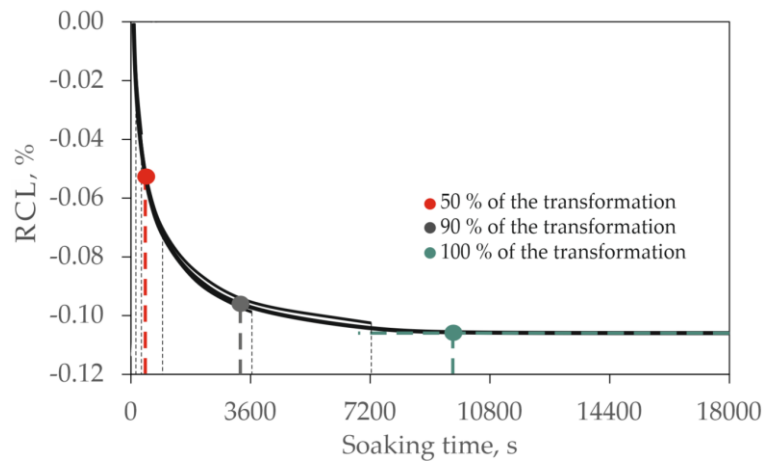


Figure 53 Austenite formation kinetics during 300 min annealing at 680 °C.

The cooling curves presented in Figure 54 do not show any disturbances, which may be related to the martensitic transformation. Therefore, the phase composition established during soaking is maintained to room temperature. Again, the differences in cooling curve slope for different samples related to phase composition differences are visible.

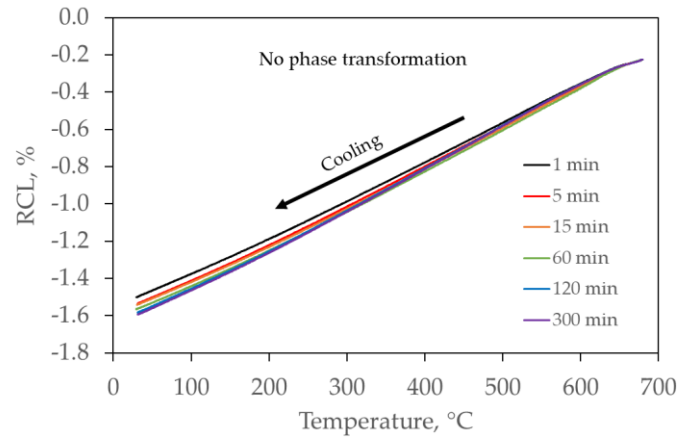


Figure 54 Cooling curves after different soaking times at 680 °C.

The summarized changes of high temperature austenite indicated in dilatometric results are presented in Figure 55. After 1 min of soaking the microstructure should contain already about 15 % of RA. Its fraction increases fast to 31 % after 15 min of soaking. Next, the changes are less intense and RA fraction stabilizes at a level of about 41 % after 120 min. The dynamics of phase composition changes is in good agreement with the dilatometry curves (Figure 53).

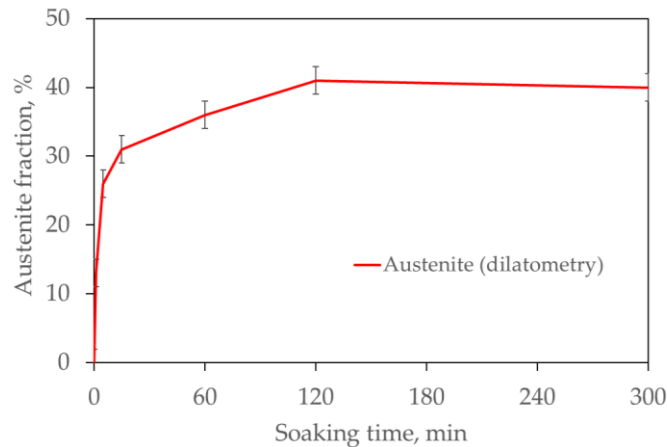


Figure 55 Fraction of high temperature austenite after different soaking time at 680 °C determined in dilatometric results.

### 6.2.2. Microstructural characterization

Figure 56 shows the microstructural evolution with the progress of intercritical soaking. After 1 min (Figure 56a) the microstructure is composed of plenty of thin RA films in the matrix of tempered martensite.

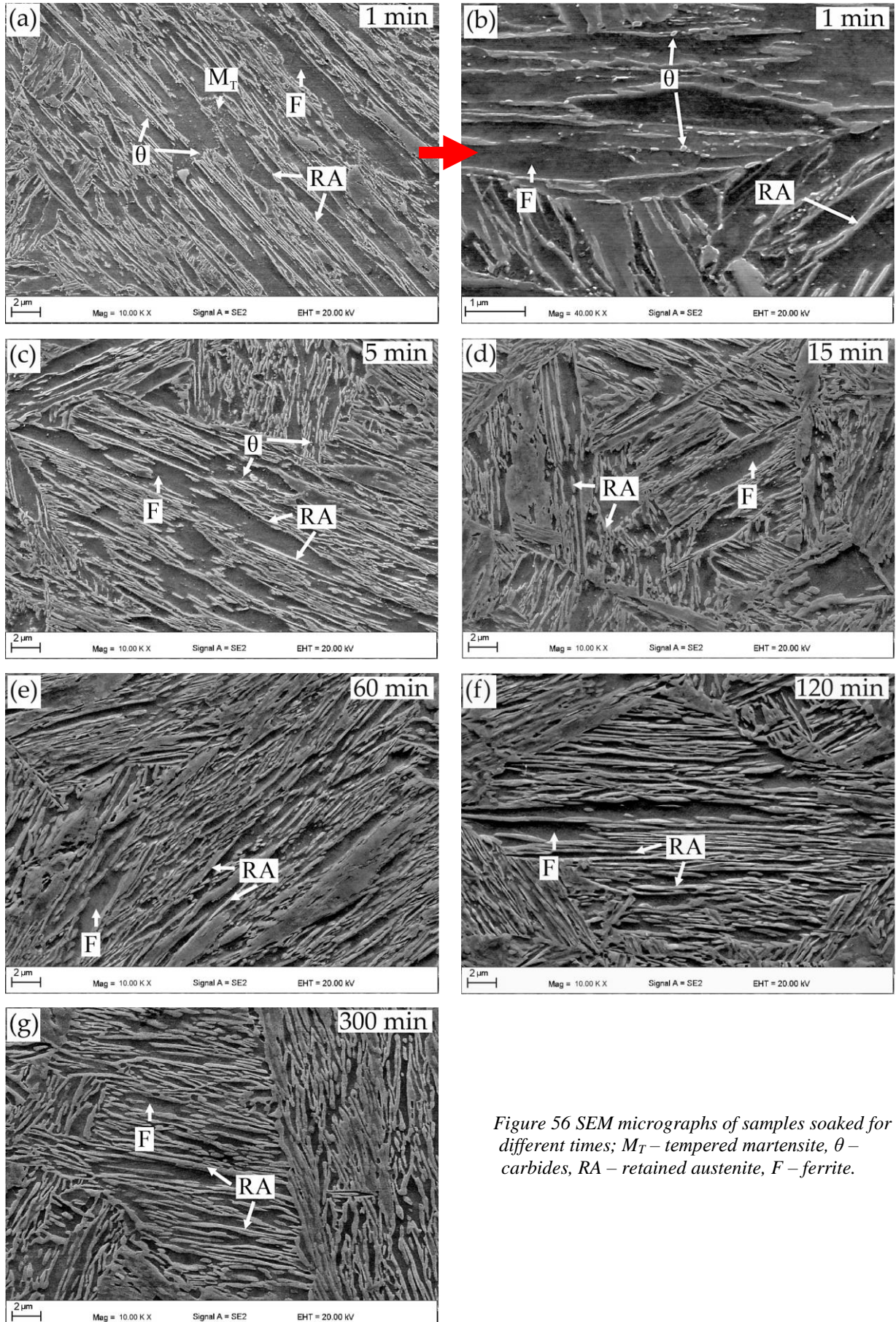


Figure 56 SEM micrographs of samples soaked for different times;  $M_T$  – tempered martensite,  $\theta$  – carbides, RA – retained austenite, F – ferrite.

The granular features recognized as carbides are present at the martensite boundaries in the vicinity of RA (Figure 56b). The carbides are visible in the microstructure up to 15 min of soaking (Figure 56a-d). With the further progress of soaking, mainly the thickening of RA and morphological homogenization of the microstructure can be seen. There is a lack of fresh martensite in microstructures of all samples. The RA lath thickness distribution and average lath thickness values are summarized in Figure 57. The RA laths exhibit a narrow thickness distribution for sample IS1, where the average lath thickness is about 100 nm. With the soaking time prolongation, the distribution of RA lath thickness becomes much wider indicating quite different RA grains in the microstructure. The average lath thickness of RA increases up to 240 nm for sample IS300. The dynamics in lath thickness changes is the highest for short times and becomes more stable for the longest ones.

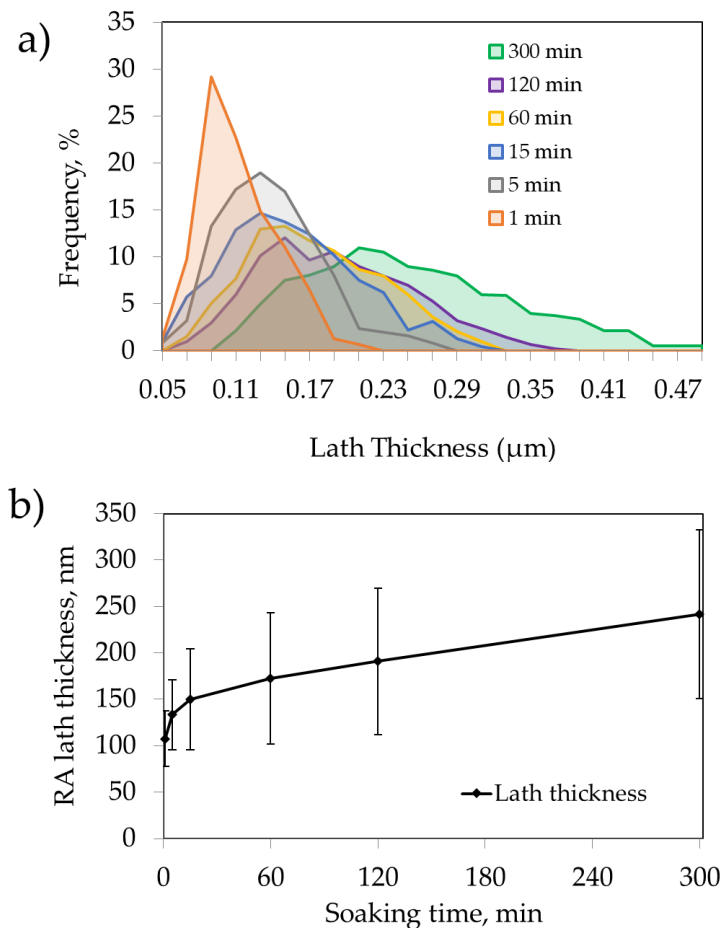


Figure 57 RA grain size redistribution (a) and summarized average grain size (b) results for samples soaked for various times.

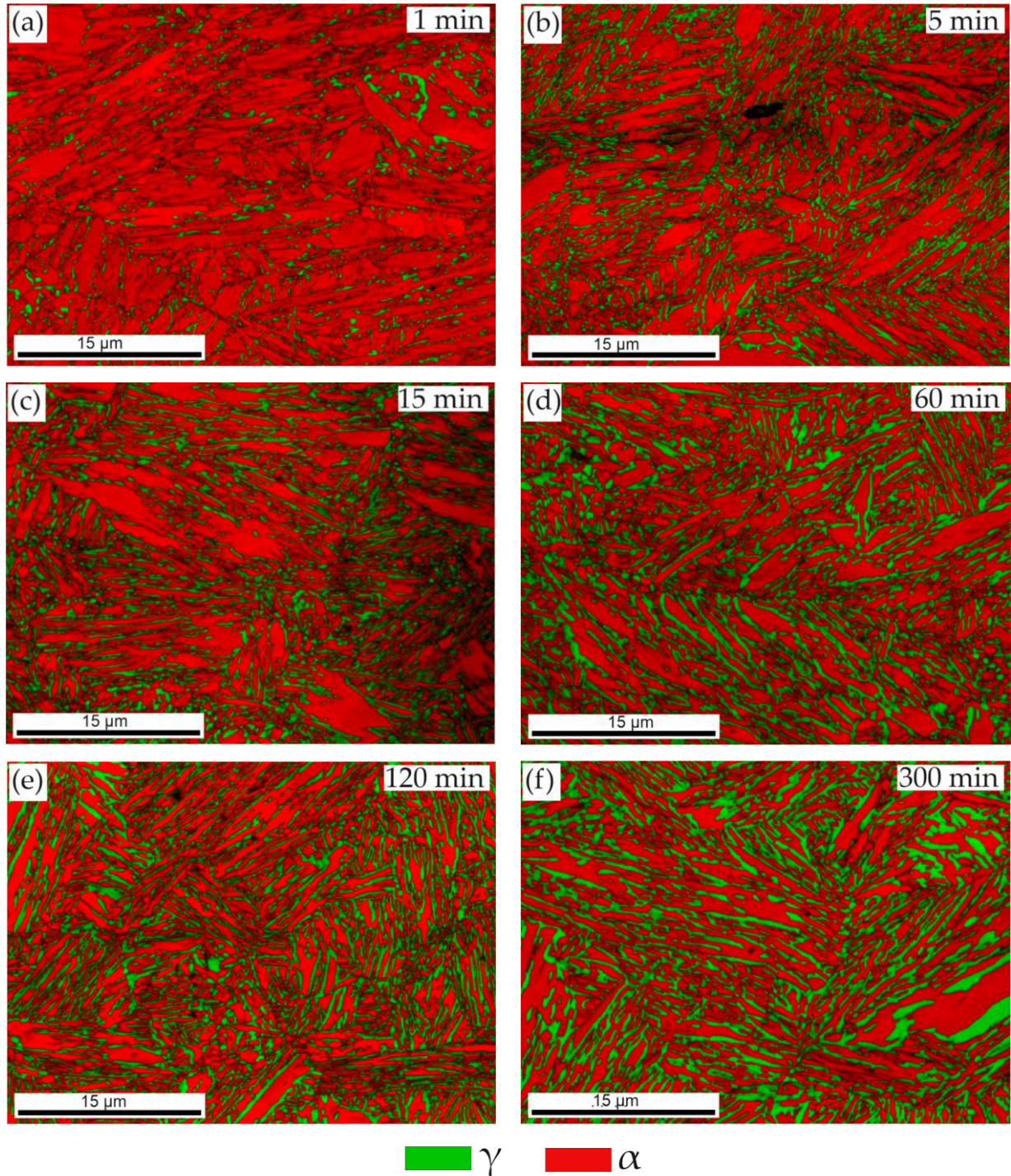


Figure 58 EBSD IQ+P maps of samples soaked for different times.

The EBSD results (Figure 58) show again that austenite nucleates at triple joints of martensite grains, as it was indicated in investigations on the influence of annealing temperature. No martensitic grains indicated by lower IQ values are visible in the IS samples (Figure 58a-f) even for sample IS300 containing the highest fraction of RA (Figure 58f).

Adam Skowronek

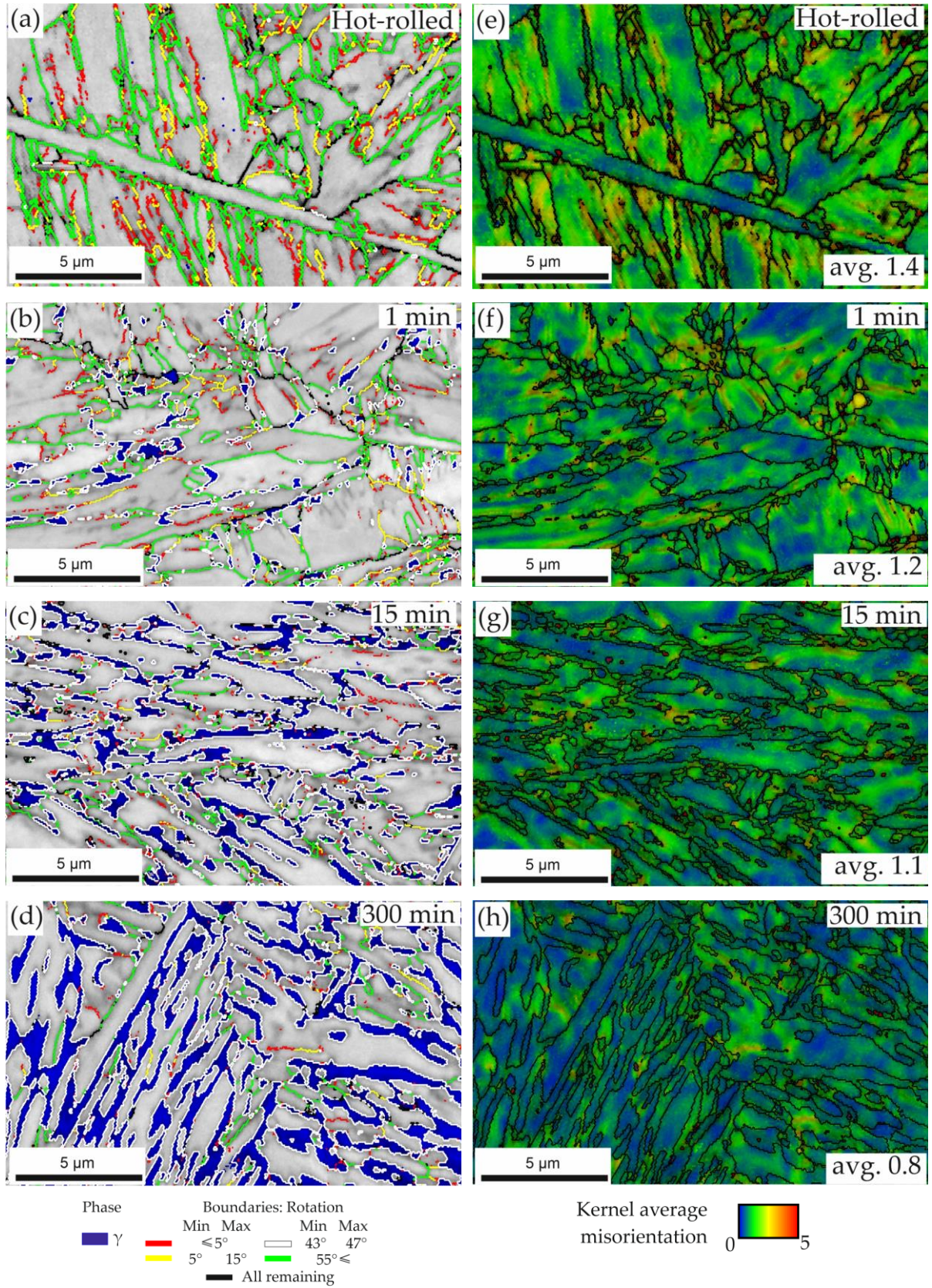


Figure 59 EBSD maps: IQ + rotation angle (a), (b), (c), (d), and IQ + KAM (e), (f), (g), (h) for hot-rolled sample and samples annealed for different times.

The analysis of EBSD data concerning relative grain orientation (Figure 59a-c) and summary graph (Figure 60) indicate that for the hot-rolled microstructure and samples soaked for short times (1 min, 5 min) the grain misorientation distribution is typical for martensitic structures. The low angle ( $< 15^\circ$ ) and high angle ( $> 55^\circ$ ) boundaries related to increased dislocation density [216] and mutual orientation of martensitic laths [217], respectively, are frequent. Along the soaking progress, their number decreases, while a fast increase in the number of grains with a misorientation of  $\sim 45^\circ$  degrees (RA – F boundaries) is visible (Figures 59 and 60b).

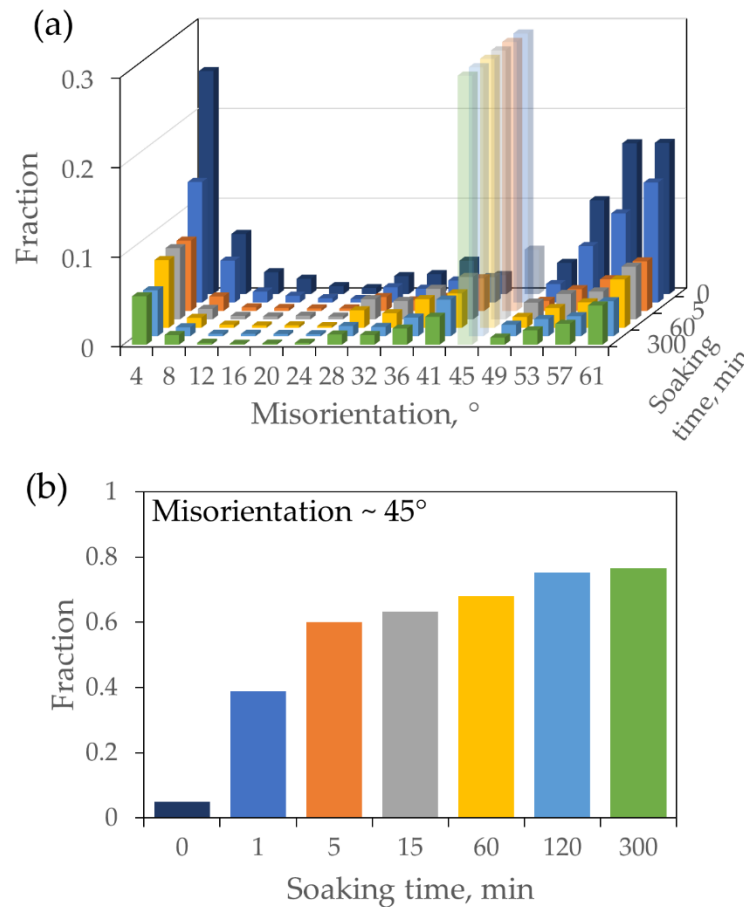


Figure 60 Changes in grain misorientation distribution with the progress of intercritical soaking time: (a) entire spectrum with focus on misorientations other than  $\sim 45^\circ$ , (b) misorientations close to  $45^\circ$ .

Based on the EBSD maps (Figure 58,59) and microsegregation results (Figure 60) it may be assumed that each single ferritic grain is surrounded by RA by an average of 60 % after 5 min of soaking and almost 80 % after 5 h, ensuring very homogeneous microstructure. This is a different relationship in comparison to cold-rolled and intercritically annealed medium-Mn steels, where both the ferrite and austenite grains are often located next to each other in much

more random manner [15,57]. This tendency may influence the different mechanical performance and yielding behavior for both types of medium-Mn steels. It has not been yet described in literature. KAM maps in Figure 59d-f show that with the progress of soaking the microstructure is relaxed because an average KAM value decreases from initial 1.4 to 0.8 after 5h. For shorter-soaked samples a higher density of lattice defects is present in RA. It seems to homogenize after 5h of soaking (Figure 59h).

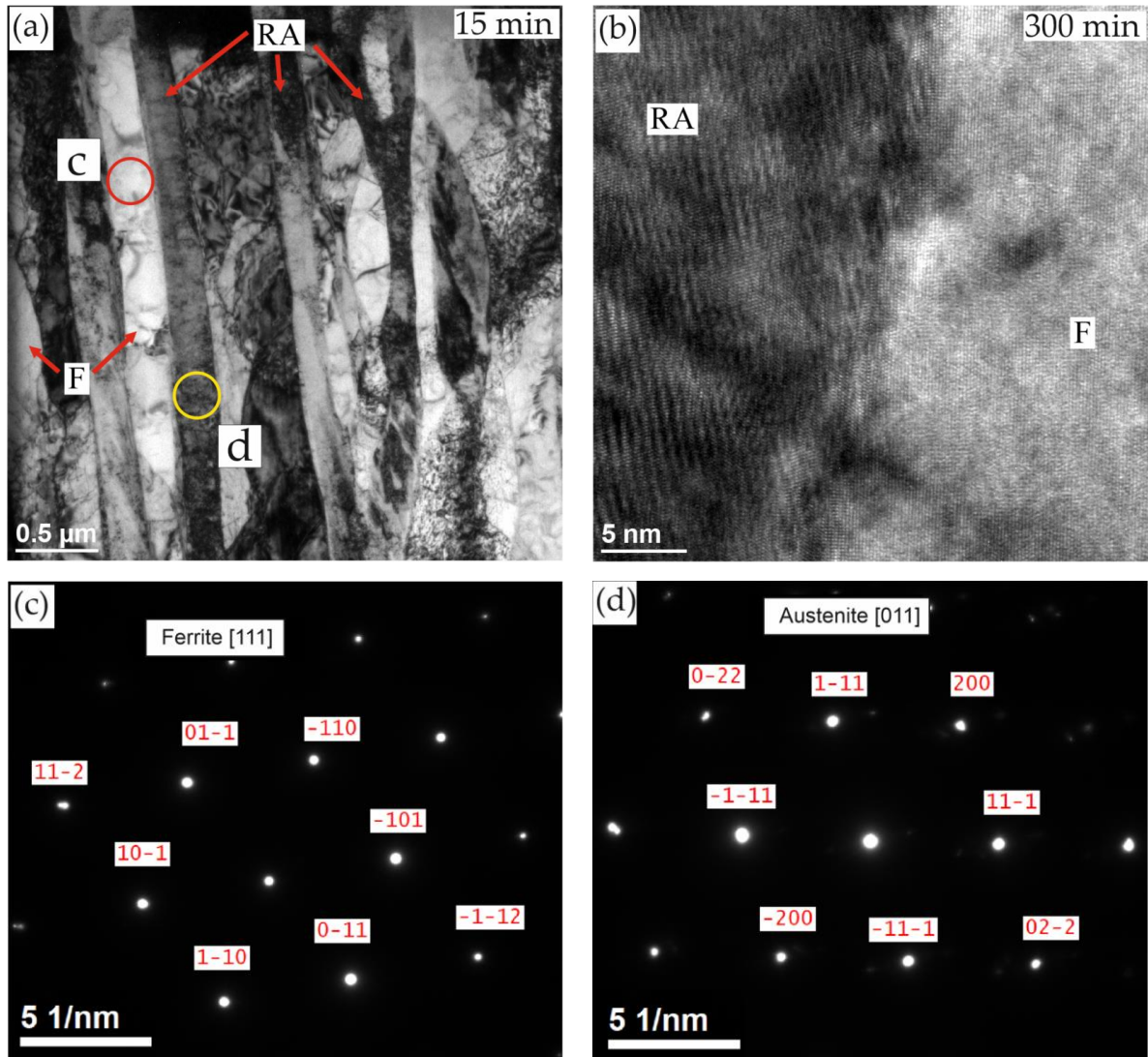


Figure 61 TEM results: (a) bright field TEM micrograph of sample IS15, (b) high-resolution bright field TEM micrograph for sample IS300, and selected area electron diffractions of (c) ferrite and (d) austenite, from the regions marked in figure (a).

The transmission electron microscopy confirms the presence of both  $\alpha$  and  $\gamma$  phases in analyzed samples (Figure 61a), which is visualized by high resolution micrographs (Figure 61b) and confirmed by selected area electron diffractions (Figure 61c, d). Both phases in form of

thin laths are alternately arranged in the microstructure. Both ferrite and retained austenite exhibit increased dislocation density, which however, is particularly higher in the case of the later which was confirmed also by KAM maps (Figure 59). The retention of high dislocation density from parent martensite is possible due to inactive recrystallization during heating and annealing of hot rolled medium-Mn steels [15,133]. The carbide precipitates in samples IS1 – IS15 (Figure 56) were also further investigated (Figure 62). They are localized in close vicinity of already formed RA (Figure 62a), where new RA grains are found in longer-soaked samples. It confirms a role of carbides as nucleation sites during intercritical annealing. The electron diffraction allowed to recognize these carbides as cementite (Figure 62b).

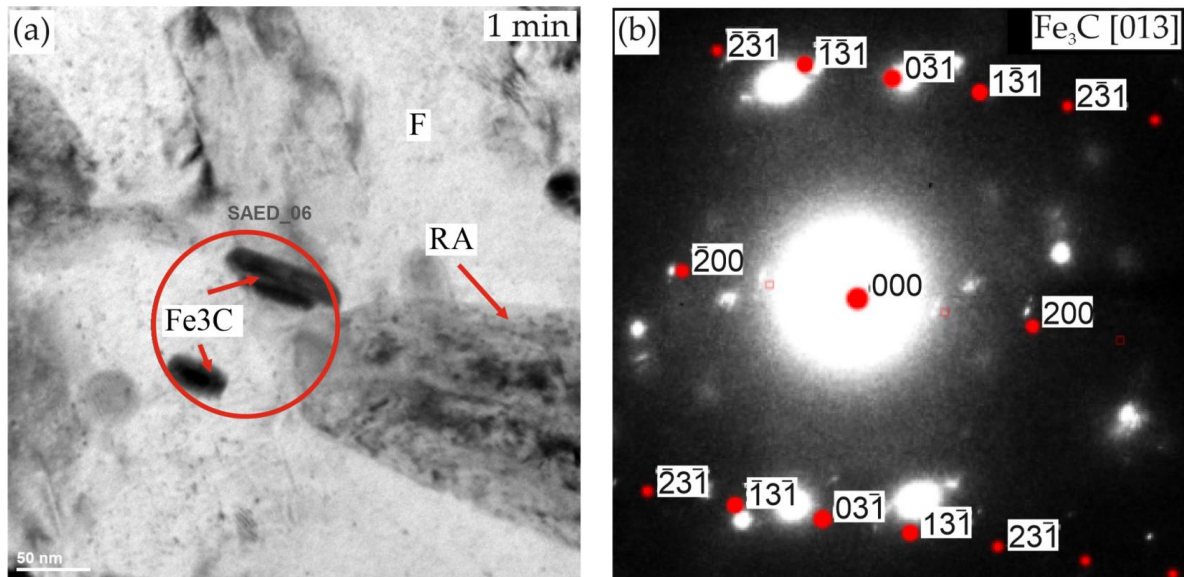


Figure 62 TEM results for sample annealed at 680 °C for 1 min: (a) TEM bright field image, and (b) selected area electron diffraction for the region marked in figure (a).

The TEM-EDS linear scans show a rapid increase of Mn concentration in the austenitic regions, while ferrite is depleted in Mn to below 3 wt.% (Figure 63). The austenite enrichment is high even in sample soaked only for 1 min because it reaches about 6.5 wt.% Mn (Figure 63a, d). With the further progress of soaking time the average Mn concentration in RA increases up to about 8 % for sample IS300 (Figure 63c, f). It should be noted that the longer-soaked samples show the heterogenous distribution of Mn. The RA regions near ferrite boundary are more enriched.

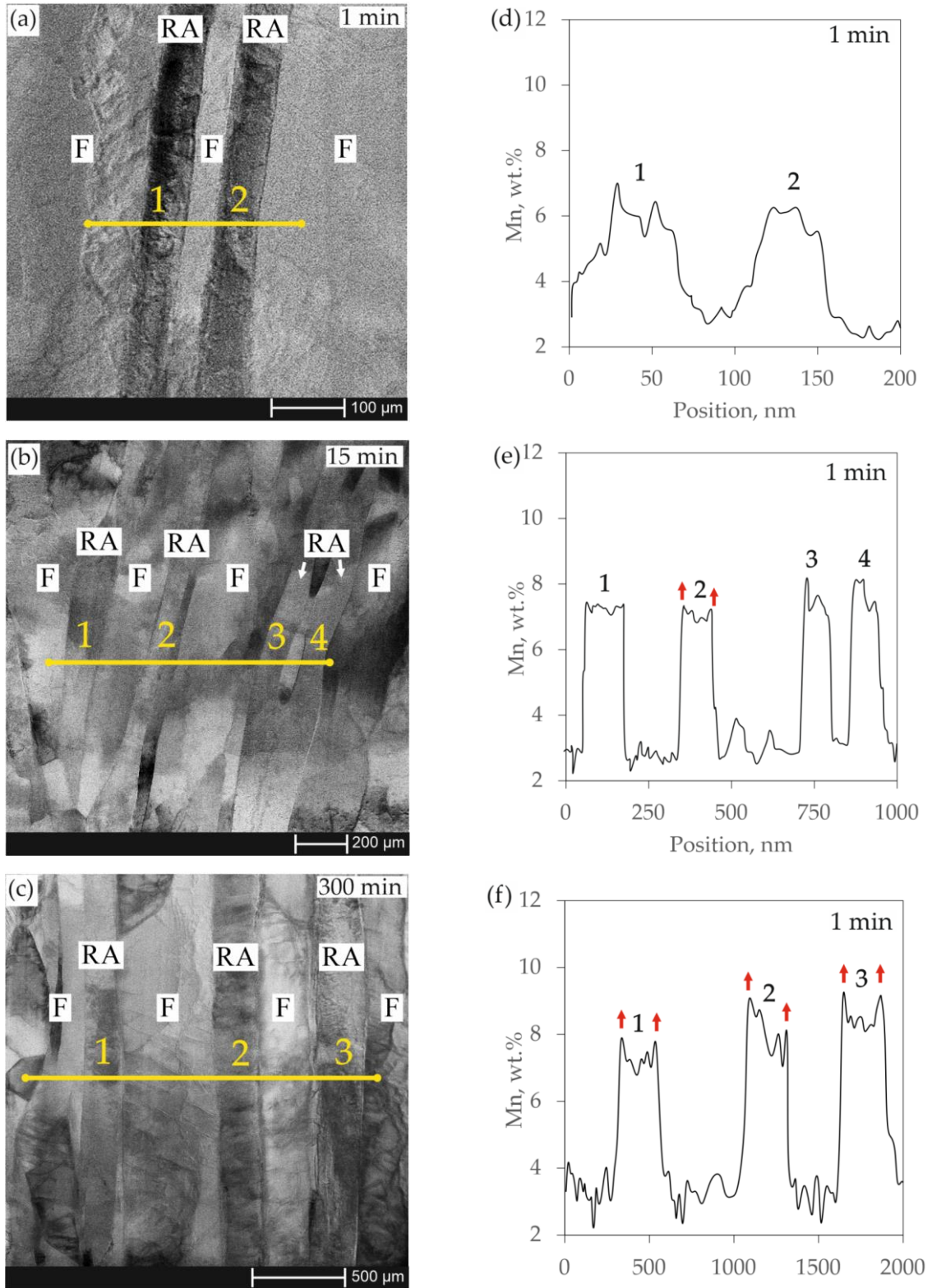


Figure 63 TEM results: (a), (b) and (c) STEM micrographs with marked EDS scan lines of samples annealed for 1min, 15 min and 60 min, respectively; (d), (e) and (f) corresponding chemical composition measurement profiles.

Along with an increasing distance from the grain boundary and approaching to RA grain center, the concentration of Mn decreases slightly. This tendency is not visible for sample IS1 (Figure 63d). For sample IS60 it takes place in some grains (Figure 63e) but becomes frequent for sample IA300 (Figure 63f). Therefore, it may be assumed that the heterogeneity redistribution of Mn is amplified by soaking time. It may have a significant impact on the local stability of retained austenite and corresponding mechanical behavior of steel.

### 6.2.3. Fraction and stability of retained austenite

The RA fraction was examined using XRD method (Figure 64). With the progress of soaking time the peaks related to RA increase in comparison to the ones related to ferrite. The quantitative results are shown in Figure 65. The RA fraction for sample IS1 counts about 16 %, and next rises rapidly to 32 % for sample IS15. The further progress of soaking is accompanied by stabilization of RA fraction at the final 41 % for sample IS300. The results of XRD investigations are highly concise with the austenite fraction calculated on the basis of dilatometric curves. The XRD results confirm the dilatometric data (Figure 54), which show that austenite in all samples exhibits full stability at room temperature. The difference between the simulations and experimental results increased with the prolongation of soaking, which should at least bring the state of the microstructure closer to the equilibrium. Therefore, it may be assumed that the current models are at the moment unable for precise prediction of intercritical annealing results.

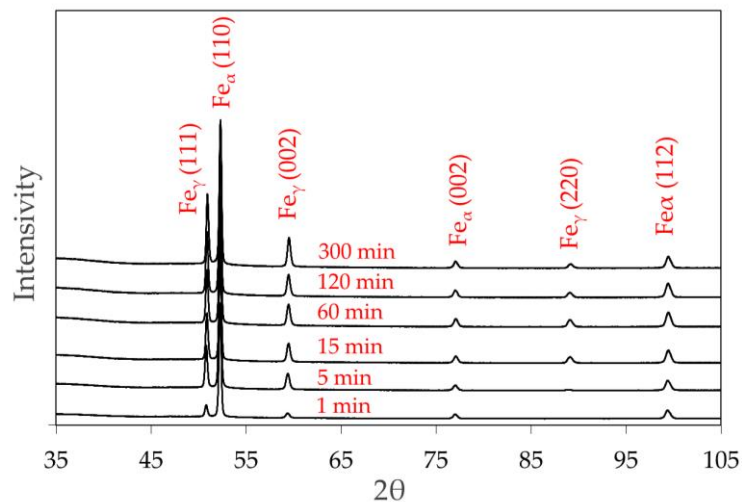


Figure 64 XRD diffraction patterns for samples soaked for different times at 680 °C.

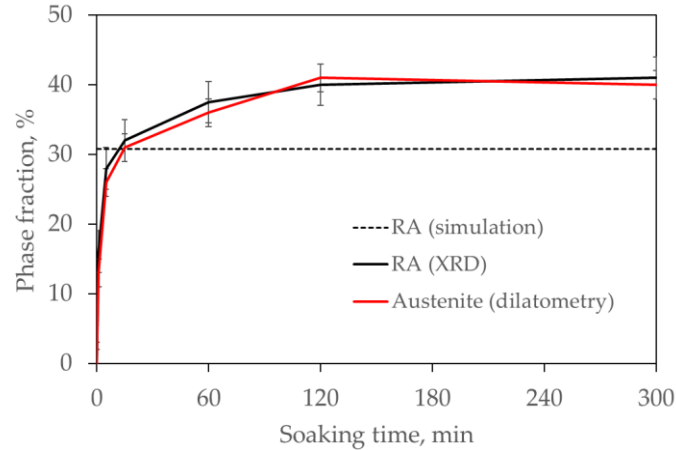


Figure 65 Comparison of austenite fractions determined from simulations and dilatometry, and the RA fraction determined from XRD for samples soaked for different times.

As showed in the chapter concerning IA temperature, apart from the fraction, the mechanical stability of RA has a decisive influence on mechanical properties of medium-Mn steels. Since none of the time-varying samples undergoes martensitic transformation during cooling, an attempt was made to determine the  $M_s$  temperature by thermodynamical calculations. The EBSD data was used to determine dimensions of both semi-axes for each of ellipsoid-like RA grain, and thus to determine the average RA grain size (volume) (Figure 66a). It is visible that all process parameters as RA formation kinetics, fraction changes and lath thickness show remarkably similar tendencies. It applies also to the average grain volume. It increases from about  $0.018 \mu\text{m}^3$  after 1 min to almost  $0.16 \mu\text{m}^3$  after 300 min. The standard deviation also increases with the progress of soaking, which results in numerous different grain sizes in the longer-treated samples.

The Mn concentration in RA determined from TEM-EDS method (Figure 63) is shown in Figure 66b. This diagram contains also changes in C concentration calculated from XRD data. The carbon concentration in RA is the highest after 1 min of soaking (0.74 wt.%) and decreases to 0.39 wt.% in sample IS300. The recorded change follows tightly the austenite formation recorded by dilatometry. The C concentration in the austenite decreases significantly in the first 15 min of soaking as the largest part of austenite forms until this time. The decrease is rapid despite the dissolution of carbides, which increases the C concentration in solid solution. The Mn concentration change behaves differently. There is a sharp increase at an early stage of IA from initial 4.8 wt.% to 6.5 wt.% after just 1 min.

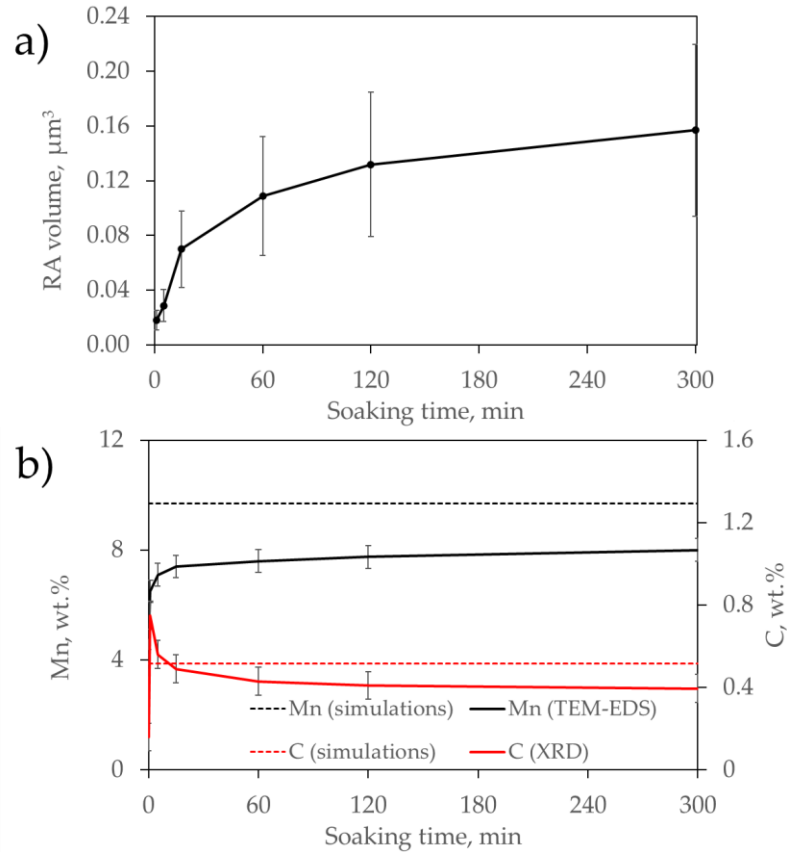


Figure 66 The evolution of factors influencing mechanical stability of retained austenite: (a) grain size expressed as the average volume, and (b) enrichment in C and Mn of the RA.

The possibility of high Mn enrichment for such short soaking time was also confirmed in other works [226,227]. With the further progress of soaking the enrichment rate decelerates, reaching about 8 % of Mn in RA after 5 h. The opposite behavior of C and Mn partitioning can be explained by the differences in their diffusion rates, which at 680 °C for the former is much faster ( $\sim 10^{-10} \text{ m}^2\text{s}^{-1}$  in ferrite and  $\sim 10^{-13} \text{ m}^2\text{s}^{-1}$  in austenite [205]) and enables C concentration to follow closely the RA fraction changes [228]. On the other hand, the diffusion rate of Mn is much slower ( $\sim 10^{-16} \text{ m}^2\text{s}^{-1}$  in ferrite and  $\sim 10^{-19} \text{ m}^2\text{s}^{-1}$  in austenite [205]), which results in relatively sluggish changes in its concentration.

The above RA characteristics (chemical composition and grain size) allowed to determine  $M_s$  temperature values for each sample by applying the equation (10). The joint stabilization of RA caused by chemical composition and grain size is represented by the solid  $M_s$  temperature curve in Figure 67. The RA exhibits the highest stability for samples IS1 and IS5 since their  $M_s$  temperatures are the lowest and are below -100 °C. With the progress of soaking time the RA stability drops fast. The  $M_s$  temperature of about 0 °C was determined for sample IS60. Further soaking prolongation results in the  $M_s$  temperature increase to about 18 °C determined for

sample IS300. These results show that despite high and continuous Mn partitioning to RA its  $M_s$  temperature rapidly increases. It is caused by depletion of increasing RA fraction in C and an increasing grain size.

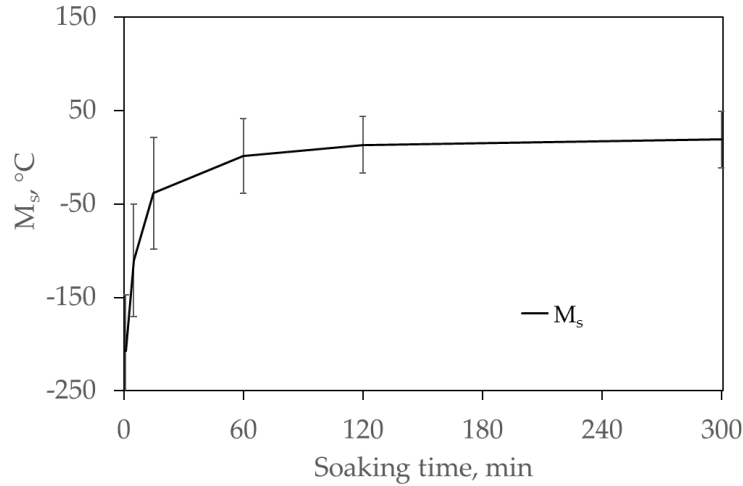


Figure 67 Changes in stability of retained austenite ( $M_s$  temperature) with the progress of intercritical soaking time.

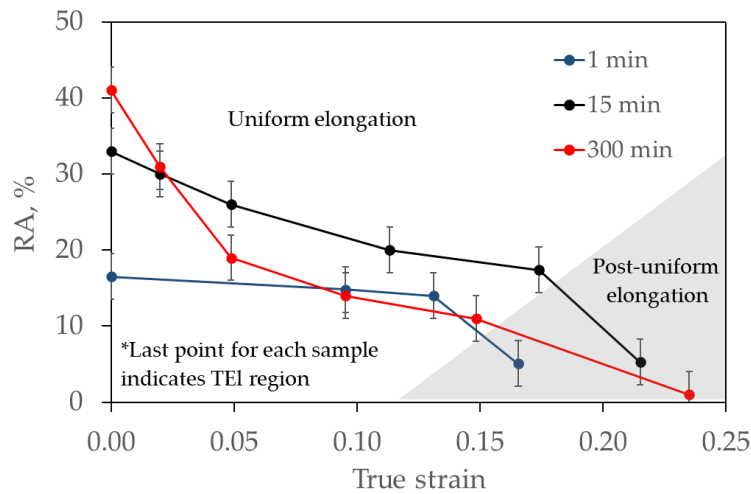


Figure 68 Changes in RA fraction with the progress of tensile strain for samples soaked for different times.

The experimental stability of retained austenite was investigated in interrupted tensile tests and subsequent XRD investigations. The results for representative samples are presented in Figure 68. Since RA in sample IS1 exhibits the lowest  $M_s$  temperature, its stability is extremely high. Therefore, its fraction decreases very slowly. Only massive deformation related to TEI region (neck region) triggers the intense SIMT in this sample (Figure 68). The SIMT effect in sample IS15 is much more intense but the changes in RA fraction as a function of strain are the

most gradual. Sample IS300 exhibits a very rapid decrease in RA fraction at low strain levels due to its low stability and the intense SIMT effect.

#### 6.2.4. Mechanical properties

Figure 69 shows hardness results for samples soaked for various times at 680 °C. Initial hardness of the hot-rolled steel was about 470 HV1. Just 1 min of soaking results in a significant hardness decrease to 317 HV1. Further alloy softening is less intense and the longest soaked sample – IS300 – exhibits hardness of about 280 HV1.

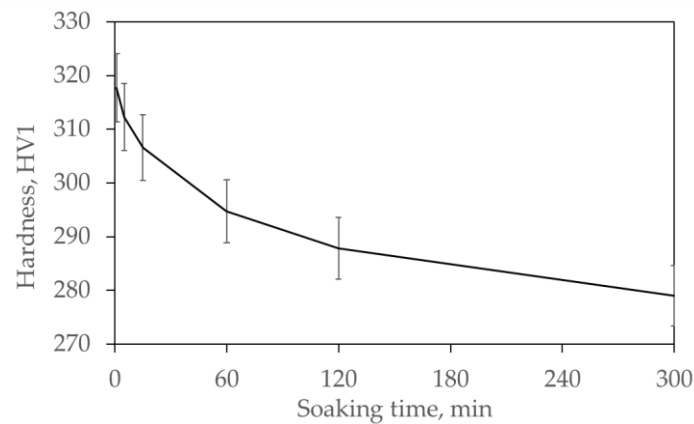


Figure 69 Changes in hardness as a function of soaking time.

The tensile curves for investigated soaking time variants are presented in Figure 70a. There is visible a clear decrease in YS value with increasing soaking time: from 860 MPa for sample IS1 to 590 MPa for sample IS300. The UTS values for all samples are similar; only little decrease from 940 MPa for sample IS1 to 890 MPa for sample IS300 can be noticed. Plasticity is the lowest for sample IS1, the UEI is 13 % and TEI ~ 18 %. The best plastic property combinations are achieved for samples IS15 (UEI of 19 % and TEI of 26 %) and IS60 (UEI of 17.5 % and TEI of 31 %). With further soaking prolongation, both UEI and TEI decrease to 16 % and 26 %, respectively, for sample IS300. Again, for samples containing an increased fraction of RA (IS15 – IS300) the PLC effect appears. It is more intense as the fraction of low stable RA increases [52]. The progress of soaking results in a clear increase of strain hardening (Figure 70b, c). Samples soaked for 1 min and 5 min exhibit a sharp drop in strain hardening rate in the initial stage of deformation, and a slow decrease later. With the progress of soaking time the strain hardening rate tends to decrease slower.

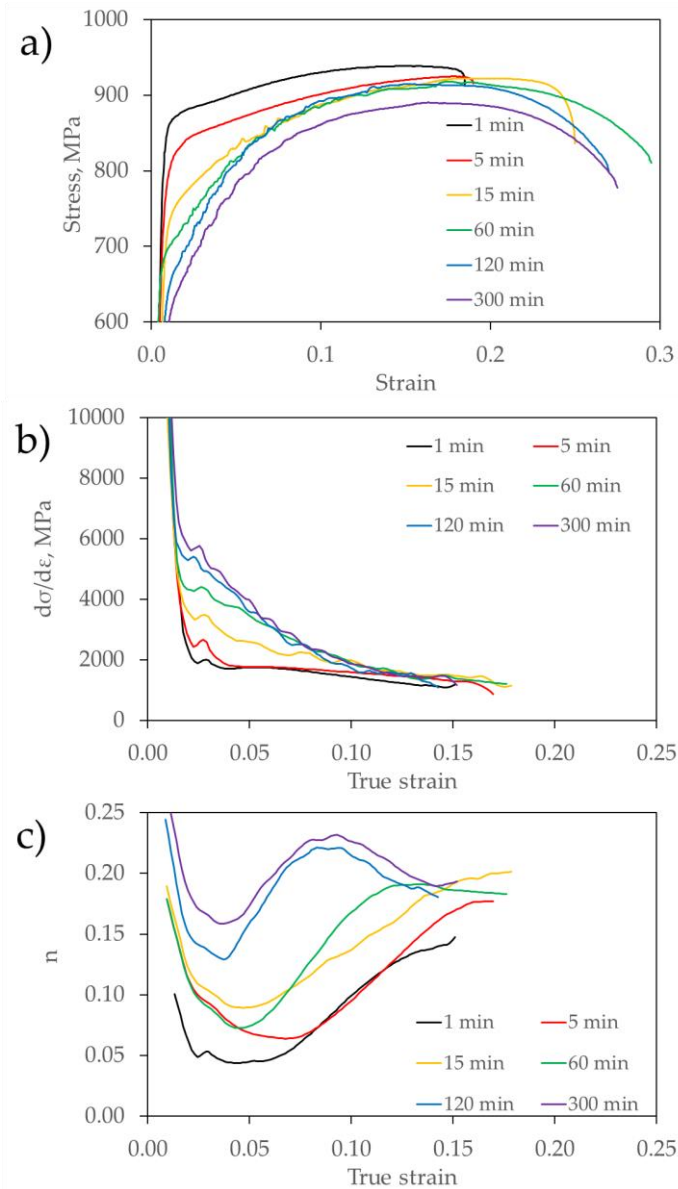


Figure 70 Mechanical properties of samples soaked for different times: (a) tensile curves, (b) strain hardening rate, (c) strain hardening exponent.

The most gradual decrease of strain hardening rate is visible for samples IS15 and IS60. Samples IS120 and IS300 show remarkably high strain hardening rate in the true strain range up to about 0.05 in comparison to shorter-soaked samples. However, much more rapid decrease of its value in later deformation stages is visible. Regarding the strain hardening exponent: for samples annealed up to 15 min its value increases with time and is higher for longer soaked samples (up to about 0.22 for sample IS15). For samples IS60 – IS300 a maximum value of strain hardening exponent was recorded, which occurs at lower strain with the soaking prolongation. Its maximum value increases for these samples only slightly to about 0.24.

### 6.2.5. Properties and microstructure of post-tensile samples

The microstructures of material cut from the UEl region of tensile samples are presented in Figure 71 as SEM micrographs and in Figure 72 as IQ+P EBSD maps.

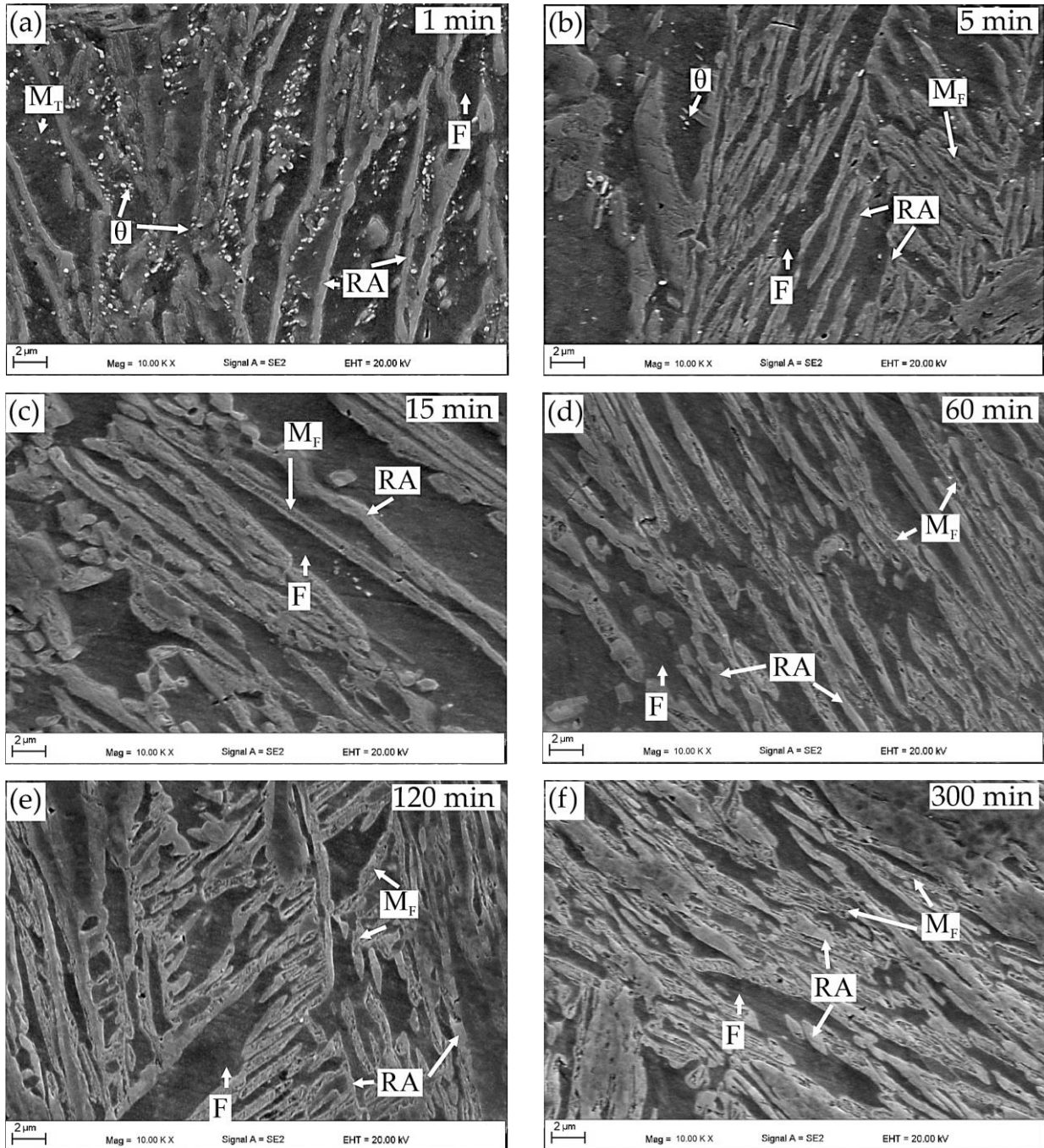


Figure 71 SEM micrographs of samples after different soaking times at 680 °C and after subsequent tensile tests (UEl region);  $M_T$  – tempered martensite,  $M_F$  – fresh martensite,  $\theta$  – carbides, RA – retained austenite, F – ferrite.

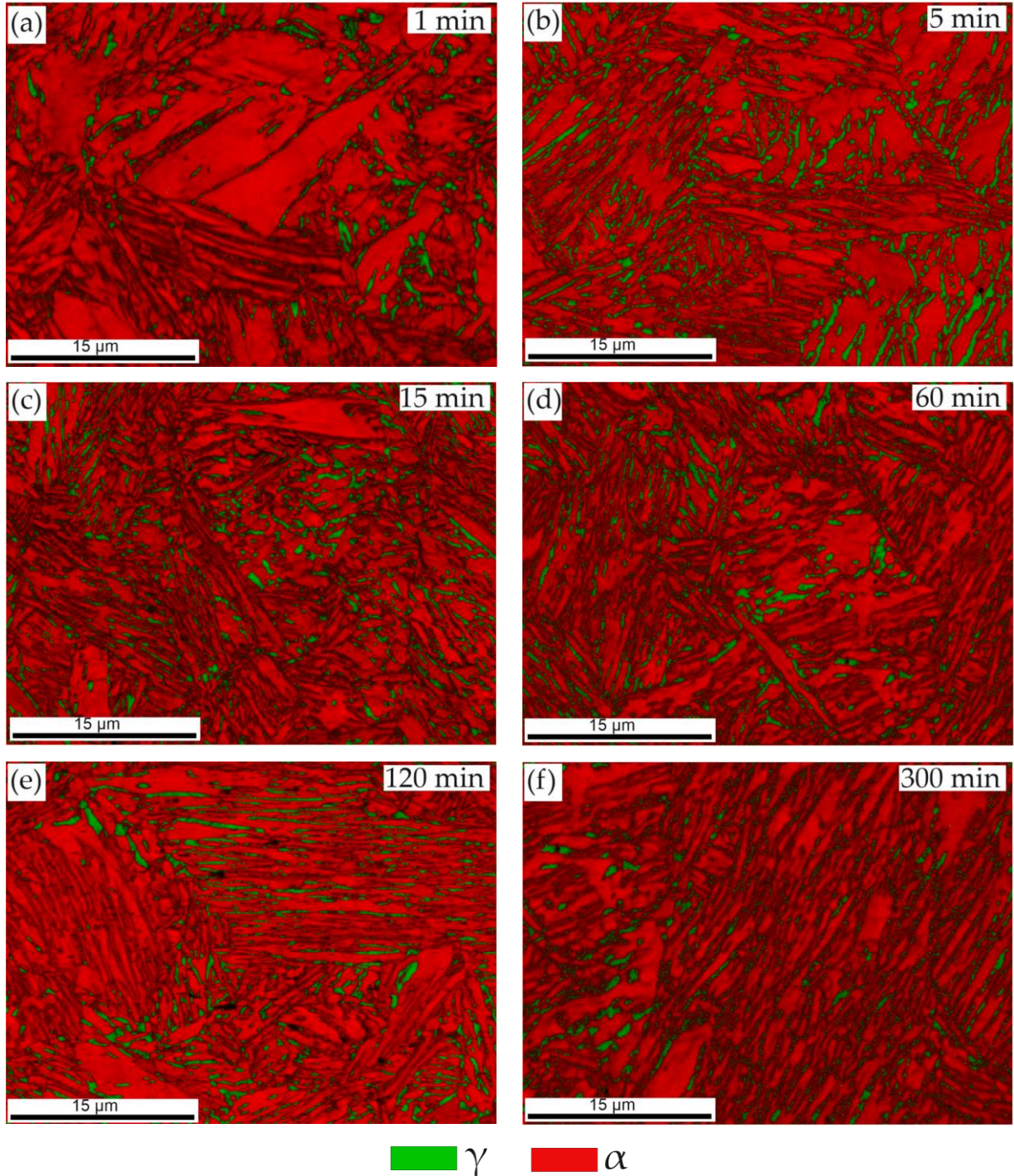


Figure 72 EBSD IQ+P maps of samples soaked for different times and after subsequent tensile tests (UEI region).

The strain-induced martensite is clearly identified as “rough” regions in the “smooth” and homogeneous RA grains (Figure 71). The number and fraction of fresh martensite grains increases for the longer-soaked samples. In samples IS1 and IS5 the martensitic grains are not visible or hard to identify. In samples IS15 and IS60 a number of grains is partially transformed.

Especially the central areas of the grains underwent SIMT. Strong fragmentation of RA grains is also revealed (Figure 72c, d). For samples IS120 and IS300 the martensitic grains are frequent; the totally transformed areas are also observed.

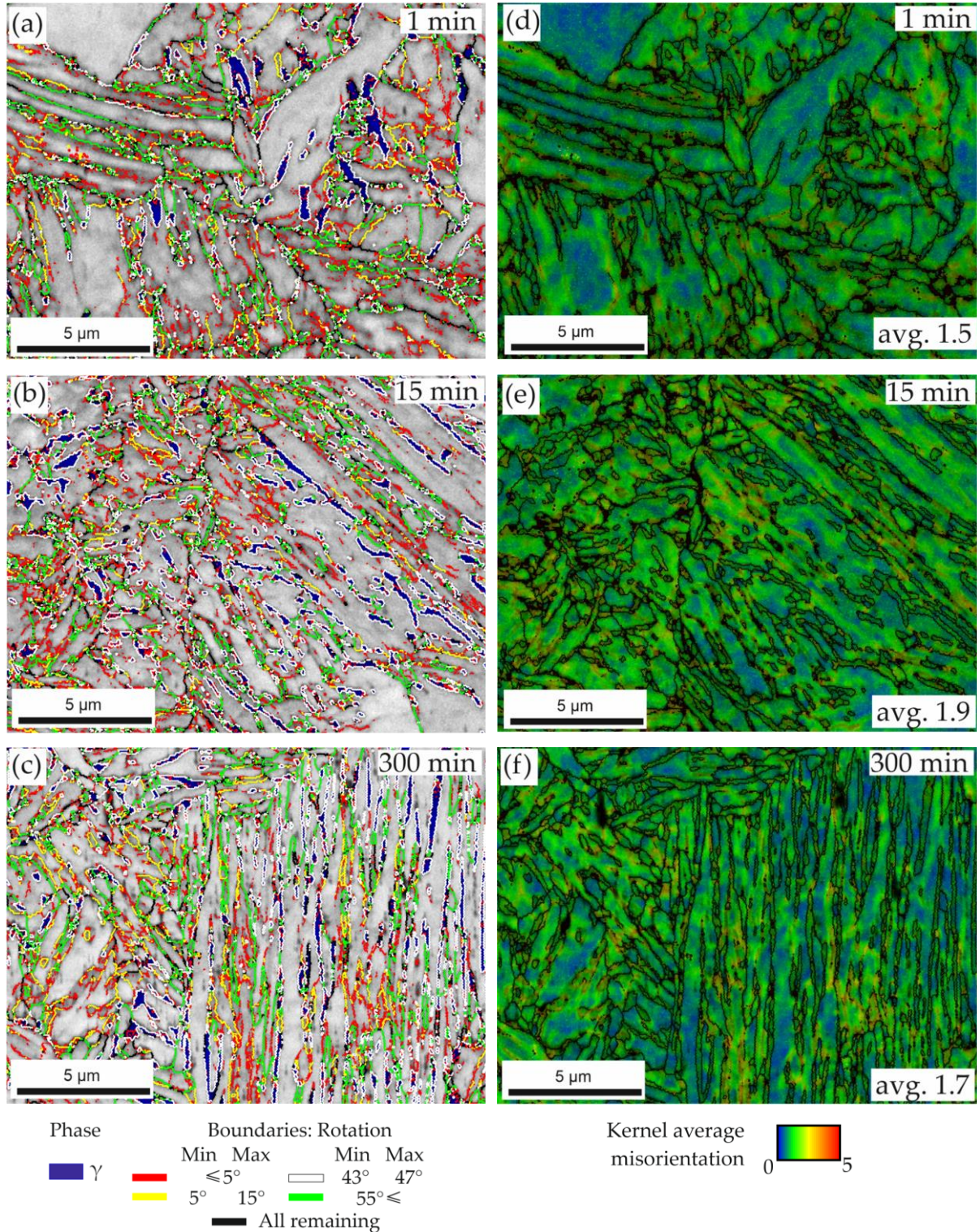


Figure 73 EBSD maps: IQ + misorientation angle (a), (b), (c), and IQ + KAM (d), (e), (f) for samples soaked for different times at 680 °C after subsequent tensile tests (UEL region).

The grain boundaries and KAM maps presented in Figure 73 show a typical evolution of microstructure during deformation [89,229]. The number of low-angle and high-angle boundaries increases, especially in the areas, in which the SIMT was active. The number of grain boundaries of about 45° related to RA – F boundaries decreases in these areas, which is more intense for the longer-soaked samples (Figure 73c). With the progress of deformation, the microstructure is distorted, which generates increased number of lattice defects - reflected in a significantly increased average KAM value (from initial 0.8 to 1.7 for sample IS300 after deformation). The KAM value seems to be tightly related to the applied strain because sample IS15 (which exhibited the highest UEI) shows the highest average KAM value.

The localization of SIMT in the central regions of RA grains is shown in TEM micrographs in Figure 74. The electron diffraction allowed to identify  $\alpha'$  (Figure 74e) phase regions inside the RA grains (Figure 74c). It was also observed in work [230]. The tensile deformation generates in the material high dislocation density in both ferrite and austenite.

The XRD quantitative results for RA fractions after tensile tests (Figure 75a) are in agreement with  $M_s$  temperature calculations (Figure 67). In sample IS1 only 2 % of initial 16 % RA transformed to martensite in the UEI region. If we take into account the transformation range expressed as a percentage difference between the fraction of austenite in the state before and after deformation, then for a sample soaked for 1 minute the transformation range will be about 12 %. Only massive deformation in the TEI region triggers the intense SIMT effect in this sample. For sample soaked for 5 min the RA fraction remaining after the tensile test is the highest (22 % from initial 28 % in UEI region). The transformation range for this sample reaches about 21 %. Next, despite a continuously increasing fraction of RA in the longer-soaked samples, its fraction remaining after deformation decreases. The transformation range reaches 45 %, 65 %, 75 % and 80 % for the samples soaked for 15 min, 60 min, 120 min and 300 min, respectively. The similar tendency is visible in the TEI region.

Despite a significant difference in stability ( $M_s$  temperature) for samples soaked for different times, each of them contains a significant fraction of retained austenite (over 10 %) maintained in the uniform elongation region (Figure 75b). It indicates either significant differences in the local stability of RA or an increase in its stability caused by the progressing martensitic transformation.

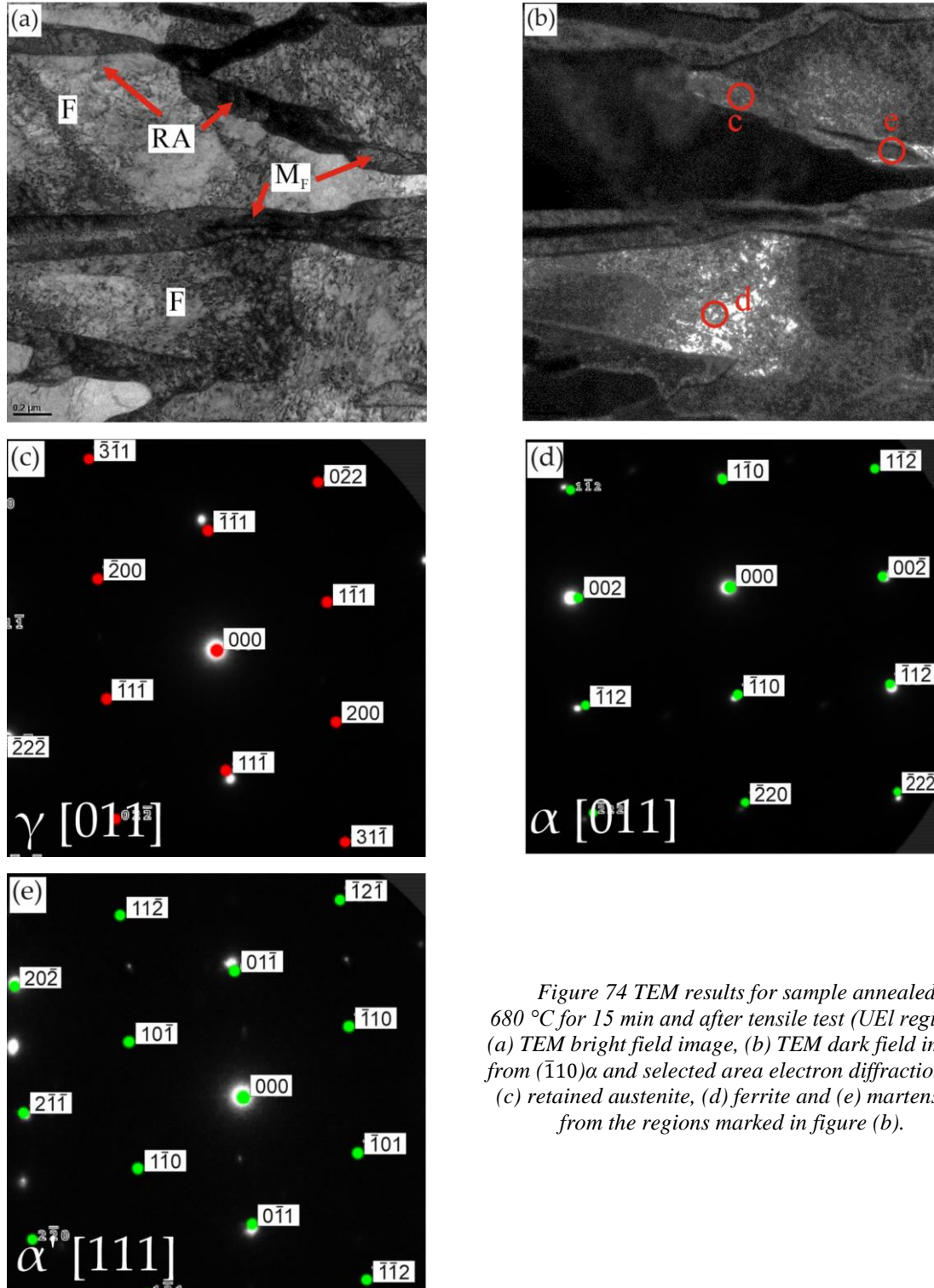


Figure 74 TEM results for sample annealed at 680 °C for 15 min and after tensile test (UEI region): (a) TEM bright field image, (b) TEM dark field image from  $(\bar{1}10)\alpha$  and selected area electron diffractions of (c) retained austenite, (d) ferrite and (e) martensite, from the regions marked in figure (b).

The tensile deformation reduces the average grain size (volume) of retained austenite to a similar level of about  $0.015 \mu\text{m}^3$  regardless of its initial average size and chemical enrichment. The SIMT resulting in parent RA fragmentation was noticed already in SEM and EBSD results

(Figure 71,72). It shows that the RA fragmentation occurring during deformation influences high stabilization of RA by decreasing the  $M_s$  temperature.

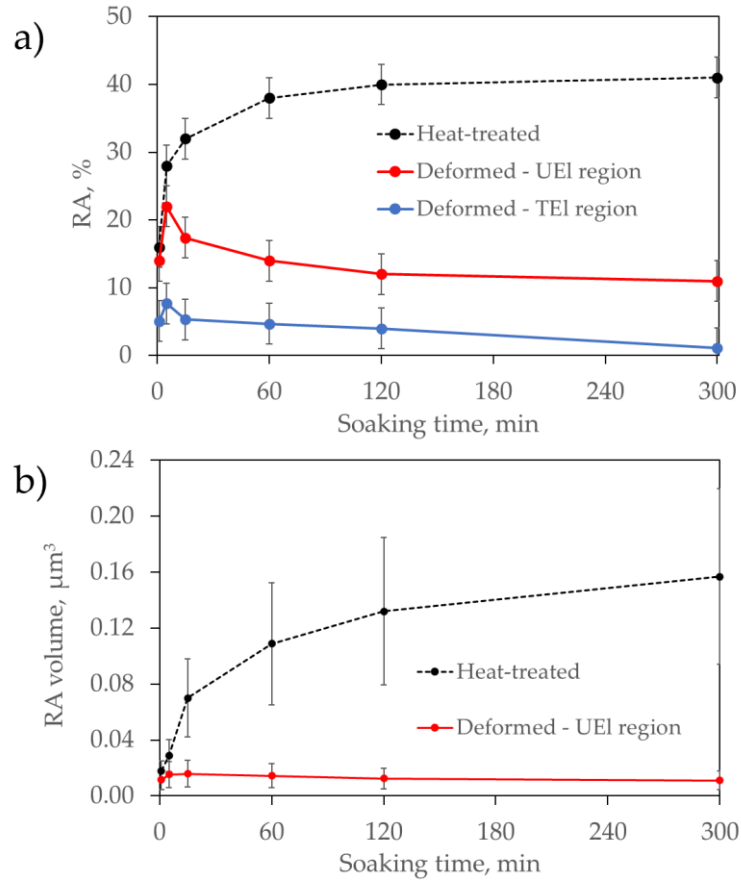


Figure 75 Changes in RA's (a) fraction (b) and average grain volume in samples annealed for different times and after tensile test (UEI and TEI regions).

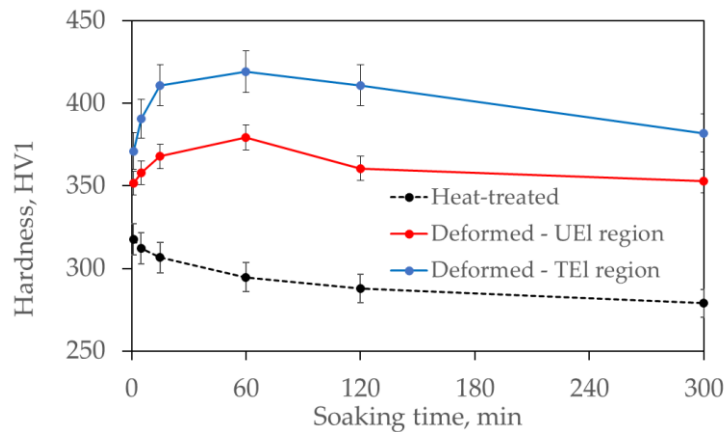


Figure 76 Changes in hardness of samples annealed for different times at 680 °C and after tensile tests (UEI and TEI regions).

Hardness of samples after the tensile test (Figure 76) is significantly higher than of the intercritically annealed material. Sample IS1 exhibits the lowest hardness after tensile tests (352 HV1 for UEl region and 371 HV1 for TEI region). The hardness is the highest for sample IS60 (380 HV1 for UEl region and 420 HV1 for TEI region). Next, for longer soaked samples the hardness decreases slightly to 353 HV1 and 382 HV1 for UEl and TEI regions.

### **6.3. Discussion**

#### **6.3.1. Impact of the phase composition on mechanical performance**

The progress of soaking time causes the similar tendency for different processes. The changes are very dynamic during the first 15 min to 60 min and next some stabilization occurs. It applies to:

- RA formation,
- Grain growth expressed by average volume and lath thickness increase,
- Microstructure homogenization,
- Chemical redistribution,
- Decrease in RA stability.

The kinetics of above-mentioned changes is related to the annealing progress (Figure 77a). The microstructure obtained after different soaking times has the clear reflection in YS (Figure 78a) and hardness (Figure 78 b). The initial hardness of material is about 470 HV1. It undergoes tempering during the heating and soaking; therefore, the hardness decreases [76]. Also the formation of high fraction of retained austenite influences a hardness drop [222]. The UTS values, despite a continuously increasing fraction of RA, decrease slightly for longer-soaked samples. In samples annealed at different temperatures, the matrix was composed of soft ferrite resulted from 60 min of soaking (Figure 46). Therefore, it did not contribute significantly to the general strengthening. In the current investigation the matrix for shorter soaked samples (< 60 min) is composed of tempered martensite, which results in higher UTS values for these samples. With the progress of soaking, the tempered martensite becomes progressively ferrite, decreasing the strength of longer soaked samples (Figure 59). Therefore, despite the increasing fraction of RA, which subsequently transforms to martensite during deformation, the high UTS may not be maintained. The similar tendency was observed in works [76,77], where hot-rolled medium-Mn steels were investigated. In cold-rolled steels, the UTS tends sometimes to grow

with soaking time, as the RA/M<sub>F</sub> fraction increases, because they do not contain the tempered martensite but recrystallized ferrite [186]. The plasticity (Figure 78c) again seems to depend mainly on the RA stability and next on its fraction. The deformation process and related microstructural changes may be divided into two steps: (1) up to UEI (Figure 77a) and (2) between UEI and TEI (Figure 77b, c). In both cases the interplay of RA fraction and stability exists; however, opposite mechanisms occur. If the stability in (1) step is too high as in samples IS1 and IS5 (Figure 77a), the SIMT effect is not triggered and the UEI is achieved early. For samples with very low RA stability (IS120 and IS 300), the massive SIMT effect occurs at an early stage of deformation and the fast exhausted strain hardening and resulting high strength of the material again limit the uniform elongation (Figure 78c). Only the compromise between the fraction and stability of RA provides the optimal mechanical and plastic properties, as it is the case in samples IS15 and IS60. During the deformation, the structural state of material changes. Even in sample IS300 exhibiting the very low stability a significant fraction of RA remains in the UEI region (<10 %).

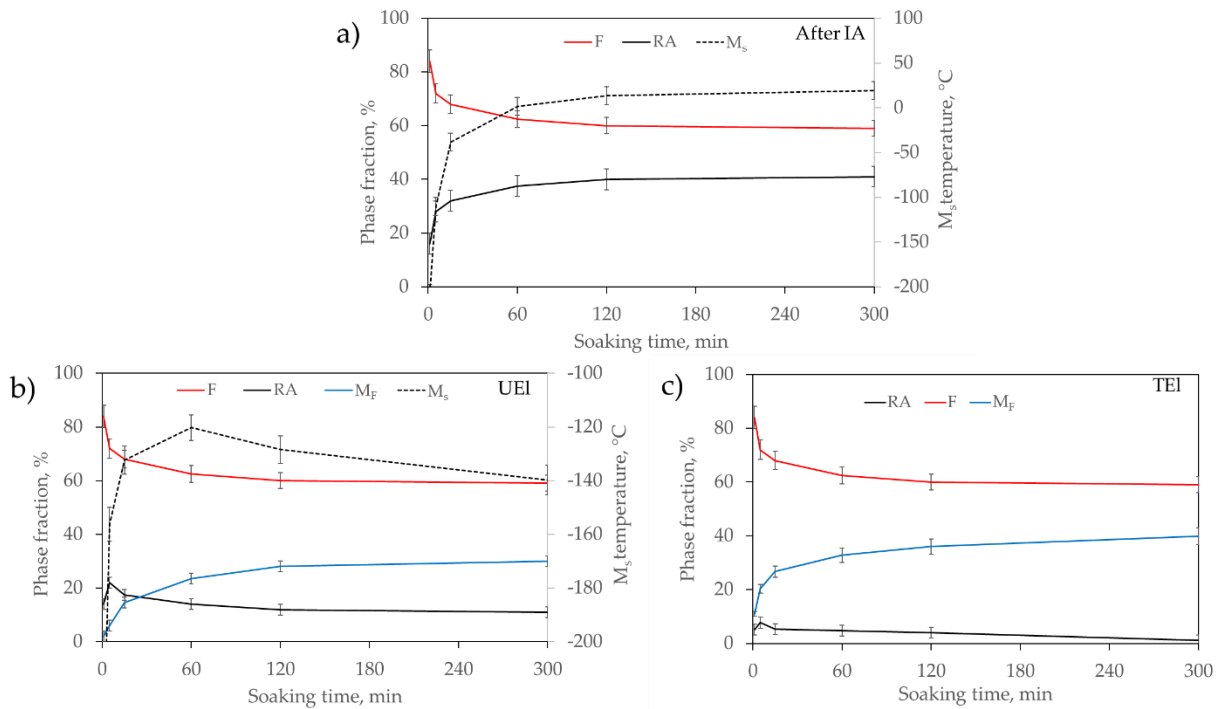


Figure 77 The summarized changes in phase composition and  $M_s$  temperature of RA with the progress of soaking at different stages: (a) after intercritical annealing, (b) in UEI region and (c) in TEI region.

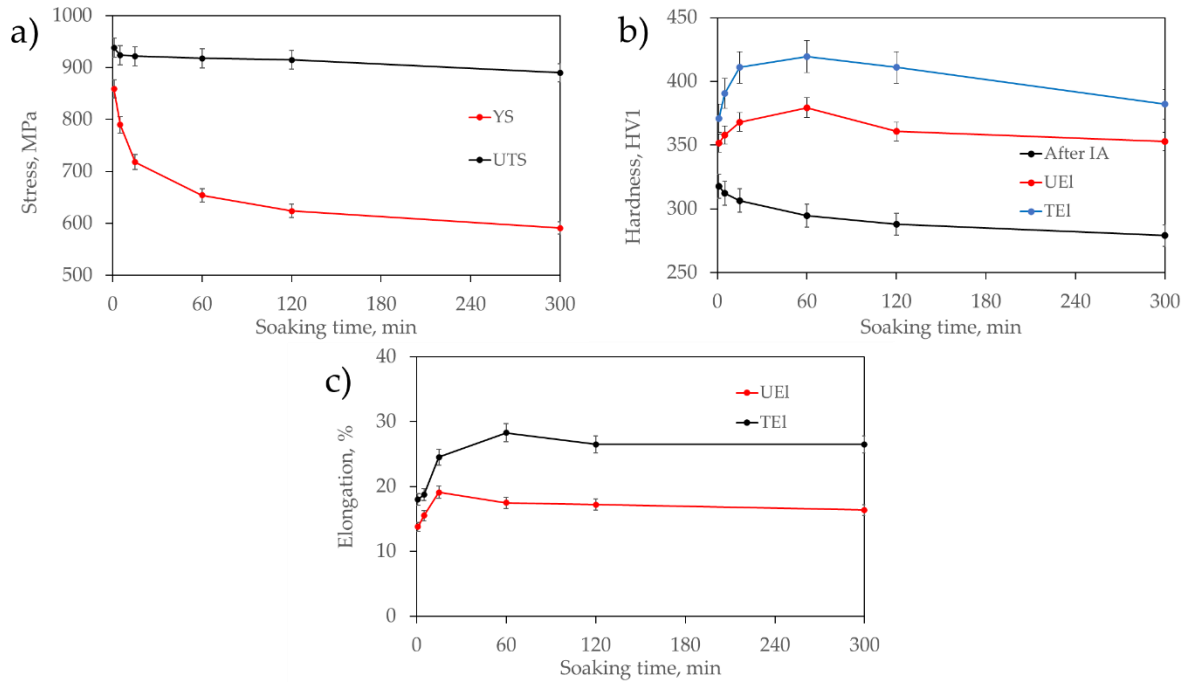


Figure 78 Summarized mechanical properties of analyzed steel with increasing soaking time: (a) strength properties, (b) hardness (c) plastic properties.

As shown by SEM (Figure 71) and EBSD (Figure 72) results, RA is fragmented by the progress of SIMT. It is accompanied by a dynamic change in its stability. Therefore, the  $M_s$  temperature was calculated again for RA grain sizes measured in the UEL region (Figure 77b). After reaching the UEL region the stability of remaining RA for all samples is very high; however, it is the lowest for IS60 sample (the highest  $M_s$  temperature). During the (2) step of deformation the transformation of remaining fraction of RA controls a TEI value. It is visible that for samples IS1 and IS5 the post-uniform elongation value is low because RA remaining in their structures is again the most stable and even the massive strain corresponding to the necking region can not transform it completely (Figure 77c). In case of long soaked samples IS120 and IS300 the RA fraction remaining after UEL is low; thus the post-uniform deformation is limited due to both a low fraction and relative high stability of RA. Among all samples both the fraction and stability of RA remaining in sample IS60 is the most favorable (Figure 77b, c), which results in high post-uniform elongation value (Figure 78c). This analysis shows how complex the influence of RA fraction and stability on mechanical properties is.

### 6.3.2. Local stability of retained austenite controlled by its grain size

Despite the different general stability of RA exhibited by different samples a deeper analysis is needed to explain why samples IS15 and IS60 show rather a gradual SIMT effect, while RA

in sample IS300 transforms massively at an early stage of deformation. As indicated by the calculations (Figure 67) for the currently investigated alloy (and vast majority of lately investigated medium-Mn steels [15]) the chemical enrichment of RA is not enough to lower the  $M_s$  temperature below the room temperature. Therefore, a grain size seems to be crucial for the RA stabilization because it allows the  $M_s$  temperature to be reduced by even several hundred degrees Celsius. Figure 79 indicates the influence of only chemical composition of RA on the  $M_s$  temperature (Figure 79a) in investigated samples. The combined influence of chemical and grain size stabilizations is presented in Figure 79b.

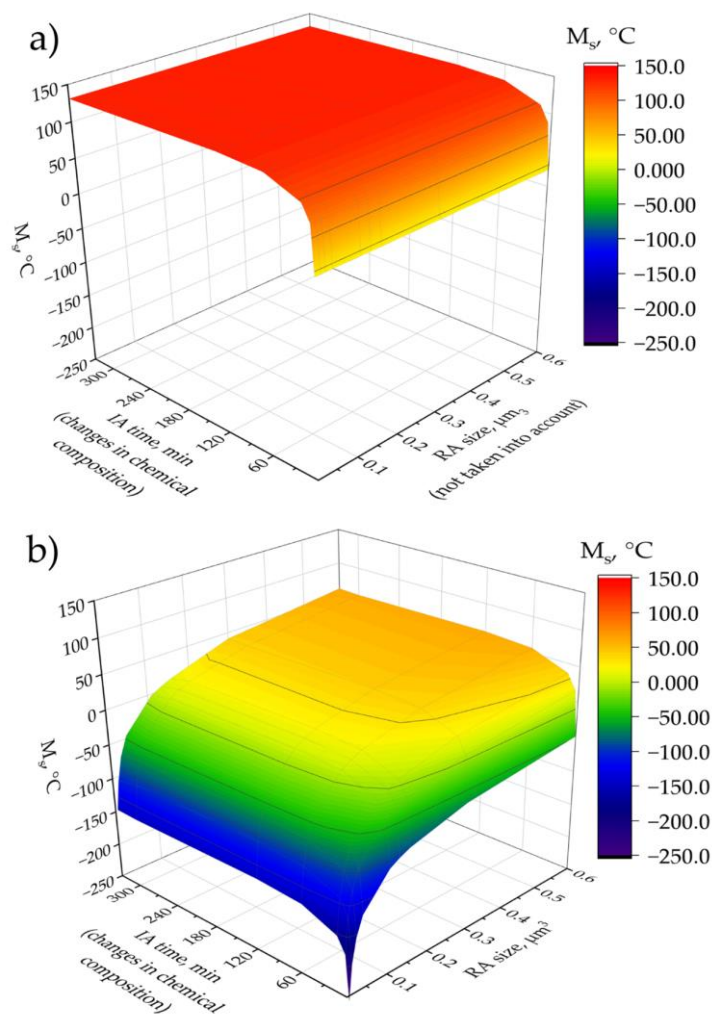


Figure 79 Changes in  $M_s$  temperature depending on (a) chemical composition, (b) combined effects of chemical composition and RA grain size.

The fine grains produced during IA support significantly the RA stabilization. However, if the average grain volume is lower than  $1 \mu\text{m}^3$  its impact is comparable or even stronger than this resulting from RA chemical composition. The sample soaked for 1 min proves this thesis:

the bulk  $M_s$  temperature of the investigated steel is 314 °C; the enrichment of austenite in C to 0.75 wt. % and in Mn to 6.5 wt.% (Figure 66) after 1 min of IA at 680 °C lowers the  $M_s$  temperature to ~23 °C. However, if we take into consideration also a grain size effect the theoretical  $M_s$  temperature reaches < -200 °C.

If we separate from Figure 79b the valid grain sizes for the respective samples, we obtain the curves visible in Figure 80 indicating the  $M_s$  temperature ranges. Such representation shows the general level and a range of RA stability for each sample, which have a direct reflection in measured mechanical properties [231]. The general stability of sample soaked for 1 min is extremely high (represented by low  $M_s$  temperature) regardless of RA grain size present in the structure (the calculated  $\Delta M_s$  reaches about 170 °C). Therefore, the SIMT effect is barely triggered even if the deformation reaches the UEI level [232].

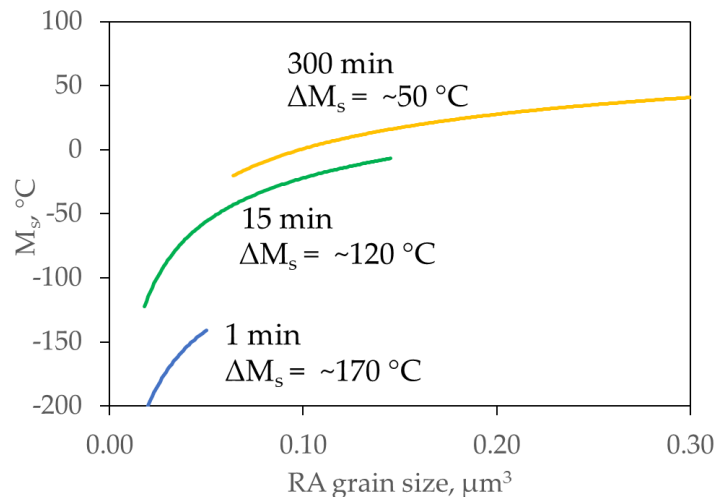


Figure 80 Effect of grain size on  $M_s$  temperature of RA in samples soaked for 1 min, 5min, and 300 min.

The general stability of sample soaked for 15 min caused by its chemical composition and grain size is significantly lower (higher  $M_s$  temperature). Moreover, the RA grain size range after this heat treatment variant is in the most curved section of the plot shown in Figure 80, which causes a very wide and favorable  $\Delta M_s$  of ~ 120 °C reaching from about -10 °C to about -130 °C to be “captured”. This optimal (according to UEI value) general stability and its wide distribution caused by grain size result in the gradual martensitic transformation during the entire tensile range, which results in the highest UEI. The strain hardening rate decreases slowly and its instantaneous hardening exponent increases gradually within the entire deformation range. The sample soaked for 300 min at 680 °C combines both the lowest overall RA stability and its very narrow range despite the wide grain size distribution present in its microstructure.

The low overall stability is caused by the low C and Mn enrichment and the biggest average RA grain size among all investigated samples. The stability range is very narrow ( $\Delta M_s$  of only 50 °C) because most RA grain sizes present in the samples are localized in the flattest section of the  $M_s$  temperature plot (Figure 80). Therefore, despite a wide distribution of RA size, its influence on the RA stability ( $M_s$  temperature) is not differentiated. It results in localized RA transformation at the early deformation stage because a large fraction of RA grains exhibits comparable mechanical stability. The initial strain hardening rate caused by this transformation is very high; however, the potential of RA is quickly exhausted [89]. Moreover, the martensitic phase fraction quickly increases. It results in a rapid increase of strength of the alloy but at the expense of plasticity. The dependence of the general (average  $M_s$  temperature) and local RA stability ( $M_s$  temperature range) shown in Figure 80 explains why the ductility of sample soaked for 300 min is worse in comparison to the sample soaked for 15 min, despite the fact that the RA fraction is significantly higher (by 8 %) for the former.

## 7. Summary and general conclusions

Figure 81 shows the results of investigations on intercritical annealing temperature and soaking time conducted in the present work. They are compared with the mechanical properties of thermomechanically processed steel [5] and with literature reports for different intercritically annealed medium-Mn steels [57,66,70,74–79,83–85,88,186]. The influence of intercritical annealing parameters on the resulting mechanical behavior is enormous, which is visible in the range of obtained results. The heat-treated samples cover a very wide range of properties, from UTS of 1360 MPa and TEI of 8 % for sample IA800, to UTS of 910 MPa and TEI of 31 % for sample IA680.

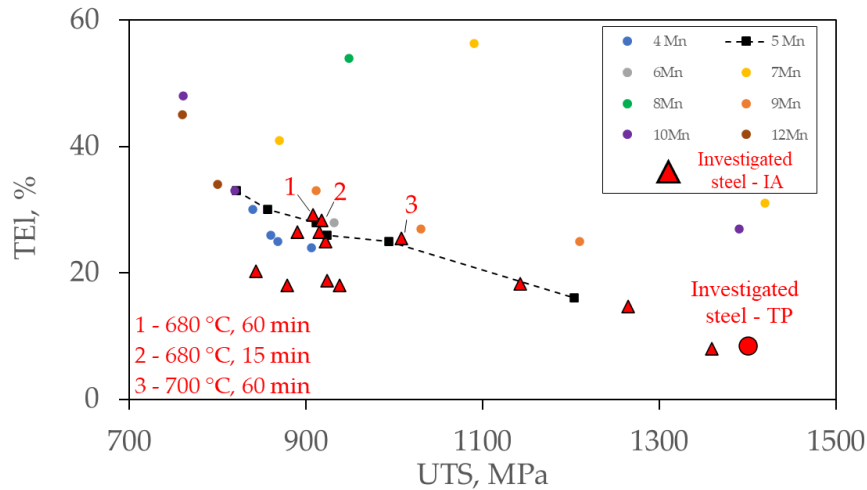


Figure 81 Comparison of mechanical properties obtained during research on intercritical annealing (IA) in comparison to the literature data [57,66,70,74–79,83–85,88,186] and mechanical properties of thermomechanically processed (TP) steel.

All investigated variants of intercritical annealing, beside IA800, show the significantly improved plasticity in comparison to the thermomechanically processed steel (Figure 82). It depends not only on the RA fraction in the microstructure but also on its stability. The results show how much potential is exhibited for this heat treatment type regarding production of automotive parts designed for the crumple zones and other responsible parts using medium-Mn steels. The best properties in terms of plasticity were obtained for samples IA680, IA700 and IS15 (Table 6). All of them exhibit mechanical properties higher than the set target ( $> 30\%$  RA,  $UEI \geq 15\%$ ,  $TEI \geq 25\%$  and  $UTS \geq 900$  MPa). These samples show the mechanical properties relationship slightly better than the tendency observed in literature [75,78,79] for similar alloy compositions. They correspond more to results obtained for medium-Mn steels of higher Mn content [57,75].

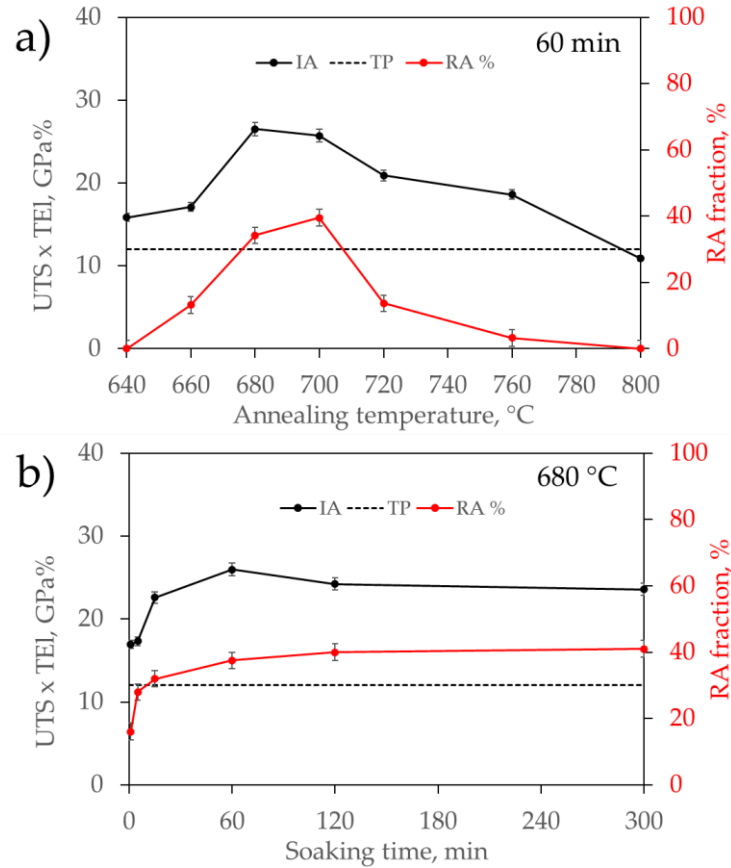


Figure 82 Summary of RA fractions and products of UTS and TEL for samples annealed at different temperatures (a) and for different times (b) compared to the thermomechanically processed steel with a UTS x TEL product of 12 GPa%.

Table 6 Heat-treatment parameters, RA fraction and mechanical properties of the most ductile samples.

Sample	IA temp., °C	IA time, min	RA, %	YS, MPa	UTS, MPa	UEL, %	TEL, %
IA680	680	60	36	670	910	17.5	31
IS15	680	15	32	720	920	19	26
IA700	700	60	41	530	1010	15	25.5

The improvement of both plasticity (Figure 83a) and a product of strength and plasticity (Figure 83b) is an important step forward in the development of AHSS because it allows to obtain comparable properties in steels of lower manganese content. This decreases not only the cost of the alloy but also may reduce technological problems related to this element, such as possible microsegregation [225,233], hydrogen embrittlement [106], hole expansion ratio [101,102] or increased hot working resistance [93].

The obtained results prove the thesis of the work that the proper adjustment of the fraction and stability of the retained austenite through optimized soaking temperature and time of

intercritical annealing allows to achieve gradual strain-induced martensitic transformation controlled by grain size and thus improved plasticity and strength-ductility product, particularly in comparison to thermomechanically processed steel [5].

The explanation of structural phenomena occurring during the intercritical annealing of hot-rolled Al-alloyed medium-Mn steel depending on the applied temperature-time parameters and optimization of these parameters resulting in improved steel plasticity allowed to achieve the aim of the work.

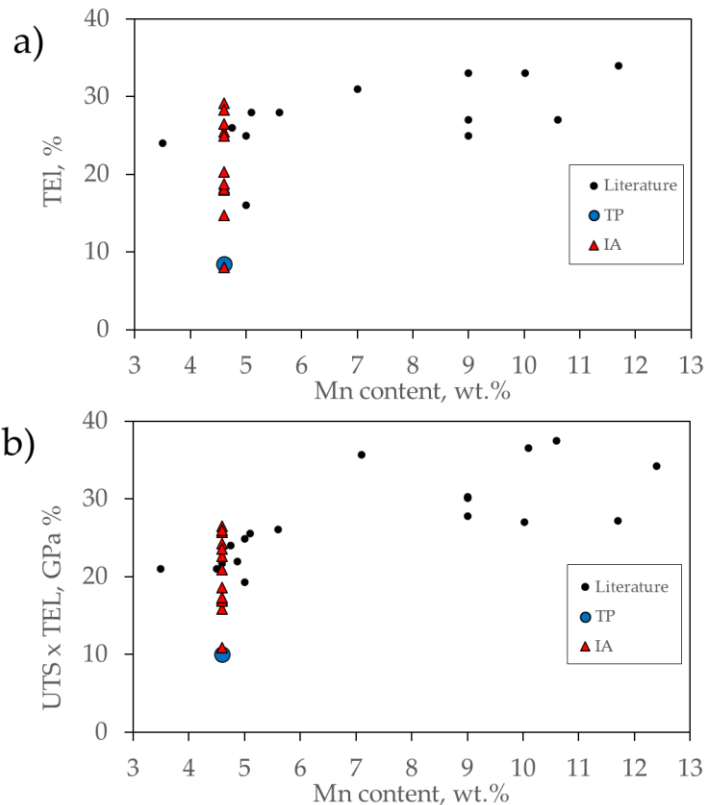


Figure 83 Comparison of mechanical properties obtained during research on intercritical annealing (IA) in comparison to thermomechanically processed steel (TP) and medium-Mn steels containing different additions of Mn [57,66,70,74–79,83–85,88,186].

The mechanical properties improvement in comparison to the results obtained in other works is related to the comprehensive application of both simulations and experimental optimization of the intercritical annealing of analyzed hot-rolled and intercritically annealed medium-Mn steel. The simulations despite some inaccuracies of current models allow to narrow the technological window, which shortens the experimental optimization. Particularly crucial in the context of plasticity is the characterization of the influence of RA stability on the SIMT effect.

The main conclusions of the work are:

1. The simulations and experimental results concerning the intercritical annealing temperature are in general in good agreement. However, the optimal experimental temperature ensuring the highest fraction of retained austenite is shifted by  $\sim 20$  °C to lower temperatures. Also, the maximum fraction of retained austenite indicated by simulations is underestimated by about 9 % in comparison to the XRD results. These differences are caused by: (1) non-equilibrium conditions of the experimental sample (due to insufficient time); (2) current models, which do not consider correctly the partitioning of Mn in modern steels with increased contents of this element, which significantly affects the kinetics of phase transformations.
2. The process time required to obtain the intercritical phase equilibrium decreases with an increase in annealing temperature. The austenization completion was registered only for samples IA720 – IA800 within 60 min of soaking. It decreases from about 56 min at 720 °C to about 35 min for sample annealed at 800 °C. Sample IA1000 obtained fully austenitic microstructure during heating because the annealing temperature is higher than  $A_{c3}$  temperature. At 680 °C all processes taking place during soaking (changes in the proportion of RA, its grain size, the redistribution of chemical elements) and thus the evolution of austenite's stability are most dynamic in the first 15 minutes of IA.
3. Both the increase in annealing temperature and time results in an increased austenite fractions in the microstructure. However, austenite formation is accompanied by its depletion in C and Mn and grain size growth. It results in RA destabilization and the martensitic transformation during cooling. Therefore, to obtain a high fraction of retained austenite at room temperature a compromise between annealing temperature and time is necessary. The highest fraction of RA possible to retain in analyzed steel is about 41 % during 60 min of annealing at 700 °C, or at least 120 min annealing at 680 °C. However, the  $M_s$  temperatures for these samples are close to room temperature.
4. The very high stability of 16 % of RA present in sample soaked for 1 min at 680 °C is promising with regard to the possibility of shortening the soaking time at higher IA temperatures. The improved stabilization of RA by its further grain refinement should allow maintaining a high fraction of this phase at room temperature.
5. In case of soaking time equal to and over 60 min mainly the fraction of high temperature austenite controls the final UTS of the steel regardless of its stability during cooling. It is reflected in continuously increasing UTS with the increase of high temperature

austenite fraction, which during cooling or deformation transforms to fresh martensite. In samples soaked for time shorter than 60 min the matrix of tempered martensite shows a similar contribution to the UTS value as the final amount of transformed RA.

6. The plasticity of intercritically annealed medium-Mn steel is highly sensitive to the presence of fresh martensite in microstructure and a fraction and stability of RA. Samples containing fresh martensite formed during cooling show a significant drop of TEI (< 18 %). In general, the plasticity increases with increasing RA fraction. However, sample IA700, despite the highest fraction of RA (>40 %), shows limited plasticity (TEI of ~25 %) due to low stability of this phase, which results in massive SIMT at an early stage of deformation. Sample IA680 containing a lower fraction of RA (34 %) shows better plasticity (TEI of over 30 %), which is the highest value among all samples due to the higher stability of RA.
7. The best combinations of mechanical properties after annealing at 680 °C were obtained for samples annealed for 15 min (UEI of 19 % and TEI of 26 %) and 60 min (UEI of 17.5 % and TEI of 31 %). Shorter-soaked samples (1 min and 5 min) exhibit too high stability, which limits SIMT effect and its contribution to mechanical properties. Longer soaked samples (120 min and 300 min) show very low stability, which results in the massive SIMT at an early stage of deformation and thus limited plasticity.
8. The local stability of retained austenite is controlled by its grain size range present in the microstructure. A wide range of retained austenite grain size should result in gradual strain-induced martensitic transformation. However, it is not always true as the function representing the influence of retained austenite grain size on its stability is parabolic. Therefore, a similar range of grain size distribution, but with a different average value, causes a significantly different progress of SIMT.
9. The relatively simple intercritical annealing process used to heat treat analyzed hot-rolled medium-Mn steel results in the high RA fraction (up to 40 %) and high mechanical properties (UTS > 900 MPa, TEI > 25 %). It proves the very high potential of this material to be used in the automotive industry. It is especially important for truck chassis, heavy duty vehicles, suspension elements, car wishbones, etc., where such thick sheets are used.

## References

- [1] S.G. Hong, K.B. Kang, C.G. Park, Strain-induced precipitation of NbC in Nb and Nb–Ti microalloyed HSLA steels, *Scr. Mater.* 46 (2002) 163–168. [https://doi.org/10.1016/S1359-6462\(01\)01214-3](https://doi.org/10.1016/S1359-6462(01)01214-3).
- [2] S. Keeler, M. Kimchi, P.J. Mc-oney, *Advanced high-strength steels application guidelines V6*, WorldAutoSteel, Ohio, USA, 2017.
- [3] N. Fonstein, *Advanced high strength sheet steels*, Springer International Publishing, Cham, 2015. <https://doi.org/10.1007/978-3-319-19165-2>.
- [4] L.A. Dobrzański, Mechanical properties and microstructure of high-manganese TWIP, TRIP and TRIPLEX type steels, *Achiev. Mater. Manuf.* 55 (2012) 230–238.
- [5] A. Grajcar, P. Skrzypczyk, D. Wozniak, Thermomechanically rolled medium-Mn steels containing retained austenite, *Arch. Metall. Mater.* 59 (2014) 1691–1697. <https://doi.org/10.2478/amm-2014-0286>.
- [6] B. Sun, *Processing, microstructure and mechanical behavior of medium manganese steels*, PhD thesis, Department of Mining and Materials Engineering, McGill University, 2017.
- [7] N. Fonstein, *Advanced high strength sheet steels: physical metallurgy, design, processing, and properties*, Aufl. 2015, Springer, Cham, 2015.
- [8] L. Meyer, F. Heisterkamp, W. Mueschenborn, Columbium, titanium and vanadium in normalized, thermo-mechanically treated and cold-rolled steels, *Symposium on High Strength Low-Alloy Steels*. (1975) 153–167.
- [9] S. Hayami, T. Furukawa, A family of high-strength cold-rolled steels, In *Microalloying*. (1975) 311–321.
- [10] M.Y. Demeri, *Advanced high-strength steels: science, technology, and applications*, ASM International, Materials Park, Ohio, 2013.
- [11] Global update: Light-duty vehicle greenhouse gas and fuel economy standards | International Council on Clean Transportation, (2017). <https://theicct.org/publications/2017-global-update-LDV-GHG-FE-standards> (accessed April 12, 2020).
- [12] *The Light Vehicle 2025*, (2018). <https://www.lightvehicle2025.eu/> (accessed April 14, 2020).
- [13] WorldAutoSteel, (2017). <https://www.worldautosteel.org/> (accessed April 14, 2020).
- [14] L. Dobrzański, W. Borek, Structure and properties of high-manganese TWIP, TRIP and TRIPLEX steels, *AJMDE*. 9 (2013). <https://doi.org/10.7158/N13-GC07.2013.9.2>.
- [15] Y.-K. Lee, J. Han, Current opinion in medium manganese steel, *Mater. Sci. Technol.* 31 (2015) 843–856. <https://doi.org/10.1179/1743284714Y.0000000722>.
- [16] Volvo S40 safety cage, (2003). <https://www.media.volvocars.com/global/en-gb/media/photos/7936/> (accessed April 12, 2020).

- [17] A. Grajcar, Nowoczesne stale wysokowytrzymałe dla motoryzacji I generacji, *Stal, Metale & Nowe Technologie*. 5–6 (2013) 150–154.
- [18] M. Blicharski, *Inżynieria materiałowa: stal*, Wydawnictwo Naukowe PWN, Warszawa, 2017.
- [19] A. Grajcar, *Inżynieria wysokowytrzymałych stali wielofazowych*, Łukasiewicz Research Network - Institute for Ferrous Metallurgy, Gliwice, 2019.
- [20] J. Adamczyk, *Inżynieria materiałów metalowych. Cz. 1*, Wydawnictwo Politechniki Śląskiej, Gliwice, 2004.
- [21] J. Zhao, Z. Jiang, eds., *Rolling of advanced high strength steels: theory, simulation and practice*, CRC Press, Taylor & Francis Group, Boca Raton, 2017.
- [22] K. Miernik, *Odporność na pękanie dwufazowych stali konstrukcyjnych typu DP*, PhD thesis, Cracow University of Technology, 2011.
- [23] K. Radwanski, *Zastosowanie mikroskopii skaningowej i dyfrakcji elektronów wstecznie rozproszonych w badaniach struktury blach ze stali wielofazowych na różnych etapach procesu ciągłego wyżarzania*, Łukasiewicz Research Network - Institute for Ferrous Metallurgy, Gliwice, 2016.
- [24] J. Adamczyk, A. Grajcar, Structure and mechanical properties of DP-type and TRIP-type sheets obtained after the thermomechanical processing, *J. Mater. Process. Technol.* 162–163 (2005) 267–274. <https://doi.org/10.1016/j.jmatprotec.2005.02.032>.
- [25] A. Grajcar, *Struktura stali C-Mn-Si-Al kształtowana z udziałem przemiany martenzytycznej indukowanej odkształceniem plastycznym*, Wydawnictwo Politechniki Śląskiej, Gliwice, 2010.
- [26] A. Kurc-Lisiecka, *Kształtowanie struktury i tekstury metastabilnego austenitu stali X5CrNi18-10 w procesie odkształcenia plastycznego na zimno*, PhD thesis, Silesian University of Technology, 2014.
- [27] A. Grajcar, *Kształtowanie struktury i własności mechanicznych wyrobów ze stali konstrukcyjnych mikrostopowych w modelowanych procesach obróbki cieplno – mechanicznej*, PhD thesis, Silesian University of Technology, 2003.
- [28] A. Kozłowska, *Wpływ temperatury na indukowaną odkształceniem przemianę martenzytyczną w wysokowytrzymałych stalach wielofazowych*, PhD thesis, Silesian University of Technology, 2020.
- [29] A. Kokosza, J. Pacyna, Mechanical stability of retained austenite in unalloyed structural steels of various carbon content, *Arch. Metall. Mater.* 55 (2010) 1001–1006. <https://doi.org/10.2478/v10172-010-0002-8>.
- [30] S. Wiewiórska, *Analiza teoretyczno-eksperymentalna procesów ciągnięcia nowej generacji drutów ze stali TRIP*, Wydawnictwo Politechniki Częstochowskiej, Częstochowa, 2011.

- [31] B.C. De Cooman, Structure–properties relationship in TRIP steels containing carbide-free bainite, *Curr. Opin. Solid. State Mater. Sci.* 8 (2004) 285–303. <https://doi.org/10.1016/j.cossms.2004.10.002>.
- [32] W. Borek, Znaczenie bliźniakowania w kształtowaniu struktury i własności stali austenitycznych wysokomanganowych, PhD thesis, Silesian University of Technology, 2010.
- [33] M. Czaja, Mechanizmy przeciwdziałania pękaniu stali austenitycznej X11MnSiAl17-1-3 w warunkach dynamicznego odkształcenia plastycznego na zimno, PhD thesis, Silesian University of Technology, 2014.
- [34] S. Vercammen, B. Blanpain, B.C. De Cooman, P. Wollants, Cold rolling behaviour of an austenitic Fe–30Mn–3Al–3Si TWIP-steel: the importance of deformation twinning, *Acta Mater.* 52 (2004) 2005–2012. <https://doi.org/10.1016/j.actamat.2003.12.040>.
- [35] I. Gutierrez-Urrutia, D. Raabe, Dislocation and twin substructure evolution during strain hardening of an Fe–22wt.% Mn–0.6wt.% C TWIP steel observed by electron channeling contrast imaging, *Acta Mater.* 59 (2011) 6449–6462. <https://doi.org/10.1016/j.actamat.2011.07.009>.
- [36] S. Kołodziej, Wpływ przemiany martenzytycznej na strukturę i własności anizotropowe stali wysokomanganowych typu TWIP odkształczanych plastycznie na zimno, PhD thesis, Silesian University of Technology, 2015.
- [37] A. Grajcar, Nowoczesne stale wysokowytrzymałe dla motoryzacji II generacji, *Stal, Metale & Nowe Technologie.* 7–8 (2013) 10–14.
- [38] J. Zhao, Y. Xi, W. Shi, L. Li, Microstructure and mechanical properties of high manganese TRIP steel, *Iron Steel Res. Int.* 19 (2012) 57–62. [https://doi.org/10.1016/S1006-706X\(12\)60088-0](https://doi.org/10.1016/S1006-706X(12)60088-0).
- [39] M.B. Jabłońska, Struktura i właściwości austenitycznej stali wysokomanganowej umacnianej wskutek mechanicznego bliźniakowania w procesach deformacji dynamicznej, Wydawnictwo Politechniki Śląskiej, Gliwice, 2016.
- [40] L. Sozańska-Jędrasik, Struktura i własności nowo opracowanych stali wysokomanganowych typu TRIPLEX, PhD thesis, Silesian University of Technology, 2020.
- [41] A. Grajcar, M. Kciuk, S. Topolska, A. Płachcińska, Microstructure and corrosion behavior of hot-deformed and cold-strained high-Mn steels, *J. Mater. Eng. Perform.* 25 (2016) 2245–2254. <https://doi.org/10.1007/s11665-016-2085-5>.
- [42] M. Jabłońska, G. Niewielski, R. Kawalla, High manganese TWIP steel - technological plasticity and selected properties, *Solid State Phenom.* 212 (2013) 87–90. <https://doi.org/10.4028/www.scientific.net/SSP.212.87>.
- [43] J. Marcisz, Statyczne i dynamiczne właściwości mechaniczne oraz mikrostruktura stali bainitycznych nanostrukturalnych, Łukasiewicz Research Network - Institute for Ferrous Metallurgy, Gliwice, 2018.

- [44] A. Kilarski, Wpływ odkształcenia plastycznego na stabilność mechaniczną austenitu szczątkowego w stalach bainitycznych, PhD thesis, Silesian University of Technology, 2015.
- [45] P. Skrzypczyk, Kształtowanie mikrostruktury i własności mechanicznych wysokowytrzymałych stali bainitycznych z austenitem szczątkowym w procesie obróbki cieplno-plastycznej, PhD thesis, Silesian University of Technology, 2015.
- [46] Z. Kania-Pifczyk, Design of chemical composition and thermomechanical processing of advanced bainitic steels with TRIP effect, PhD thesis, Łukasiewicz Research Network - Institute for Ferrous Metallurgy, 2018.
- [47] C. Garcia-Mateo, F.G. Caballero, Ultra-high-strength bainitic steels, *ISIJ Int.* 45 (2005) 1736–1740. <https://doi.org/10.2355/isijinternational.45.1736>.
- [48] K. Sugimoto, J. Sakaguchi, T. Iida, T. Kashima, Stretch-flangeability of a high-strength TRIP type bainitic sheet steel., *ISIJ Int.* 40 (2000) 920–926. <https://doi.org/10.2355/isijinternational.40.920>.
- [49] A. Królicka, G. Lesiuk, R. Kuziak, K. Radwański, A. Janik, The role of microstructure morphology on fracture mechanisms of continuously cooled bainitic steel designed for rails application, *Metall. Mater. Trans. A.* 54 (2023) 487–504. <https://doi.org/10.1007/s11661-022-06886-w>.
- [50] E. Skołek, K. Wasiak, W. Świątnicki, The microstructure and phase composition of 35CrSiMn5-5-4 steel after quenching and partitioning heat treatment, *Arch. Metall. Mater.* 61 (2016) 1337–1342. <https://doi.org/10.1515/amm-2016-0274>.
- [51] Z.C. Li, H. Ding, R.D.K. Misra, Z.H. Cai, Microstructure-mechanical property relationship and austenite stability in medium-Mn TRIP steels: The effect of austenite-reverted transformation and quenching-tempering treatments, *Mater. Sci. Eng. A.* 682 (2017) 211–219. <https://doi.org/10.1016/j.msea.2016.11.048>.
- [52] A. Kozłowska, B. Grzegorzczak, M. Morawiec, A. Grajcar, Explanation of the PLC effect in advanced high-strength medium-Mn steels. a review, *Materials.* 12 (2019) 4175. <https://doi.org/10.3390/ma12244175>.
- [53] H. Farahani, Solid state phase transformations in medium manganese steels, PhD thesis, Delft University of Technology, 2018.
- [54] S. Lee, S.-J. Lee, S. Santhosh Kumar, K. Lee, B.C.D. Cooman, Localized deformation in multiphase, ultra-fine-grained 6 pct Mn transformation-induced plasticity steel, *Metall. Mater. Trans. A.* 42 (2011) 3638–3651. <https://doi.org/10.1007/s11661-011-0636-9>.
- [55] L. Luo, W. Li, L. Wang, S. Zhou, X. Jin, Tensile behaviors and deformation mechanism of a medium Mn-TRIP steel at different temperatures, *Mater. Sci. Eng. A.* 682 (2017) 698–703. <https://doi.org/10.1016/j.msea.2016.11.017>.

- [56] M. Zhang, L. Li, J. Ding, Q. Wu, Y.-D. Wang, J. Almer, F. Guo, Y. Ren, Temperature-dependent micromechanical behavior of medium-Mn transformation-induced-plasticity steel studied by in situ synchrotron X-ray diffraction, *Acta Mater.* 141 (2017) 294–303. <https://doi.org/10.1016/j.actamat.2017.09.030>.
- [57] J. Han, S.-J. Lee, J.-G. Jung, Y.-K. Lee, The effects of the initial martensite microstructure on the microstructure and tensile properties of intercritically annealed Fe–9Mn–0.05C steel, *Acta Mater.* 78 (2014) 369–377. <https://doi.org/10.1016/j.actamat.2014.07.005>.
- [58] A. Grajcar, D. Woźniak, A. Kozłowska, Non-metallic inclusions and hot-working behaviour of advanced high-strength medium-Mn steels, *Arch. Metall. Mater.* 61 (2016) 811–820. <https://doi.org/10.1515/amm-2016-0137>.
- [59] A. Grajcar, P. Skrzypczyk, R. Kuziak, K. Gołombek, Effect of finishing hot-working temperature on microstructure of thermomechanically processed Mn-Al multiphase steels, *Steel Res. Int.* 85 (2014) 1058–1069. <https://doi.org/10.1002/srin.201300227>.
- [60] J. Speer, R. Rana, D. Matlock, A. Glover, G. Thomas, E. De Moor, Processing variants in medium-Mn steels, *Metals.* 9 (2019) 771. <https://doi.org/10.3390/met9070771>.
- [61] A. Glover, P.J. Gibbs, C. Liu, D.W. Brown, B. Clausen, J.G. Speer, E. De Moor, Deformation behavior of a double soaked medium manganese steel with varied martensite strength, *Metals.* 9 (2019) 761. <https://doi.org/10.3390/met9070761>.
- [62] B. Avishan, M. Tavakolian, S. Yazdani, Two-step austempering of high performance steel with nanoscale microstructure, *Mater. Sci. Eng. A.* 693 (2017) 178–185. <https://doi.org/10.1016/j.msea.2017.03.104>.
- [63] A. Kozłowska, M. Morawiec, A. Skowronek, A. Grajcar, K. Matus, P.M. Nuckowski, Enhancing mechanical properties of hot-rolled Al-alloyed medium-Mn steel by novel double-step intercritical annealing, *Mater. Sci. Eng. A.* 865 (2023) 144650. <https://doi.org/10.1016/j.msea.2023.144650>.
- [64] A. Arlazarov, Evolution of microstructure and mechanical properties of medium Mn steels and their relationship., Université de Lorraine, 2015.
- [65] Q. Lai, M. Gouné, A. Perlade, T. Pardoën, P. Jacques, O. Bouaziz, Y. Bréchet, Mechanism of austenite formation from spheroidized microstructure in an intermediate Fe-0.1C-3.5Mn steel, *Metall. Mater. Trans. A.* 47 (2016) 3375–3386. <https://doi.org/10.1007/s11661-016-3547-y>.
- [66] P.J. Gibbs, E. De Moor, M.J. Merwin, B. Clausen, J.G. Speer, D.K. Matlock, Austenite stability effects on tensile behavior of manganese-enriched-austenite transformation-induced plasticity steel, *Metall. Mater. Trans. A.* 42 (2011) 3691–3702. <https://doi.org/10.1007/s11661-011-0687-y>.

- [67] T.-H. Lee, H.-Y. Ha, B. Hwang, S.-J. Kim, E. Shin, Effect of carbon fraction on stacking fault energy of austenitic stainless steels, *Metall. Mater. Trans. A.* 43 (2012) 4455–4459. <https://doi.org/10.1007/s11661-012-1423-y>.
- [68] P. Podany, C. Reardon, M. Koukolikova, R. Prochazka, A. Franc, Microstructure, mechanical properties and welding of low carbon, medium manganese TWIP/TRIP steel, *Metals.* 8 (2018) 263. <https://doi.org/10.3390/met8040263>.
- [69] S. Traint, A. Pichler, R. Sierlinger, H. Pauli, E.A. Werner, Low-alloyed TRIP-steels with optimized strength, forming and welding properties, *Steel Res. Int.* 77 (2006) 641–649. <https://doi.org/10.1002/srin.200606442>.
- [70] J. Shi, X. Sun, M. Wang, W. Hui, H. Dong, W. Cao, Enhanced work-hardening behavior and mechanical properties in ultrafine-grained steels with large-fractioned metastable austenite, *Scr. Mater.* 63 (2010) 815–818. <https://doi.org/10.1016/j.scriptamat.2010.06.023>.
- [71] X. Li, R. Song, N. Zhou, J. Li, An ultrahigh strength and enhanced ductility cold-rolled medium-Mn steel treated by intercritical annealing, *Scr. Mater.* 154 (2018) 30–33. <https://doi.org/10.1016/j.scriptamat.2018.05.016>.
- [72] J. Trzaska, Empirical formulae for the calculation of austenite supercooled transformation temperatures, *Arch. Metall. Mater.* 60 (2015) 181–185. <https://doi.org/10.1515/amm-2015-0029>.
- [73] T.-H. Lee, C.-S. Oh, S.-J. Kim, Effects of nitrogen on deformation-induced martensitic transformation in metastable austenitic Fe–18Cr–10Mn–N steels, *Scripta Materialia.* 58 (2008) 110–113. <https://doi.org/10.1016/j.scriptamat.2007.09.029>.
- [74] C.-H. Seo, K.H. Kwon, K. Choi, K.-H. Kim, J.H. Kwak, S. Lee, N.J. Kim, Deformation behavior of ferrite–austenite duplex lightweight Fe–Mn–Al–C steel, *Scr. Mater.* 66 (2012) 519–522. <https://doi.org/10.1016/j.scriptamat.2011.12.026>.
- [75] D.W. Suh, J.H. Ryu, M.S. Joo, H.S. Yang, K. Lee, H.K.D.H. Bhadeshia, Medium-alloy manganese-rich transformation-induced plasticity steels, *Metall. Mater. Trans. A.* 44 (2013) 286–293. <https://doi.org/10.1007/s11661-012-1402-3>.
- [76] A. Arlazarov, M. Gouné, O. Bouaziz, A. Hazotte, G. Petitgand, P. Barges, Evolution of microstructure and mechanical properties of medium Mn steels during double annealing, *Mater. Sci. Eng. A.* 542 (2012) 31–39. <https://doi.org/10.1016/j.msea.2012.02.024>.
- [77] W.Q. Cao, C. Wang, J. Shi, M.Q. Wang, W.J. Hui, H. Dong, Microstructure and mechanical properties of Fe–0.2C–5Mn steel processed by ART-annealing, *Mater. Sci. Eng. A.* 528 (2011) 6661–6666. <https://doi.org/10.1016/j.msea.2011.05.039>.
- [78] H. Luo, H. Dong, New ultrahigh-strength Mn-alloyed TRIP steels with improved formability manufactured by intercritical annealing, *Mater. Sci. Eng. A.* 626 (2015) 207–212. <https://doi.org/10.1016/j.msea.2014.12.049>.

- [79] G.K. Bansal, D.A. Madhukar, A.K. Chandan, A. K., G.K. Mandal, V.C. Srivastava, On the intercritical annealing parameters and ensuing mechanical properties of low-carbon medium-Mn steel, *Mater. Sci. Eng. A*. 733 (2018) 246–256. <https://doi.org/10.1016/j.msea.2018.07.055>.
- [80] D.-W. Suh, S.-J. Park, T.-H. Lee, C.-S. Oh, S.-J. Kim, Influence of Al on the microstructural evolution and mechanical behavior of low-carbon, manganese transformation-induced-plasticity steel, *Metall. Mater. Trans. A*. 41 (2010) 397–408. <https://doi.org/10.1007/s11661-009-0124-7>.
- [81] B.-J. Hu, Q. Zheng, Y. Lu, C. Jia, T. Liang, C. Zheng, D. Li, Stabilizing austenite via intercritical Mn partitioning in a medium Mn steel, *Scr. Mater.* 225 (2023) 115162. <https://doi.org/10.1016/j.scriptamat.2022.115162>.
- [82] T. Li, S. Yan, D. An, X. Li, J. Chen, Austenite transformation associated with  $\delta$ -ferrite phase in a medium-Mn steel after cold-rolling and intercritical annealing, *Mater. Process. Technol.* 306 (2022) 117632. <https://doi.org/10.1016/j.jmatprotec.2022.117632>.
- [83] S.-J. Park, B. Hwang, K.H. Lee, T.-H. Lee, D.-W. Suh, H.N. Han, Microstructure and tensile behavior of duplex low-density steel containing 5mass% aluminum, *Scr. Mater.* 68 (2013) 365–369. <https://doi.org/10.1016/j.scriptamat.2012.09.030>.
- [84] M.-M. Wang, C.C. Tasan, D. Ponge, A. Kostka, D. Raabe, Smaller is less stable: Size effects on twinning vs. transformation of reverted austenite in TRIP-maraging steels, *Acta Mater.* 79 (2014) 268–281. <https://doi.org/10.1016/j.actamat.2014.07.020>.
- [85] S. Lee, B.C. De Cooman, Tensile behavior of intercritically annealed 10 pct Mn multi-phase steel, *Metall. Mater. Trans. A*. 45 (2014) 709–716. <https://doi.org/10.1007/s11661-013-2047-6>.
- [86] H. Aydin, I.-H. Jung, E. Essadiqi, S. Yue, Twinning and tripping in 10% Mn steels, *Mater. Sci. Eng. A*. 591 (2014) 90–96. <https://doi.org/10.1016/j.msea.2013.10.088>.
- [87] C.-Y. Lee, J. Jeong, J. Han, S.-J. Lee, S. Lee, Y.-K. Lee, Coupled strengthening in a medium manganese lightweight steel with an inhomogeneously grained structure of austenite, *Acta Mater.* 84 (2015) 1–8. <https://doi.org/10.1016/j.actamat.2014.10.032>.
- [88] H.-W. Yen, S.W. Ooi, M. Eizadjou, A. Breen, C.-Y. Huang, H.K.D.H. Bhadeshia, S.P. Ringer, Role of stress-assisted martensite in the design of strong ultrafine-grained duplex steels, *Acta Mater.* 82 (2015) 100–114. <https://doi.org/10.1016/j.actamat.2014.09.017>.
- [89] Y. Ma, W. Song, S. Zhou, A. Schwedt, W. Bleck, Influence of intercritical annealing temperature on microstructure and mechanical properties of a cold-rolled medium-Mn steel, *Metals*. 8 (2018) 357. <https://doi.org/10.3390/met8050357>.
- [90] N. Fonstein, The effect of chemical composition on formation of ferrite–martensite structures and mechanical properties of dual-phase steels, in: *Advanced High Strength Sheet Steels*, Springer International Publishing, Cham, 2015: pp. 139–184. [https://doi.org/10.1007/978-3-319-19165-2\\_4](https://doi.org/10.1007/978-3-319-19165-2_4).

- [91] H. Aydin, Design considerations for the third generation advanced high strength steel, PhD thesis, 2013.
- [92] J.-H. Kang, T. Ingendahl, J. von Appen, R. Dronskowski, W. Bleck, Impact of short-range ordering on yield strength of high manganese austenitic steels, *Mater. Sci. Eng. A.* 614 (2014) 122–128. <https://doi.org/10.1016/j.msea.2014.07.016>.
- [93] A. Skowronek, D. Woźniak, A. Grajcar, Effect of Mn addition on hot-working behavior and microstructure of hot-rolled medium-Mn steels, *Metals.* 11 (2021) 354. <https://doi.org/10.3390/met11020354>.
- [94] R. Kuziak, R. Kawalla, S. Waengler, Advanced high strength steels for automotive industry, *Arch. Civ. Mech. Eng.* 8 (2008) 103–117. [https://doi.org/10.1016/S1644-9665\(12\)60197-6](https://doi.org/10.1016/S1644-9665(12)60197-6).
- [95] Z. Gronostajski, R. Kuziak, Metalurgiczne, technologiczne i funkcjonalne podstawy zaawansowanych wysokowytrzymałych stali dla przemysłu motoryzacyjnego, *Prace IMŻ.* 62 (2010) 22–26.
- [96] Y.-U. Heo, Y.-Y. Song, S.-J. Park, H.K.D.H. Bhadeshia, D.-W. Suh, Influence of silicon in low density Fe-C-Mn-Al steel, *Metall. Mater. Trans. A.* 43 (2012) 1731–1735. <https://doi.org/10.1007/s11661-012-1149-x>.
- [97] R. Rana, ed., *Automotive steels: design, metallurgy, processing and applications*, Elsevier ; Woodhead Publishing, Amsterdam : Duxhead, United Kingdom, 2017.
- [98] K. Sato, M. Ichinose, Y. Hirotsu, Y. Inoue, Effects of deformation induced phase transformation and twinning on the mechanical properties of austenitic Fe-Mn-Al alloys., *ISIJ Int.* 29 (1989) 868–877. <https://doi.org/10.2355/isijinternational.29.868>.
- [99] C. Liu, Q. Peng, Z. Xue, M. Deng, S. Wang, C. Yang, Microstructure-tensile properties relationship and austenite stability of a Nb-mo micro-alloyed medium-Mn TRIP steel, *Metals.* 8 (2018) 615. <https://doi.org/10.3390/met8080615>.
- [100] S.K. Paul, A critical review on hole expansion ratio, *Materialia.* 9 (2020) 100566. <https://doi.org/10.1016/j.mtla.2019.100566>.
- [101] N. Pathak, C. Butcher, M. Worswick, Assessment of the critical parameters influencing the edge stretchability of advanced high-strength steel sheet, *J. Mater. Eng. Perform.* 25 (2016) 4919–4932. <https://doi.org/10.1007/s11665-016-2316-9>.
- [102] S. Allain, D. Urban, C. Wong, M. Huang, B. Yan, Formability characterization of a new generation high strength steels, 2003. <https://doi.org/10.2172/1001171>.
- [103] B.S. Levy, M. Gibbs, C.J. Van Tyne, Failure during sheared edge stretching of dual-phase steels, *Metall. Mater. Trans. A.* 44 (2013) 3635–3648. <https://doi.org/10.1007/s11661-013-1718-7>.
- [104] R. Schneider, K. Steineder, D. Krizan, C. Sommitsch, Effect of the heat treatment on the microstructure and mechanical properties of medium-Mn-steels, *Mater. Sci. Technol.* 35 (2019) 2045–2053. <https://doi.org/10.1080/02670836.2018.1548957>.

- [105] J.H. Kim, E.J. Seo, M.-H. Kwon, S. Kang, B.C. De Cooman, Effect of quenching temperature on stretch flangeability of a medium Mn steel processed by quenching and partitioning, *Mater. Sci. Eng. A.* 729 (2018) 276–284. <https://doi.org/10.1016/j.msea.2018.05.083>.
- [106] Q.Y. Liu, Y. Yan, J.P. Xu, S.Q. Yang, J.X. Li, Y.J. Su, L.J. Qiao, Effect of prestrain on hydrogen-induced delayed cracking for medium Mn steels, *Mater. Eng. Perform.* 29 (2020) 1929–1938. <https://doi.org/10.1007/s11665-020-04706-z>.
- [107] J. Han, J.-H. Nam, Y.-K. Lee, The mechanism of hydrogen embrittlement in intercritically annealed medium Mn TRIP steel, *Acta Mater.* 113 (2016) 1–10. <https://doi.org/10.1016/j.actamat.2016.04.038>.
- [108] J.P. Hirth, Effects of hydrogen on the properties of iron and steel, *Metall. Trans. A.* 11 (1980) 861–890. <https://doi.org/10.1007/BF02654700>.
- [109] J.H. Ryu, Y.S. Chun, C.S. Lee, H.K.D.H. Bhadeshia, D.W. Suh, Effect of deformation on hydrogen trapping and effusion in TRIP-assisted steel, *Acta Mater.* 60 (2012) 4085–4092. <https://doi.org/10.1016/j.actamat.2012.04.010>.
- [110] C. Shao, W. Hui, Y. Zhang, X. Zhao, Y. Weng, Effect of intercritical annealing time on hydrogen embrittlement of warm-rolled medium Mn steel, *Mater. Sci. Eng. A.* 726 (2018) 320–331. <https://doi.org/10.1016/j.msea.2018.04.100>.
- [111] Y. Zhang, W. Hui, X. Zhao, C. Wang, W. Cao, H. Dong, Effect of reverted austenite fraction on hydrogen embrittlement of TRIP-aided medium Mn steel (0.1C-5Mn), *Eng. Fail. Anal.* 97 (2019) 605–616. <https://doi.org/10.1016/j.engfailanal.2019.01.018>.
- [112] A.R. Troiano, The role of hydrogen and other interstitials in the mechanical behavior of metals: (1959 Edward de Mille Campbell Memorial Lecture), *Metallogr. Microstruct. Anal.* 5 (2016) 557–569. <https://doi.org/10.1007/s13632-016-0319-4>.
- [113] I.M. Robertson, The effect of hydrogen on dislocation dynamics, *Eng. Fract. Mech.* 68 (2001) 671–692. [https://doi.org/10.1016/S0013-7944\(01\)00011-X](https://doi.org/10.1016/S0013-7944(01)00011-X).
- [114] S.P. Lynch, Hydrogen embrittlement (HE) phenomena and mechanisms, in: *Stress Corrosion Cracking*, Elsevier, 2011: pp. 90–130. <https://doi.org/10.1533/9780857093769.1.90>.
- [115] A. Skowronek, M. Morawiec, A. Kozłowska, W. Pakieła, Effect of hot deformation on phase transformation kinetics in isothermally annealed 3Mn-1.6Al steel, *Materials.* 13 (2020) 5817. <https://doi.org/10.3390/ma13245817>.
- [116] F. Hou, Y. Bai, A. Shibata, N. Tsuji, Microstructure evolution during thermomechanical processing in 3Mn-0.1C medium-Mn steel, *Mater. Sci. Technol.* 35 (2019) 2101–2108. <https://doi.org/10.1080/02670836.2018.1548099>.
- [117] A. Ito, A. Shibata, N. Tsuji, Thermomechanical processing of medium manganese steels, *Mater. Sci. Forum.* 879 (2016) 90–94. <https://doi.org/10.4028/www.scientific.net/MSF.879.90>.

- [118] A. Grajcar, W. Zalecki, W. Burian, A. Kozłowska, Phase equilibrium and austenite decomposition in advanced high-strength medium-Mn bainitic steels, *Metals*. 6 (2016) 248. <https://doi.org/10.3390/met6100248>.
- [119] A. Skowronek, A. Kozłowska, A. Grajcar, M. Morawiec, Microstructure-property relationships and mechanical stability of retained austenite in medium-C TRIP steel at different deformation temperatures, *Arch. Metall. Mater.* 65 (2020) 941–949. <https://doi.org/10.24425/amm.2020.132842>.
- [120] F.G. Caballero, H.K.D.H. Bhadeshia, K.J.A. Mawella, D.G. Jones, P. Brown, Very strong low temperature bainite, *Mater. Sci. Technol.* 18 (2002) 279–284. <https://doi.org/10.1179/026708301225000725>.
- [121] C. Garcia-Mateo, F.G. Caballero, H.K.D.H. Bhadeshia, Low temperature bainite, *Phys. IV France*. 112 (2003) 285–288. <https://doi.org/10.1051/jp4:2003884>.
- [122] B. Garbarz, W. Burian, Microstructure and properties of nanoduplex bainite–austenite steel for ultra-high-strength plates, *Steel Res. Int.* 85 (2014) 1620–1628. <https://doi.org/10.1002/srin.201300453>.
- [123] F.G. Caballero, C. García-Mateo, J. Chao, M.J. Santofimia, C. Capdevila, C.G. de Andrés, Effects of morphology and stability of retained austenite on the ductility of TRIP-aided bainitic steels, *ISIJ Int.* 48 (2008) 1256–1262. <https://doi.org/10.2355/isijinternational.48.1256>.
- [124] C. Garcia-Mateo, F.G. Caballero, J. Chao, C. Capdevila, C. Garcia de Andres, Mechanical stability of retained austenite during plastic deformation of super high strength carbide free bainitic steels, *Mater. Sci.* 44 (2009) 4617–4624. <https://doi.org/10.1007/s10853-009-3704-4>.
- [125] S.B. Singh, H.K.D.H. Bhadeshia, Estimation of bainite plate-thickness in low-alloy steels, *Mater. Sci. Eng. A*. 245 (1998) 72–79. [https://doi.org/10.1016/S0921-5093\(97\)00701-6](https://doi.org/10.1016/S0921-5093(97)00701-6).
- [126] J. Marcisz, B. Garbarz, A. Janik, W. Zalecki, Controlling the content and morphology of phase constituents in nanobainitic steel containing 0.6%C to obtain the required ratio of strength to plasticity, *Metals*. 11 (2021) 658. <https://doi.org/10.3390/met11040658>.
- [127] X.Y. Long, F.C. Zhang, J. Kang, B. Lv, X.B. Shi, Low-temperature bainite in low-carbon steel, *Mater. Sci. Eng. A*. 594 (2014) 344–351. <https://doi.org/10.1016/j.msea.2013.11.089>.
- [128] X.Y. Long, J. Kang, B. Lv, F.C. Zhang, Carbide-free bainite in medium carbon steel, *Mater. Des.* 64 (2014) 237–245. <https://doi.org/10.1016/j.matdes.2014.07.055>.
- [129] M. Soliman, H. Mostafa, A.S. El-Sabbagh, H. Palkowski, Low temperature bainite in steel with 0.26wt% C, *Mater. Sci. Eng. A*. 527 (2010) 7706–7713. <https://doi.org/10.1016/j.msea.2010.08.037>.
- [130] X.L. Wang, K.M. Wu, F. Hu, L. Yu, X.L. Wan, Multi-step isothermal bainitic transformation in medium-carbon steel, *Scr. Mater.* 74 (2014) 56–59. <https://doi.org/10.1016/j.scriptamat.2013.10.019>.

- [131] A. Skowronek, E. Cordova-Tapia, P. Tobajas-Balseira, C. Garcia-Mateo, J.A. Jiménez, R. Petrov, A. Grajcar, Bainite plate thickness reduction and microstructure tailoring by double austempering of Al-rich 3Mn steel, *Mater. Sci. Eng. A.* 853 (2022) 143743. <https://doi.org/10.1016/j.msea.2022.143743>.
- [132] J. Burja, B. Šuler, M. Češnjaj, A. Nagode, Effect of intercritical annealing on the microstructure and mechanical properties of 0.1C-13Cr-3Ni martensitic stainless steel, *Metals*. 11 (2021) 392. <https://doi.org/10.3390/met11030392>.
- [133] Y.H. Choi, J.H. Ryu, S.W. Lee, K. Lee, B.J. Lee, J.-K. Kim, J.S. Lee, D.-W. Suh, Influence of initial microstructures on intercritical annealing behaviour in a medium Mn steel, *Mater. Sci. Technol.* 35 (2019) 2092–2100. <https://doi.org/10.1080/02670836.2018.1475445>.
- [134] Y. Li, D.S. Martín, J. Wang, C. Wang, W. Xu, A review of the thermal stability of metastable austenite in steels: Martensite formation, *Mater. Sci. Technol.* 91 (2021) 200–214. <https://doi.org/10.1016/j.jmst.2021.03.020>.
- [135] D. Barbier, Extension of the martensite transformation temperature relation to larger alloying elements and contents, *Adv. Eng. Mater.* 16 (2014) 122–127. <https://doi.org/10.1002/adem.201300116>.
- [136] G. Krauss, Martensite in steel: strength and structure, *Mater. Sci. Eng. A.* 273–275 (1999) 40–57. [https://doi.org/10.1016/S0921-5093\(99\)00288-9](https://doi.org/10.1016/S0921-5093(99)00288-9).
- [137] S.M.C. van Bohemen, Bainite and martensite start temperature calculated with exponential carbon dependence, *Mater. Sci. Technol.* 28 (2012) 487–495. <https://doi.org/10.1179/1743284711Y.0000000097>.
- [138] A. Arlazarov, E. Soares Barreto, N. Kabou, D. Huin, Evolution of Ms temperature as a function of composition and grain size, *Metall. Mater. Trans. A.* 51 (2020) 6159–6166. <https://doi.org/10.1007/s11661-020-06022-6>.
- [139] S. Lee, B.C. De Cooman, Effect of the intercritical annealing temperature on the mechanical properties of 10 pct Mn multi-phase steel, *Metall. Mater. Trans. A.* 45 (2014) 5009–5016. <https://doi.org/10.1007/s11661-014-2449-0>.
- [140] F. Huyan, Computational materials design of medium Mn steels, PhD thesis, KTH Royal Institute of Technology, 2018.
- [141] A. Stormvinter, A. Borgenstam, J. Ågren, Thermodynamically based prediction of the martensite start temperature for commercial steels, *Metall. Mater. Trans. A.* 43 (2012) 3870–3879. <https://doi.org/10.1007/s11661-012-1171-z>.
- [142] C. Liu, F. Xiong, G. Liu, Y. Wang, Y. Cao, Z. Xue, Q. Peng, Austenite stability and deformation behavior in medium Mn steel processed by cyclic quenching art heat treatment, *Materials*. 14 (2021) 7132. <https://doi.org/10.3390/ma14237132>.

- [143] S. van der Zwaag, L. Zhao, S.O. Kruijver, J. Sietsma, Thermal and mechanical stability of retained austenite in aluminum-containing multiphase TRIP steels, *ISIJ Int.* 42 (2002) 1565–1570. <https://doi.org/10.2355/isijinternational.42.1565>.
- [144] J. Wang, S. Van Der Zwaag, Stabilization mechanisms of retained austenite in transformation-induced plasticity steel, *Metall. Mater. Trans. A.* 32 (2001) 1527–1539. <https://doi.org/10.1007/s11661-001-0240-5>.
- [145] A. Arlazarov, M. Gouné, O. Bouaziz, A. Hazotte, Critical factors governing the thermal stability of austenite in an ultra-fined grained Medium-Mn steel, *Philos. Mag. Lett.* 97 (2017) 125–131. <https://doi.org/10.1080/09500839.2017.1290293>.
- [146] J. Hidalgo, K.O. Findley, M.J. Santofimia, Thermal and mechanical stability of retained austenite surrounded by martensite with different degrees of tempering, *Mater. Sci. Eng. A.* 690 (2017) 337–347. <https://doi.org/10.1016/j.msea.2017.03.017>.
- [147] X.C. Xiong, B. Chen, M.X. Huang, J.F. Wang, L. Wang, The effect of morphology on the stability of retained austenite in a quenched and partitioned steel, *Scr. Mater.* 68 (2013) 321–324. <https://doi.org/10.1016/j.scriptamat.2012.11.003>.
- [148] P.J. Jacques, F. Delannay, J. Ladrière, On the influence of interactions between phases on the mechanical stability of retained austenite in transformation-induced plasticity multiphase steels, *Metall. Mater. Trans. A.* 32 (2001) 2759–2768. <https://doi.org/10.1007/s11661-001-1027-4>.
- [149] B. Fultz, J.I. Kim, Y.H. Kim, H.J. Kim, G.O. Fior, J.W. Morris, The stability of precipitated austenite and the toughness of 9Ni steel, *Metall. Trans. A.* 16 (1985) 2237–2249. <https://doi.org/10.1007/BF02670423>.
- [150] K. Davut, S. Zaefferer, The effect of texture on the stability of retained austenite in Al-alloyed TRIP steels of Al-alloyed TRIP Steels, *Mater. Res. Soc. Sympos. Proceedings.* 1296 (2011) 1–6. <https://doi.org/10.1557/opl.2011.1447>.
- [151] D. De Knijf, C. Föjler, L.A.I. Kestens, R. Petrov, Factors influencing the austenite stability during tensile testing of quenching and partitioning steel determined via in-situ electron backscatter diffraction, *Mater. Sci. Eng. A.* 638 (2015) 219–227. <https://doi.org/10.1016/j.msea.2015.04.075>.
- [152] C.A. Apple, G. Krauss, The effect of heating rate on the martensite to austenite transformation in Fe-Ni-C alloys, *Acta Metall.* 20 (1972) 849–856. [https://doi.org/10.1016/0001-6160\(72\)90077-6](https://doi.org/10.1016/0001-6160(72)90077-6).
- [153] J. Han, Y.-K. Lee, The effects of the heating rate on the reverse transformation mechanism and the phase stability of reverted austenite in medium Mn steels, *Acta Mater.* 67 (2014) 354–361. <https://doi.org/10.1016/j.actamat.2013.12.038>.
- [154] Y.-K. Lee, H.-C. Shin, D.-S. Leem, J.-Y. Choi, W. Jin, C.-S. Choi, Reverse transformation mechanism of martensite to austenite and amount of retained austenite after reverse

- transformation in Fe-3Si-13Cr-7Ni (wt-%) martensitic stainless steel, *Mater. Sci. Technol.* 19 (2003) 393–398. <https://doi.org/10.1179/026708303225009742>.
- [155] Y. Ma, Medium-manganese steels processed by austenite-reverted-transformation annealing for automotive applications, *Mater. Sci. Technol.* 33 (2017) 1713–1727. <https://doi.org/10.1080/02670836.2017.1312208>.
- [156] J.-M. Jang, S.-J. Kim, N.H. Kang, K.-M. Cho, D.-W. Suh, Effects of annealing conditions on microstructure and mechanical properties of low carbon, manganese transformation-induced plasticity steel, *Met. Mater. Int.* 15 (2009) 909–916. <https://doi.org/10.1007/s12540-009-0909-7>.
- [157] S. Lee, B.C. De Cooman, On the selection of the optimal intercritical annealing temperature for medium Mn TRIP steel, *Metall. Mater. Trans. A.* 44 (2013) 5018–5024. <https://doi.org/10.1007/s11661-013-1860-2>.
- [158] A. Skowronek, A. Grajcar, A. Kozłowska, A. Janik, M. Morawiec, R.H. Petrov, Temperature-dependent microstructural evolution of Al-rich medium-Mn steel during intercritical annealing, *Metall. Mater. Trans. A.* 53 (2022) 3012–3021. <https://doi.org/10.1007/s11661-022-06721-2>.
- [159] H. Huang, O. Matsumura, T. Furukawa, Retained austenite in low carbon, manganese steel after intercritical heat treatment, *Mater. Sci. Technol.* 10 (1994) 621–626. <https://doi.org/10.1179/mst.1994.10.7.621>.
- [160] X. Wan, G. Liu, Z. Yang, H. Chen, Flash annealing yields a strong and ductile medium Mn steel with heterogeneous microstructure, *Scr. Mater.* 198 (2021) 113819. <https://doi.org/10.1016/j.scriptamat.2021.113819>.
- [161] Thermo-Calc Software, Users Guide, Version 3.0, (2013). [https://www.thermocalc.com/media/7994/tcc\\_usersguide.pdf](https://www.thermocalc.com/media/7994/tcc_usersguide.pdf) (accessed April 18, 2020).
- [162] W. Ding, R. Wang, Y. Li, B. Wang, High elongation of medium-manganese steel containing 1.0 wt.% Al after a short intercritical annealing time, *Mater. Res. Technol.* 9 (2020) 7262–7272. <https://doi.org/10.1016/j.jmrt.2020.04.091>.
- [163] E. Bonnevie, G. Ferrière, A. Ikhlef, D. Kaplan, J.M. Orain, Morphological aspects of martensite–austenite constituents in intercritical and coarse grain heat affected zones of structural steels, *Mater. Sci. Eng. A.* 385 (2004) 352–358. <https://doi.org/10.1016/j.msea.2004.06.033>.
- [164] H. Luo, J. Shi, C. Wang, W. Cao, X. Sun, H. Dong, Experimental and numerical analysis on formation of stable austenite during the intercritical annealing of 5Mn steel, *Acta Mater.* 59 (2011) 4002–4014. <https://doi.org/10.1016/j.actamat.2011.03.025>.
- [165] H. Dong, W.Q. Cao, J. Shi, Formation of an ultrafine-grained austenite-containing microstructure from a cold-rolled medium-manganese steel processed using intercritical annealing, *Mater. Sci. Forum.* 762 (2013) 31–37. <https://doi.org/10.4028/www.scientific.net/MSF.762.31>.

- [166] C. Wang, J. Shi, C.Y. Wang, W.J. Hui, M.Q. Wang, H. Dong, W.Q. Cao, Development of ultrafine lamellar ferrite and austenite duplex structure in 0.2C5Mn steel during ART-annealing, *ISIJ Int.* 51 (2011) 651–656. <https://doi.org/10.2355/isijinternational.51.651>.
- [167] K.M.H. Bhadhon, X. Wang, E.A. McNally, J.R. McDermid, Effect of intercritical annealing parameters and starting microstructure on the microstructural evolution and mechanical properties of a Medium-Mn third generation advanced high strength steel, *Metals*. 12 (2022) 356. <https://doi.org/10.3390/met12020356>.
- [168] X. Zhang, R. Teng, T. Liu, Y. Shi, Z. Lv, Q. Zhou, X. Wang, Y. Wang, H. Liu, Z. Xing, Improving strength–ductility synergy in medium Mn steel by combining heterogeneous structure and TRIP effect, *Mater. Charact.* 184 (2022) 111661. <https://doi.org/10.1016/j.matchar.2021.111661>.
- [169] K. Sugimoto, H. Tanino, Influence of cooling process routes after intercritical annealing on impact toughness of duplex type medium Mn steel, *Metals*. 11 (2021) 1143. <https://doi.org/10.3390/met11071143>.
- [170] T. Furukawa, H. Huang, O. Matsumura, Effects of carbon content on mechanical properties of 5%Mn steels exhibiting transformation induced plasticity, *Mater. Sci. Technol.* 10 (1994) 964–970. <https://doi.org/10.1179/mst.1994.10.11.964>.
- [171] H.A. Derazkola, E. García Gil, A. Murillo-Marrodán, D. Méresse, Review on dynamic recrystallization of martensitic stainless steels during hot deformation: Part I—experimental study, *Metals*. 11 (2021) 572. <https://doi.org/10.3390/met11040572>.
- [172] H. Karbasian, A.E. Tekkaya, A review on hot stamping, *Mater. Process. Technol.* 210 (2010) 2103–2118. <https://doi.org/10.1016/j.jmatprotec.2010.07.019>.
- [173] J. Villalobos, A. Del-Pozo, B. Campillo, J. Mayen, S. Serna, Microalloyed steels through history until 2018: review of chemical composition, processing and hydrogen service, *Metals*. 8 (2018) 351. <https://doi.org/10.3390/met8050351>.
- [174] M. Soleimani, A. Kalhor, H. Mirzadeh, Transformation-induced plasticity (TRIP) in advanced steels: A review, *Mater. Sci. Eng. A*. 795 (2020) 140023. <https://doi.org/10.1016/j.msea.2020.140023>.
- [175] R. Petrov, L. Kestens, A. Wasilkowska, Y. Houbaert, Microstructure and texture of a lightly deformed TRIP-assisted steel characterized by means of the EBSD technique, *Mater. Sci. Eng. A*. 447 (2007) 285–297. <https://doi.org/10.1016/j.msea.2006.10.023>.
- [176] A.K. Lis, J. Lis, L. Jeziorski, Advanced ultra-low carbon bainitic steels with high toughness, *J. Mater. Process. Technol.* 64 (1997) 255–266. [https://doi.org/10.1016/S0924-0136\(96\)02575-7](https://doi.org/10.1016/S0924-0136(96)02575-7).
- [177] S. Wiewiorowska, Determination of content of retained austenite in steels with TRIP effect deformed at different strain rates, *Steel Res. Int.* 81 (2010) 262–265.

- [178] Z. Bojarski, T. Bóld, Structure and properties of carbide-free bainite, *Acta Metall.* 22 (1974) 1223–1234. [https://doi.org/10.1016/0001-6160\(74\)90136-9](https://doi.org/10.1016/0001-6160(74)90136-9).
- [179] A. Kawałek, J. Rapalska-Nowakowska, H. Dyja, B. Koczurkiewicz, Physical and numerical modelling of heat treatment the precipitation-hardening complex-phase steel (CP), *Metalurgija - Sisak Then Zagreb-*. 52 (2013) 23–26.
- [180] M. Opiela, *Kształtowanie struktury i własności mechaniczne odkuwek ze stali mikrostopowych w procesie obróbki cieplno-plastycznej*, Wydawnictwo Politechniki Śląskiej, 2015.
- [181] M. Kucharska, *Wpływ parametrów procesu ciągnięcia na ilość przemienionego austenitu szczytkowego w martenzyt oraz na własności drutów ze stali TRIP o zawartości 0,4%C*, PhD thesis, Czestochowa University of Technology, 2019.
- [182] R. Kuziak, *Modelowanie zmian struktury i przemian fazowych zachodzących w procesach obróbki cieplno-plastycznej stali*, Instytut Metalurgii Żelaza, Gliwice, 2005.
- [183] J. Han, A critical review on medium-Mn steels: Mechanical properties governed by microstructural morphology, *Steel Res. Int.* 12 (2022) 2200238. <https://doi.org/10.1002/srin.202200238>.
- [184] D.T. Han, Y.B. Xu, Y. Zou, Z.P. Hu, S.Q. Chen, Y.M. Yu, Effect of Al on the microstructure and mechanical properties of hot-rolled medium-Mn steel, *Mater. Sci. Forum.* 941 (2018) 292–298. <https://doi.org/10.4028/www.scientific.net/MSF.941.292>.
- [185] H. Bin, L. Haiwen, Y. Feng, D. Han, Recent progress in medium-Mn steels made with new designing strategies, a review, *Mater. Sci. Technol.* 44 (2017) 1457–1464.
- [186] A. Arlazarov, M. Goune, O. Bouaziz, A. Hazotte, F. Kegel, Effect of intercritical annealing time on microstructure and mechanical behavior of advanced medium Mn steels, in: *Materials Science Forum*, Trans Tech Publications, Quebec City, Canada, 2011: pp. 706–709. <https://doi.org/10.4028/www.scientific.net/MSF.706-709.2693>.
- [187] Sente Software Ltd., A collection of free downloadable papers on the development and application of JMatPro, (2005). <https://www.sentesoftware.co.uk/biblio.html> (accessed March 25, 2020).
- [188] ASTM A1033-04. Standard practice for quantitative measurement and reporting of hypoeutectoid carbon and low-alloy steel phase transformations; ASTM International: West Conshohocken, (2004). <https://www.astm.org/> (accessed July 25, 2020).
- [189] H.-S. Yang, H.K.D.H. Bhadeshia, Uncertainties in dilatometric determination of martensite start temperature, *Mater. Sci. Technol.* 23 (2007) 556–560. <https://doi.org/10.1179/174328407X176857>.
- [190] B. Pawłowski, P. Bała, R. Dziurka, Improper interpretation of dilatometric data for cooling transformation in steels, *Arch. Metall. Mater.* 59 (2014) 1159–1161. <https://doi.org/10.2478/amm-2014-0202>.

- [191] J. Zhang, D.-F. Chen, C.-Q. Zhang, W.-S. Hwang, M.-R. Han, The effects of heating/cooling rate on the phase transformations and thermal expansion coefficient of C–Mn as-cast steel at elevated temperatures, *Mater Res.* 30 (2015) 2081–2089. <https://doi.org/10.1557/jmr.2015.173>.
- [192] A. Grajcar, A. Skowronek, K. Radwański, Mechanical behavior and stability of dispersed retained austenite in thermomechanically rolled and isothermally-treated TRIP-aided multiphase steel, *Mater. Sci. Eng. A.* 830 (2021) 142300. <https://doi.org/10.1016/j.msea.2021.142300>.
- [193] C.B. Finfrock, M.M. Thrun, D. Bhattacharya, T.J. Ballard, A.J. Clarke, K.D. Clarke, Strain rate dependent ductility and strain hardening in Q&P steels, *Metall. Mater. Trans. A.* 52 (2021) 928–942. <https://doi.org/10.1007/s11661-020-06127-y>.
- [194] T. Tokarski, G. Cios, A. Kula, P. Bała, High quality transmission Kikuchi diffraction analysis of deformed alloys - Case study, *Mater. Charact.* 121 (2016) 231–236. <https://doi.org/10.1016/j.matchar.2016.10.013>.
- [195] J. Wu, P.J. Wray, C.I. Garcia, M. Hua, A.J. Deardo, Image quality analysis: a new method of characterizing microstructures, *ISIJ Int.* 45 (2005) 254–262. <https://doi.org/10.2355/isijinternational.45.254>.
- [196] M.J. Santofimia, R.H. Petrov, L. Zhao, J. Sietsma, Microstructural analysis of martensite constituents in quenching and partitioning steels, *Mater. Charact.* 92 (2014) 91–95. <https://doi.org/10.1016/j.matchar.2014.03.003>.
- [197] J.-Y. Kang, Qualities of electron backscatter diffraction patterns and image contrast from a ferritic-martensitic steel microstructure, *Mater. Charact.* 187 (2022) 111826. <https://doi.org/10.1016/j.matchar.2022.111826>.
- [198] Y. Wang, J. Hua, M. Kong, Y. Zeng, J. Liu, Z. Liu, Quantitative analysis of martensite and bainite microstructures using electron backscatter diffraction, *Microsc. Res. Tech.* 79 (2016) 814–819. <https://doi.org/10.1002/jemt.22703>.
- [199] R. Unnikrishnan, S. Northover, H. Jazaeri, P. Bouchard, Investigating plastic deformation around a reheat-crack in a 316H austenitic stainless steel weldment by misorientation mapping, *Procedia Struct. Integr.* 2 (2016) 3501–3507. <https://doi.org/10.1016/j.prostr.2016.06.436>.
- [200] D. De Knijf, A. Puype, C. Föjer, R. Petrov, The influence of ultra-fast annealing prior to quenching and partitioning on the microstructure and mechanical properties, *Mater. Sci. Eng. A.* 627 (2015) 182–190. <https://doi.org/10.1016/j.msea.2014.12.118>.
- [201] N. van Dijk, A. BUTT, L. Zhao, J. Sietsma, S. Offerman, J. Wright, S. Zwaag, Thermal stability of retained austenite in TRIP steels studied by synchrotron X-ray diffraction during cooling, *Acta Mater.* 53 (2005) 5439–5447. <https://doi.org/10.1016/j.actamat.2005.08.017>.
- [202] A. Gołaszewski, J. Szawłowski, W. Świątnicki, Multiphase steel microstructure and properties optimisation through a new heat treatment process, *Mater. Sci. Technol.* 37 (2021) 1083–1089. <https://doi.org/10.1080/02670836.2021.1986934>.

- [203] P.J. Du, D.P. Yang, M.K. Bai, X.C. Xiong, D. Wu, G.D. Wang, H.L. Yi, Austenite stabilisation by two step partitioning of manganese and carbon in a Mn-TRIP steel, *Mater. Sci. Technol.* 35 (2019) 2084–2091. <https://doi.org/10.1080/02670836.2019.1572316>.
- [204] E. De Moor, D.K. Matlock, J.G. Speer, M.J. Merwin, Austenite stabilization through manganese enrichment, *Scr. Mater.* 64 (2011) 185–188. <https://doi.org/10.1016/j.scriptamat.2010.09.040>.
- [205] A. dit Clémenta, K. Hoummadaa, J. Drilletb, V. Hébertb, P. Maugisa, Effects of cementite size and chemistry on the kinetics of austenite formation during heating of a high-formability steel, *Comput. Mater. Sci.* 182 (2020) 109786. <https://doi.org/10.1016/j.commatsci.2020.109786>.
- [206] A. Glover, J. Speer, E. De Moor, Tempering and austempering of double soaked medium manganese steels, *Front. Mater.* 1124 (2021) 622131. <https://doi.org/10.3389/fmats.2020.622131>.
- [207] L. Van Long, D. Van Hien, N.T. Thanh, N.C. Tho, V.T. Do, Impact of cold-rolling and heat treatment on mechanical properties of dual-phase treated low carbon steel, *Adv. Mater. Sci. Eng.* 2020 (2020) 1–9. <https://doi.org/10.1155/2020/1674837>.
- [208] A. Navarro-López, J. Sietsma, M.J. Santofimia, Effect of prior athermal martensite on the isothermal transformation kinetics below Ms in a low-C high-Si steel, *Metall. Mater. Trans. A.* 47 (2016) 1028–1039. <https://doi.org/10.1007/s11661-015-3285-6>.
- [209] H. Talebi, M. Jahazi, H. Melkonyan, Retained austenite decomposition and carbide precipitation during isothermal tempering of a medium-carbon low-alloy bainitic steel, *Materials.* 11 (2018) 1441. <https://doi.org/10.3390/ma11081441>.
- [210] M. Onsøien, M. M'Hamdi, A. Mo, A CCT diagram for an offshore pipeline steel of X70 type, *Welding Journal (Miami, Fla.)*. 88 (2009) 1S-6S.
- [211] F.G. Caballero, C. Capdevila, C.G.D. Andrés, Modelling of kinetics of austenite formation in steels with different initial microstructures, *ISIJ Int.* 41 (2001) 1093–1102. <https://doi.org/10.2355/isijinternational.41.1093>.
- [212] S. Kobayashi, H. Fukunishi, Reduction of thermal expansion of ferritic/martensitic heat resistant steels -alloying effects on thermal expansion of  $\alpha$ -Fe Phase-, *ISIJ Int.* 60 (2020) 2983–2989.
- [213] H. Roumen, J. Sidor, L. Kestens, eds., *Advanced high-strength steels: microstructure and texture evolution*, in: *Encyclopedia of Iron, Steel, and Their Alloys*, CRC Press, 2016. <https://doi.org/10.1081/E-EISA>.
- [214] T. Bhattacharyya, S.B. Singh, S. Das, A. Haldar, D. Bhattacharjee, Development and characterisation of C–Mn–Al–Si–Nb TRIP aided steel, *Mater. Sci. Eng. A.* 528 (2011) 2394–2400. <https://doi.org/10.1016/j.msea.2010.11.054>.
- [215] J. Reichert, M. Militzer, W. Poole, L. Collins, A new approach using EBSD to quantitatively distinguish complex transformation products along the HAZ in X80 linepipe steel, in:

- Proceedings of the Biennial International Pipeline Conference, IPC, 2014. <https://doi.org/10.1115/IPC2014-33668>.
- [216] N.P. Gurao, S. Suwas, Generalized scaling of misorientation angle distributions at meso-scale in deformed materials, *Sci Rep.* 4 (2014) 5641. <https://doi.org/10.1038/srep05641>.
- [217] A. Kaijalainen, M. Liimatainen, V. Kesti, J. Heikkala, T. Liimatainen, D. Porter, Influence of composition and hot rolling on the subsurface microstructure and bendability of ultrahigh-strength strip, *Metall. Mater. Trans. A.* 47 (2016) 4175–4188. <https://doi.org/10.1007/s11661-016-3574-8>.
- [218] S. Zajac, V. Schwinn, K.-H. Tacke, Characterisation and quantification of complex bainitic microstructures in high and ultra-high strength linepipe steels, *Mater. Sci. Forum.* 500–501 (2005) 387–394. <https://doi.org/10.4028/www.scientific.net/MSF.500-501.387>.
- [219] D.M. Field, D.C. Van Aken, Dynamic strain aging phenomena and tensile response of medium-Mn TRIP steel, *Metall. Mater. Trans. A.* 49 (2018) 1152–1166. <https://doi.org/10.1007/s11661-018-4481-y>.
- [220] Z. Xiong, A. Kostryzhev, N.E. Stanford, E. Pereloma, Microstructures and mechanical properties of dual phase steel produced by laboratory simulated strip casting, *Mater. Des.* 88 (2015) 537–549. <https://doi.org/10.1016/j.matdes.2015.09.031>.
- [221] J.-K. Hwang, The microstructure dependence of drawability in ferritic, pearlitic, and TWIP steels during wire drawing, *Mater. Sci.* 54 (2019) 8743–8759. <https://doi.org/10.1007/s10853-019-03499-4>.
- [222] A. Gramlich, W. Bleck, Tempering and intercritical annealing of air-hardening 4 wt% medium manganese steels, *Steel Res. Int.* 92 (2021) 2100180. <https://doi.org/10.1002/srin.202100180>.
- [223] D.-W. Suh, S.-J. Kim, Medium Mn transformation-induced plasticity steels: Recent progress and challenges, *Scr. Mater.* 126 (2017) 63–67. <https://doi.org/10.1016/j.scriptamat.2016.07.013>.
- [224] D. Barbier, N. Gey, S. Allain, N. Bozzolo, M. Humbert, Analysis of the tensile behavior of a TWIP steel based on the texture and microstructure evolutions, *Mater. Sci. Eng. A.* 500 (2009) 196–206. <https://doi.org/10.1016/j.msea.2008.09.031>.
- [225] J. Hidalgo, C. Celada-Casero, M.J. Santofimia, Fracture mechanisms and microstructure in a medium Mn quenching and partitioning steel exhibiting macrosegregation, *Mater. Sci. Eng. A.* 754 (2019) 766–777. <https://doi.org/10.1016/j.msea.2019.03.055>.
- [226] Q. Guo, H.-W. Yen, H. Luo, S.P. Ringer, On the mechanism of Mn partitioning during intercritical annealing in medium Mn steels, *Acta Mater.* 225 (2022) 117601. <https://doi.org/10.1016/j.actamat.2021.117601>.
- [227] S.-J. Lee, S. Lee, B.C. De Cooman, Mn partitioning during the intercritical annealing of ultrafine-grained 6% Mn transformation-induced plasticity steel, *Scr. Mater.* 64 (2011) 649–652. <https://doi.org/10.1016/j.scriptamat.2010.12.012>.

- [228] L. Král, B. Million, J. Čermák, Diffusion of carbon and manganese in Fe-C-Mn, *Defect Diffus. Forum.* 263 (2007) 153–158. <https://doi.org/10.4028/www.scientific.net/DDF.263.153>.
- [229] K. Muszka, D. Zych, P. Lisiecka - Graca, Ł. Madej, J. Majta, Experimental and molecular dynamic study of grain refinement and dislocation substructure evolution in HSLA and IF steels after severe plastic deformation, *Metals.* 10 (2020) 1122. <https://doi.org/10.3390/met10091122>.
- [230] T. Tsuchiyama, T. Inoue, J. Tobata, D. Akama, S. Takaki, Microstructure and mechanical properties of a medium manganese steel treated with interrupted quenching and intercritical annealing, *Scr. Mater.* 122 (2016) 36–39. <https://doi.org/10.1016/j.scriptamat.2016.05.019>.
- [231] A. Skowronek, A. Grajcar, C. Garcia-Mateo, J. Jimenez, R. Petrov, Time-dependent evolution of volume fraction and stability of retained austenite in a hot-rolled and intercritically annealed Al-alloyed medium-Mn steel, *Metall. Mater. Trans. A.* (2023). <https://doi.org/10.1007/s11661-023-06998-x>.
- [232] Y. Zou, Y.B. Xu, D.T. Han, Z.P. Hu, R.D.K. Misra, L.F. Cao, H. Song, Combined contribution of Cu-rich precipitates and retained austenite on mechanical properties of a novel low-carbon medium-Mn steel plate, *Mater. Sci.* 54 (2019) 3438–3454. <https://doi.org/10.1007/s10853-018-3021-x>.
- [233] J. Liang, Z. Zhao, D. Tang, N. Ye, S. Yang, W. Liu, Improved microstructural homogeneity and mechanical property of medium manganese steel with Mn segregation banding by alternating lath matrix, *Mater. Sci. Eng. A.* 711 (2018) 175–181. <https://doi.org/10.1016/j.msea.2017.11.046>.

## **Abstract**

### **Improvement of the ductility of high-strength medium-Mn steels through intercritical annealing**

The aim of this work was to explain structural phenomena occurring during the intercritical annealing of medium-Mn steel depending on the applied temperature-time parameters and optimization of these parameters resulting in improved steel plasticity. The hot-rolled martensitic alloy containing 0.16C-4.7Mn-1.6Al-0.2Si-0.2Mo was subjected to the tests. The literature part of the work is a review of high-strength steels and a summary of previous research in the field of intercritical annealing of medium manganese steels. Factors influencing the amount and stability of retained austenite were determined. The temperature and time parameters of the process used so far and their impact on mechanical properties of the alloy were analyzed.

In order to prove the thesis of the dissertation, tests of mechanical properties and detailed structural tests of steel were performed. The thermodynamic simulations and experimental tests with the use of scanning and transmission electron microscopy, X-ray tests and EBSD tests allowed to quantify the structural features of steel after various variants of heat treatment. They were of fundamental importance for the implementation of the objective of the work.

The evolution of phase composition and stability of retained austenite was studied as a function of annealing temperature in the range from 640 °C to 1000 °C for 60 min and as a function of soaking time in the range from 1 min to 300 min at 680 °C. The quantitative assessment of the fraction of retained austenite, its chemical composition and its grain size were essential for the implementation of the objective of the work. This made it possible to correlate individual characteristics with the obtained mechanical properties of steel after various treatment variants. It was found that the amount of austenite increases with increasing annealing temperature and soaking time. However, this is associated with a decrease in its stability due to the decreasing enrichment in C and Mn and the increasing grain size. This causes that the retained austenite fraction obtained after cooling initially increases with increasing the annealing temperature and soaking time, and after reaching the limit stability it begins to decrease rapidly. The high stability of the retained austenite inhibits the strain-induced martensitic transformation. On the other hand, its low stability induces the massive martensitic transformation at low strain levels. Both extreme variants result in lowering the steel plasticity. To obtain the maximum elongation of the sample, it is necessary to obtain a compromise between a high proportion of retained austenite and its adequate overall stability controlled by a wide grain size distribution enabling the gradual SIMT within the entire deformation range.

## **Streszczenie**

### **Poprawa plastyczności wysokowytrzymałych stali średniomanganowych przez wyżarzanie międzykrytyczne**

Celem pracy było wyjaśnienie zjawisk strukturalnych zachodzących podczas wyżarzania międzykrytycznego walcowanej na gorąco stali średniomanganowej z dodatkiem Al w zależności od zastosowanych parametrów temperaturowo-czasowych obróbki cieplnej oraz optymalizacja tych parametrów, skutkująca poprawą plastyczności stali. Badaniom poddano stop zawierający 0,16C-4,7Mn-1,6Al-0,2Si-0,2Mo w stanie walcowanym na gorąco, charakteryzujący się mikrostrukturą martenzytyczną. Część literaturowa pracy stanowi przegląd stali wysokowytrzymałych oraz podsumowanie dotychczasowych badań w zakresie wyżarzania międzykrytycznego stali średniomanganowych. Określono czynniki wpływające na udział i stabilność austenitu szczątkowego. Przeanalizowano parametry temperaturowe i czasowe stosowanego dotychczas procesu oraz ich wpływ na właściwości mechaniczne stopu.

W celu udowodnienia tezy rozprawy wykonano badania właściwości mechanicznych oraz szczegółowe badania mikrostrukturalne stali. Podstawowe znaczenie dla realizacji celu pracy miały symulacje termodynamiczne oraz badania eksperymentalne z wykorzystaniem dylatometrii, skaningowej i transmisyjnej mikroskopii elektronowej, badania rentgenowskie oraz analizy EBSD, które pozwoliły na ilościowe określenie cech strukturalnych stali po różnych wariantach obróbki cieplnej.

Zbadano ewolucję składu fazowego i stabilność austenitu szczątkowego w funkcji temperatury wyżarzania w zakresie od 640°C do 1000°C przez 60 min oraz w funkcji czasu wygrzewania w zakresie od 1 min do 300 min w 680°C. Ilościowa ocena frakcji austenitu szczątkowego, jego składu chemicznego oraz wielkości ziarna były niezbędne do realizacji celu pracy. Umożliwiło to skorelowanie poszczególnych charakterystyk z uzyskanymi właściwościami mechanicznymi stali po różnych wariantach obróbki. Stwierdzono, że ilość austenitu rośnie wraz ze wzrostem temperatury wyżarzania i czasu wygrzewania. Wiąże się to jednak ze spadkiem jego stabilności w związku ze zmniejszającym się wzbogaceniem w C i Mn oraz rosnącą wielkością ziarna. Powoduje to, że frakcja austenitu szczątkowego rośnie do osiągnięcia stabilności granicznej, a następnie zaczyna gwałtownie spadać. Wysoka stabilność austenitu szczątkowego hamuje przemianę martenzytyczną wywołaną odkształceniem. Z drugiej strony, jego niska stabilność powoduje masową przemianę martenzytyczną przy niskich wartościach odkształcenia. Oba skrajne warianty skutkują obniżeniem plastyczności stali. W celu uzyskania maksymalnego wydłużenia próbki konieczne jest uzyskanie kompromisu pomiędzy dużym udziałem austenitu szczątkowego, a odpowiednią stabilnością kontrolowaną przez szeroki zakres wielkości ziarna, umożliwiającą stopniową przemianę martenzytyczną w całym zakresie odkształcenia.

## **Streszczenie poszerzone**

### **Poprawa plastyczności wysokowytrzymałych stali średniomanganowych przez wyżarzanie międzykrytyczne**

#### **1. Wstęp**

Przemysł motoryzacyjny jest dynamicznie rozwijającym się sektorem światowej gospodarki. Intensywna konkurencja i wprowadzenie nowych materiałów o niskiej gęstości, takich jak stopy aluminium, magnezu, materiały polimerowe oraz kompozytowe, stawiało nowe wyzwania dla producentów stali w ciągu ostatnich dwóch dekad. Ponowne skupienie uwagi na roli poszczególnych pierwiastków stopowych powszechnie stosowanych w stalach oraz rozwój nowoczesnych technologii metalurgicznych, obróbki plastycznej i opracowanie zaawansowanych metod obróbki cieplnej doprowadziło do powstania różnego rodzaju nowych stali o szerokim zakresie właściwości mechanicznych i odkształcalności.

Ograniczeniem stali konwencjonalnych jest tendencja do zmniejszania się plastyczności wraz ze wzrostem ich wytrzymałości. Od początku lat 90-tych XX w. przemysł motoryzacyjny poszukiwał stali, które połączą w sobie wysokie własności wytrzymałościowe i plastyczne. Przełomowym krokiem w rozwoju stali było wprowadzenie metastabilnego austenitu szczątkowego do mikrostruktury. Dzięki jego indukowanej odkształceniem przemianie martenzytycznej (SIMT) możliwe było uzyskanie niespotykanego dotąd umocnienia odkształceniowego wyrobów stalowych. Pozwoliło to skutecznie opóźnić formowanie się szyjki podczas rozciągania, a tym samym zwiększyć ciągliwość stali, przy jednoczesnym zachowaniu wysokiej wytrzymałości lub nawet jej podwyższeniu. Otworzyło to drogę do produkcji materiałów o niespotykanych dotąd właściwościach mechanicznych. Nowe podejście do projektowania składu chemicznego i obróbki cieplnej zaowocowało szybkim rozwojem nowoczesnych, wysokowytrzymałych stali dla motoryzacji (AHSS).

Nowe rodzaje stali, takie jak stale średniomanganowe, oraz nowoczesna obróbka cieplna, taka jak wyżarzanie międzykrytyczne, są obecnie intensywnie rozwijane. Utworzenie struktury wielofazowej o odpowiednich proporcjach, rozmieszczeniu, morfologii i stabilności wymaga zarówno precyzyjnego projektowania składu chemicznego, jak i właściwej kontroli parametrów obróbki cieplnej, takich jak szybkość nagrzewania i chłodzenia, temperatura oraz czas. Wysiłek ten jest jednak umotywowany możliwością produkcji nowych gatunków stali o

podwyższonych własnościach plastycznych oraz wytrzymałościowych przy kosztach produkcji zbliżonych w stosunku do obecnie stosowanych materiałów konstrukcyjnych w motoryzacji.

Jedną z metod wytwarzania stali średniomanganowych jest obróbka termomechaniczna zaadaptowana ze stali bainitycznych z efektem TRIP. Po zakończeniu obróbki na gorąco stal chłodzi się do temperatury przemiany bainitycznej. W tej temperaturze następuje wytrzymanie izotermiczne, w którego trakcie tworzy się osnowa bainityczna, a nieprzemieniony austenit ulega stabilizacji poprzez wzbogacenie w węgiel.

Pomimo wysokich wskaźników ekonomicznych i relatywnie prostego procesu produkcyjnego stale średniomanganowe wytwarzane metodą obróbki termomechanicznej wykazują ograniczoną przydatność przemysłową. Wydzielenia węglików oraz bimodalna morfologia drobno- i gruboziarnistego austenitu w tak wytworzonych stalach wpływają na ich podatność na pękanie oraz ograniczoną plastyczność. Stale średniomanganowe na osnowie bainitu wykazują zazwyczaj bardzo wysoką wytrzymałość, ale zwykle odbywa się to kosztem ograniczonej odkształcalności blach. Zahamowana redystrybucja Mn podczas niskotemperaturowego wytrzymania izotermicznego zmniejsza potencjał składu chemicznego tych stali.

Analiza literaturowa dotycząca zaawansowanych stali wielofazowych o wysokiej wytrzymałości pozwoliła stwierdzić, że ich plastyczność jest ściśle związana z frakcją i stabilnością austenitu szczątkowego w mikrostrukturze. Obecnie obróbką cieplną zapewniającą najwyższy stosunek fazowy austenitu szczątkowego do osnowy (faza  $\alpha$ ) jest wyżarzanie międzykrytyczne. Dotychczasowe badania dowodzą skuteczności tego podejścia w kontekście uzyskiwania wysokiej plastyczności i odkształcalności stali średniomanganowych.

## **2. Materiał do badań**

Obiektem badań była gorącowalcowana stal średniomanganowa o grubości 4,5 mm i składzie chemicznym przedstawionym w Tabeli 1. Zawartość poszczególnych pierwiastków stopowych dobrano tak, aby zapewnić wysokie właściwości mechaniczne, technologiczne i wskaźniki ekonomiczne. Stale średniomanganowe zawierają zwykle od 3 do 12 % Mn. Badana stal zawiera 4,7 % tego pierwiastka, aby umożliwić stabilizację austenitu i jednocześnie ograniczyć koszt materiału. Stosunkowo niską zawartość węgla dobrano tak, aby ograniczyć jego szkodliwy wpływ na spawalność stali. Wprowadzono również dodatki krzemu i aluminium, aby zapobiec wydzieleniu się węglików. Ze względu na dużą hartowność,

wyjściowa mikrostruktura stali po walcowaniu na gorąco składała się z martenzytu ze śladowymi ilościami austenitu szczątkowego.

Pierwszym podejściem do obróbki tej stali była obróbka termomechaniczna. W efekcie otrzymana została mikrostruktura złożona z ferrytu bainitycznego, martenzytu i austenitu szczątkowego (~9 %). Taka mikrostruktura zaowocowała bardzo wysoką wytrzymałością materiału ( $R_{p0,2}$  ~950 MPa i  $R_m$  ~1400 MPa), jednak jego wydłużenie całkowite było ograniczone do 8,5 %. Z tego względu konieczne było zastosowanie innego podejścia do obróbki cieplnej materiału w celu poprawy jego plastyczności. Bazując na przeglądzie literatury wybrano wyżarzanie międzykrytyczne.

*Tabela 1 Skład chemiczny badanej stali.*

Pierwiastek, % wag.							
C	Mn	Al	Si	Mo	S	P	Fe
0.16	4.7	1.6	0.20	0.20	0.005	0.008	93.12

### **3. Cel i zakres pracy**

Pomimo trwających badań nad wyżarzaniem międzykrytycznym stali średniomanganowych, złożona natura metastabilnego austenitu stanowi nadal przeszkodę na drodze do optymalizacji ich własności mechanicznych. Frakcja i stabilność austenitu szczątkowego, które w głównej mierze wpływają na plastyczność stali, są kontrolowane przez wiele czynników, począwszy od składu chemicznego austenitu, a kończąc na jego orientacji krystalograficznej. Czynniki te z kolei są zależne od parametrów obróbki plastycznej oraz cieplnej. Zidentyfikowano następujące luki badawcze w zakresie wyżarzania międzykrytycznego stali średniomanganowych:

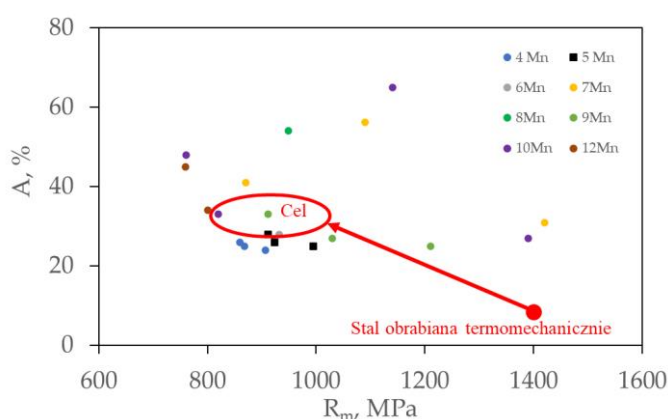
- Badania stali średniomanganowych koncentrują się głównie na stalach walcowanych na zimno, podczas gdy stale walcowane na gorąco charakteryzuje inna wyjściowa morfologia i stopień umocnienia. Stale średniomanganowe walcowane na gorąco wymagają dokładnych, systematycznych badań, ponieważ mogą znaleźć zastosowanie w szerokim obszarze transportu pasażerskiego oraz towarowego, jak również innych gałęziach przemysłu wykorzystującego grubsze blachy.
- Początkowo stale średniomanganowe zawierały głównie Si, co pogarszało ich podatność na cynkowanie. Z tego powodu Si należy zastąpić przez Al. Należy opisać wpływ Al na temperatury krytyczne i kinetykę przemian fazowych.

- Wpływ C i Mn na stabilizację austenitu szczątkowego został już szczegółowo zbadany. Wyjaśnić należy jednak wpływ wielkości ziarna i jego dystrybucji w mikrostrukturze na stabilność mechaniczną austenitu szczątkowego i wynikające z niej właściwości mechaniczne stopu.
- Obecne stale średniomanganowe są często produkowane w procesach wielogodzinnych w relatywnie niskich temperaturach. Należy zweryfikować możliwość skrócenia wyżarzania międzykrytycznego poprzez podwyższenie temperatury wyżarzania.

Biorąc pod uwagę powyższe aspekty, **celem pracy jest wyjaśnienie zjawisk strukturalnych zachodzących podczas wyżarzania międzykrytycznego walcowanej na gorąco stali średniomanganowej z dodatkiem Al w zależności od zastosowanych parametrów temperaturowo-czasowych obróbki cieplnej oraz optymalizacja tych parametrów, skutkująca poprawą plastyczności stali.**

Przeprowadzone studia literaturowe oraz współzależność mikrostruktury oraz przebiegu odkształcenia na zimno uzasadniają przyjęcie następującej tezy badawczej:

**Właściwe dobranie udziału i stabilności austenitu szczątkowego poprzez optymalizację temperatury i czasu wyżarzania międzykrytycznego pozwala na uzyskanie stopniowej, indukowanej odkształceniem przemiany martenzytycznej kontrolowanej wielkością ziarna, a tym samym poprawę plastyczności stali, szczególnie w porównaniu ze stałą obrabianą termomechanicznie.**



Rysunek 1 Cel badań w odniesieniu do obecnie badanych stali średniomanganowych wyżarzanych międzykrytycznie oraz stali obrabianej termomechanicznie.

Celem badań jest uzyskanie stali wielofazowej o końcowej mikrostrukturze zawierającej ponad 30 % austenitu szczątkowego i osnowę ferrytyczną. Minimalny poziom docelowych

właściwości mechanicznych to:  $A_r = 15\%$ ,  $A = 25\%$  i  $R_m = 900$  MPa (Rysunek 1). Taki poziom właściwości wyrażony jako  $R_m \times A > 23$  GPa% wykazują dotychczas stale średniomanganowe z większą zawartością manganu; dlatego wskazana poprawa właściwości mechanicznych badanej stali 5Mn-1,6Al jest wyzwaniem badawczym.

#### **4. Metodologia**

Aby osiągnąć cel i udowodnić tezę rozprawy przeprowadzono szereg badań. Pierwszym krokiem były symulacje termodynamiczne, których celem było wyznaczenie ewolucji mikrostrukturalnej wraz ze wzrostem temperatury i wpływ tej temperatury na skład chemiczny poszczególnych faz. Wyznaczono również temperatury krytyczne stali, tj.  $A_{c1}$ ,  $A_{c3}$ ,  $M_s$ . Scharakteryzowano również wpływ szybkości chłodzenia na przemiany fazowe. Następnie wykorzystano dylatometrię do weryfikacji wyników symulacji. Ten krok pozwolił na dobranie początkowych parametrów procesu wyżarzania międzykrytycznego, takich jak szybkość nagrzewania i chłodzenia oraz zakres obszaru międzykrytycznego.

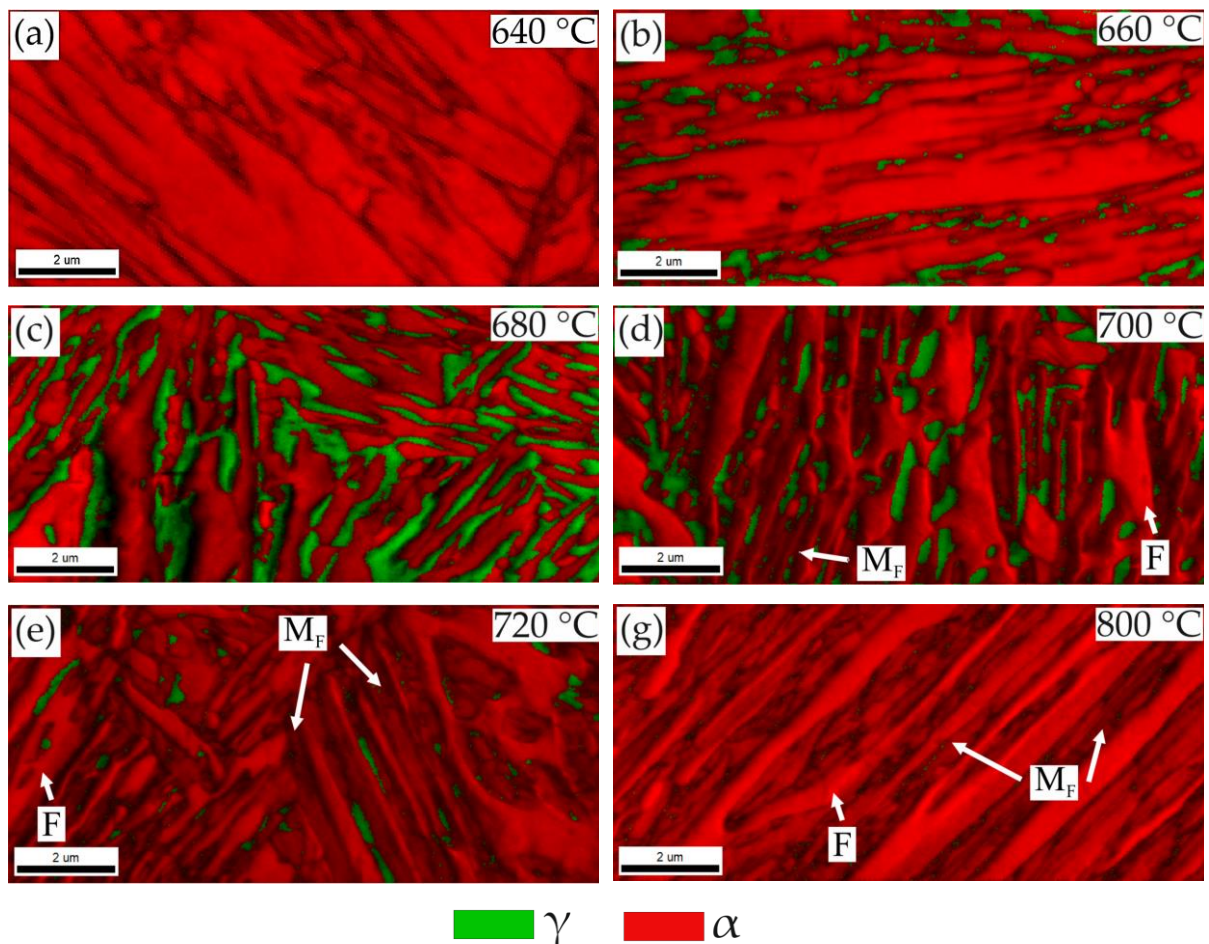
Drugi etap pracy polegał na badaniach wpływu temperatury wyżarzania na mikrostrukturę oraz własności mechaniczne stali. Przy wyborze wariantów obróbki cieplnej wzięto pod uwagę szeroki zakres temperatur, obejmujący cały obszar międzykrytyczny ( $640\text{ }^\circ\text{C} - 1000\text{ }^\circ\text{C}$  przez 1 h). Symulacje obróbki cieplnej przeprowadzono za pomocą dylatometrii, dostosowując parametry wyjściowe określone w pierwszym etapie badań. Próbki poddane obróbce cieplnej poddano serii badań jakościowych i ilościowych w celu określenia zmian składu fazowego, wielkości i morfologii ziaren (SEM, EBSD) wraz ze wzrostem temperatury. Określono również udział i skład chemiczny austenitu szczątkowego (od których zależy jego stabilność). Następnie przeprowadzono badania twardości i statyczną próbę rozciągania, aby zbadać właściwości mechaniczne stali po różnych wariantach obróbki cieplnej i skorelować je z cechami mikrostrukturalnymi. Krok ten pozwolił na dobranie optymalnej temperatury po obróbce, w której stal charakteryzuje się najwyższą plastycznością oraz korzystną frakcją i stabilnością austenitu szczątkowego.

Ostatnim etapem badań było określenie wpływu czasu wyżarzania na mikrostrukturę i właściwości mechaniczne stali. Do scharakteryzowania procesu zastosowano szeroki zakres czasu wyżarzania od 1 min do 300 min w temperaturze wybranej w drugim etapie badań ( $680\text{ }^\circ\text{C}$ ). Ten krok obejmował metodologię opisaną w poprzednim akapicie. Jednak większy nacisk położono na charakterystykę ogólnej stabilności mechanicznej austenitu szczątkowego i jej zakresu. W tym celu zastosowano obliczenia termodynamiczne oraz przerywaną statyczną

próbę rozciągania. Zdeformowaną mikrostrukturę zbadano również pod kątem składu fazowego, frakcji austenitu szczątkowego oraz zmian twardości. Umożliwiło to precyzyjne określenie wpływu poszczególnych faz na właściwości mechaniczne stali oraz wyjaśnienie procesów zachodzących podczas odkształcania.

## 5. Wyniki badań

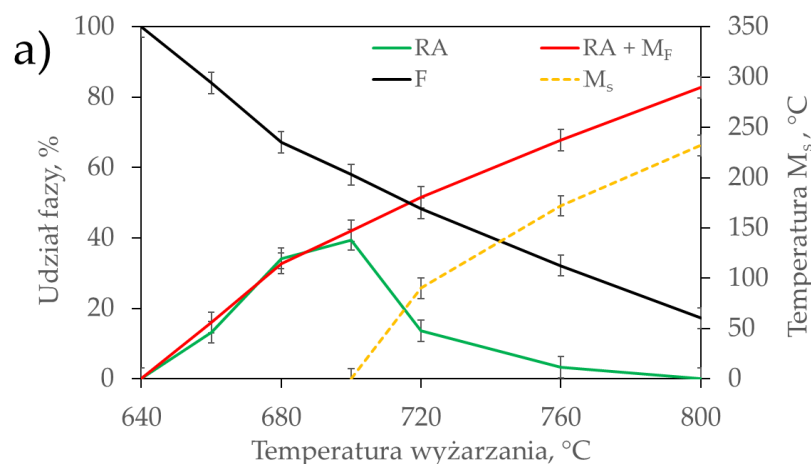
Rysunek 2 przedstawia mapy EBSD mikrostruktur otrzymanych podczas wyżarzania stali w różnych temperaturach. Wraz ze wzrostem temperatury wyżarzania pierwotna mikrostruktura martenzytyczna ulega odpuszczeniu. Wraz z przekroczeniem temperatury  $A_{c1}$  w końcowej strukturze zaczyna pojawiać się listwowy austenit szczątkowy, osiągając największy udział (powyżej 35 %) dla próbek wyżarzanych w 680 oraz 700 °C. Po obróbce w 700 °C stabilność austenitu jest jednak bardzo niska, co powoduje jego częściową przemianę nawet podczas preparatyki próbek, co widoczne jest poprzez obszary o niższej wartości IQ.



Rysunek 2 Mapy EBSD IQ+P dla próbek wyżarzanych w różnych temperaturach;  $M_F$  – martenzyt,  $F$  – ferryt.

Wraz z dalszym wzrostem temperatury wyżarzania udział austenitu szczątkowego szybko maleje ze względu na spadającą stabilność, a co za tym idzie, jego przemianę podczas chłodzenia stali. Jest to wynikiem coraz mniejszego wzbogacenia austenitu w pierwiastki stopowe takie jak C oraz Mn oraz rozrostu jego ziarna.

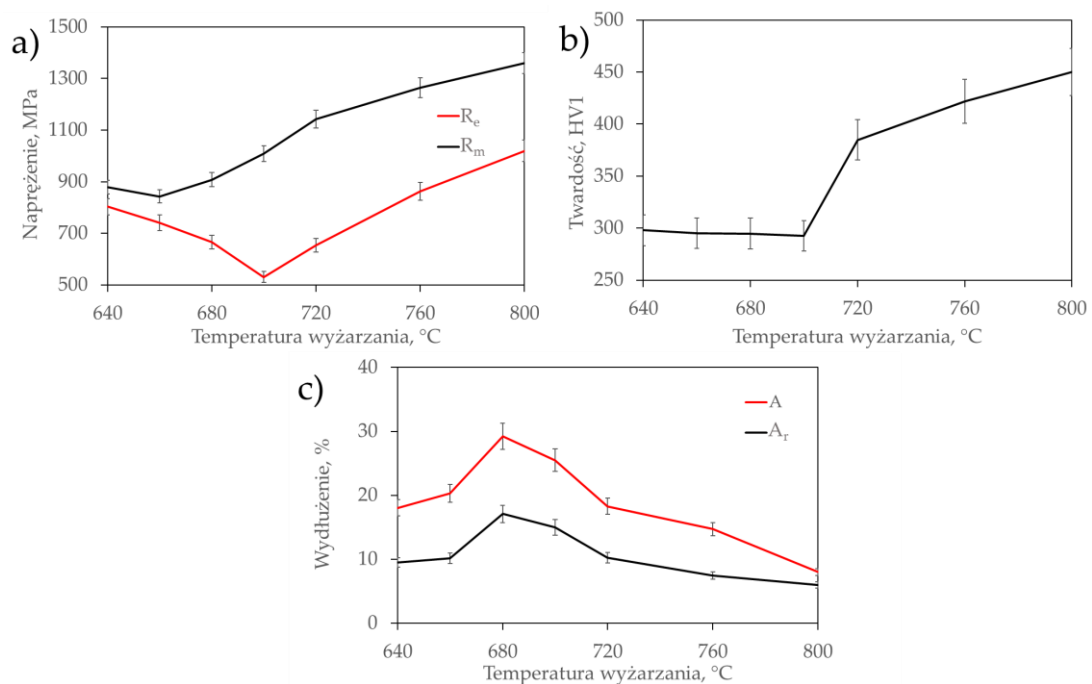
Ewolucja mikrostruktury towarzysząca podwyższaniu temperatury wyżarzania międzykrytycznego ma znaczący wpływ na właściwości mechaniczne badanej stali. Analiza i porównanie ewolucji mikrostruktury (Rysunek 3) oraz wynikających z niej właściwości mechanicznych (Rysunek 4) pozwalają przypisać rolę każdej fazie. Wartości  $R_e$  i twardości są bezpośrednio związane z początkową mikrostrukturą stali. Obydwa parametry zmniejszają swoją wartość wraz ze wzrostem temperatury wyżarzania, a co za tym idzie, postępowaniem odpuszczania martenzytu i tworzeniem się austenitu, do odpowiednio 531 MPa oraz 290 HV1 po wyżarzaniu w 700 °C. Następnie, zarówno  $R_e$  jak i twardość rosną, ponieważ zwiększa się udział twardego i wysokowytrzymałego martenzytu w strukturze. Wartość  $R_m$  rośnie w sposób ciągły wraz ze wzrostem temperatury wyżarzania (od 880 MPa po obróbce w 640 °C do 1360 MPa po obróbce w 800 °C), niezależnie od stosunku austenitu szczątkowego oraz martenzytu.  $R_m$  jest zależne głównie od końcowej frakcji „świeżego” martenzytu w zakresie wydłużenia jednorodnego.



Rysunek 3 Zmiany składu fazowego i temperatury  $M_s$  w zależności od temperatury wyżarzania międzykrytycznego; RA – austenit szczątkowy, F – ferryt,  $M_F$  – martenzyt,  $M_s$  – temperatura rozpoczęcia przemiany martenzytycznej.

Odmianą tendencję obserwuje się w przypadku właściwości plastycznych badanej stali. Wydłużenie rośnie wraz ze wzrostem frakcji austenitu szczątkowego (do 31 % dla próbek wyżarzanej w 680 °C), ale jego wartość znacznie spada, gdy w mikrostrukturze obecny jest

martenzyt. Co ważne, plastyczność jest już ograniczona w próbce wyżarzanej w 700 °C, zawierającej początkowo najwyższą frakcję austenitu szczątkowego spośród wszystkich wariantów temperaturowych. Powodem tego jest niska stabilność austenitu szczątkowego. Próbka wyżarzana w 680 °C (zawierająca o ponad 5% mniej austenitu szczątkowego niż próbka wyżarzana w 700 °C) osiąga ponad 30 % wydłużenia dzięki stopniowemu efektowi SIMT. Z drugiej strony stabilność termiczna austenitu szczątkowego dla próbki wyżarzanej w 700 °C jest bardzo niska. Występuje w niej intensywna przemiana martenzytyczna przy niskim poziomie odkształcenia, co odbywa się kosztem ograniczonej plastyczności ( $A = 25,5 \%$ ).

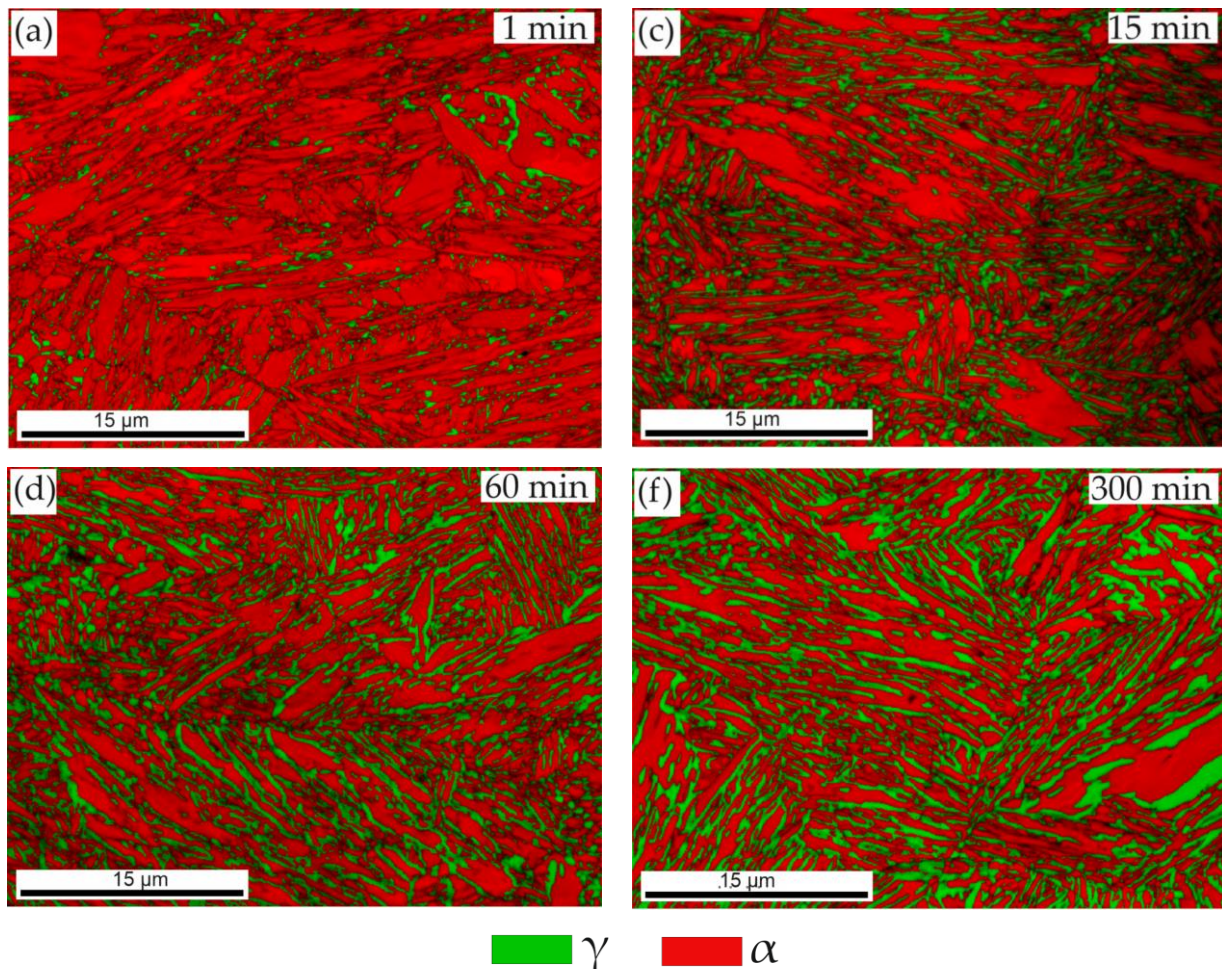


Rysunek 4 Zestawienie właściwości mechanicznych analizowanej stali wraz ze wzrostem temperatury wyżarzania: (a) właściwości wytrzymałościowe, (b) twardość, (c) plastyczność.

W przypadku próbek wyżarzanych przez różny czas w 680 °C udział austenitu w ich mikrostrukturze stale rośnie (Rysunek 5). Ziarna tej fazy rosą wzdłuż granic pierwotnych listew martenzytycznych, otaczając stopniowo martenzyt odpuszczony. Udział austenitu szczątkowego w próbce wyżarzanej przez 1 min wynosi 16 %, a dla próbki wyżarzanej przez 300 min osiąga ponad 40 %. Zwiększający się udział austenitu szczątkowego skutkuje szybkim obniżeniem stabilności tej fazy (Rysunek 6) ze względu na rosnącą wielkość ziarna oraz ograniczone stężenia C oraz Mn w roztworze stałym.

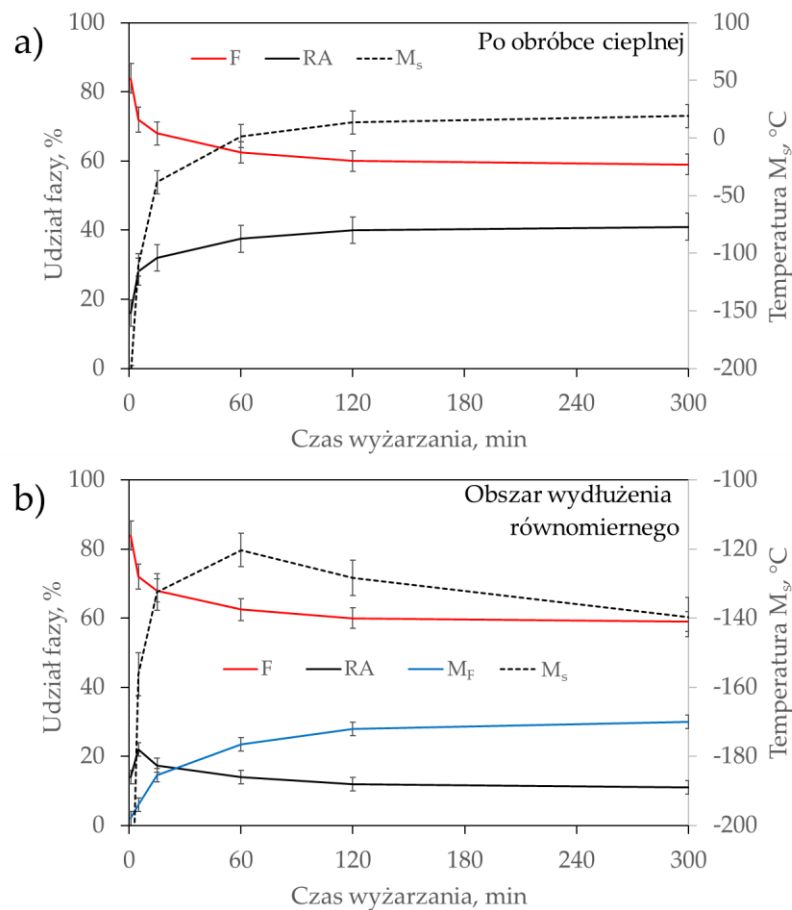
Mikrostruktura uzyskana po różnych czasach wygrzewania ma wyraźne odzwierciedlenie w granicy plastyczności i twardości (Rysunek 7). Pierwotny martenzyt ulega odpuszczaniu

podczas nagrzewania oraz wyżarzania, w związku z tym maleje twardość (z 317 HV1 po 1 min do 280 HV1 po 300 min) oraz  $R_e$  (z 860 MPa po 1 min do 590 MPa po 300 min) badanego stopu. Powstawanie dużej frakcji austenitu szczątkowego również wpływa na spadek twardości. Wartości  $R_m$ , pomimo stale rosnącego udziału austenitu szczątkowego, nieznacznie spadają (z 940 MPa po 1 min do 890 MPa po 300 min). W próbkach wygrzewanych w różnych temperaturach osnowę tworzy miękki ferryt powstały w wyniku 60 min wyżarzania. Faza ta nie przyczynia się znacząco do ogólnego umocnienia stopu. W badaniach dotyczących czasu wyżarzania osnowa próbek wyżarzanych krócej niż 60 min składa się z odpuszczonego martenzytu, co skutkuje wyższymi wartościami  $R_m$ . Wraz z postępem wyżarzania odpuszczany martenzyt staje się stopniowo ferrytem, zmniejszając wytrzymałość stopu. Dlatego pomimo rosnącego udziału austenitu szczątkowego, który następnie podczas odkształcenia przemienia się w martenzyt, wartość  $R_m$  stopu spada.



Rysunek 5 Mapy EBSD IQ+P dla próbek wyżarzanych przez różny czas w 680 °C.

Plastyczność stopu zależy ponownie głównie od stabilności austenitu szczytkowego, a w drugiej kolejności od jego udziału. Jeśli stabilność jest zbyt wysoka, jak w próbkach wyżarzanych przez 1 min oraz 5 min, efekt SIMT nie jest wyzwalany i wydłużenie jest niskie (~18 %). W przypadku próbek o bardzo niskiej stabilności austenitu szczytkowego (wyżarzanych przez 120 min oraz 300 min) masywny efekt SIMT występuje na wczesnym etapie odkształcenia, a wysokie umocnienie odkształceniowe i wynikająca z tego wysoka wytrzymałość stali ponownie ograniczają wydłużenie do ok. 26 %. Dopiero kompromis pomiędzy frakcją a stabilnością austenitu szczytkowego zapewnia optymalne właściwości mechaniczne i plastyczne, jak w próbce wyżarzanej przez 60 min, gdzie wydłużenie wynosi 31 %.

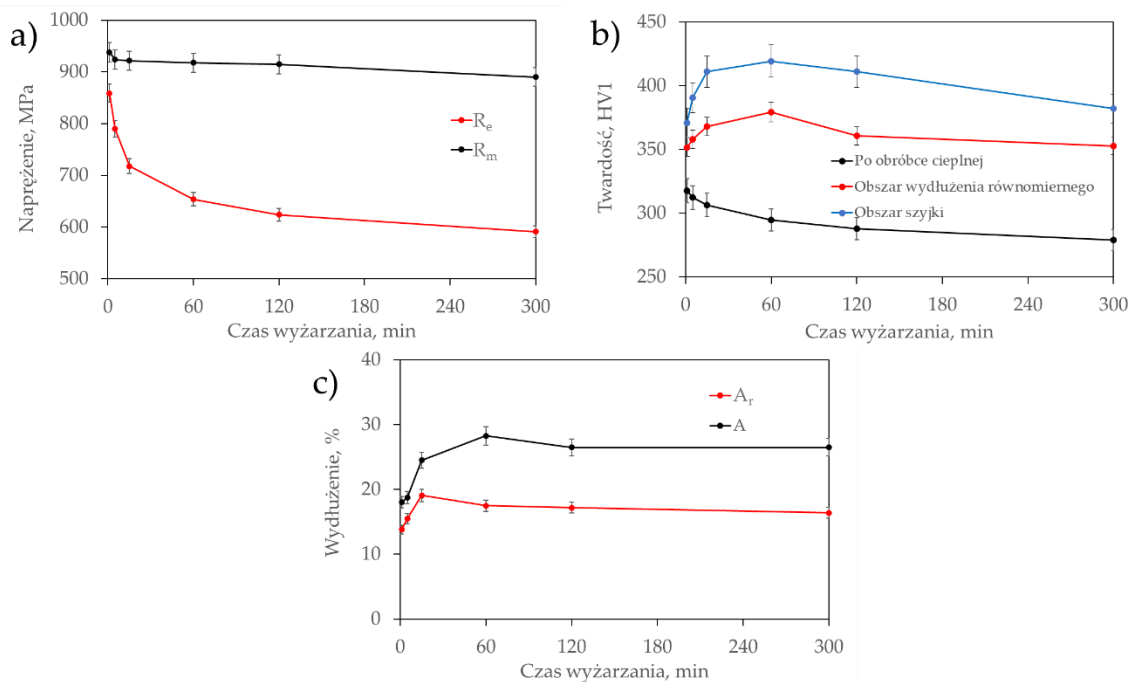


Rysunek 6 Zestawione zmiany składu fazowego i temperatury  $M_s$  austenitu wraz z postępem wygrzewania na różnych etapach: (a) po wyżarzeniu międzykrytycznym, (b) w obszarze wydłużenia równomiernego.

Ogólnie rzecz biorąc, drobne ziarna austenitu otrzymane podczas wyżarzania międzykrytycznego znacznie zwiększają stabilność tej fazy. Jeśli jednak średnia objętość ziarna jest mniejsza niż  $1 \mu\text{m}^3$ , jego wpływ jest porównywalny lub nawet wyższy niż efekt stabilizacji

chemicznej. Rysunek 8 pokazuje zakresy temperatury  $M_s$  dla wielkości ziarna austenitu występujących w różnych próbkach. Taka reprezentacja pokazuje zarówno średni poziom i zakres stabilności austenitu dla każdej próbki, co ma bezpośrednie odzwierciedlenie we własnościach mechanicznych.

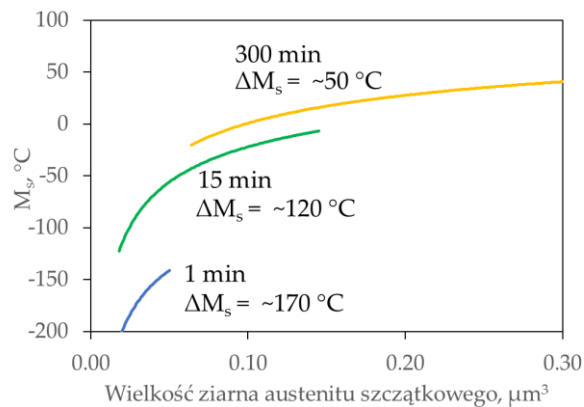
Ogólna stabilność próbki wyżarzanej przez 1 min jest niezwykle wysoka (niska temperatura  $M_s$ ), niezależnie od wielkości ziarna austenitu szczątkowego obecnego w strukturze. Dlatego efekt SIMT jest aktywowany w bardzo niewielkim stopniu. Skutkuje to niskimi właściwościami plastycznymi i wytrzymałościowymi.



Rysunek 7 Zestawione właściwości mechaniczne analizowanej stali wraz ze wzrostem czasu wygrzewania: (a) właściwości wytrzymałościowe, (b) twardość, (c) właściwości plastyczne.

W próbce wyżarzanej przez 15 min ogólna stabilność austenitu szczątkowego jest znacznie niższa (wyższa temperatura  $M_s$ ). Co więcej, zakres wielkości ziarna austenitu szczątkowego w tej próbce znajduje się w najbardziej zakrzywionej części wykresu, co powoduje „uchwycenie” bardzo szerokiego i korzystnego  $\Delta M_s$ , wynoszącego około 120 °C. Ta optymalna (w kontekście wartości wydłużenia równomiernego) stabilność ogólna i jej szeroki zakres, spowodowane różną wielkością ziarna, skutkują stopniowym efektem SIMT w całym zakresie rozciągania, a tym samym wysoką plastycznością. Próbkę wyżarzana przez 300 min pomimo szerokiego zakresu wielkości ziarna łączy w sobie zarówno najniższą średnią stabilność austenitu szczątkowego, jak i jego bardzo wąski zakres. Niska ogólna stabilność jest spowodowana najniższym wzbogaceniem chemicznym i największą średnią wielkością ziarna austenitu

szcątkowego spośród wszystkich próbek. Zakres stabilności jest wąski ( $\Delta M_s$  wynosi około 50 °C), ponieważ większość ziaren austenitu szcątkowego obecnego w próbkach jest zlokalizowana w najbardziej płaskiej części krzywej temperatury  $M_s$ . Dlatego pomimo szerokiego zakresu wielkości ziarna, jego wpływ na stabilność austenitu szcątkowego nie jest zróżnicowany. Powoduje to masową przemianę austenitu szcątkowego w początkowej fazie deformacji, ponieważ duża frakcja ziaren austenitu szcątkowego wykazuje podobną stabilność mechaniczną. Przedstawiona na Rysunku 8 zależność stabilności średniej i lokalnej austenitu wyjaśnia, dlaczego wydłużenie równomierne próbki wyżarzanej przez 300 min jest gorsze w porównaniu z próbką wyżarzaną przez 15 min, mimo że dla tej pierwszej udział austenitu szcątkowego jest wyższy o 8 %.

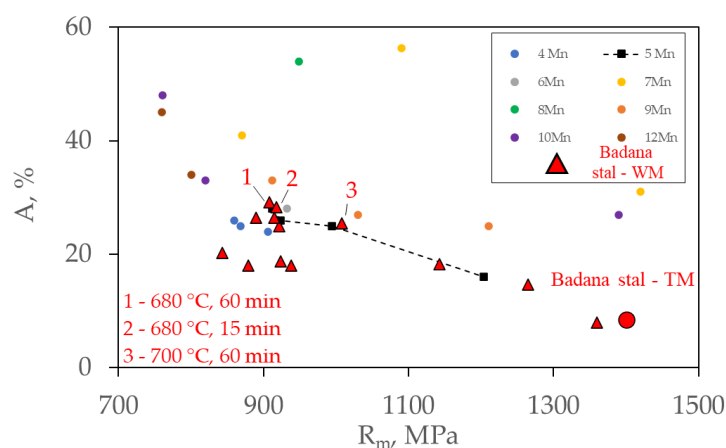


Rysunek 8 Wpływ wielkości ziarna austenitu szcątkowego na temperaturę  $M_s$  próbek wyżarzanych przez 1 min, 5 min i 300 min w 680 °C.

## 6. Wnioski

Na rysunku 9 przedstawiono wyniki badań nad parametrami wyżarzania międzykrytycznego przeprowadzonych w niniejszej pracy. Są one porównane z właściwościami stali obrabianej termomechanicznie oraz z doniesieniami literaturowymi dla różnych stali średniomanganowych wyżarzanych międzykrytycznie. Wszystkie badane warianty wyżarzania międzykrytycznego, poza wyżarzaniem w 800 °C, skutkują znacznie lepszą plastycznością w porównaniu ze stalą obrabianą termomechanicznie. Próbki o najlepszych własnościach mechanicznych zostały zestawione w Tabeli 2. Wszystkie wykazują właściwości wyższe niż założone w pracy ( $> 30\%$  austenitu szcątkowego,  $A_r \geq 15\%$ ,  $A \geq 25\%$  i  $R_m \geq 900$  MPa). Próbki te wykazują właściwości mechaniczne nieco lepsze niż tendencja obserwowana w literaturze dla podobnych składów chemicznych. Odpowiadają one bardziej wynikom uzyskanym dla stali średniomanganowych o wyższej zawartości tego pierwiastka. Poprawa

plastyczności jest ważnym krokiem rozwoju stali średniomanganowych, ponieważ pozwala na uzyskanie porównywalnych właściwości mechanicznych w stalach o niższej zawartości manganu. Nie tylko pozwala to na obniżenie kosztu stopu, ale także może wpłynąć na zmniejszenie problemów technologicznych związanych z tym pierwiastkiem, takich jak możliwa mikrosegregacja, kruchość wodorowa czy zwiększone opory podczas obróbki plastycznej na gorąco. Uzyskane wyniki potwierdzają tezę pracy, że właściwe dobranie udziału i stabilności austenitu szczątkowego poprzez optymalizację temperatury czasu wyżarzania międzykrytycznego pozwala na uzyskanie stopniowej, indukowanej odkształceniem przemiany martenzytycznej sterowanej wielkością ziarna, a tym samym poprawę plastyczności stali, szczególnie w porównaniu ze stalą obrabianą termomechanicznie.



Rysunek 9 Porównanie właściwości mechanicznych uzyskanych podczas badań nad wyżarzaniem międzykrytycznym (WM) w porównaniu ze stalą obrabianą termomechanicznie (TM) i stalami średniomanganowymi o innych zawartościach Mn.

Tabela 2 Parametry obróbki cieplnej, udział austenitu szczątkowego i właściwości mechaniczne próbek o najwyższej plastyczności, RA - austenit szczątkowy.

Temp., °C	Czas, min	RA, %	Re, MPa	Rm, MPa	Ar, %	A, %
680	60	36	670	910	17.5	31
680	15	32	720	920	19	26
700	60	41	530	1010	15	25.5

Wyjaśnienie zjawisk strukturalnych zachodzących podczas wyżarzania międzykrytycznego walcowanej na gorąco stali średniomanganowej z dodatkiem Al w zależności od zastosowanych parametrów temperaturowo-czasowych obróbki cieplnej oraz optymalizacja

tych parametrów skutkująca poprawą plastyczności stali pozwoliła na osiągnięcie założonego celu pracy.

Główne wnioski z pracy to:

1. Czas procesu potrzebny do uzyskania międzykrytycznej równowagi fazowej skraca się wraz ze wzrostem temperatury wyżarzania. W temperaturze 680 °C wszystkie zjawiska/procesy zachodzące podczas wygrzewania (zmiany udziału i wielkości ziarna austenitu szczątkowego, redystrybucja pierwiastków), a tym samym ewolucja stabilności austenitu są najbardziej dynamiczne w pierwszych 15 minutach wyżarzania.
2. Zarówno wzrost temperatury jak i czasu wyżarzania powodują zwiększenie udziału austenitu w mikrostrukturze. Powstawaniu austenitu towarzyszy jednak zubożenie tej fazy w C i Mn oraz wzrost wielkości ziarna. Czynniki te powodują spadek jej stabilności. Najwyższy możliwy do utrzymania udział austenitu szczątkowego w analizowanej stali wynosi około 41 % podczas 60 min wyżarzania w temperaturze 700°C lub co najmniej 120 min wyżarzania w temperaturze 680 °C.
3. Plastyczność analizowanej stali rośnie wraz ze wzrostem udziału austenitu szczątkowego. Jednak próbka wyżarzana w 700 °C pomimo najwyższej frakcji austenitu szczątkowego (>40 %) wykazuje ograniczoną plastyczność (~26 %) ze względu na niską stabilność tej fazy, co skutkuje nasilonym efektem SIMT na wczesnym etapie deformacji.
4. Lokalna stabilność austenitu szczątkowego jest kontrolowana przez zakres wielkości jego ziarna w mikrostrukturze. Szeroki zakres wielkości ziaren powinien skutkować stopniową przemianą martenzytyczną indukowaną odkształceniem. Jednak zasada ta nie obowiązuje zawsze, ponieważ funkcja przedstawiająca wpływ wielkości ziarna austenitu szczątkowego na jego stabilność jest paraboliczna. Zatem podobny zakres wielkości ziarna, ale o innej wartości średniej, powoduje różny przebieg SIMT.
5. Zastosowanie stosunkowo prostego procesu wyżarzania międzykrytycznego analizowanej, gorącowałcowanej stali średniomanganowej powoduje uzyskanie wysokiego udziału austenitu szczątkowego (do 40 %) oraz wysokich właściwości mechanicznych ( $R_m > 900$  MPa,  $A > 25$  %). Świadczy to o bardzo dużym potencjale analizowanej stali do jej zastosowania w przemyśle motoryzacyjnym i innych.